

## University of Southampton Research Repository ePrints Soton

Copyright © and Moral Rights for this thesis are retained by the author and/or other copyright owners. A copy can be downloaded for personal non-commercial research or study, without prior permission or charge. This thesis cannot be reproduced or quoted extensively from without first obtaining permission in writing from the copyright holder/s. The content must not be changed in any way or sold commercially in any format or medium without the formal permission of the copyright holders.

When referring to this work, full bibliographic details including the author, title, awarding institution and date of the thesis must be given e.g.

AUTHOR (year of submission) "Full thesis title", University of Southampton, name of the University School or Department, PhD Thesis, pagination



FACULTY OF ENGINEERING, SCIENCE & MATHEMATICS  
School of Engineering Sciences

**MATERIALS SELECTION FOR MICROSYSTEMS ACTUATORS**

by

**Prasanna Srinivasan**

Thesis for the degree of Doctor of Philosophy

August 2008

*In ever loving remembrance  
of my Dad Late. Srinivasan Arunachalam*

# ABSTRACT

The recent developments of novel thin film materials and their associated processes have marked the onset of change in the design philosophy of Micro-Electro-Mechanical Systems (MEMS) from process centric to performance centric. This presents an opportunity to improve the performance of MEMS devices by materials selection beyond the commonly preferred candidates compatible with the Complimentary-Metal-Oxide-Semiconductor (CMOS) processes which forms the principal motivation of the present research. This thesis focuses on the selection of suitable materials choices for realising high performance MEMS actuators. The thermomechanical design for a generic cantilever bi-layered structure was evolved using a temperature dependent quasi-static analysis. The closed form solutions for mechanical performances (displacement/tip slope, blocked force/moment, work per unit volume) were obtained applying Timoshenko bimetallic theory for an Euler-Bernoulli beam subjected to electrothermal, piezoelectric and shape memory actuations. The thermal performance (actuation frequency) was evaluated using lumped heat capacity models. Contours of equal performance were plotted in the domain of governing material properties on Ashby's selection maps to identify and rank promising candidates for further analysis. A few novel material combinations such as Zn and Ni on Si and Diamond-like-carbon (DLC) substrates perform better than conventional material combination (Al on Si) for high work per volume bimaterial electrothermal actuators. Actuation frequencies of the order of  $\sim 10$  kHz can be achieved electrothermally at scales less than  $100 \mu\text{m}$  using engineering alloys. Although engineering polymers on Si are promising for high displacement electrothermal actuators, their low elastic moduli have to be compensated by a large thickness for an optimal performance. Pb based piezoceramics on Si/DLC substrates are promising for high force piezoelectric MEMS actuators. Piezoelectric actuators operate at mechanical resonance ( $> 100$  kHz) and hence the achievable frequencies are greater than that of the electrothermal actuators. However, the work per unit volume delivered is lower than that of the electrothermal actuators. Nitinol (NiTi shape memory alloy) on Si/DLC are promising material combination for high work per volume actuation at a few hundred Hz. Actuation achieved by electrothermal buckling of a fixed-fixed structure was found to be superior to the bimaterial flexural

actuators in delivering a large work per volume. A detailed comparison of the maximum achievable performance for different actuation schemes was made to facilitate the selection of actuators and the associated material choices for any application. The suitability of Al-Si bimaterial electrothermal actuators for low speed distributed flow control applications was assessed by comparing their performance with the more obviously suitable Si-PZT bimaterial piezoelectric actuators. A detailed processing route for microfabricating Al-Si<sub>3</sub>N<sub>4</sub> bimaterial electrothermal actuators was developed and the associated micromachining issues were discussed. The experimental evaluation of the mechanical and thermal performance metrics of the microfabricated structures is expected to be accomplished in the future, for comparison with the analytical estimates and for subsequent validation by finite element analysis. The general framework of the materials selection strategy and the ranking of the potential candidates presented here will form a basis for the rational design of the MEMS actuators with an improved performance. The outcomes of this thesis also have set up an agenda for long term research goals which include exploration of novel actuator shapes/schemes, understanding of the process-property relations to tailor thin film properties and a comprehensive assessment of other novel substrate materials and their processes for MEMS actuator structures.

# LIST OF CONTENTS

<b>i</b>	<b>List of figures</b>	<b>vii</b>
<b>ii</b>	<b>List of tables</b>	<b>xiii</b>
<b>iii</b>	<b>Declaration of authorship</b>	<b>xiv</b>
<b>iv</b>	<b>Acknowledgements</b>	<b>xvi</b>
<b>v</b>	<b>Symbols and abbreviations used</b>	<b>xviii</b>
<b>1</b>	<b>Performance of microsystems - A materials perspective</b>	
1.1	Introduction to microsystems	1
1.2	Influence of materials on the performance of MEMS actuators	3
1.3	Materials issues in MEMS design	6
1.4	Motivation and research objectives	7
1.5	Thesis structure	7
<b>2</b>	<b>Materials selection for bimaterial electrothermal microactuators</b>	
2.1	MEMS materials set for BMET actuator structures - A review	9
2.2	Mechanics of a thermal bimaterial actuator	11
2.3	Evaluation of the performance metrics	12
2.3.1	Evaluation of free-end slope	12
2.3.2	Evaluation of blocked moment	13
2.3.3	Evaluation of maximum work per volume	13
2.4	Optimisation of the performance metrics of BMET actuators	15
2.4.1	Optimisation of free-end slope/displacement	15
2.4.2	Optimisation of blocked moment	17

2.4.3	Optimisation of maximum work per volume	19
2.5	Candidate materials for bimaterial actuator design	21
2.6	Materials selection process for BMET actuators	32
2.7	Summary	34
<b>3</b>	<b>Effect of heat transfer on materials selection for bimaterial electrothermal actuators</b>	
3.1	Effect of electrothermal heating on the actuator response	35
3.2	Thermomechanical design of a BMET actuator - An overview	37
3.3	Evaluation of equivalent thermal properties	39
3.3.1	Equivalent thermal conductivity	39
3.3.2	Equivalent volume specific heat	40
3.3.3	Equivalent emissivity	40
3.3.4	Power generated per unit volume	40
3.4	Steady state temperature field of a bimaterial cantilever	41
3.5	Transient thermal response of a bimaterial cantilever	43
3.6	Effectiveness and efficiency of a BMET actuator	45
3.7	Heat transfer consideration in the materials selection	47
3.8	Influence of thermal response on the materials selection	62
3.9	Summary	73
<b>4</b>	<b>Design of electrothermal buckling microactuators</b>	
4.1	Design configuration for an improved performance	75
4.2	Mechanics of an out-of-plane electrothermal buckling actuator	76
4.3	Estimation of the critical temperature difference for ETB actuation	77
4.4	Failure characteristics of an ETB actuator structure	78

4.5	Evaluation of the performance metrics of ETB actuator structure	80
4.5.1	Maximum deflection	80
4.5.2	Blocked force and the maximum work per volume	80
4.5.3	Electromechanical efficiency	83
4.6	Transient thermal response of an ETB actuator structure	84
4.7	Influence of pre-stress on the performance of ETB actuator	86
4.8	Candidate materials for ETB actuators	88
4.9	Summary	90

## **5 Materials selection for bimaterial piezoelectric microactuators**

5.1	Introduction on the piezoelectric microactuators	92
5.2	Mechanics of a BMPE actuator structure	94
5.3	Performance limits of BMPE actuator structures	97
5.4	Materials selection process for BMPE actuators	110
5.5	Summary	113

## **6 Materials selection for thermally actuated pneumatic and phase change microactuators**

6.1	Introduction on thermo-pneumatic and phase change microactuators	114
6.2	Mechanics of a thermally actuated pneumatic actuator	116
6.3	Mechanical design of the diaphragm structure	118
6.3.1	Diaphragm as an axi-symmetric plate	119
6.3.2	Effect of pre-tension on the actuator performance	127
6.3.3	Effect of boss size on the actuator performance	128
6.4	Thermal performance of thermo-pneumatic actuator	131
6.5	Candidate materials for thermo-pneumatic actuators	134



6.6	Candidate materials for phase change actuators	135
6.7	Performance limits of thermo-pneumatic and phase change actuators	136
6.8	Summary	139
<b>7 Selection of microactuators based on performance</b>		
7.1	Transition in the design philosophy of MEMS	140
7.2	Comparison of the performance limits of microactuators	140
7.3	Detailed design of microactuators for boundary layer flow control	146
7.3.1	Role of MEMS technology in flow control	146
7.3.2	Introduction on distributed flow control	147
7.3.3	Mechanics of a bimaterial flow control actuator	151
7.3.4	Analysis of the design space for flow control microactuators	152
7.3.5	Finite element analysis of a BMET actuator structure	161
7.4	Micromachining of Al-Si <sub>3</sub> N <sub>4</sub> BMET microactuators	164
7.5	Summary	179
<b>8 Conclusions and recommendations</b>		
8.1	Discussion and summary	181
8.2	Key contributions of the research	183
8.3	Future scope and recommendation	184
8.4	Closing remarks	186
<b>References</b>		187

# LIST OF FIGURES

Figure no.	Caption	Page no.
2.1a - b	(a) Geometric definition of a bimaterial cantilever; (b) Free body diagram of a bimaterial cantilever subjected to a uniform temperature difference, $\Delta T$ .	11
2.2	Operating characteristics of a bimaterial electrothermal actuator.	14
2.3	Contours of optimal thickness ratio, $\log_{10}(\xi_o)$ for a given material pair to deliver maximum free-end slope, blocked moment and work per unit volume.	16
2.4	Contours of optimal normalised moment, $\log_{10}(M_{no})$ for a given pair of materials.	18
2.5	Contours of optimal normalised work per unit volume, $\log_{10}(W_{no})$ for a given pair of materials.	20
2.6a - e	Comparison of the operating characteristics of bimaterial actuators made of different substrates with (a) Nickel, (b) Copper, (c) Aluminium, (d) Gold, and (e) Polyimide for $\xi = 0.5$ .	22
2.7a - e	Comparison of the energy indices of (a) Nickel, (b) Copper, (c) Aluminium, (d) Gold, and (e) Polyimide on different substrates.	23
2.8	Contours of $\log_{10}(W_{no})$ for different materials on a silicon substrate.	25
2.9	Contours of equal performance for different classes of materials on a silicon substrate plotted on Ashby's selection chart [17].	26
2.10a - b	Contours of $\log_{10}(W_{no})$ with reference to (a) $\text{SiO}_2$ substrate, (b) PMMA substrate.	29
2.11a - b	Contours of $\log_{10}(M_{no})$ with reference to (a) $\text{SiO}_2$ substrate, (b) PMMA substrate.	31
3.1	Schematic of a bimaterial cantilever heated electrically.	37
3.2a - b	(a) Thermal model of a bimaterial cantilever; (b) Energy flow across the control volume considered.	41
3.3a - b	Contours of (a) $\log_{10}(P_1)$ , (b) $\log_{10}(V_1)$ for different classes of materials on silicon which acts as a heat source.	50

<b>Figure no.</b>	<b>Caption</b>	<b>Page no.</b>
3.4	Contours of equal $\log_{10}(P_1)$ for materials of different classes on (a) DLC, (b) PMMA substrates.	51
3.5	Comparison of the isotherms for different classes of materials on silicon with Ashby selection chart [17] considering heat dissipation due to conduction ( $V = 5$ volts).	52
3.6a - b	Steady state isotherms for different classes of materials on (a) Aluminium ( $V = 0.1$ volts), (b) PMMA ( $V = 5$ volts).	54
3.7a - b	Isotherms for different classes of materials on silicon considering heat dissipation due to conduction and free convection for (a) $L = 100 \mu\text{m}$ , (b) $L = 1$ mm.	55
3.8a - b	Contours of effectiveness indices normalised with respect to $(\Delta\alpha)$ for different classes of materials on silicon (a) Contours of equal $\log_{10}(M_{EI})$ ; (b) Contours of equal $\log_{10}(W_{EI})$ .	56
3.9	A typical transient cooling curve of a bimaterial approximated by linear response.	57
3.10	Contours of equal efficiency, $\log_{10}(\eta_{em})$ for different bimaterial combinations with reference to a silicon substrate.	59
3.11	Effect of operating temperatures on the actuation frequency and the work per volume.	59
3.12a - b	Contours of equal actuation frequency, $\log_{10}(f)$ for different classes of materials on silicon for (a) $L = 100\mu\text{m}$ , (b) $L = 1$ mm at $\xi = 0.5$ .	60
3.13a - b	Contours of equal actuation frequency, $\log_{10}(f)$ for different classes of materials on (a) DLC substrate, (b) PMMA substrate at $\xi = 0.5$ .	61
3.14a - b	Effect of forced convection on the (a) steady state isotherms (in Kelvin); (b) actuation frequency, $\log_{10}(f)$ for different classes of materials on silicon at small scale ( $L = 100 \mu\text{m}$ ).	70
3.15	Increase in the actuation frequency, $\log_{10}(f)$ accomplished by (a) reducing the scale ( $L = 60\mu\text{m}$ ); (b) reducing the operating temperature range (573 K - 423 K) for different materials on Si.	71
3.16	Contours of equal resonant frequency (fundamental flexural mode), $\log_{10}(f_s)$ for different materials on silicon for an optimal thickness ratio at small scale ( $L = 100 \mu\text{m}$ ).	72

Figure no.	Caption	Page no.
4.1a - b	(a) Schematic of the fixed-fixed beam structure subjected to electrothermal buckling; (b) Free body diagram of the structure subjected to equivalent system of forces and moments.	76
4.2	Variation of the thermal buckling index with the thermal expansion coefficient of the material.	77
4.3	Contours of limiting value of $\log_{10}(L/r_g)$ for different classes of materials on Ashby's $E$ vs. $\sigma_f$ selection map.	79
4.4a - b	(a) Schematic of an ETB structure actuating an external lateral spring of stiffness, $k_s$ ; (b) Free body diagram of an ETB actuator structure actuating the external spring.	81
4.5	Operating characteristics of an ETB actuator ( $L/t \sim 60$ ; $b = 62 \mu\text{m}$ ; $t = 2 \mu\text{m}$ ). The constant value of $y_{\text{max}}$ irrespective of the materials chosen is attributed to the fixed buckling strain for a given geometry.	82
4.6a - b	(a) One dimensional transient thermal model of an ETB actuator structure; (b) Energy transfer across the control volume considered.	85
4.7	A plot of efficiency ratio, $\eta_{\text{em}}^p/\eta_{\text{em}}$ as a function of dimensionless strain, $\epsilon'$ .	87
4.8a - b	(a) Iso-stress contours, $\log_{10}(\sigma_c)$ in GPa for Si ETB structure for a range of slenderness ratios and critical temperature differences; (b) Transient thermal response of a Si ETB actuator structure. All temperature values are in Kelvin.	89
5.1	Schematic of a bimaterial cantilever piezoelectric actuator structure.	94
5.2	Schematic of a cantilever BMPE actuator (a) actuation in $d_{31}$ mode, (b) actuation in $d_{33}$ mode.	96
5.3a - c	Contours of equal tip slope ( $\log_{10}(\Theta_{\text{no}})$ ), blocked moment ( $\log_{10}(M_{\text{no}})$ ) and work per volume ( $\log_{10}(W_{\text{no}})$ ) for a range of piezoelectric materials on (a) Si, (b) DLC, and (c) PMMA substrates.	100-101
5.4	Contours of equal actuation frequency ( $\log_{10}(f_s)$ ) for different piezoelectric materials on Si, DLC and PMMA substrates ( $L = 100 \mu\text{m}$ ; $L/t = 30$ ).	101
5.5	Contours of electromechanical efficiency, $\log_{10}(\eta_{\text{em}})$ for different piezoelectric materials on Si, DLC and PMMA substrates.	102

Figure no.	Caption	Page no.
5.6	Effect of different material combinations on the actuation voltage for an optimal performance under a constant electric field.	104
5.7	Effect of material combinations on the loss coefficient (hence the $Q$ - factor) of BMPE actuators for a range of substrates considered.	105
5.8a - b	(a) Ideal electromechanical transduction circuit for BMPE actuators; (b) Equivalent circuit of the ideal transduction obtained by applying Thevenin and Norton theorems.	106
5.9	Contours of blocked capacitance index, $[C_{be}]_I$ , for different active materials on Si and DLC substrates.	109
5.10	Contours of equal electromechanical transduction index, $\log_{10}((\phi)_I)$ for different materials on the range of substrates considered.	109
6.1	Schematic of a thermo-pneumatic actuator structure.	117
6.2	Schematic of a circular axi-symmetric clamped diaphragm actuated thermo-pneumatically.	119
6.3	Operating characteristics of thermo-pneumatic actuator.	121
6.4	A plot of optimal material index, $M_{po}$ as a function of $T_r$ .	123
6.5a - b	(a) Contours of optimal aspect ratios of an axi-symmetric plate for a range of dimensionless moduli within the temperature range considered; (b) Contours of $P_r$ , $V_r$ and $W_r$ as a function of $E'$ and $T_r$ for an axi-symmetric plate structure ( $V' = 50$ ; $\beta = 50$ ).	125
6.6a - b	(a) Contours of optimal aspect ratios of an axi-symmetric membrane for a range of dimensionless moduli within the temperature range considered; (b) Contours of $P_r$ , $V_r$ and $W_r$ as a function of $E'$ and $T_r$ for an axi-symmetric membrane structure ( $V' = 50$ ; $\beta = 50$ ; $k_m = 100$ ).	126
6.7	Schematic of a circular axi-symmetric clamped diaphragm with boss actuated thermo-pneumatically.	129
6.8	Variation in $B_{bp}$ with respect to the ratio of boss radii, $\zeta_b$ .	129
6.9a - b	(a) Contours of optimal aspect ratios of axi-symmetric plate with boss for a range of dimensionless moduli within the temperature range considered ( $\zeta_b = 0.5$ ); (b) Contours of $P_r$ , $V_r$ and $T_r$ as function of $E'$ and $T_r$ for axi-symmetric plate with a boss feature ( $V' = 50$ ; $\beta_o = 50$ ; $\zeta_b = 0.5$ ).	130

<b>Figure no.</b>	<b>Caption</b>	<b>Page no.</b>
6.10	(a) One dimensional heat transfer model for transient thermal response; (b) Energy transfer across the control volume considered.	133
7.1	Comparison of the performance of NiTi shape memory alloy with different classes of engineering materials with respect to silicon substrates.	144
7.2	A fully developed boundary layer over a flat plate [151].	147
7.3	Schematic of an active open loop flow control implementation.	149
7.4	Schematic of a bimaterial cantilever valve actuator operating against a pressure difference.	151
7.5a	Performance of Al-Si BMET actuators for turbulent boundary layer flow control.	154
7.5b	Design envelope for Al-Si BMET actuator structures for turbulent boundary layer control.	155
7.6a	Performance of PZT-Si BMPE actuators for turbulent boundary layer flow control.	157
7.6b	Design envelope for PZT-Si BMPE actuator structures for turbulent boundary layer control.	158
7.7	Transient heat transfer loss per cycle to the ambient for a temperature difference of 125 °C.	160
7.8	Vertical deflection of the actuator structure due to pre-stress and pressure difference. All deflections are in m.	162
7.9	Steady state temperature field for a BMET actuator corresponding to valve closure. All temperatures are in Kelvin.	162
7.10	Vertical deflection of the BMET structure at the valve closure position. All deflections are in m.	163
7.11	Near iso-thermal state in the transient thermal response of the BMET actuator structure. All temperatures are in Kelvin.	163
7.12	Process flow sequence to micromachine Al-Si <sub>3</sub> N <sub>4</sub> BMET actuator structures.	165 -169
7.13a	Layout of BET-1 mask used in processing steps 5 and 11. The shaded region represents the chrome coated opaque area.	171

<b>Figure no.</b>	<b>Caption</b>	<b>Page no.</b>
7.13b	Layout of BET-2 mask used in processing step 16. The shaded region represents the chrome coated opaque area.	172
7.14	Effect of etch time on the undercut of (a) clamped structure, (b) cantilever structure. (No. of cycles = 33, etching/passivation time = 12/7 s, RF platen power = 13W, etch duration = 16 min 30 s).	173
7.15	Effect of etch time on the undercut of (a) clamped structure, (b) cantilever structure. (No. of cycles = 18, etching/passivation time = 12/7 s, RF platen power = 13W, etch duration = 9 min 5 s).	174
7.16	Unreleased clamped structure for the reduced etch time (No. of cycles = 18, etching/passivation time = 12/7 s, RF platen power = 13W, etch duration = 9 min 5 s).	175
7.17a - c	Optical microscopic images of microfabricated Al-Si <sub>3</sub> N <sub>4</sub> cantilever bimaterial actuators of length (a) $L = 40 \mu\text{m}$ , (b) $L = 100 \mu\text{m}$ , and (c) $L = 200 \mu\text{m}$ .	176
7.18	Optical microscopic images of microfabricated Al-Si <sub>3</sub> N <sub>4</sub> fixed-fixed bimaterial actuators of length (a) $L = 40 \mu\text{m}$ , (b) $L = 180 \mu\text{m}$ , and (c) $L = 200 \mu\text{m}$ .	177
7.19	Optical microscopic image of Al-Si <sub>3</sub> N <sub>4</sub> cantilever bimaterial actuator of length, $L = 200 \mu\text{m}$ with damaged electrical contact due to over etch.	178

# LIST OF TABLES

Table no.	Caption	Page no.
2.1	Material properties of conventional materials employed in MEMS design.	21
2.2	Optimal normalised maximum work per volume, $W_{no}$ for different thin films on various substrates considered. The units are in $\text{Jm}^{-3}\text{K}^{-2}$ .	25
2.3	Candidate materials for thermal bimaterial actuators which can deliver large $W_{no}$ on different substrates.	28
2.4	Candidate materials for thermal bimaterial actuators which can deliver large $M_{no}$ on different substrates.	30
3.1	Material properties of single crystal silicon.	48
3.2	Properties of different materials considered based on their thermoelastic performance on silicon.	63
3.3	Performance based on heat transfer analysis for different materials on Si substrate.	64
3.4	Performance based on heat transfer analysis for different films on DLC, Invar and PMMA substrates.	65
3.5	Comparison of the effectiveness indices of different films on Si substrate.	66
3.6	Comparison of the effectiveness indices of different films on DLC, Invar and PMMA substrates.	67
5.1	Elastic and piezoelectric properties of some active materials which might be considered for the BMPE actuator structures	98
5.2	Electromechanical properties of some active materials which might be considered for the BMPE actuator structures.	99
6.1	Properties of materials and gases considered in this study. All properties are representative values at ambient condition (1 atm., 20 °C).	134
6.2	Effect of substrate materials on the actuation frequencies of a polymeric (PMMA) diaphragm ( $t_d = 2 \mu\text{m}$ , $w_c = 100 \mu\text{m}$ and $t_s = 250 \mu\text{m}$ ) thermo-pneumatic actuator for a heater temperature difference of $\sim 150 \text{ }^\circ\text{C}$ .	135
6.3	Properties of paraffin wax.	135
7.1	Comparison of the performance of different actuation schemes at the microscale.	141



# DECLARATION OF AUTHORSHIP

I, PRASANNA SRINIVASAN declare that the thesis entitled MATERIALS SELECTION FOR MICROSYSTEMS ACTUATORS and the work presented in the thesis are both my own, and have been generated by me as the result of my own original research. I confirm that:

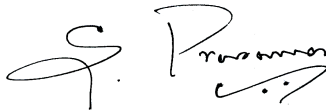
- this work was done wholly or mainly while in candidature for a research degree at this University;
- where any part of this thesis has previously been submitted for a degree or any other qualification at this University or any other institution, this has been clearly stated;
- where I have consulted the published work of others, this is always clearly attributed;
- where I have quoted from the work of others, the source is always given. With the exception of such quotations, this thesis is entirely my own work;
- I have acknowledged all main sources of help;
- where the thesis is based on work done by myself jointly with others, I have made clear exactly what was done by others and what I have contributed myself;
- ~~none of this work has been published before submission, or~~ [delete as appropriate] parts of this work have been published as: [please list references]

## Refereed Journal Publications

1. P. Srinivasan and S. M. Spearing, "Optimal materials selection for bimaterial piezoelectric microactuators", *Journal of Microelectromechanical Systems*, vol. 17, no. 2, pp. 462-472, 2008.
2. P. Srinivasan and S. M. Spearing, "Effect of heat transfer on materials selection for bimaterial electrothermal actuators", *Journal of Microelectromechanical Systems*, vol. 17, no. 3, pp. 653-667, 2008.
3. P. Srinivasan and S. M. Spearing, "Materials selection and design of microelectrothermal bimaterial actuators", *Journal of Microelectromechanical Systems*, vol. 16, pp. 248-259, 2007.

## Conference Proceedings

1. P. Srinivasan and S. M. Spearing, "Design of electrothermal buckling microactuators", *19<sup>th</sup> Micromechanics Europe Workshop, Aachen, Germany*, pp. 89-92, 2008.
2. P. Srinivasan and S. M. Spearing, "Influence of materials on the performance limits of microactuators", *MRS Fall 2007 symposium*, pp. 1052-DD07-03, 2007.
3. P. Srinivasan and S. M. Spearing, "Effect of electrothermal heating and scaling on the materials selection process for bimaterial actuators", *17<sup>th</sup> Micromechanics Europe Workshop, Southampton*, pp. 145-148, 2006.
4. P. Srinivasan and S. M. Spearing, "Materials selection and design of microelectrothermal actuators", *IET Seminar on MEMS sensors and actuators*, pp. 260-265, 2006.



**Signed:** .....

**Date:**.....10<sup>th</sup> October 2008.....

# ACKNOWLEDGEMENTS

This work would not have taken the present shape without the consistent help and unflinching support of many people over the last three years. I was extremely fortunate to be among some great minds and good hearts during the course of my research.

Firstly, I would like to express my sincere thanks to my research supervisor Prof. S. Mark Spearing, Head of the School of Engineering Sciences, *University of Southampton* for being a source of inspiration and support during the tenure of my research. It was a great learning experience for me to be professionally associated with him and I thoroughly enjoyed every aspect of my research under his able guidance.

I cannot forget Prof. Neil Stephen, Computational Engineering Design Group, *University of Southampton* who played a significant role in improving the quality of my thesis through his witty comments and suggestions. Every technical discussion with him on the mechanics of actuation improved my level of understanding on the subject. I really enjoyed his professional acquaintance during the tenure of my research.

Due thanks to Dr. Atul Bhaskar, Computational Engineering Design, *University of Southampton* for his valuable suggestions in improving the structural models of the actuators.

I sincerely thank Prof. Sergei Chernyshenko, *Imperial College, London*, for educating me on the fundamentals of fluid dynamics relevant to flow control. His wealth of knowledge in flow physics helped me to acquire the relevant background required for the device design. I gratefully acknowledge his contribution in Section 7.3 which added a new dimension to this thesis from application perspective.

The microfabrication task would not have been accomplished without the prolonged help and support of many people. I sincerely thank Prof. Mark Sheplak, Vijay Chandrasekharan, Benjamin Griffin and Matt Williams from the Interdisciplinary Microsystems Group, *University of Florida, Gainesville, U.S.A* for their tremendous effort over the last one year in micromachining the actuator structures.

I would like to acknowledge the expertise I received from Prof. Michael Kraft and Dr. Steve Beeby, Electronics and Computer Science, *University of Southampton*, and Dr. Liudi Jiang, School of Engineering Sciences, *University of Southampton* on the micromachining processes which bolstered my effort towards the design of optical masks.

The financial assistance provided by the governing bodies of the *Overseas Research Student Awards Scheme* and the *University of Southampton* is gratefully acknowledged. Due thanks to Prof. S. Mark Spearing again for assisting me to procure travel awards for attending conferences besides funding for the optical masks.

I would like to thank our research group secretary, Gwyneth Skiller for her wonderful support on administrative activities. The assistance provided by Paul Bosson for the maintenance and support of the computing facilities is duly acknowledged.

I thank all the members of the Materials and Surface Engineering research group for creating an intellectual and friendly environment throughout my PhD program. My research colleagues Mandar, Sun Dan, Jenny, Mark Craig, Xiao, Nick, Toby, Sobia, Pete, Lily, Fitri, Andrew and Thomas deserve a special mention here. Due to thanks to my friend Raja, TCS, India for his long standing support since my *IIT-Madras* days.

Last but not the least; I would like to thank my mom, sister, brother-in-law and my cousin, Rajesh for their patience, love and support throughout the tenure of my research.

# SYMBOLS AND ABBREVIATIONS USED

## List of symbols

English Symbols	Definitions	Units
$b$	Width of the actuator structure	m
$d$	piezoelectric strain coefficient	CN <sup>-1</sup> or mV <sup>-1</sup>
$f$	Actuation frequency	Hz
$f_b$	Bursting frequency of the low speed streaks	Hz
$f_s$	Structural resonant frequency	Hz
$h$	Heat transfer coefficient	Wm <sup>-2</sup> K <sup>-1</sup>
$k$	Electromechanical coupling factor of piezoelectric material	-
$k_b$	Bending stiffness of the actuator	Nm <sup>-1</sup>
$k_m$	Non-dimensional pre-tension parameter	-
$k_s$	Spring stiffness	Nm <sup>-1</sup>
$k_s^f$	Stiffness of the fluid cavity	Nm <sup>-5</sup>
$k^\theta$	Circular wave number, i.e., number of waves per unit spatial length	m <sup>-1</sup>
$l$	Wall unit of the fluid	m
$n_s$	Number of streaks within the area to be controlled	-
$\dot{q}$	Heat generation per unit volume	Wm <sup>-3</sup>
$\hat{q}$	Heat flux	Wm <sup>-2</sup>
$r_g$	Radius of gyration	m
$s$	Specific entropy	Jkg <sup>-1</sup> K <sup>-1</sup>
$t$	Total thickness of the actuator structure	m
$t_d$	Thickness of the diaphragm	m
$t_1, t_2$	Thicknesses of the bi-layers 1 and 2 respectively	m
$t_c'$	Time taken to cool between the operating temperature limits	s
$y$	Displacement of the actuator structure	m
$y_{\max}$	Maximum displacement of the actuator structure	m

English Symbols	Definitions	Units
$Bi$	Biot number	-
$C$	Specific heat capacity of the substance	$\text{Jkg}^{-1}\text{K}^{-1}$
$C_{be}$	Blocked electrical capacitance	farad
$C_m$	Stiffness component in electromechanical domain	$\text{Nm}^{-1}$
$D$	Flexural rigidity of an isotropic plate structure	$\text{Nm}^{-1}$
$E$	Elastic modulus of the material	$\text{Nm}^{-2}$
$E_s$	Strain energy per unit volume	$\text{Jm}^{-3}$
$E'_s$	Electrical energy per unit volume stored	$\text{Jm}^{-3}$
$E_1$	Energy index of a bimaterial structure	-
$E_1, E_2$	Elastic moduli of the bi-layers 1 and 2 respectively	$\text{Nm}^{-2}$
$E^p$	Electric field across the piezoelectric layer	$\text{Vm}^{-1}$
$E_C^p$	Coercive field of the piezoelectric material	$\text{Vm}^{-1}$
$E_{IC}^p$	Intrinsic coercive field of the piezoelectric material	$\text{Vm}^{-1}$
$E'$	Dimensionless modulus (ratio of elastic modulus to the atmospheric pressure)	-
$F_b$	Blocked force	N
$F_o$	Fourier number	-
$G$	Transfer function for the electromechanical system	$\text{NV}^{-1}$
$K$	Bulk modulus of the material	$\text{Nm}^{-2}$
$L$	Length scale of the actuator structure	m
$L_c$	Characteristic length, i.e. ratio of the volume to the surface area	m
$L_m$	Lumped mass component in electromechanical domain	kg
$M_b$	Blocked moment	Nm
$M_{bo}$	Optimal blocked moment	Nm
$M_n$	Normalised blocked moment	$\text{Nm.m}^{-3}\text{K}^{-1}$
$M_{no}$	Optimal normalised blocked moment	$\text{Nm.m}^{-3}\text{K}^{-1}$
$M_{bp}$	Material index of the bossed plate structure	-

English Symbols	Definitions	Units
$M_{\text{eff}}$	Effectiveness based on moment	$\text{NmW}^{-1}$
$M_{\text{m}}$	Material index of the membrane structure	-
$M_{\text{p}}$	Material index of the plate structure	-
$M_{\text{EI}}$	Effectiveness index corresponding to $M_{\text{eff}}$	$\text{NW}^{-1} \text{m}^{-1}$
$M_1$	Moment index of bimaterial structure	-
$M_1, M_2$	Normalised internal moments in the bi-layers 1 and 2 respectively	N
$N_1, N_2$	Normalised internal forces in the bi-layers 1 and 2 respectively	$\text{Nm}^{-1}$
$P_{\text{c}}$	Fundamental critical load required to buckle the structure	N
$P_{\text{r}}$	Pressure ratio, $P_2/P_1$	-
$P_1$	Electrothermal power index	$\text{mKW}^{-1}$
$P_1, P_2$	Initial and final states of the pressure	$\text{Nm}^{-2}$
$R$	Radius of the circular diaphragm structure	m
$Re$	Reynolds number	-
$R_{\text{c}}$	Radius of the curvature of the beam	m
$R_{\text{m}}$	Mechanical damping constant in electromechanical domain	$\text{Nm}^{-1}\text{s}$
$T_{\text{av}}$	Nominal average temperature	K
$T_{\text{b}}$	Base temperature	K
$T_{\text{p}}, T_{\text{v}}$	Peak and valley temperatures of the operating range	K
$T_{\text{r}}$	Temperature ratio, $T_2/T_1$	-
$T_1, T_2$	Initial and final states of the temperature	K
$T_{\infty}$	Ambient temperature	K
$T^{\text{C}}$	Curie temperature of the piezoelectric material	K
$U_{\text{t}}$	Internal energy per unit volume	$\text{Jm}^{-3}$
$U_{\infty}$	Free stream velocity of the fluid	$\text{ms}^{-1}$
$V$	Electrical voltage applied across the circuit	V

<b>English Symbols</b>	<b>Definitions</b>	<b>Units</b>
$V_r$	Volume ratio, $V_2/V_1$	-
$V_I$	Voltage index for a bi-layer	$W^{-1}mK$
$V_1, V_2$	Initial and final states of the volume	$m^3$
$V'$	Ratio of the cavity volume to the diaphragm volume	-
$V^*$	Frictional velocity of the fluid	$ms^{-1}$
$W$	Maximum work per unit volume	$Jm^{-3}$
$W_{eff}$	Effectiveness based on work per unit volume	$JW^{-2}$
$W_o$	Optimal maximum work per volume	$Jm^{-3}$
$W_n$	Normalised maximum work per volume	$Jm^{-3}K^{-2}$
$W_{no}$	Optimal normalised maximum work per volume	$Jm^{-3}K^{-2}$
$W_{EI}$	Effectiveness index corresponding to $W_{eff}$	$NW^{-2}$
$Z_L, Z_T$	External and total impedances in the electromechanical domain	$Nm^{-1}s$

<b>Greek Symbols</b>	<b>Definitions</b>	<b>Units</b>
$\alpha$	Thermal expansion coefficient of the material	$m.m^{-1}K^{-1}$
$\alpha_1, \alpha_2$	Thermal expansion coefficients of the bi-layers 1 and 2 respectively	$m.m^{-1}K^{-1}$
$\alpha_{eq}^d$	Equivalent thermal diffusivity	$m^2s^{-1}$
$\beta$	Aspect ratio, i.e., $L/t$ for beam and $2R/t_d$ for circular diaphragm	-
$\chi$	Loss coefficient	-
$\delta$	Boundary layer thickness	m
$\epsilon_{rec}$	Recovery strain	-
$\epsilon_r^d$	Relative dielectric constant of the piezoelectric material	-
$\epsilon^t$	Thermal emissivity of the material	-
$\epsilon_{eq}^t$	Equivalent thermal emissivity	-



<b>Greek Symbols</b>	<b>Definitions</b>	<b>Units</b>
$\sigma_f$	Failure strength of the material	$\text{Nm}^{-2}$
$\gamma$	Adiabatic index	-
$\eta_m$	Mechanical efficiency of the actuator	-
$\eta_{em}$	Electromechanical efficiency	-
$\eta_{em}^p$	Electromechanical efficiency for pre-stressed structures	-
$\kappa$	Thermal conductivity of the material	$\text{Wm}^{-1}\text{K}^{-1}$
$\kappa_{eq}$	Equivalent thermal conductivity	$\text{Wm}^{-1}\text{K}^{-1}$
$\lambda$	Ratio of the elastic moduli of the bi-layers, $E_1/E_2$	-
$\rho$	Density of the substance	$\text{kgm}^{-3}$
$\rho_r$	Electrical resistivity of the material	$\Omega \text{ m}$
$\rho C$	Volume specific heat of the substance	$\text{Jm}^{-3}\text{K}^{-1}$
$(\rho C)_{eq}$	Equivalent volume specific heat	$\text{Jm}^{-3}\text{K}^{-1}$
$\sigma_{nf}$	Normalised strength of the material	-
$\tau_w$	Wall shear stress	$\text{Nm}^{-2}$
$\nu_f$	Kinematic viscosity of the fluid	$\text{m}^2\text{s}^{-1}$
$\xi$	Ratio of the thickness of the bi-layers, $t_1/t_2$	-
$\xi_o$	Optimal thickness ratio	-
$\zeta_b$	Boss ratio of the diaphragm	-
$\Delta t'$	Time increment between initial and final instant	s
$\Delta T$	Nominal temperature difference	K
$(\Delta T)_{BI}$	Thermal buckling index	K
$(\Delta T)_c$	Critical temperature difference corresponding to the onset of buckling	K
$(\Delta T)_c^p$	Critical temperature difference corresponding to the onset of buckling for pre-stressed structures	K
$\Delta\alpha$	Difference in the thermal expansion coefficients of the bi-layers, $(\alpha_1 - \alpha_2)$	$\text{m.m}^{-1}\text{K}^{-1}$
$\phi$	Transduction ratio in electromechanical circuit	$\text{NV}^{-1}$
$\Theta_{eff}$	Effectiveness based on slope	$\text{W}^{-1}$

<b>Greek Symbols</b>	<b>Definitions</b>	<b>Units</b>
$\Theta_f$	Free-end slope	-
$\Theta_{fo}$	Optimal free-end slope	-
$\Theta_n$	Slope based material parameter corresponding to $\Theta_f$	$\text{m.m}^{-1}\text{K}^{-1}$
$\Theta_{no}$	Optimal slope based material parameter corresponding to $\Theta_{fo}$	$\text{m.m}^{-1}\text{K}^{-1}$
$\Theta_{EI}$	Effectiveness index corresponding to $\Theta_{eff}$	$\text{mW}^{-1}$

Any new symbols introduced in the text are defined in the appropriate context as they appear.

### List of abbreviations

<b>Abbreviations</b>	<b>Definitions</b>
BMET	Bimaterial electrothermal
BMPE	Bimaterial piezoelectric
BMSM	Bimaterial shape memory
CMOS	Complimentary metal oxide semi-conductor
ETB	Electrothermal buckling
IC	Integrated circuits
MEMS	Micro-electro-mechanical systems
MOSFET	Metal oxide semi-conductor field effect transistor

Any new abbreviations introduced in the text are defined in the appropriate context as they appear.

# Chapter 1

## Performance of Microsystems - A Materials Perspective

“The interaction between the function, material, shape and process lie at the heart of the material selection process”

- M. F. Ashby, *Material Selection in Mechanical Design*, Chapter 2

### 1.1 Introduction to microsystems

Microsystems or Micro-Electro-Mechanical Systems (MEMS) constitute devices and structures on the scale of a few tens to hundreds of microns but generally not exceeding 1 mm. The feasibility of designing such structures provides an opportunity to realise devices which have impact on the performance of many macro scale engineering systems into which they are integrated. As a result, many exciting avenues have opened recently in different areas of application exploiting the use of MEMS. Some notable areas of application of MEMS devices include, automotive (e.g. accelerometers triggering for air bag deployment), aerospace (e.g. pressure/temperature sensors, flow control devices), biological (e.g. DNA microchip, microcages, microtweezers), bio-medical (e.g. microfluidic pumps used in bio-chips) and consumer electronics (e.g. micromirrors and microswitches). Put simply, MEMS are micromachines engineered to perform certain specific tasks at the microscale. Depending on their function, being active or passive or autonomous, the architecture of most MEMS devices normally consists of on-chip integration of some or all the following functional units namely; a sensory unit (consisting of sensors), an effector unit (consisting of actuators) and the interface power electronics. The ability to integrate MEMS and the electronic integrated circuits (IC) has further enhanced the MEMS functionality by including signal processing, display and control functions. Of late, the physical domains of the integrated functional units have transcended the electromechanical boundaries with the realisation of novel devices incorporating micro reaction chambers/cavities (consisting of microfluidic channels/ducts with heater elements) to perform certain chemical/bio-chemical reactions. The definition of MEMS is therefore tending to become broader in sense beyond the traditionally referred electromechanical systems.

The state-of-the-art attained in MEMS sensor development is more advanced compared to that attained for actuators. This is evident from the lag in realisation of MEMS

actuators as commercial products behind other system level components. This observation provides the principal motivation for this thesis. Although MEMS technology is very promising, the small number of commercially successful MEMS devices clearly indicates the challenges involved in commercialisation of this technology. This may be attributed to several factors including; materials issues, processing constraints and cost, besides the continuous effort to improve the reliability of the devices. The maturation of this technology in realising high performance devices strongly relies on the seamless translation of the associated physical mechanisms at the microscale to equivalent appropriate engineering requirements. This effort has been supported by the recent advances in the development of new materials and processes for thin film layered structures at the microscale thereby opening a gateway for further development. Therefore, with the development of new materials and processes, opportunities arise to overcome the challenges posed in meeting the critical functional requirements in most MEMS applications.

The objective of the present research is to assess quantitatively the role of engineering materials in order to realise high performance MEMS actuators. There has been a general lack of commercial interest in the research aligned in this direction due to the inherent risks associated with investment in the development of new materials and processes. Also, the lead time associated with the development of new materials and processes is long compared to other areas of technology. Consequently, the literature relevant to this area of research is very limited, with the majority published by the academic research groups. Although a few laboratories around the world are involved in the development, processing and characterisation of thin film materials at the microscale, little has hitherto been translated into commercial products. Nevertheless, there are many exciting opportunities to contribute significantly to this knowledge domain which has the potential to bring immense long term benefits.

The continuous research in processing thin film metals, polymers and engineering ceramics on arbitrary substrates has benefited MEMS technology in expanding its limited materials set. As a result, multilayered thin film structures [1, 2] and buried skeleton structures [3] have been considered for MEMS actuators. Furthermore, the on-going fundamental research to develop and process new particulate composite materials with improved properties [4] has further emboldened the effort to integrate MEMS and

CMOS circuits monolithically. With this backdrop regarding materials research relevant to MEMS devices, it is timely to investigate the optimal choice of materials which deliver best performance. The seminal content of this thesis is therefore to identify and rank promising candidate materials by evolving a suitable materials selection strategy for some commonly employed MEMS actuator structures in a generic bi-layered configuration.

Actuators in general, are mechanical transducers which transform any form of input energy to an output mechanical motion. The ability to realise such structures at the microscale has provided the possibility to manipulate objects and structures at that scale. Depending on the magnitude of the external mechanical impedance, a trade-off between the achievable force and displacement is obtained with the available output energy associated with the actuator. A realistic definition of the external mechanical impedance is essential in order to design an actuator which delivers the best performance. Recent studies on the selection of actuators for applications [5], and their classification into families based on their mechanisms and performance [6], provides a basis to identify potential areas for overall improvement in actuator design. Although different actuation mechanisms have been identified and studied, the preference for most commonly employed MEMS actuation schemes such as electrostatic, electrothermal, piezoelectric and shape memory can be attributed to their acceptable performance, ease of fabrication and long term reliability. Optimal design of such actuators requires development of an understanding of the governing mechanisms associated with various actuation schemes which facilitates identifying novel materials for the best performance.

## **1.2 Influence of materials on the performance of MEMS actuators**

In order to identify potential materials choices for improving the performance of MEMS actuators, it is worthwhile to understand the baseline performance of commonly employed MEMS actuators; i.e., electrostatic, electrothermal and piezoelectric actuators. The performance of these actuators in different configurations specific to various microsystems has been already discussed in the literature. However, a reasonably accurate estimate allowing direct comparison of the achievable performance limits with due consideration to length scales is unavailable. The present work is built

on a previous study of the performance maps for various actuator families at the micro and macro scales [6] so that promising materials choices are identified and ranked for commonly employed MEMS actuation schemes.

Electrostatic actuation is preferred for those applications which require a relatively large displacement ( $\sim 10\text{-}40\ \mu\text{m}$ ) at high frequencies ( $\sim 100\ \text{kHz} - 1\ \text{MHz}$ ). Actuation is due to the attractive Coulombic forces between the parallel plates of capacitive MEMS structures. Their change in capacitance due to external perturbation is also exploited for many sensing applications. The most prominent commercial application of electrostatic MEMS actuators is in the digital micromirror devices [7] developed by *Texas Instruments Inc., U.S.A.* The device is an optical chip which consists of an array of micromirrors capable of generating high resolution digital images for the improved performance of projection systems.

Microelectrothermal actuators in general, are particularly promising for applications requiring a large specific work. They are capable of actuating either in-the-plane [8] or out-of-the-plane [9] of the substrate. Actuation is usually achieved by thermal expansion of the materials caused by Joule heating of the substrate materials followed by ambient cooling. Their performance is governed by electrothermal and thermomechanical responses which are dictated by the mechanical, thermal and electrical properties of the materials employed. They are capable of delivering a reasonably large force ( $\sim 10^2\text{-}10^3\ \mu\text{N}$ ) and displacement ( $\sim 10\ \mu\text{m}$ ).

Actuation due to the converse piezoelectric effect based on electromechanical transduction in certain groups of thin film materials (characterised by non-centrosymmetric crystals lacking inversion symmetry) is attractive for MEMS actuator applications. Relatively large forces, of the order  $\sim 1\ \text{mN}$  can be achieved using piezoelectric actuation [6] at the microscale. Some common applications of piezoelectric actuation include inkjet printer heads [10] and micromotors [11]. Actuation frequencies of the order of  $\sim 10^1\text{-}10^2\ \text{kHz}$  can be achieved by piezoelectric actuation. A notable commercial application of piezoelectric actuation is the variable droplet inkjet printer heads developed by *Epson* [12]. *Daewoo Electronics Co. Ltd.*,

came close to commercialising their piezoelectrically actuated thin film micromirror arrays [13] intended for application in projection systems.

The performance of these commercial or near-commercial MEMS actuators is not only affected directly by the materials used but also indirectly by the processes employed for micromachining them. The processing steps have a significant bearing on the material properties and the process-induced residual stresses developed in thin film structures. A good fundamental understanding of the effect of critical process parameters on the material properties and residual stresses is available for a few materials which are the legacy of integrated circuits (IC) fabrication routes. However, for most materials this has not yet been accomplished, and this represents a critical effort in the development path for new materials. Therefore, significant attention is required to address the issues relevant to materials and their associated processes to realise high performance MEMS devices.

Thin film bimaterial structures are the most commonly preferred forms for electrothermal, piezoelectric and shape memory actuators and represent a generic architecture for MEMS actuator structures. The micromachining processes to create such structures are simple which involves deposition of thin film of a material on a substrate. The differential expansion between the layers can be exploited for achieving out-of-the-plane actuation which is difficult to obtain by other means. Actuation normal to the wafer plane is required for many applications such as micromirrors, microvalves and flow control actuators. However, the development of processes resulting in significant reduction of pre-stress in thin films when deposited on an arbitrary substrate is one of the key issues which need to be addressed for most material combinations in order to realise high performance actuators. The present work focuses on the performance improvement achieved from the materials selection for out-of-the-plane microactuators, acknowledging the constraints imposed by the processing routes and thin film pre-stress.

### **1.3 Materials issues in MEMS design**

Design of MEMS in particular is challenging due to the fact that a limited group of materials are available to meet the highly integrated, multi-functional roles of the components [14] and the associated manufacturing processes. This can be attributed to the evolution of MEMS from IC fabrication routes, i.e., Complimentary Metal Oxide Semiconductors (CMOS) and Metal Oxide Semiconductor Field Effect Transistor (MOSFET) technologies. Although materials which inherit the CMOS/MOSFET legacy such as Si, Ge and Al are automatically eligible for MEMS, they are not necessarily the best candidates particularly for micromechanical transducers. This presents a situation where performance of the system depends primarily on the ability to modify the geometry and topology of the structures made of these limited available materials. Although there have been persistent efforts to handle in-plane complexities in the device features by manipulating the topology [15, 16], the ease of achieving the required shapes which give best performance is severely hampered using the currently available micromachining processes. Therefore the constraints imposed by the materials available, and the associated microfabrication routes, on the performance of MEMS devices are partly responsible for the existing gap between research in which a wide variety of materials are used, and commercialisation in which very few materials are employed. This situation persists even though the overall MEMS market size is expected to grow consistently. Hence there is a necessity to establish a materials selection strategy to identify novel candidates which offer better performance than the existing set of materials.

Materials selection is a critical process in the design cycle of all engineering products and systems. About 80,000 materials have been reported to be available for engineers to consider during the preliminary design phase of any engineering system [17]. Hence an effective materials selection strategy is required to identify the potential candidates which can be considered for further analysis. Materials selection strategies in general, are very system specific because they are determined by the physical mechanisms associated with a particular system in order to meet certain functional requirements. An effective strategy is one that facilitates identification and ranking of the potential



candidates for the various functional requirements based on their performance associated with the physical mechanisms.

#### **1.4 Motivation and research objectives**

As MEMS diverge from the conventional CMOS technology, there is a need to expand the range of available materials and associated fabrication routes beyond silicon and its associated materials set. The growing interest in developing thin films of arbitrary materials on various substrates further assists the efforts to engineer materials at the microscale. Hence an opportunity exists to realise high performance MEMS devices by selecting the best materials for further development. The first step in achieving this goal is to identify potential candidates and to rank them based on their performance for various actuation schemes. Although a step towards this goal was made previously for electrostatic actuators by comparing the relevant material indices using Ashby's selection charts [18], further effort is still required to establish design guidelines for other actuation schemes.

The key objectives of the present work are: to develop an analytical framework for selecting the best materials for electrothermal, piezoelectric and shape memory actuators with bimaterial architectures, to rank the potential candidate materials based on their performance for a given set of functional requirements, to study the effect of scaling on the materials selection process which thereby affects the performance and finally to compare the achievable performance limits of different actuation schemes in order to select actuators for given set of system level requirements.

#### **1.5 Thesis structure**

This thesis is organised as follows. Chapter 2 presents an analytical framework for optimal materials selection for bimaterial electrothermal (BMET) microactuators based on the temperature independent quasi-static response of a bimaterial cantilever structure applying simple beam theory. Chapter 3 discusses the effect of resistive heating and scaling on the materials selection for BMET actuator structures by analysing the

competition between different modes of heat transfer at the microscale ( $10\ \mu\text{m} \leq L \leq 1\ \text{mm}$ ). Chapter 4 discusses the analytical framework relevant to electrothermal buckling (ETB) microactuators and comparison of their performance to that of BMET actuators. Chapter 5 discusses a strategy for identifying optimal combinations of active materials and substrates which deliver best performance for bimaterial piezoelectric (BMPE) microactuators. Chapter 6 presents design guidelines for the diaphragms of thermally actuated pneumatic and phase change microactuators. Chapter 7 discusses the selection of actuators for different applications by comparing the performance limits of various actuation schemes. Detailed design and analysis of a BMET actuator structure using finite element models are also presented for a boundary layer flow control application. Relevant mask designs and suitable processes to micromachine representative Al-Si<sub>3</sub>N<sub>4</sub> BMET actuators for a range of length scales are also discussed. Lastly, chapter 8 presents the conclusions drawn from this research highlighting the scope for further research studies.

# Chapter 2

## Materials selection for Bimaterial Electrothermal Microactuators

### 2.1 MEMS materials set for BMET actuator structures - A review

Electrothermal actuators in general, are particularly promising for delivering large displacements (1-100  $\mu\text{m}$ ) and/or high forces (10-100  $\mu\text{N}$ ). Thermal bimaterial actuators, made by simple MEMS fabrication processes provide an easy means to obtain out-of-plane motion which is otherwise difficult to achieve. Their actuation typically utilizes the resistance heating of the actuator elements resulting in differential thermal expansion.

Several bimaterial electrothermal actuators have been demonstrated: a diamond-like carbon (DLC)/Ni microcage [19], a polymeric microgripper made of epoxy based SU8 integrated with Ti/Pt [20] and Au-polyimide on silicon wafers [21] have been suggested as bio-compatible actuators for handling living cells in biomedical and biological applications. Submicron scale electrothermal actuators [22] have been proposed as precise end-effectors for robots. Aluminium films on single crystal silicon [9] have been developed for optical applications such as positioning micromirrors. Thermally actuated probe arrays made of gold on silicon nitride were used for nanolithography [23] applications. A ternary alloy,  $\text{Al}_x\text{Ga}_{1-x}\text{As}$  deposited on GaAs substrate [24], and SU8 polymer coated on silicon [25] were considered for micromachined cantilevers for use in atomic force microscopy. In all these applications it is clear that the choice of materials has been largely driven by what is available to the designers rather than what should be considered for an optimal performance.

Although different approaches to electrothermal actuation [26-29] provide flexibility in meeting functional requirements, surprisingly little attention has focussed on optimising microsystems design based on materials selection. The few published works in this area include: a comparison of the performance of Ti-Al films and Al on Si [30] emphasizing the potential of Ti-Al films in bimaterial actuator design, application of Ashby's approach for selecting suitable candidate materials for purely mechanical elements of

the actuator [31] and comparison of the performance of bimetals and their reliability in macrosystem applications via performance maps [32].

Selection of a particular material depends on its performance against a given set of functional requirements. The thermoelastic performance metrics considered for actuator structures are blocked moment, free-end slope and the maximum work per volume. Blocked moment and free-end slope correspond to the maximum force and maximum displacement achievable. Material combinations that can deliver a large tip slope/displacement, when thermally actuated under fixed-free conditions are suitable candidates for applications such as micromirrors. Blocked force is an important performance criterion for valve structures in microfluidic devices. Maximum work per unit volume is a relevant metric in the design of actuators for displacement micropumps or other flow control devices.

The primary objective of the present study is to develop an approach for identifying potential candidate materials in the preliminary design phase of microelectrothermal actuators which can deliver the best steady state thermomechanical response. Hence variations in the temperature field due to electric effects, heat losses due to different modes of heat transfer and estimation of maximum permissible actuation temperature are not addressed at this stage but discussed in detail in Chapter 3. The materials selection strategy has not considered the effect of scale and processing routes on the material properties at microscale, the influence of pre-stress in the microfabricated structures on the performance and the effect of oxidation/corrosion of materials in the ambient environment. These factors clearly require consideration in the detailed design of a bimaterial actuator.

This chapter is organised as follows. Section 2.2 discusses the mechanics of a thermal bimaterial actuator. Closed form solutions for thermoelastic performance metrics and comparison with results of finite element analysis are illustrated in Section 2.3. The mathematical formulations associated with the optimisation of the performance metrics are discussed in Section 2.4. Section 2.5 presents the materials selection strategy based on the optimisation of performance metrics. Section 2.6 discusses the process employed for candidate materials selection and other factors to be accounted for during the

materials selection. Finally, Section 2.7 summarises the key inferences drawn from this analysis.

## 2.2 Mechanics of a thermal bimaterial actuator

Figure 2.1a shows a thermally actuated bimaterial cantilever structure made of two dissimilar materials with Young's moduli  $E_1$ ,  $E_2$  and thermal expansion coefficients  $\alpha_1, \alpha_2$ . The thicknesses of the layers are  $t_1$  and  $t_2$  and  $L$  is the beam length. In the analysis that follows, forces and moments are normalised by the width,  $b$ . Figure 2.1b shows the effective internal forces ( $N_1$ ,  $N_2$ ) and moments ( $M_1$ ,  $M_2$ ) developed in each layer when the bimaterial is subjected to a uniform temperature difference,  $\Delta T$ . The variable  $\Delta T$  is the difference between the nominal temperature of the bimaterial,  $T$  and the ambient temperature,  $T_\infty$ .

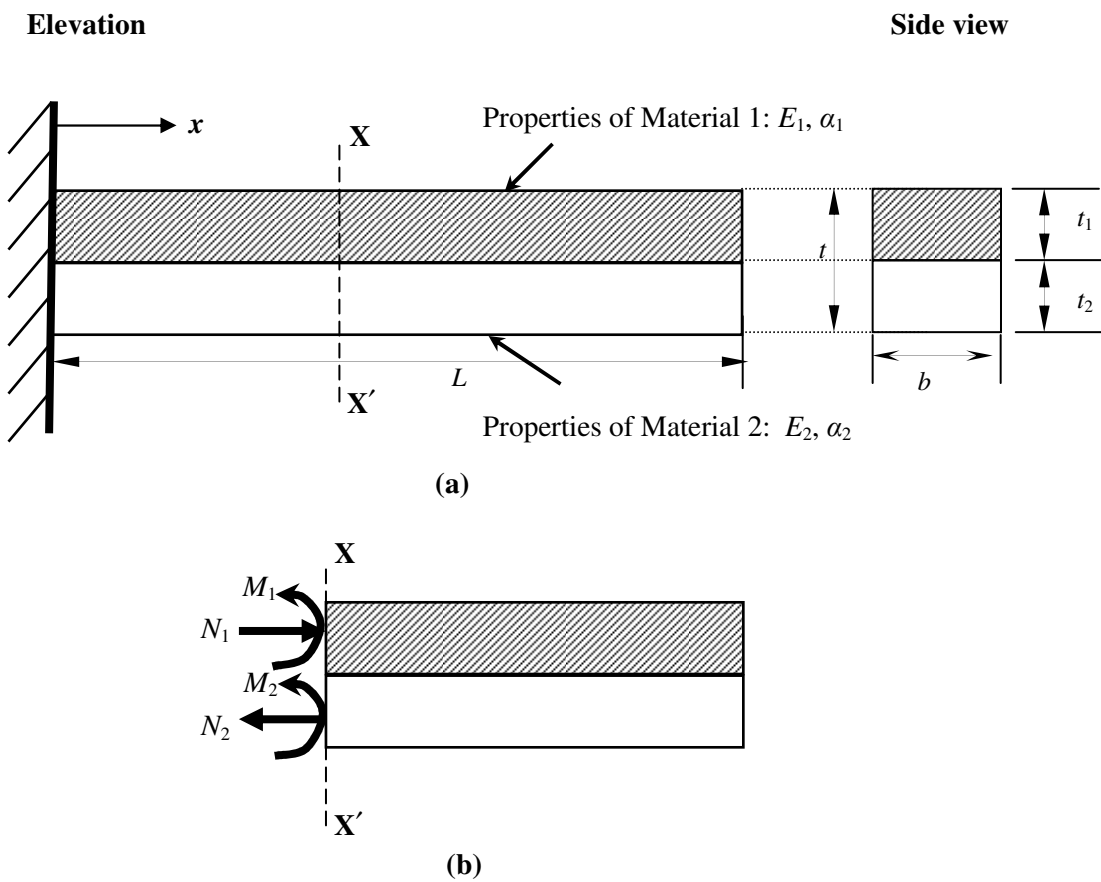


Figure 2.1 (a) Geometric definition of a bimaterial cantilever; (b) Free body diagram of a bimaterial cantilever subjected to a uniform temperature difference,  $\Delta T$ .

Timoshenko [33] was first to develop the fundamental mechanics of a bimaterial (or bimetallic strip) subjected to a uniform temperature difference,  $\Delta T$ . Making the usual assumptions of simple beam theory and applying compatibility, equilibrium and constitutive relations, the system of forces and moments is obtained as

$$M_1 = \frac{E_1 t^3 \xi^3}{12 R_c (1 + \xi)^3} \quad (2.1)$$

$$M_2 = \frac{E_2 t^3 \xi^3}{12 R_c (1 + \xi)^3} \quad (2.2)$$

$$N_1 = -N_2 = \frac{-E_1 t^2 (1 + \lambda \xi^3)}{6 R_c \lambda (1 + \xi)^3} \quad (2.3)$$

where  $\lambda = E_1/E_2$  is the ratio of elastic moduli,  $\xi = t_1/t_2$  is the thickness ratio,  $\Delta\alpha = (\alpha_1 - \alpha_2)$  is the difference in thermal expansion coefficient of the materials and  $R_c$  is the radius of curvature which is given by

$$\frac{1}{R_c} = \frac{6(\Delta\alpha)(\Delta T)(1 + \xi)^2}{t \left( 3(1 + \xi)^2 + (1 + \lambda \xi) \left( \frac{1}{\lambda \xi} + \xi^2 \right) \right)} \quad (2.4)$$

## 2.3 Evaluation of the performance metrics

### 2.3.1 Evaluation of free-end slope, $\Theta_f$

The free-end slope developed when a cantilever bimaterial is subjected to a uniform temperature difference,  $\Delta T$  relative to the ambient temperature, is given by

$$\Theta_f = \frac{L}{R_c}. \quad (2.5)$$

Substituting equation (2.4) in (2.5) gives an expression for the free end slope,  $\Theta_f$  as

$$\Theta_f = \frac{6(\Delta\alpha)(\Delta T)L}{t \left( \frac{3\lambda\xi(1+\xi)^2 + (1+\lambda\xi)(1+\lambda\xi^3)}{\lambda\xi(1+\xi)^2} \right)}. \quad (2.6)$$

### 2.3.2 Evaluation of blocked moment, $M_b$

When the rotational degree of freedom is constrained at the free end of a cantilever bimaterial, a moment ( $M_b$ , the blocked moment) is developed when subjected to a uniform temperature difference. This blocked moment can be evaluated by applying the principle of superposition between the free-end slope given by equation (2.6) and an equivalent free-end slope due to an arbitrary mechanical moment,  $M_b$  obtained using composite beam theory [34]. The blocked moment,  $M_b$  is evaluated as

$$M_b = \frac{E_1 t^2 (\Delta\alpha)(\Delta T)}{\left( \frac{2(1+\xi)(1+\lambda\xi)}{\xi} \right)}. \quad (2.7)$$

### 2.3.3 Evaluation of maximum work per volume, $W$

In general, actuators are required to deliver finite displacements while applying finite loads. Therefore the most general performance metric for a compact actuator is the maximum work that can be delivered per unit volume.

Figure 2.2 shows graphically the operating characteristics of a linear bimaterial actuator in the domain of moment and slope developed at the free end. Point C on the ordinate  $M$  corresponds to the fixed-fixed condition and point D on the abscissa,  $\Theta$  corresponds to the fixed-free condition. Any point on the line CD corresponds to a rotational compliant

condition with moments and slopes bounded by those at C and D. The maximum work per volume,  $W$  is equal to the triangular area OAB and it is given by

$$W = \frac{M_b \Theta_f}{8Lt}. \quad (2.8)$$

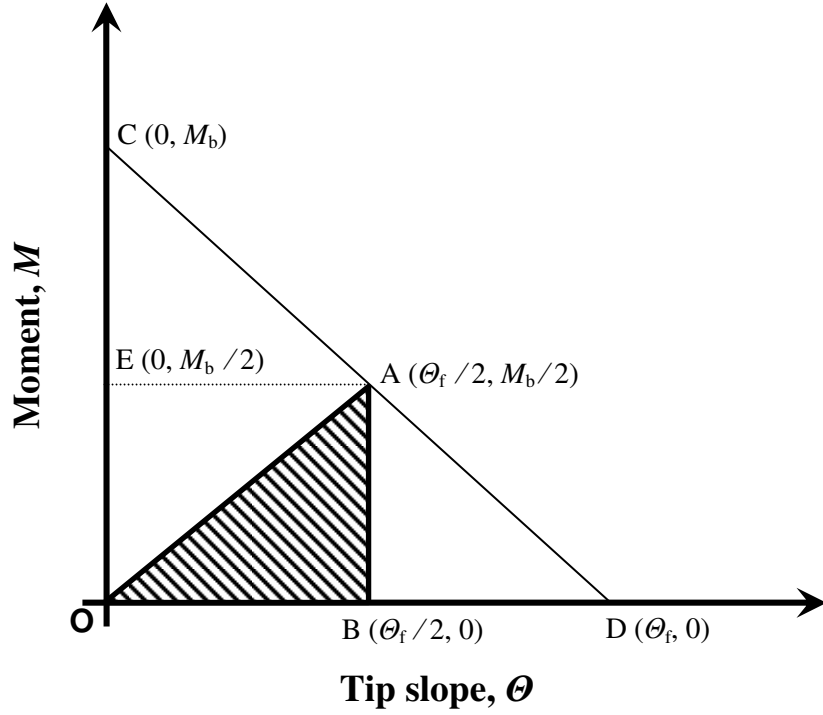


Figure 2.2 Operating characteristics of a bimaterial electrothermal actuator.

Substituting equations (2.6) and (2.7) in (2.8) gives an expression for the maximum work per volume:

$$W = \frac{3E_1(\Delta\alpha)^2(\Delta T)^2}{8 \left( 3(1+\lambda\xi) + \left( \frac{(1+\lambda\xi)^2(1+\lambda\xi^3)}{\lambda\xi(1+\xi)^2} \right) \right) \left( \frac{1+\xi}{\xi} \right)} \quad (2.9)$$

The closed form relations for performance metrics given by equations (2.6), (2.7) and (2.9) were compared to the results obtained by finite element analysis. A SOLID45 finite element routine implemented in ANSYS 10.0 was used to analyse cantilever structures with an aspect ratio,  $L/t=10$  for  $0.01 < \xi < 100$ ,  $0.01 < \lambda < 100$ , with a



temperature difference  $\Delta T = 100^\circ\text{C}$ . In all cases, the numerical solutions obtained from finite element analysis agreed with these analytical solutions to within 1%.

## 2.4 Optimisation of the performance metrics of BMET actuators

### 2.4.1 Optimisation of free-end slope/displacement

From equation (2.6) it is evident that the free-end slope of a thermal bimaterial actuator solely depends on the materials used (quantified by  $E$  and  $\alpha$ ), the thickness ratio and the geometry ( $L, t$ ) for a given temperature change,  $\Delta T$ . This observation simplifies the task of optimising the design in order to maximise  $\Theta_f$ . Since the material domain is discrete in nature, i.e. a given material has particular values of  $E$  and  $\alpha$  which are independent, it is most productive to optimise  $\Theta_f$  with respect to the thickness ratio,  $\xi$  for a given pair of materials. This implies that for a given  $\Delta\alpha$  and a fixed aspect ratio ( $L/t$ ) under a constant temperature difference,  $\Delta T$  the denominator in equation (2.6) should be minimised in order to obtain a maximum performance. A normalised slope,  $\Theta_n$  corresponding to the free-end slope,  $\Theta_f$  is defined using equation (2.6) which is given as

$$\Theta_n = \frac{\Theta_f}{(\Delta T)\beta} = \frac{6(\Delta\alpha)}{(3 + Z_\theta)} \quad (2.10)$$

where  $\beta = L/t$  is the aspect ratio of the cantilever bimaterial and

$$Z_\theta = \frac{(1 + \lambda\xi)(1 + \lambda\xi^3)}{\lambda\xi(1 + \xi)^2}. \quad (2.11)$$

To maximise  $\Theta_n$  (and hence  $\Theta_f$ ) for a given  $(\Delta\alpha)$ ,  $Z_\theta$  should be minimised subject to the condition

$$\lambda > 0 \text{ is a constant and } \xi > 0. \quad (2.12)$$

The optimal thickness ratio that provides maximum  $\Theta_n$  is given by

$$\frac{\partial Z_\theta}{\partial \xi} = 0 \text{ for a constant } \lambda. \quad (2.13)$$

Substituting equation (2.11) in equation (2.13) gives one admissible solution for the optimal thickness ratio,  $\xi_0$  which is given as

$$\xi_0 = \frac{1}{\sqrt{\lambda}} \Rightarrow E_1 t_1^2 = E_2 t_2^2. \quad (2.14)$$

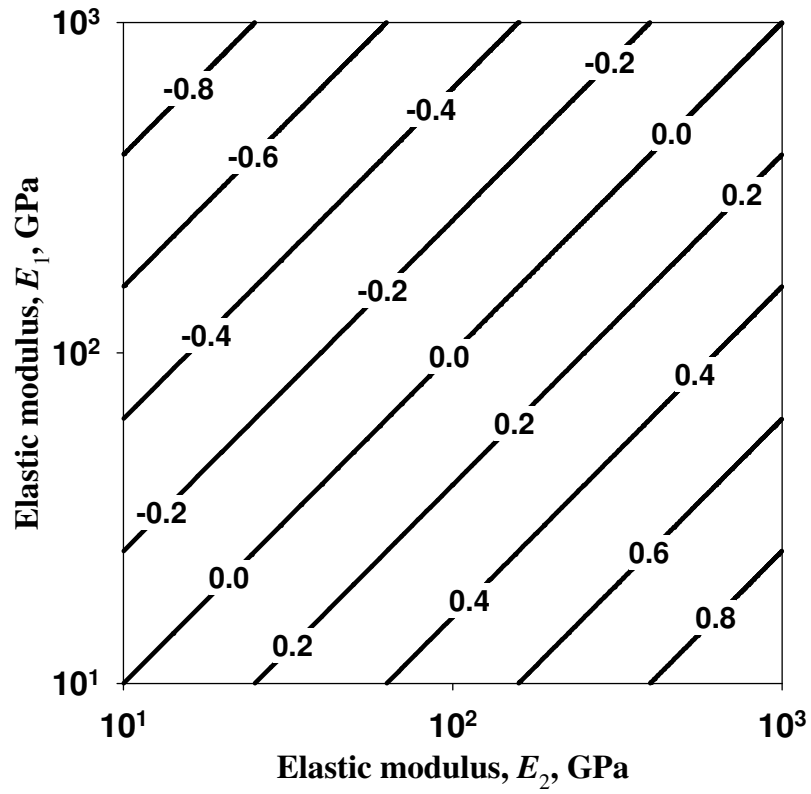


Figure 2.3 Contours of optimal thickness ratio,  $\log_{10}(\xi_0)$  for a given material pair to deliver maximum free-end slope, blocked moment and work per unit volume.

Equation (2.14) reveals that the thicknesses of the bi-layers  $t_1$  and  $t_2$  should be such that the moments  $M_1$  and  $M_2$  across any section should produce a constant circular bending

i.e.  $(M_1/t_1) = (M_2/t_2)$ . Therefore solving equations (2.10), (2.11) and (2.14) gives the optimal normalised,  $\Theta_{no}$  corresponding to the optimal free-end slope,  $\Theta_{fo}$ :

$$\Theta_{no} = \frac{\Theta_{fo}}{(\Delta T)\beta} = \frac{3(\Delta\alpha)}{2} \quad (2.15)$$

From equation (2.15) it is clear that the optimal normalised slope for a thermally actuated bimaterial is dependent only on the difference in thermal expansion coefficients,  $(\Delta\alpha)$  of the two materials. However, the optimal thickness ratio does depend on the ratio of the elastic moduli,  $\lambda$ . Figure 2.3 shows a plot of optimal thickness ratio,  $\xi_0$  as a function of  $\lambda$ . It is clear from the plot that decreasing  $\lambda$  must be compensated by an increase in  $\xi_0$  for an optimal performance corresponding to a particular material combination.

#### 2.4.2 Optimisation of blocked moment

From equation (2.7) it is evident that the blocked moment developed by a thermal bimaterial actuator depends on the properties of the bimaterial employed and the thickness ratio for a constant thickness,  $t$  under a given temperature change  $(\Delta T)$ . Using equation (2.7) a non-dimensional parameter,  $M_I$ , termed the moment index is defined which is given by

$$M_I = \frac{M_n}{E_1(\Delta\alpha)} = \frac{1}{2Z_M} \quad (2.16)$$

where,  $M_n = M_b/t^2(\Delta T)$  is the normalised moment corresponding to  $M_b$  and

$$Z_M = \frac{(\xi+1)}{\xi}(\lambda\xi+1). \quad (2.17)$$

The moment index,  $M_I$  should be maximised in order to achieve maximum  $M_n$  (as well as  $M_b$ ). Hence  $Z_M$  should be minimised subject to the condition:

$$\lambda > 0 \text{ is constant and } \xi > 0. \quad (2.18)$$

The optimal thickness ratio for a given pair of materials that minimizes  $Z_M$  is obtained by

$$\frac{\partial Z_M}{\partial \xi} = 0 \text{ for a constant } \lambda. \quad (2.19)$$

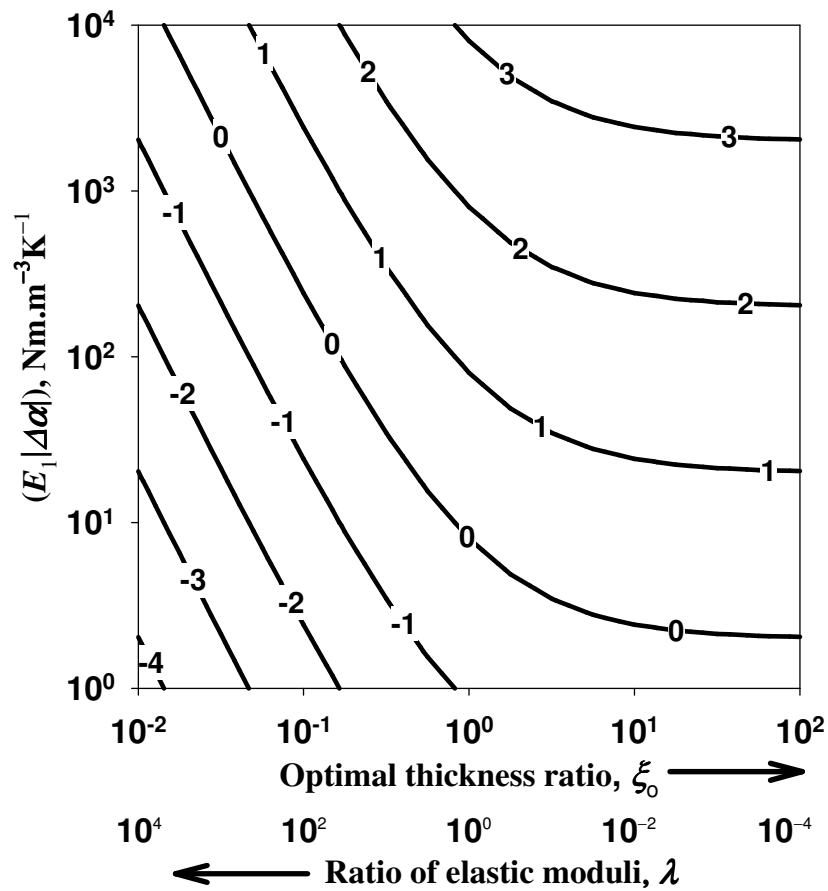


Figure 2.4 Contours of optimal normalised moment,  $\log_{10}(M_{no})$  for a given pair of materials.

Substituting equation (2.17) in equation (2.19) gives one admissible solution for the optimal thickness ratio,  $\xi_0$  that minimises  $Z_M$  and this is same as that given by equation (2.14). This is because the  $M_b$  developed is directly proportional to  $\Theta_f$  and hence the optimality condition pertaining to  $\Theta_f$  also corresponds to that of  $M_b$  and hence Figure 2.3 can also be utilized. Solving equations (2.14), (2.16) and (2.17) gives the optimal

normalised moment,  $M_{no}$  corresponding to the optimal blocked moment,  $M_{bo}$  for a given pair of materials and is given as

$$M_{no} = \frac{M_{bo}}{t^2(\Delta T)} = \frac{E_1(\Delta\alpha)}{2\left(\frac{\xi_o + 1}{\xi}\right)^2}. \quad (2.20)$$

Figure 2.4 shows the contours for  $\log_{10}(M_{no})$  as a function of  $E_1(\Delta\alpha)$  and  $\xi_o$  obtained using equation (2.20). It is clear from the graph that if one of the materials in a bimaterial is replaced by another material with a lower Young's modulus and larger thermal expansion coefficient, then its thickness has to be increased in accordance to the equation (2.14) to obtain a maximum blocked moment corresponding to that particular material pair.

#### 2.4.3 Optimisation of maximum work per volume ( $W$ )

As illustrated by equation (2.8) the maximum work per volume ( $W$ ) for an actuator is directly proportional to the product of the blocked moment,  $M_b$  and free-end slope,  $\Theta_f$ . Since the optimality condition for the free end slope and blocked moment corresponds to the relation given by equation (2.14), the optimality condition for  $W$  also converges to the same relation. Using equation (2.9) a non-dimensional parameter,  $E_1$ , the energy index can be defined:

$$E_1 = \frac{W_n}{E_1(\Delta\alpha)^2} = \frac{3}{8Z_E} \quad (2.21)$$

where,  $W_n = W/(\Delta T)^2$  is the normalised maximum work/volume corresponding to  $W$

$$Z_E = \frac{(1 + \lambda\xi)^2(1 + \xi^3\lambda)}{\lambda\xi^2(\xi + 1)} + \frac{3(\lambda\xi + 1)(\xi + 1)}{\xi}. \quad (2.22)$$

The optimal normalised work per volume,  $W_{no}$  for a given pair of materials is obtained by solving equations (2.14), (2.21) and (2.22) and it is given as

$$W_{no} = \frac{W_o}{(\Delta T)^2} = \frac{3E_1(\Delta\alpha)^2}{32\left(\frac{\xi_o + 1}{\xi_o}\right)^2}. \quad (2.23)$$

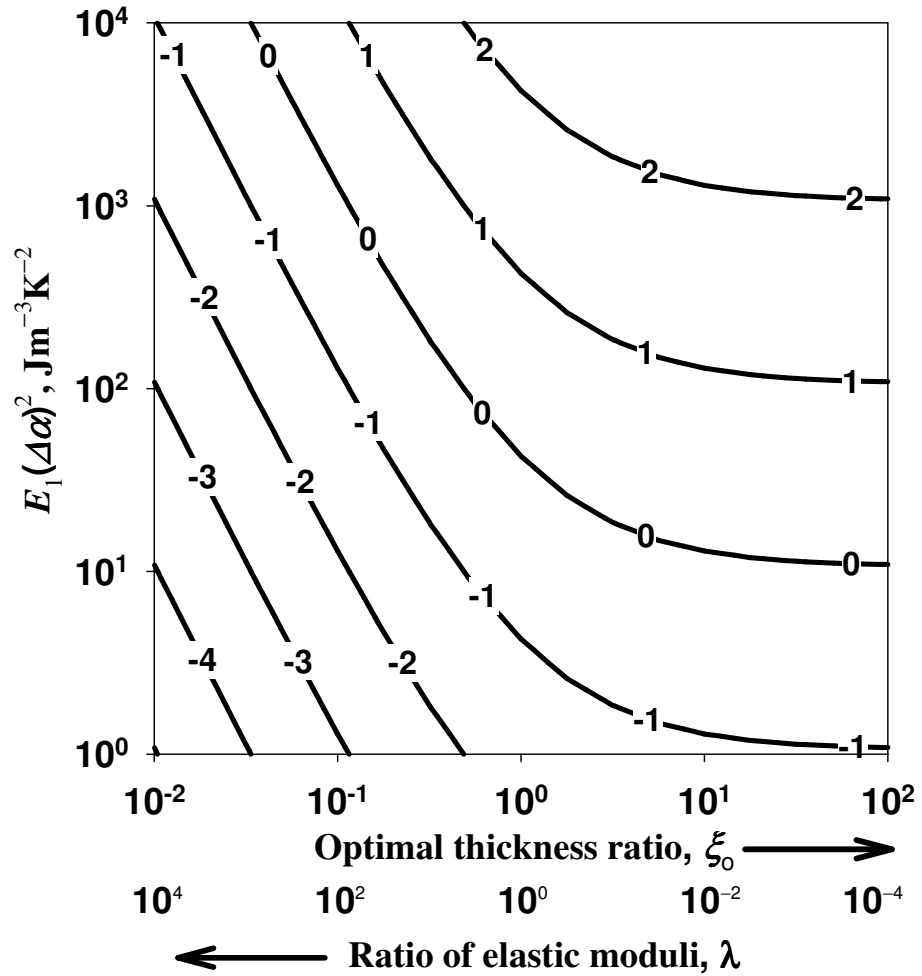


Figure 2.5 Contours of optimal normalised work per unit volume,  $\log_{10}(W_{no})$  for a given pair of materials.

Figure 2.5 shows a plot of  $\log_{10}(W_{no})$  for a given pair of materials as a function of  $E_1(\Delta\alpha)^2$  and  $\xi_o$  based on equation (2.23).

## 2.5 Candidate materials for bimaterial actuator design

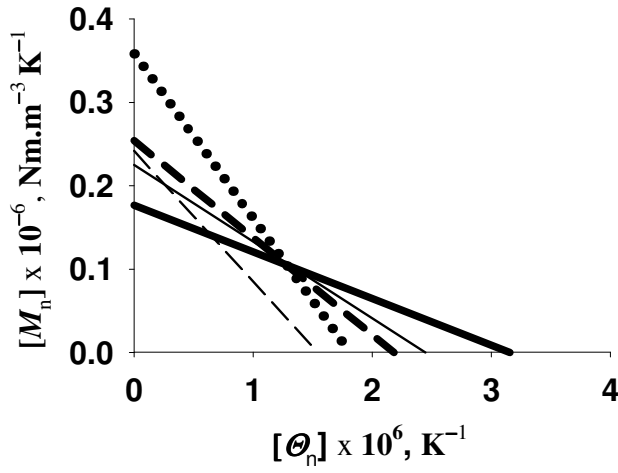
Before exploring the optimal choice of materials and their corresponding thickness ratio it is worthwhile to understand the trade-offs between force and displacement for a restricted combination of commonly used MEMS materials. Table 2.1 list the properties of a limited range of materials, which have been previously considered for MEMS actuators.

MEMS materials set	Young's Modulus, $E$ GPa	Thermal expansion coefficient, $\alpha$ $\mu\text{m.m}^{-1}\text{K}^{-1}$
Al	~ 68	~ 24
Au	~ 77	~ 14.4
Cu	~ 110	~ 16.4
Diamond-like Carbon (DLC)	~ 700	~ 1.2
Ni	~ 207	~ 13.1
Polyimide (a typical polymer)	~ 4	~ 20
Si ( Polycrystalline)	~ 165	~ 2.5
SiC	~ 460	~ 4.5
Si <sub>3</sub> N <sub>4</sub>	~ 260	~ 2.8
SiO <sub>2</sub>	~ 75	~ 0.4

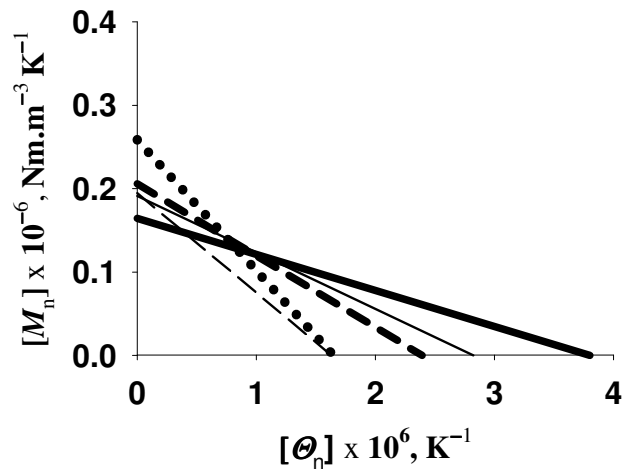
Table 2.1 Material properties of conventional materials employed in MEMS design.

Figure 2.6 shows a comparison of the operating characteristics (normalised moment vs. normalised slope) of thermal bimaterial actuators made of metals and polymer (Ni, Cu, Al, Au and polyimide) on various substrates (SiO<sub>x</sub>, SiN<sub>x</sub>, DLC, SiC and Si) for a particular thickness ratio ( $\xi = 0.5$ ). It is apparent that there are significant differences in performance among the limited choices considered. Graphs of the form shown in Figure 2.6, which correspond to equations (2.10) and (2.16), are useful in selecting an optimal material pair for a fixed value of thickness ratio,  $\xi$  within the range of choices considered.

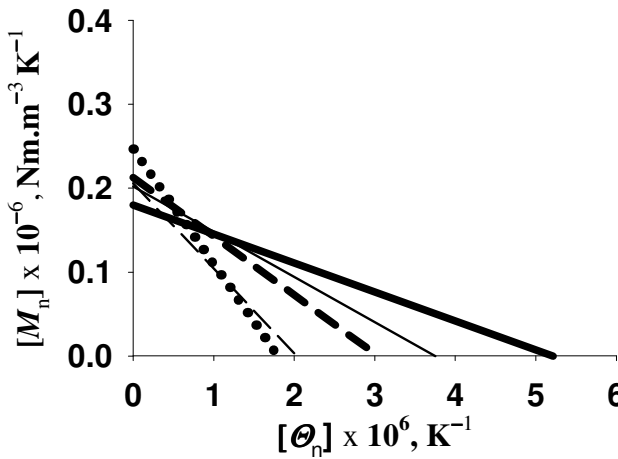
Figure 2.7 shows comparison of the energy index ( $E_1$ ) at different thickness ratios,  $\xi$  for the same range of thin films on different substrates. This set of curves, corresponding to equation (2.21) illustrates that there is an optimum thickness ratio for a given pair of materials at which maximum work can be delivered. The graphs shown in Figure 2.7 are useful in identifying the best thickness ratio for a given pair of materials.



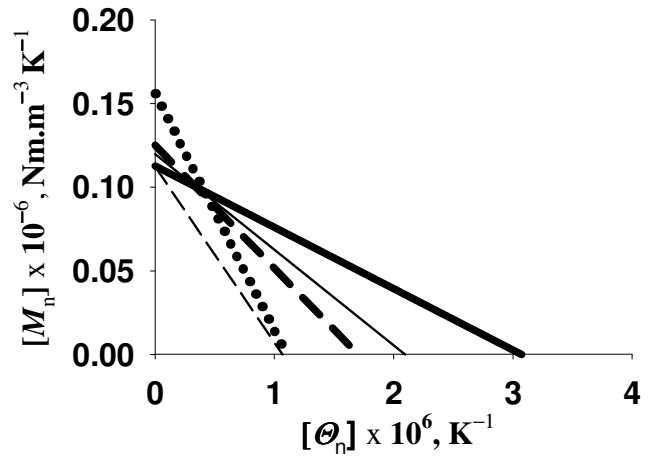
(a)



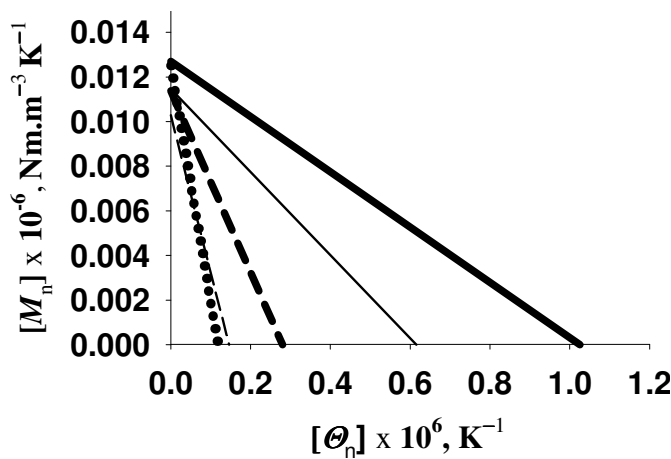
(b)



(c)



(d)



(e)



Figure 2.6 Comparison of the operating characteristics of bimaterial actuators made of different substrates with (a) Nickel, (b) Copper, (c) Aluminium, (d) Gold, and (e) Polyimide for  $\zeta = 0.5$ .



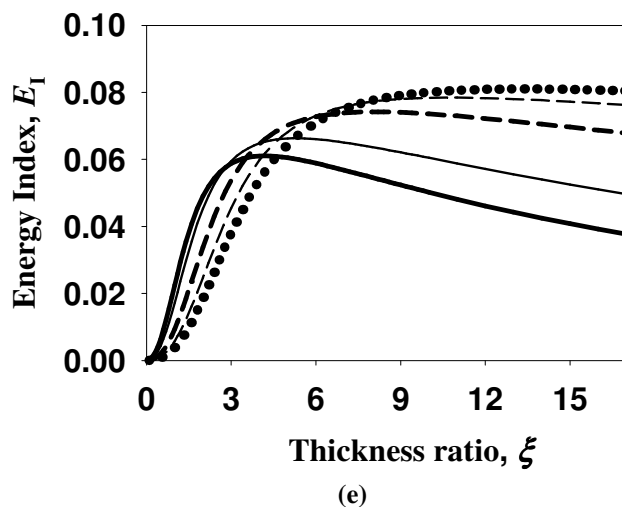
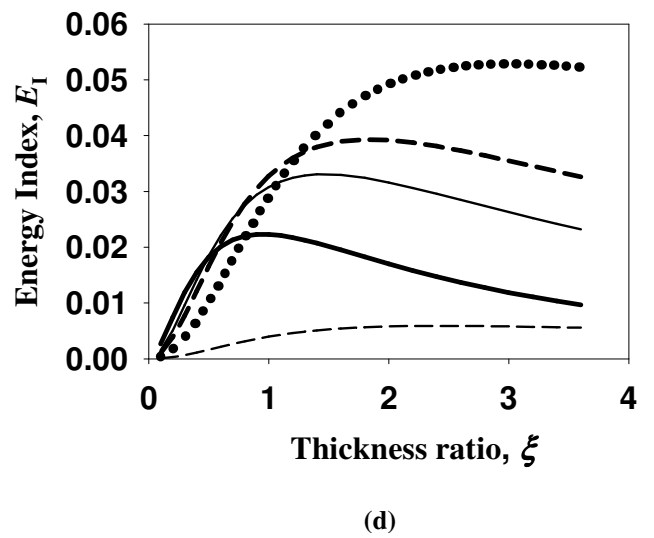
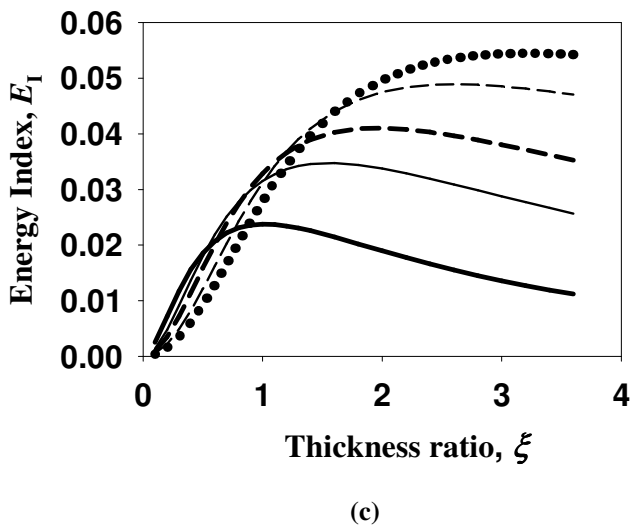
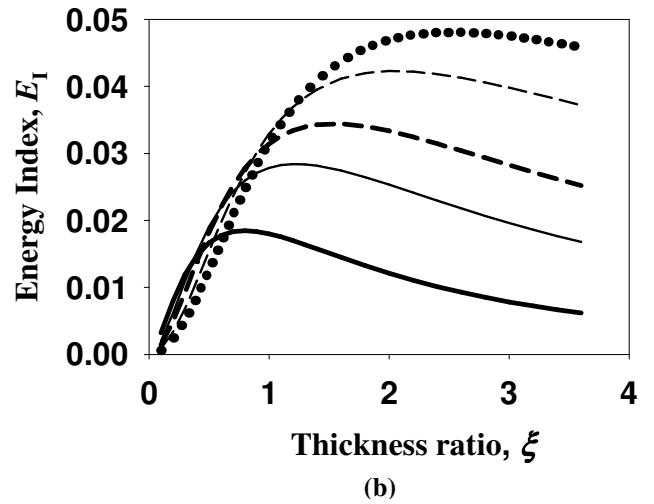
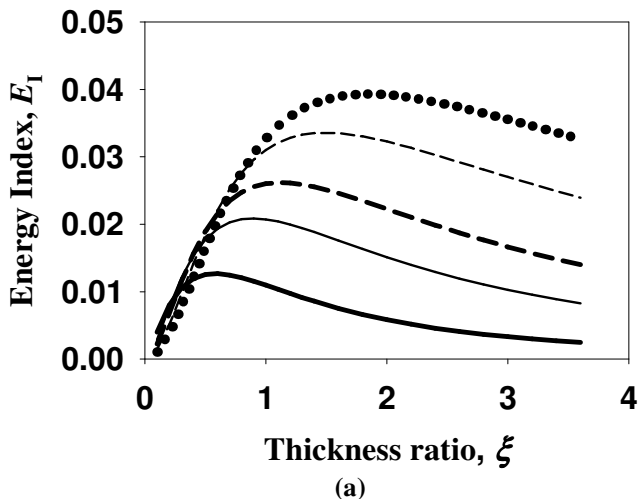


Figure 2.7 Comparison of the energy indices of (a) Nickel, (b) Copper, (c) Aluminium, (d) Gold, and (e) Polyimide on different substrates.

Table 2.2 shows the maximum  $W_{no}$  that can be achieved for different thin films on the various substrates considered.

In order to make a more effective selection spanning the material domain it is essential to take a different strategy. Ashby has shown the utility of employing selection maps [17] by classifying the material kingdom into specific classes within the domain of various material properties. These selection maps can be modified for the current purpose of materials selection for thermal bimaterial actuators.

By fixing the properties of one material, it is possible to plot contours of iso-performance on the selection map for a wide range of available materials. New materials for thermal bimaterial actuators can be explored by plotting contours of  $W_{no}$  in the domain of governing properties (Young's modulus,  $E$  and thermal expansion coefficient,  $\alpha$ ). Figure 2.8 shows contours of  $\log_{10}(W_{no})$  plotted with respect to a silicon substrate. New candidate materials for any substrate can be identified by comparing the performance contours corresponding to it with other candidate materials.

Figure 2.9 shows contours for optimal performance with reference to silicon overlaid on Ashby's selection map in the domain of  $E$ - $\alpha$ . The contour lines corresponding to  $\log_{10}(M_{no})$  are linear and parallel to constant  $E\alpha$  lines in the Ashby's chart while the contours of  $\log_{10}(W_{no})$  are parabolic. Both these contours become asymptotic at the properties of silicon. Contours of  $\log_{10}(\Theta_{no})$  are straight lines parallel to the abscissa because  $\Theta_{no}$  is independent of Young's modulus of the materials as shown in equation (2.15).

It is clear from this plot that engineering polymers and engineering alloys promise the highest  $W_{no}$  on a silicon substrate within the range considered. Critical examination of materials in these classes reveals polymers (polymethylmethacrylate (PMMA), polystyrene (PS), nylon, melamine (MEL), polydimethylsiloxane (PDMS)) and metals (beryllium, steel, zinc, copper), which have not been widely considered for thermal bimaterial actuators. It should be noted that the polymers require a very large thickness on silicon substrates to compensate for their low Young's modulus, which may be inadmissible in some applications.

Substrate Materials	Thin film materials				
	Ni	Cu	Al	Au	Polyimide
SiO <sub>2</sub>	0.42	0.52	0.90	0.32	0.09
Si <sub>3</sub> N <sub>4</sub>	0.57	0.70	1.25	0.38	0.09
DLC	1.16	1.23	1.93	0.67	0.11
SiC	0.51	0.66	1.26	0.33	0.08
Si	0.49	0.60	1.09	0.34	0.08

Table 2.2 Optimal normalised maximum work per volume,  $W_{no}$  for different thin films on various substrates considered. The units are in  $\text{Jm}^{-3}\text{K}^{-2}$ .

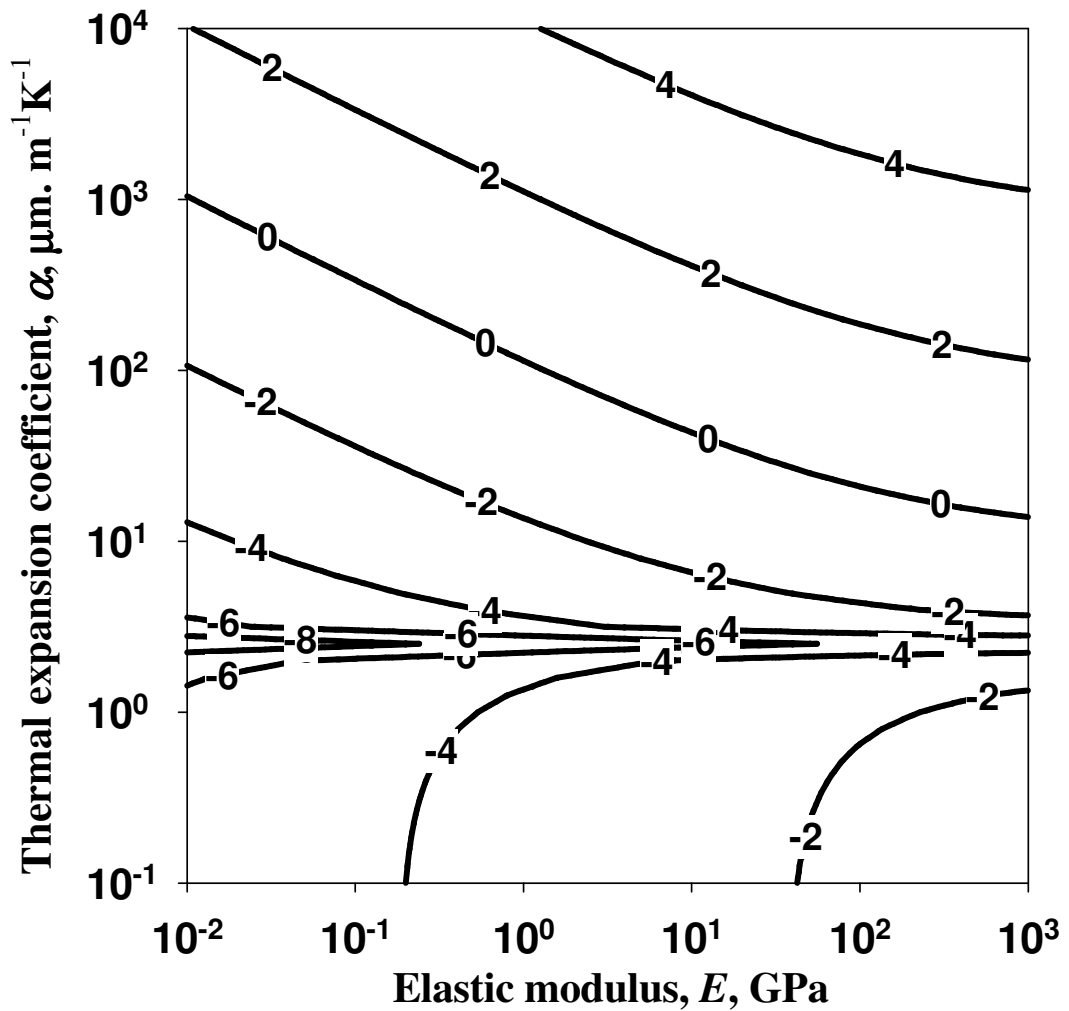


Figure 2.8 Contours of  $\log_{10}(W_{no})$  for different materials on a silicon substrate.

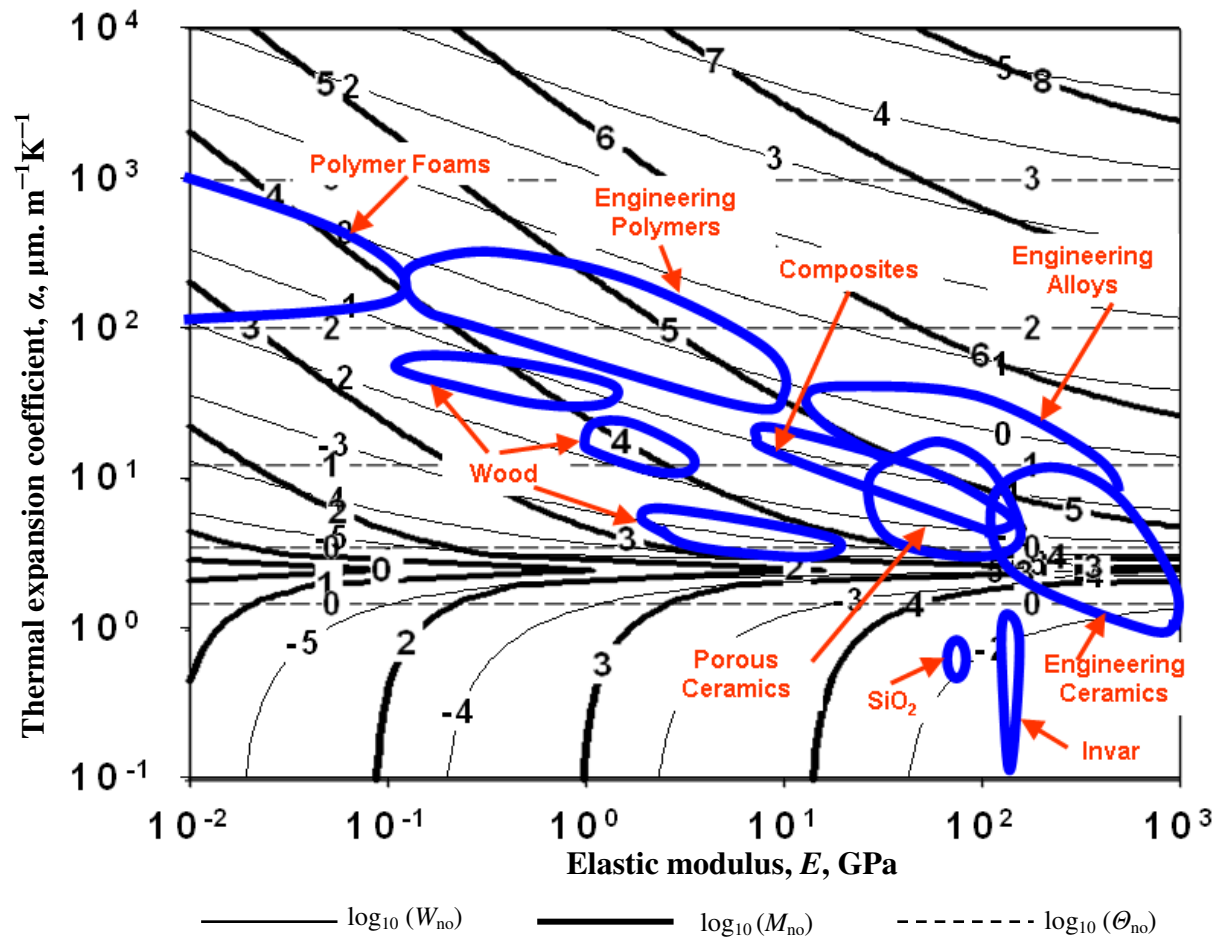


Figure 2.9 Contours of equal performance for different classes of materials on a silicon substrate plotted on Ashby's selection chart [17].

Optimisation based on  $W_{no}$  is useful for identifying materials capable of delivering both large moment and slope. Table 2.3 shows a comparison of the performance of a few engineering polymers and alloys that deliver  $W_{no}$  significantly greater than  $\sim 0.01 \text{ Nm.m}^{-3} \text{ K}^{-2}$  (i.e.  $\log_{10}(W_{no}) > -1$ ) on three different substrates (Si, SiO<sub>2</sub> and PMMA). As expected, polymers deliver large slope and small moment while metals deliver vice-versa. For applications such as micropumps, where work per unit volume is the relevant metric, it is desirable to use materials capable of delivering a reasonably large moment and slope.

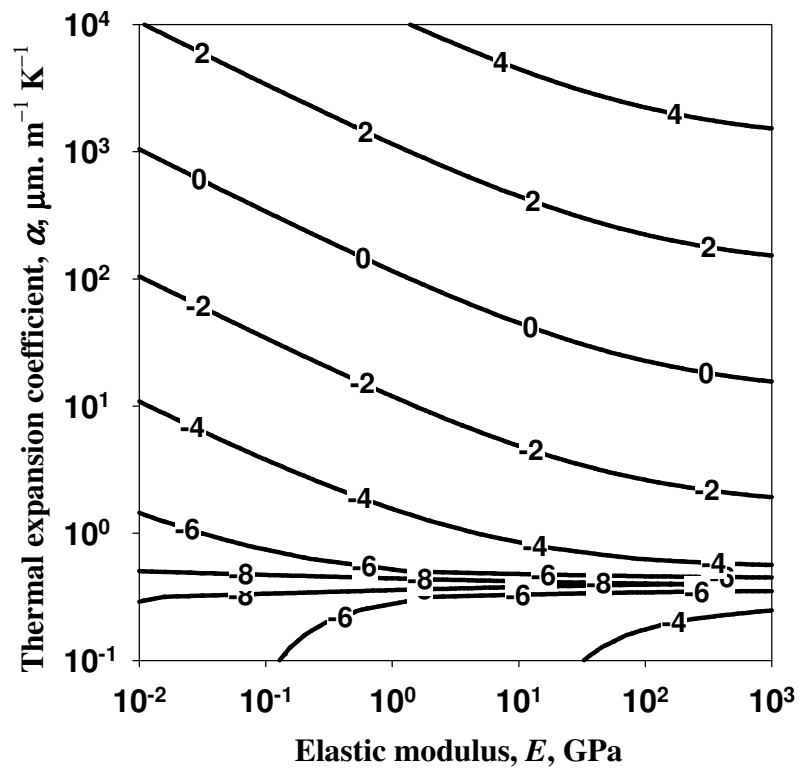
Materials such as Epoxies, Zn, Al, Mg, PDMS, MEL, Pb, Cu, Steel and Ni on Si/SiO<sub>2</sub> substrates and Ti, Zn on a PMMA substrate deliver a reasonably large  $W_{no}$  with corresponding  $M_n$  varying between  $0.04 \times 10^6 - 0.4 \times 10^6 \text{ Nm.m}^{-3} \text{ K}^{-1}$  and  $\Theta_n$  between  $20 \times 10^{-6} - 90 \times 10^{-6} \text{ K}^{-1}$ . Some of these combinations have not been considered so far for thermal bimaterial actuators for applications requiring a large work per volume. Figures 2.10a and 2.10b show contours of  $\log_{10}(W_{no})$  plotted with reference to SiO<sub>2</sub> and PMMA substrates respectively.

A similar analysis is carried out to identify the materials that can be considered for large moment applications. Table 2.4 lists a selection of materials identified from such plots for  $M_{no}$  significantly greater than  $\sim 10^5 \text{ Nm.m}^{-3} \text{ K}^{-1}$  for the same three different substrates. It is clear from this result that few engineering alloys and ceramics, including Zn, Al, Mg, Steel, Ni, Be, Cu and Zr<sub>2</sub>O<sub>3</sub> on Si/SiO<sub>2</sub> deliver a large moment while polymers deliver a relatively small force. Figures 2.11a and 2.11b show contours of  $\log_{10}(M_{no})$  with reference to SiO<sub>2</sub> and PMMA respectively.

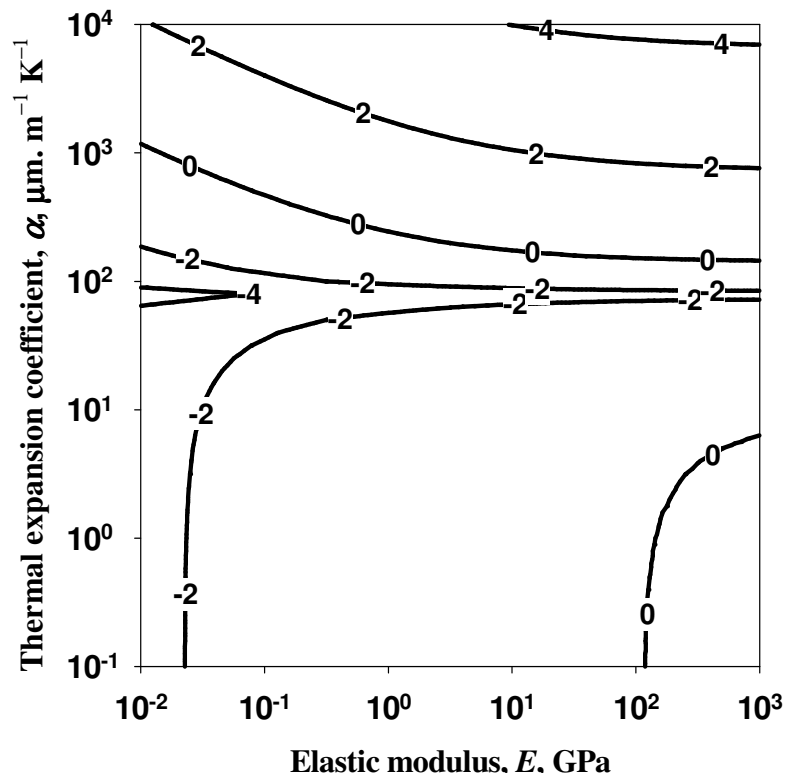
For applications where a large slope is the relevant metric, materials such as PP, Nylon, PMMA, PDMS, Epoxies and PS on Si or SiO<sub>2</sub>, Ge, BeO, Nb, Invar and ceramic substrates deliver  $\Theta_{no}$  of order  $10^{-4} \text{ K}^{-1}$ . Therefore it is apparent from Figure 2.9 that polymers can be considered favourably for such applications although the non-linear time and temperature dependent response of polymers require further consideration.

S. No	Candidate Materials	$E_2$ GPa	$\alpha_2$ $\mu\text{m.m}^{-1}\text{K}^{-1}$	PMMA [ $E_1 = 2.5 \text{ GPa}$ , $\alpha_1 = 75 \mu\text{m.m}^{-1}\text{K}^{-1}$ ]				Si [ $E_1 = 165 \text{ GPa}$ , $\alpha_1 = 2.49 \mu\text{m.m}^{-1}\text{K}^{-1}$ ]				SiO <sub>2</sub> [ $E_1 = 75 \text{ GPa}$ , $\alpha_1 = 0.4 \mu\text{m.m}^{-1}\text{K}^{-1}$ ]			
				$W_{\text{no}}$ $\text{Jm}^{-3}\text{K}^{-2}$	$M_n \times 10^{-6}$ $\text{Nm.m}^{-3}\text{K}^{-1}$	$\Theta_n \times 10^6$ $\text{K}^{-1}$	$\eta_m$	$W_{\text{no}}$ $\text{Jm}^{-3}\text{K}^{-2}$	$M_n \times 10^{-6}$ $\text{Nm.m}^{-3}\text{K}^{-1}$	$\Theta_n \times 10^6$ $\text{K}^{-1}$	$\eta_m$	$W_{\text{no}}$ $\text{Jm}^{-3}\text{K}^{-2}$	$M_n \times 10^{-6}$ $\text{Nm.m}^{-3}\text{K}^{-1}$	$\Theta_n \times 10^6$ $\text{K}^{-1}$	$\eta_m$
1	Al	68	24	0.43	0.04	77	0.02	1.09	0.27	32	0.05	0.93	0.21	35	0.05
2	Al <sub>2</sub> O <sub>3</sub>	370	7	0.91	0.07	101	0.05	0.13	0.15	7	0.01	0.16	0.12	11	0.02
3	B	320	8	0.88	0.07	100	0.05	0.18	0.16	9	0.02	0.20	0.13	12	0.02
4	Be	303	12	0.79	0.07	95	0.03	0.42	0.25	14	0.02	0.39	0.19	17	0.02
5	BeO	345	7	0.92	0.07	102	0.06	0.11	0.13	7	0.01	0.14	0.12	10	0.02
6	Cast Iron	165	12	0.74	0.06	95	0.04	0.35	0.20	14	0.03	0.34	0.16	17	0.03
7	Cu	110	16	0.61	0.06	88	0.03	0.60	0.23	21	0.04	0.54	0.18	24	0.04
8	DLC	700	1.2	1.14	0.08	111	0.15	-	-	-	-	-	-	-	-
9	Epoxies	2	55	-	-	-	-	0.42	0.04	79	0.12	0.41	0.04	82	0.14
10	Ge	102	6	0.84	0.06	104	0.10	-	-	-	-	-	-	-	-
11	Invar	145	0.4	1.02	0.07	112	0.14	-	-	-	-	-	-	-	-
12	MEL	8	40	0.12	0.02	53	0.01	0.71	0.10	56	0.10	0.67	0.09	59	0.10
13	Mg	45	26	0.37	0.04	73	0.02	1.01	0.23	35	0.06	0.88	0.18	39	0.06
14	Nb	105	7	0.81	0.06	102	0.08	-	-	-	-	0.10	0.08	10	0.04
15	Ni	207	13	0.73	0.06	93	0.03	0.49	0.24	16	0.03	0.44	0.19	19	0.02
16	Nylon	0.62	80	-	-	-	-	0.31	0.02	116	0.12	0.31	0.02	119	0.16
17	Pb	14	29	0.24	0.03	69	0.02	0.56	0.11	40	0.09	0.53	0.10	43	0.09
18	PDMS	4	60	-	-	-	-	0.93	0.09	86	0.12	0.88	0.08	89	0.12
19	PMMA	3	75	-	-	-	-	0.98	0.07	109	0.13	0.93	0.07	112	0.13
20	PP	2	120	0.11	0.01	68	0.00	2.10	0.10	176	0.14	1.98	0.09	179	0.14
21	PS	3	73	-	-	-	-	1.07	0.08	105	0.13	1.02	0.08	108	0.13
22	Si	165	2.5	0.93	0.07	109	0.12	-	-	-	-	-	-	-	-
23	Si <sub>3</sub> N <sub>4</sub>	300	2.8	1.03	0.08	108	0.12	-	-	-	-	-	-	-	-
24	SiO <sub>2</sub>	75	0.4	0.93	0.07	112	0.13	-	-	-	-	-	-	-	-
25	Steel	207	13	0.73	0.06	93	0.03	0.49	0.24	16	0.03	0.44	0.19	19	0.02
26	Ti	110	9	0.77	0.06	99	0.07	0.13	0.11	10	0.03	0.16	0.10	12	0.03
27	W	400	4	1.01	0.08	106	0.09	-	-	-	-	-	-	-	-
28	Zn	97	31	0.33	0.04	66	0.01	2.40	0.45	43	0.05	1.89	0.33	46	0.04
29	Zr <sub>2</sub> O <sub>3</sub>	200	12	0.75	0.06	95	0.04	0.38	0.22	14	0.03	0.36	0.17	17	0.03

Table 2.3 Candidate materials for thermal bimaterial actuators which can deliver large  $W_{\text{no}}$  on different substrates.



(a)



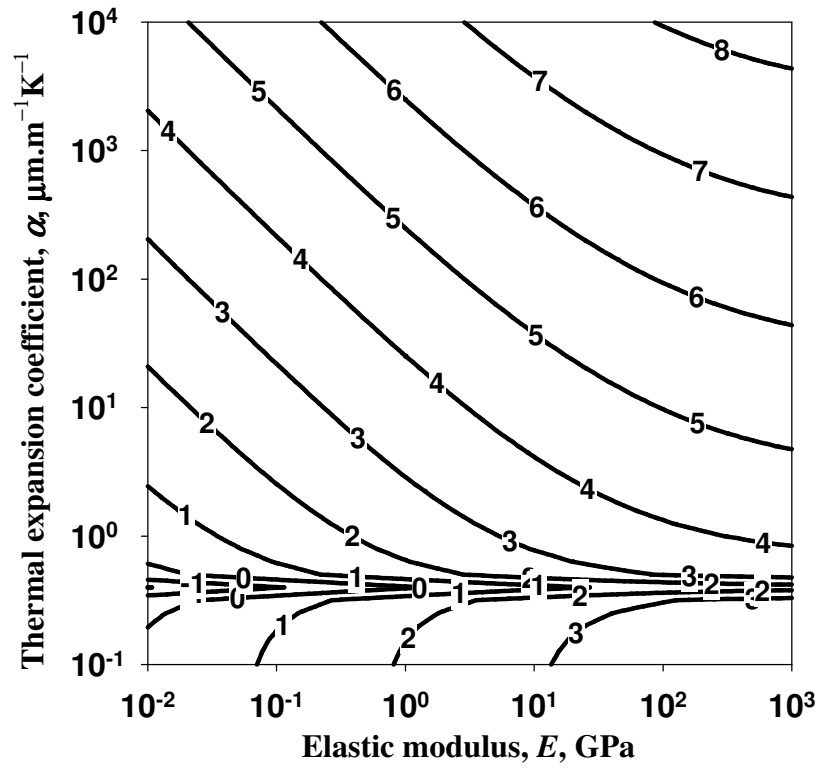
(b)

Figure 2.10 Contours of  $\log_{10}(W_{no})$  with reference to (a)  $\text{SiO}_2$  substrate, (b) PMMA substrate.

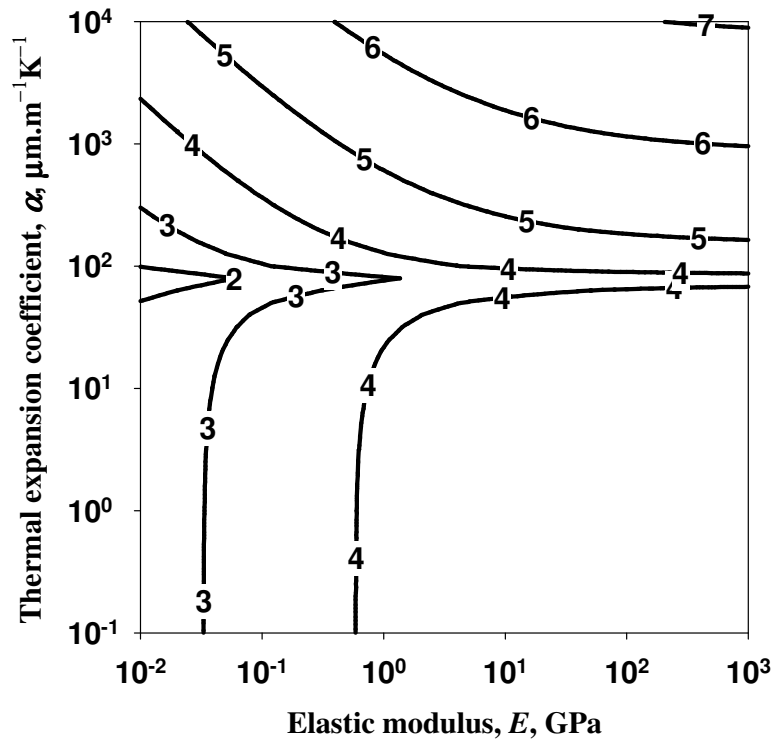
S. No	Candidate materials	$E_2$	$\alpha_2$	$M_{no} \times 10^{-6}$		
				PMMA [ $E_1, \alpha_1$ ]	Si [ $E_1, \alpha_1$ ]	SiO <sub>2</sub> [ $E_1, \alpha_1$ ]
				GPpa	$\mu\text{m.m}^{-1}\text{K}^{-1}$	Nm.m <sup>-3</sup> .K <sup>-1</sup>
1	Al	68	24	-	0.23	0.21
2	Al <sub>2</sub> O <sub>3</sub>	370	7.4	0.07	0.11	0.12
3	B	320	8.3	0.07	0.13	0.13
4	Be	303	11.5	0.07	0.20	0.19
5	BeO	345	7	0.07	0.10	0.12
6	Cast Iron	165	12	0.06	0.16	0.16
7	Cu	110	16.4	0.06	0.19	0.18
8	DLC	700	1.18	0.08	-	-
9	Epoxies	2	55	-	-	-
10	Ge	102	5.75	0.06	-	0.06
11	Invar	145	0.36	0.07	-	-
12	MEL	8	40	-	0.09	0.09
13	Mg	45	26.1	0.04	0.20	0.18
14	Nb	105	7.3	0.06	0.07	0.08
15	Ni	207	13.1	0.06	0.20	0.19
16	Nylon	0.62	80	-	-	-
17	Pb	14	29.1	-	0.10	0.10
18	PDMS	4	60	-	0.08	0.08
19	PMMA	2.5	75	-	0.07	0.07
20	PP	2	120	-	0.09	0.09
21	PS	3	72.5	-	0.08	0.08
22	Si	112	2.49	0.07	-	-
23	Si <sub>3</sub> N <sub>4</sub>	300	2.8	0.08	-	-
24	SiO <sub>2</sub>	75	0.4	0.07	-	-
25	Steel	207	13.1	0.06	0.20	0.19
26	Ti	110	9	0.06	0.09	0.10
27	W	400	4.3	0.08	0.04	0.07
28	Zn	97	31.2	0.04	0.37	0.33
29	Zr <sub>2</sub> O <sub>3</sub>	200	12	0.06	0.17	0.17

Table 2.4 Candidate materials for thermal bimaterial actuators which can deliver large  $M_{no}$  on different substrates.





(a)



(b)

Figure 2.11 Contours of  $\log_{10}(M_{n0})$  with reference to (a)  $\text{SiO}_2$  substrate, (b) PMMA substrate.

Another factor to be considered in materials selection based on work per volume is the mechanical efficiency of the actuator,  $\eta_m$  which is defined here as the ratio of the maximum work per volume,  $W$  of a thermally actuated bimaterial to the total strain energy per volume of the two individual material layers that constitutes the bimaterial. From Table 2.3 it is clear that, although polymers deliver a much lower moment, they offer higher efficiency on the various substrates considered compared to metals.

## **2.6 Materials selection process for BMET actuators**

The choice of a particular material for an actuator design also depends on its compatibility with the fabrication process, the ability to achieve the desired shape and the functionality required [17]. The methodology for materials selection for thermal bimaterial actuators described in the previous section is based on the mechanics of actuation. This reveals a few candidate materials from the large set of materials available. However, the success of an actuator design depends on the extent to which the defined performance metrics capture the overall required performance. Therefore the suitability of these candidate materials for a thermal bimaterial actuator has to be further explored by considering additional factors such as the maximum actuation temperature, power requirements, dissipation effects due to heat loss, compatibility with micromachining and of course, the cost. Chapter 3 analyses the influence of some of these additional factors, which could further refine the materials selection process. The key aim of this analysis is to obtain a ranking of different material combinations during preliminary design. Therefore, the present materials selection strategy has not accounted for the variation in material properties due to temperature and scale, and assumes a linear elastic material model for all classes of materials over the entire temperature range for small deflections. Clearly this would lead to an inaccurate estimate of the performance, particularly for polymers. Nevertheless, the present approach has utility in selecting candidate materials for thermal bimaterial actuators.

In the preliminary design phase, the candidate materials are selected based on the primary performance requirements as described by the performance metrics defined herein. These candidate materials need to be further filtered based on other considerations such as maximum actuation temperature which is also limited by the

yield/fracture strength of the materials at the microscale, power requirements which are determined by the electrical property (i.e. resistivity) of the materials, heat dissipation which is dictated by the thermal properties (thermal conductivity and emissivity) and flow physics (convective effects) and the residual stresses developed during micromachining processes. Besides these design constraints, application specific requirements such as response time, sensitivity, linearity and resistance to oxidation/corrosion in the ambient environment will also have a bearing on the selection of the materials. However, for many applications, there is likely to be a finite, small temperature difference,  $\sim 100$  K, which is well within the capabilities of almost all the materials explored. For such applications the process described herein is directly applicable.

Perhaps the most significant result of this work is the confirmation that existing microfabricatable materials (such as aluminium and silicon) offer good options for high performance thermal bimaterial actuators. The order of  $W_{no}$  for DLC on metallic substrates such as Ni, Cu and Al is same as Al on Si. Therefore for high work or force actuators, Al on Si ( $W_{no} = 1.09 \text{ Jm}^{-3}\text{K}^{-2}$ ,  $M_{no} = 0.23 \times 10^{-6} \text{ Nm.m}^{-3}\text{K}^{-1}$ ), is a very capable material combination that is significantly bettered only by Zn on Si ( $W_{no} = 2.4 \text{ Jm}^{-3}\text{K}^{-2}$ ,  $M_{no} = 0.37 \times 10^{-6} \text{ Nm.m}^{-3}\text{K}^{-1}$ ). For high displacement actuators, PMMA on Si ( $\Theta_n = 108.7 \times 10^{-6} \text{ K}^{-1}$ ) is comparable to any other choice. This observation also applies to possible alternate substrates, such as  $\text{SiO}_2$  or PMMA, which despite their extreme values of thermal expansion coefficient do not provide significant improvements over Si as the substrate material. A majority of materials belonging to different classes in the  $E$ - $\alpha$  domain lies approximately between 0.1 and  $10 \text{ Jm}^{-3}\text{K}^{-2}$ . Hence improvement in  $W_{no}$  beyond this order of magnitude is not achievable by optimal materials selection.

Zinc is one candidate that has not been used so far for microelectrothermal actuators despite its potentially superior performance to aluminium. Zn/ZnO films of up to a few microns can be grown on silicon substrates by sputter deposition [35, 36]. Few published works are available characterising zinc film properties relevant to microsystems applications. Therefore, the feasibility of using zinc for thermal bimaterial actuators would require a detailed investigation. By contrast, PMMA films of up to a

few hundreds of microns can be coated on silicon by conventional spin coating, which is a proven fabrication route [37].

An important outcome of the present work is the evolution of a strategy for the systematic selection of suitable candidate materials for bimaterial microelectrothermal actuators. This strategy can also be applied to select suitable candidate materials for other types of actuators such as piezoelectric, magnetostrictive and shape memory. The governing mechanics for these actuators is based on the relationship connecting the structural response, the field strength and the material parameters (piezoelectric strain coefficients for piezoelectric actuation and magnetostrictive coefficients for magnetostrictive actuation).

## 2.7 Summary

Closed form relations for thermoelastic performance metrics were derived using beam theory by applying structural mechanics relations. These performance metrics (free-end slope, blocked moment and work per volume) that determine the operating characteristics of a bimaterial actuator were optimised for maximum performance for a given material pair and their corresponding optimal thickness ratios were evaluated. The suitability of conventional semi-conductor materials for micromechanical transducer design was discussed relevant to performance enhancement and new candidate materials were obtained for silicon substrates by plotting iso-performance contours. Finally, an analytical framework for selecting novel material combinations for thermal bimaterial actuators was presented, which could serve as a useful tool for identifying potential candidate materials for other actuation schemes in bimaterial architecture.

Although a few promising candidates for various functional requirements were identified based on their thermoelastic response, the overall performance of BMET actuators are affected by the electrothermal response as well, which is characterised by the parameter  $\Delta T$  whose effects are normalised in the analysis done so far. Hence design studies based on the electrothermal response has to be carried out to identify potential material combinations satisfying both thermoelastic and electrothermal functional requirements. Chapter 3 discussed the relevant electrothermal analysis for the purpose of materials selection for BMET actuators.

# Chapter 3

## Effect of Heat Transfer on Materials Selection for Bimaterial Electrothermal Actuators

### 3.1 Effect of electrothermal heating on the actuator response

The transduction mechanism in electrothermal actuation is characterised by the deliverance of output kinetic energy by electrothermal heating of the mechanical structures. This requires best performance not only in the thermoelastic domain as discussed in chapter 2 but also in the electrothermal domain as well which is signified by the term  $\Delta T$  in equations (2.4). Seldom will a material have properties delivering maximum performance in all the governing physical domains of a system. The analysis discussed in this chapter is focussed on the influence of electrothermal heat transfer analysis on the materials selection for BMET actuator structures.

There have been a few published works on electrothermal heat transfer in microsystems, including: Estimation of the time constant and lateral resonances of Al-Si bimetals [38] for resonant sensors and microswitches applications, an experimental investigation of the electrothermal behaviour of a Diamond-like Carbon (DLC) - Ni microcage device for handling living biological cells [19], estimation of the temperature field in an SU8-Pt polymeric microgripper [20] by numerical simulations, evaluation of the transient thermal field of an Au-Si micro cantilever actuated by a laser pulse for wireless MEMS applications [39] and the effect of electrical/thermal properties on the temperature of silicon micro cantilevers used in atomic force microscopy for nanotopographic measurements [40]. All these works analysed the performance of specific BMET actuators employed in different microsystems for various applications. However, a more generalised electrothermal analysis to guide the materials selection for realising high performance actuators has not been previously attempted. The present analysis aims to identify promising candidates for BMET actuators at small scales ( $10\mu\text{m} \leq L \leq 1\text{mm}$ ) by building on previous works focussed on the overall selection of actuation principles, at the macro [5] and micro [6] scales.

The key performance metrics for BMET actuators depends on both thermoelastic and electrothermal responses of the bimaterial i.e., the displacement (slope), force

(moment), work per unit volume per cycle, the actuation frequency and the effectiveness. This chapter therefore discusses a strategy for selecting suitable candidate materials for bimaterial structures based on electrothermal heat transfer analyses in order to improve the performance. The process of materials selection explained here follows the previous chapter in which displacement, force and work per unit volume of the actuators were maximised for a constant, uniform temperature difference. Therefore the resulting set of materials identified in these two studies would be promising candidates for BMET actuators. The objective of the present analysis is to develop an analytical framework for materials selection for BMET actuators considering electrothermal heat transfer effects.

The relevant performance metrics for BMET actuators which depend on the heat transfer response are the actuation frequency, effectiveness and electromechanical efficiency. A high actuation frequency is required for applications such as micromirror devices [9], microgrippers, fibre optic switches [28] and boundary layer flow control devices. Effectiveness is defined here as a measure of displacement or force or work achieved within a cycle per unit electrical energy consumed; the choice is dependent upon the application. The characteristic electromechanical efficiency is defined here as the ratio of the total mechanical work done by the actuator to the electrical energy supplied.

The competition between different modes of heat transfer which constitutes the total heat transfer loss varies according to the actuator scales. This variation in the competing heat transfer modes affects the thermomechanical response of the actuators. The effect of scaling and its influence on the response which eventually determines the materials selection is therefore addressed.

This chapter is organised as follows. Section 3.2 gives an overview of the thermomechanical design of BMET actuators. Section 3.3 discusses the evaluation of the equivalent thermal properties of a bimaterial. Evaluation of the steady state and transient thermal responses of a bimaterial are presented in Sections 3.4 and 3.5 respectively. Section 3.6 discusses the estimation of the functional effectiveness and the electromechanical efficiency of a bimaterial. Section 3.7 illustrates the application of heat transfer models for materials selection. Section 3.8 discusses the influence of

scaling and heat transfer on the materials selection for BMET actuator structures. Section 3.9 summarises the key inferences drawn from this analysis.

### 3.2 Thermomechanical design of a BMET actuator - An overview

Figure 3.1 shows a schematic of an electrothermally actuated bimaterial cantilever structure. The relevant material properties are Young's modulus ( $E$ ), thermal expansion coefficient ( $\alpha$ ), thermal conductivity ( $\kappa$ ), thermal emissivity ( $\varepsilon^t$ ), specific heat capacity ( $C$ ) and density ( $\rho$ ). The subscripts 1 and 2 correspond to the respective material layers. The thicknesses of the two layers are  $t_1$  and  $t_2$  respectively. The width of the beam is  $b$  and its length is  $L$ . The base and ambient temperatures are  $T_b$  and  $T_\infty$  respectively. The relevant optimal performance metrics to gauge the maximum quasi-static thermomechanical response obtained from a bimaterial are given by the equations (2.15), (2.20) and (2.23). These equations can be rewritten as

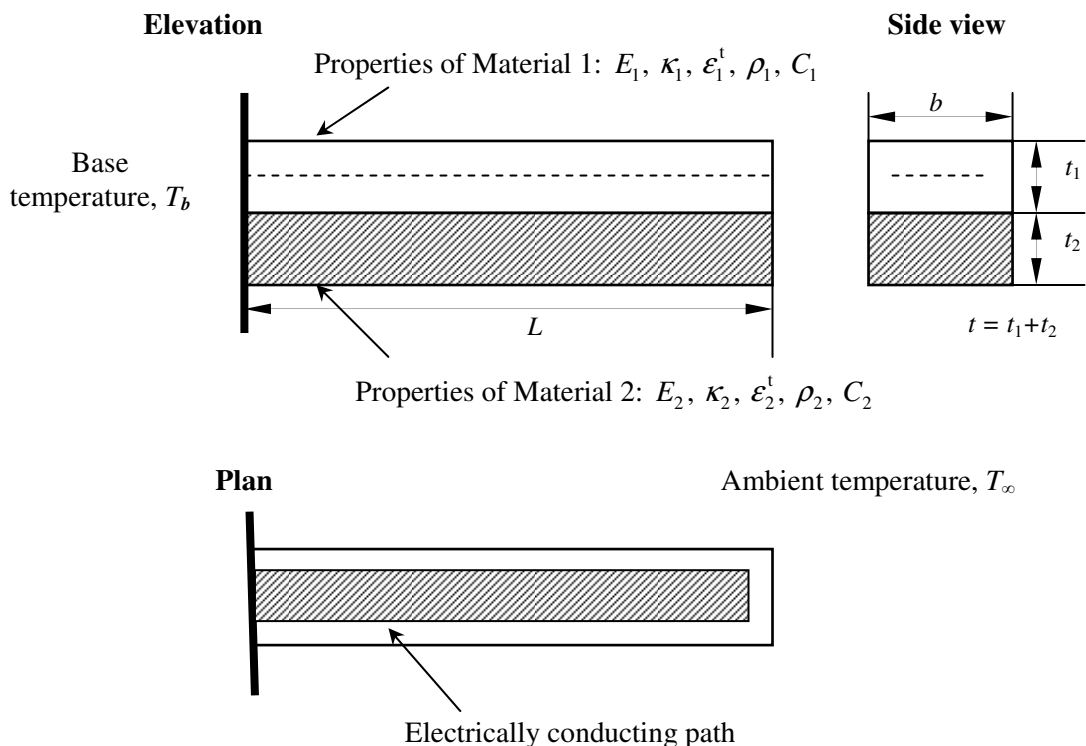


Figure 3.1 Schematic of a bimaterial cantilever heated electrically.

$$\Theta_{fo} = \frac{3L(\Delta\alpha)(\Delta T)}{2t} = \frac{\Theta_{no}L(\Delta T)}{t} \quad (3.1)$$

$$M_o = \frac{E_1bt^2(\Delta\alpha)(\Delta T)}{2\left(\frac{1+\xi_o}{\xi_o}\right)^2} = M_{no}bt^2(\Delta T) \quad (3.2)$$

$$W_o = \left(\frac{3E_1(\Delta\alpha)^2(\Delta T)^2}{32}\right)\left(\frac{\xi_o}{1+\xi_o}\right)^2 = W_{no}(\Delta T)^2 \quad (3.3)$$

where  $\Theta_{fo}$ ,  $M_{bo}$  and  $W_o$  are the optimal thermomechanical responses for a given pair of materials. The normalised optimal responses,  $\Theta_{no}$ ,  $M_{no}$  and  $W_{no}$  are the respective material parameters which correspond to the optimal slope, blocked moment and work per unit volume for a given geometry and temperature difference.

The estimates of the performance given by equations (3.1), (3.2) and (3.3) are exact only if the temperature of the bimaterial is constant along its length. However, in reality, the variable  $\Delta T$  is not constant owing to heat generation along the conducting path. It is a non-linear function of electrical and thermal properties of the materials employed for a given geometry. The present study therefore considers the average temperature in the evaluation of the variable  $\Delta T$ . Since for an optimal response, the ratio of thicknesses of the bi-layers is a function of the elastic moduli ratio of the bimaterial (equation (2.14)), it is possible to express  $\Delta T$  as a function of mechanical, electrical and thermal properties. The present analysis investigates the influence of the competing heat transfer modes on  $\Delta T$  which in turn affects the thermomechanical response of the bimaterial. A detailed heat transfer analysis is required for more complicated actuator geometries.

A BMET actuator is a microscale structure with in-plane dimensions in the range of 10-1000  $\mu\text{m}$ . Actuation is typically achieved by resistive heating followed by uncontrolled cooling. The small scale allows a lumped heat capacity formulation to be used as the surface convective resistance is large compared to the internal conduction resistance. This is quantified by the Biot number,  $Bi$  [41] which is given by



$$Bi = \frac{hL_c}{\kappa_{eq}} \quad (3.4)$$

where  $L_c = V/A_s$  is the characteristic length which is given by the ratio of the volume,  $V$  to the surface area,  $A_s$  of the actuator,  $\kappa_{eq}$  is the equivalent thermal conductivity of the actuator materials and  $h$  is the heat transfer coefficient of the actuator surface. The surface area to the volume ratio for microscale structures is usually very large and therefore the Biot number is very small ( $\sim 0.01-0.1$ ) which justifies the use of a lumped heat capacity model.

### 3.3 Evaluation of equivalent thermal properties

From equation (2.14) it is clear that the optimal thickness ratio of the bimetals depends only on the ratio of the Young's moduli and is independent of the thermal expansion coefficients of the materials. Therefore the equivalent thermal properties of a bimaterial with an optimal thickness ratio also depend on the Young's moduli of the bimetals. The equivalent thermal properties relevant to the present analysis are thermal conductivity, volume specific heat and thermal emissivity. Furthermore, the power generated per unit volume due to Joule heating also must be evaluated for the thermal analysis.

#### 3.3.1 Equivalent thermal conductivity, $\kappa_{eq}$

The equivalent thermal conductivity,  $\kappa_{eq}$  is defined as the property of an equivalent homogenous material of unit thickness and unit area of cross section which when maintained under a unit thermal gradient would transfer the same energy as the bimaterial layers under the same conditions and it is given as

$$\kappa_{eq} = \frac{\kappa_1 \xi_0 + \kappa_2}{1 + \xi_0}. \quad (3.5)$$

### 3.3.2 Equivalent volume specific heat, $(\rho C)_{\text{eq}}$

The equivalent volume specific heat,  $(\rho C)_{\text{eq}}$  is similarly defined as

$$(\rho C)_{\text{eq}} = \frac{(\rho_1 C_1)\xi_o + (\rho_2 C_2)}{\xi_o + 1}. \quad (3.6)$$

### 3.3.3 Equivalent emissivity, $\epsilon_{\text{eq}}^t$

The equivalent emissivity,  $\epsilon_{\text{eq}}^t$  is defined as the property of an equivalent homogenous material which would emit the same amount of radiation from its surface when maintained at a given temperature as the bimaterial layers under the same conditions. The expression for the equivalent emissivity is given as

$$\epsilon_{\text{eq}}^t = \frac{\epsilon_1^t(b+t_1) + \epsilon_2^t(b+t_2)}{b+t}. \quad (3.7)$$

### 3.3.4 Power generated per volume, $\dot{q}$

The heating element in the actuator is usually one of the bimaterial layers; typically the one which generate nominal current densities ( $\sim 10^9 \text{ Am}^{-2}$ ) as used in IC's using a small voltage source. Silicon, being the most commonly employed substrate material in microsystems, is often considered as the heating element because its electrical resistivity can be varied over a wide range ( $10^3 - 10^{-7} \Omega\text{m}$ ) by doping with boron [42]. The electrical conducting path runs along the U shaped heating element as shown in Figure 3.1. End effects are ignored and the length of the conductor is assumed to be  $2L$ . The power generated per unit volume of the actuator when heated by a constant voltage source is given as

$$\dot{q} = \frac{V^2}{4\rho_r L^2 (1 + 1/\xi_o)} \quad (3.8)$$

where  $V$  is the constant actuation voltage used for Joule heating and  $\rho_r$  is the resistivity of the heating element. The effect of any insulating oxide layer sandwiched between the bimaterial layers is ignored in the present analysis.

### 3.4 Steady state temperature field of a bimaterial cantilever

Figure 3.2a shows a one dimensional heat transfer model of a cantilever beam with equivalent thermal properties heated electrically by a constant voltage  $V$ . The base which acts as a heat sink is maintained at a constant temperature,  $T_b$  and the ambient temperature is  $T_\infty$ . The cross sectional area of the beam is  $b \times t$  and the perimeter of the cross section is  $2 \times (b + t)$ . The total heat generated due to electrical heating is dissipated by conduction, convection and radiation. The heat transfer at the free end of the beam at  $x = L$  is negligible and therefore modelled as a thermally insulated section.

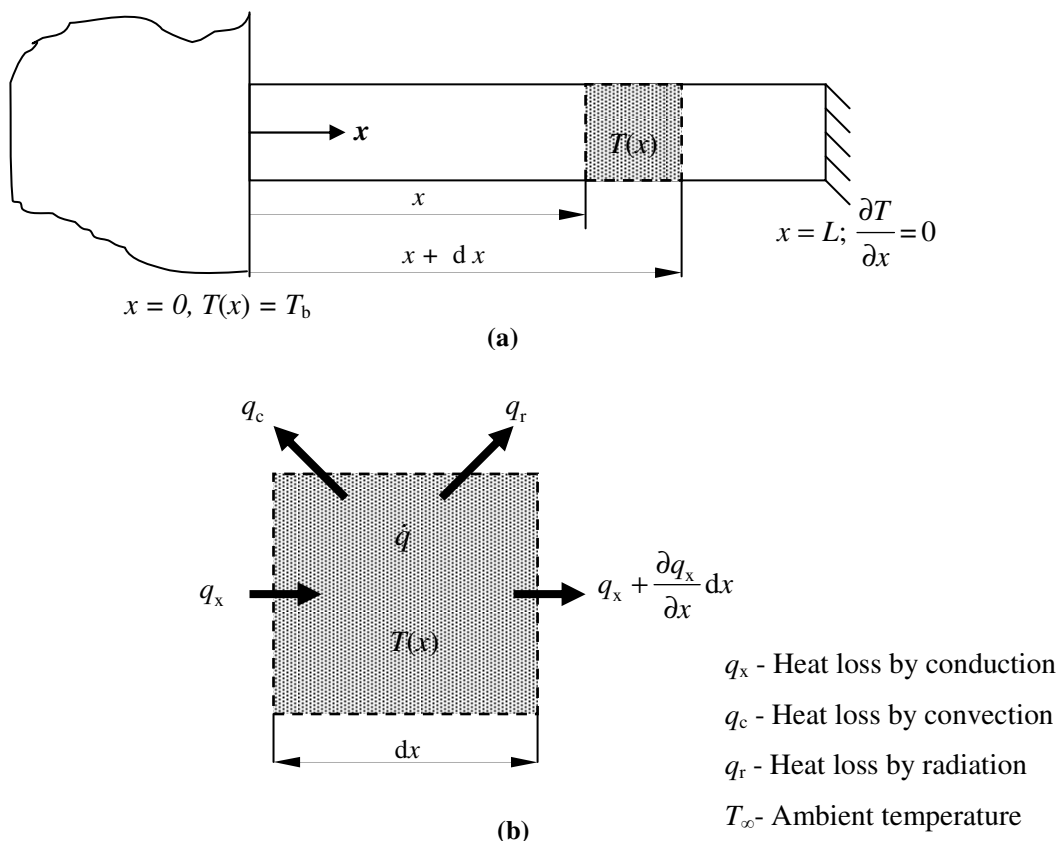


Figure 3.2 (a) Thermal model of a bimaterial cantilever; (b) Energy flow across the control volume considered.

Figure 3.2b shows the energy flow across an elemental control volume considered at a distance of  $x$  from the base. Let  $T(x)$  be the temperature of the control volume and  $dT$  be the temperature change over the length  $dx$ . The total thermal energy generated within the control volume is lost by diffusion to the base, convection to the surrounding fluid medium and radiation. Using the energy balance relation, an expression for the temperature field,  $T(x)$  along the length of the beam is obtained with/without convection and radiation effects.

The temperature field considering only the conduction effects is given as:

$$T(x) - T_b = \left( \frac{x\dot{q}}{\kappa_{\text{eq}}} \right) \left( L - \frac{x}{2} \right) \quad (3.9)$$

The accuracy of the temperature estimates can be improved by considering the convection and radiation effects. The corresponding temperature field is given by

$$\left( \frac{T(x) - \left( T_{\infty} + \frac{\dot{q}}{\kappa_{\text{eq}} m^2} \right)}{T_b - \left( T_{\infty} + \frac{\dot{q}}{\kappa_{\text{eq}} m^2} \right)} \right) = \frac{\cosh m(L-x)}{\cosh(mL)} \quad (3.10)$$

where  $m = \sqrt{\frac{2h_t(b+t)}{\kappa_{\text{eq}} bt}}$ ,  $h_t = h + \sigma \mathcal{E}_{\text{eq}}^t (T(x)^2 + T_{\infty}^2)(T(x) + T_{\infty})$  is the overall heat transfer

coefficient,  $h$  is the convective heat transfer coefficient and  $\sigma = 5.67 \times 10^{-8} \text{ Wm}^{-2}\text{K}^{-4}$  is the Stefan-Boltzmann constant. The characteristic temperature of the bimaterial is defined by the mean temperature,  $T_{\text{av}}$  along its length. For the temperature field considering the conduction effects alone,  $T_{\text{av}}$  is given as:

$$T_{\text{av}} - T_b = \frac{L^2 \dot{q}}{3 \kappa_{\text{eq}}} \quad (3.11)$$

For temperature field considering convection and radiation effects,  $T_{\text{av}}$  is given by:

$$\left( \frac{T_{av} - \left( T_{\infty} + \frac{\dot{q}}{\kappa_{eq} m_{av}^2} \right)}{T_{av} - \left( T_{\infty} + \frac{\dot{q}}{\kappa_{eq} m_{av}^2} \right)} \right) = \frac{\tanh(m_{av}L)}{m_{av}L} \quad (3.12)$$

where  $m_{av}$  is the value of  $m$  at  $T(x) = T_{av}$ . For in-plane cantilever bimaterial structures suspended on a wafer, the effect of gas conduction significantly affects the temperature of the structures if the thickness of the trapped fluid film between the wafer and the structures is very small (a few microns). However, for a large fluid film thickness (a few tens to hundreds of microns), the gas conduction has less influence on the temperature of the structures owing to free convective currents. The accuracy of the temperature estimates predicted in this study is reasonably good for large thickness of the trapped fluid film.

Using equation (3.11) a parameter called the electrothermal power index,  $P_1$  is defined considering the heat transfer loss due to conduction only and it is given by

$$P_1 = \frac{1}{3\kappa_{eq}} = \left( \frac{(T_{av} - T_b)}{\dot{q}L^2} \right) \approx \frac{(\Delta T)}{\dot{q}L^2}. \quad (3.13)$$

$P_1$  is a material dependent parameter which gives a measure of the achievable temperature for a bimaterial of fixed length when heated by a source generating unit power per volume of the material. Since materials selection is generally based on the relative estimates of the performance, convective effects are ignored in the evaluation of the  $P_1$  as they do not have any bearing on the selection criteria.

### 3.5 Transient thermal response of a bimaterial cantilever

The actuation frequency of BMET actuators depends on the time taken by the actuators to heat and cool alternately between the prescribed operating temperatures. The time taken by the actuators to be heated to a given temperature can be controlled to a certain

extent by altering the electrical resistivity of the heating element (e.g. silicon) by doping. The cooling phase is usually uncontrolled, and it depends on the thermal properties of the substrate materials and the ambient conditions. If  $T_p$  and  $T_v$  are the peak and valley temperatures ( $T_p > T_v$ ) between which a bimaterial actuator operates, then the time corresponding to heating ( $t'_h$ ) and cooling ( $t'_c$ ) phases can be obtained by solving the implicit transient thermal model using numerical integration. The temperature at any time step corresponding to the heating phase of the cycle is given by:

$$T^{i+1} = \frac{T^i + F_o \left( T_b + Bi.T_\infty + \left( \frac{\dot{q}_t L^2}{\kappa_{eq}} \right) \right)}{1 + F_o (Bi + 1)} \quad (3.14)$$

For cooling phase of the cycle, the temperature at any time step is given as

$$T^{i+1} = \frac{T^i + F_o (T_b + Bi.T_\infty)}{1 + F_o (Bi + 1)} \quad (3.15)$$

where  $T^i$  and  $T^{i+1}$  are the temperatures of the bimaterial at the successive instants  $t'$  and  $t' + \Delta t'$ ,  $\dot{q}_t$  is the constant electrothermal power generated per unit volume during the heating phase,  $F_o = \kappa_{eq} \Delta t' / (\rho C)_{eq} L^2$  is the Fourier number and  $Bi = 2h(b + t)L^2 / \kappa_{eq} bt$  is the Biot number.

The losses associated with the heating phase for a high constant electrothermal power generation per unit volume ( $\dot{q}_t \sim 10^{12} - 10^{13} \text{ Wm}^{-3}$ ) is usually low ( $< 0.1 \dot{q}_t$ ). As a result, the electrical energy supplied can be assumed to be equal to the internal thermal energy stored within the bimaterial when raised from  $T_v$  to  $T_p$ . Therefore, for a linear ramp up from  $T_v$  to  $T_p$  the transient thermal response corresponding to the heating phase given by equation (3.14) reduces to

$$\dot{q}_t \approx \frac{(\rho C)_{eq} (T_p - T_v)}{t'_h}. \quad (3.16)$$

Since the electrothermal heating rate is faster than the cooling rate by an order of  $\sim 10^1$ - $10^2$ , it can be ignored in the computation of the cyclic frequency. The characteristic actuation frequency can thus be evaluated as

$$f \approx \frac{1}{t'_c}. \quad (3.17)$$

For  $t'_h = 1/10f$  the electrothermal power generated per unit volume of the bimaterial during heating phase can be evaluated from equation (3.16) in terms of the actuation frequency and it is given as

$$\dot{q}_t = 10f(\rho C)_{\text{eq}}(T_p - T_v). \quad (3.18)$$

It should be noted that the actuation frequency depends on the operating temperatures,  $T_p$  and  $T_v$  for the given pair of materials and the length scale.

### 3.6 Effectiveness and efficiency of a BMET actuator

A thermomechanical design criterion which governs materials selection for many BMET actuators is the displacement or force or work per cycle achieved for the given amount of electrical energy supplied. Therefore the effectiveness of BMET actuators is quantified here based on the optimal displacement or force or work per cycle achieved from a given pair of materials for unit electrical energy consumed. The effectiveness can be either displacement (slope) based,  $\Theta_{\text{eff}}$ , force (moment) based,  $M_{\text{eff}}$  or work based,  $W_{\text{eff}}$ . Designing an actuator with the required effectiveness is determined by the functional requirements. Using equations (3.1), (3.2) and (3.3) expressions for the effectiveness of the BMET actuators are obtained as

$$\Theta_{\text{eff}} = \frac{\Theta_{\text{fo}}}{\dot{q}Lbt} = \frac{\Theta_{\text{no}}(\Delta T)}{bt^2\dot{q}} \quad (3.19)$$

$$M_{\text{eff}} = \frac{M_b}{\dot{q}Lbt} = \frac{M_{\text{no}}t(\Delta T)}{\dot{q}L} \quad (3.20)$$

$$W_{\text{eff}} = \frac{M_{\text{eff}} \Theta_{\text{eff}}}{8} = \frac{W_{\text{no}} (\Delta T)^2}{\dot{q}^2 L b t}. \quad (3.21)$$

Functional effectiveness in the thermomechanical domain is the ability to utilise the available thermal energy to the deliver the required mechanical performance (displacement/force/work per volume). Substituting equation (3.13) in (3.19), (3.20) and (3.21) effectiveness can be obtained in terms of the mechanical and thermal properties of the bimaterial which are given as

$$\Theta_{\text{eff}} = \frac{\Theta_{\text{no}} (\Delta T)}{b t^2 \dot{q}} = \frac{(\Delta \alpha) L^2}{2 \kappa_{\text{eq}} b t^2} \quad (3.22)$$

$$M_{\text{eff}} = \frac{M_{\text{no}} t (\Delta T)}{\dot{q} L} = \frac{E_1 (\Delta \alpha) L t}{6 \left( \frac{1 + \xi_o}{\xi_o} \right)^2 \kappa_{\text{eq}}} \quad (3.23)$$

$$W_{\text{eff}} = \frac{W_{\text{no}} (\Delta T)^2}{\dot{q}^2 L b t} = \frac{E_1 (\Delta \alpha)^2 L^3}{96 \left( \frac{1 + \xi_o}{\xi_o} \right)^2 \kappa_{\text{eq}}^2 b t}. \quad (3.24)$$

By normalising equations (3.22), (3.23) and (3.24) with respect to geometry, indices for effectiveness based on the displacement, force and work per cycle can be obtained as

$$\Theta_{\text{EI}} = \frac{\Theta_{\text{eff}} b t^2}{L^2} = \frac{(\Delta \alpha)}{2 \kappa_{\text{eq}}} \quad (3.25)$$

$$M_{\text{EI}} = \frac{M_{\text{eff}}}{L t} = \frac{E_1 (\Delta \alpha)}{6 \kappa_{\text{eq}} \left( \frac{1 + \xi_o}{\xi_o} \right)^2} \quad (3.26)$$



$$W_{EI} = \frac{W_{\text{eff}}bt}{L^3} = \frac{E_1(\Delta\alpha)^2}{96\kappa_{\text{eq}}^2 \left( \frac{1+\xi_0}{\xi_0} \right)^2} \quad (3.27)$$

where  $\Theta_{EI}$ ,  $M_{EI}$  and  $W_{EI}$  are indices for effectiveness based on slope, moment and work respectively for a fixed geometry of actuator.

The candidate materials selected besides being functionally effective should also be efficient in performance. Therefore, the electromechanical efficiency,  $\eta_{\text{em}}$  is defined here as the ratio of the optimal mechanical power output to the electrical power input for a given pair of materials. The electromechanical efficiency of a bimaterial actuator structure is given as

$$\eta_{\text{em}} = \frac{P_{\text{av}}}{\dot{q}_t} = \frac{P_{\text{av}}}{10f(\rho C)_{\text{eq}}(T_p - T_v)} \quad (3.28)$$

where  $P_{\text{av}} = \frac{1}{(\Delta t')} \int_{t'}^{t'+\Delta t'} \left| \frac{dW_o}{dt'} \right| dt'$  is the average mechanical power output which depends on the transient thermal response of the bimaterial during the cooling phase for the temperature difference achieved with the given amount of electrical power supplied. The choices of materials which are functionally effective are not necessarily efficient because efficiency depends on the work per volume delivered for a given amount of input electrical energy supplied as opposed to the effectiveness which depends on the blocked force/displacement of the actuator.

### 3.7 Heat transfer considerations in the materials selection

The competition between the different modes of heat transfer which contribute to the thermal energy dissipation varies with the length scale of the bimaterial structure. As a consequence the thermomechanical response affecting the materials selection will also depend on scale (10  $\mu\text{m}$  - 1 mm). Hence, the performance of different classes of materials on a given substrate is examined as function of scale to identify promising candidates.

Silicon is one of the most commonly preferred substrate materials for microsystems due to its wide availability and ease of microfabrication besides having favourable properties in the various physical domains. For illustration silicon is chosen as one of the bimaterial layers and is also assumed to act as the heat source. Table 3.1 shows the properties of single crystal silicon used for this analysis. The bimaterial is assumed to be actuated using a constant DC voltage source. The heat generated by the bimaterial is dissipated by diffusion to the base and convection to the surrounding fluid medium. The temperature of the base is assumed to be at,  $T_b = 323$  K and the ambient at  $T_\infty=293$  K. The heat loss by radiation is neglected which is reasonable, given the attainable temperature limits ( $\sim 773$  K) for the range of materials from different classes considered. The steady state thermal field considering the combined effect of conduction and convection depends on ratio of the perimeter to the area of the cross section which is a function of thickness of the bimaterial considering  $b > t$  for most actuator structures. A conservative estimate of the temperature is therefore obtained by assuming the cross section of the beam to be square with  $L/t = 30$ . The operating temperature difference for most microsystems is usually about  $\sim 100$  K. The present analysis aims to estimate the maximum performance limits achievable by electrothermal heating of bimaterial structures. Hence operating temperature range of 250 K with a peak temperature,  $T_p = 573$  K is assumed in the present study considering the maximum temperature permissible in the material domain ( $\sim 673$  K for ceramic substrates) at small scales.

Young's Modulus, $E_1 \sim 165$ GPa
Thermal conductivity, $\kappa_1 \sim 150$ Wm <sup>-1</sup> K <sup>-1</sup>
Thermal expansion coefficient, $\alpha_1 \sim 2.49$ $\mu\text{m.m}^{-1}\text{K}^{-1}$
Electrical resistivity, $\rho_r \sim 10^{-4}$ $\Omega\text{m}$
Specific heat capacity, $C_1 \sim 700$ Jkg <sup>-1</sup> K <sup>-1</sup>
Density, $\rho_1 \sim 2280$ kgm <sup>-3</sup>

Table 3.1 Material properties of single crystal silicon.

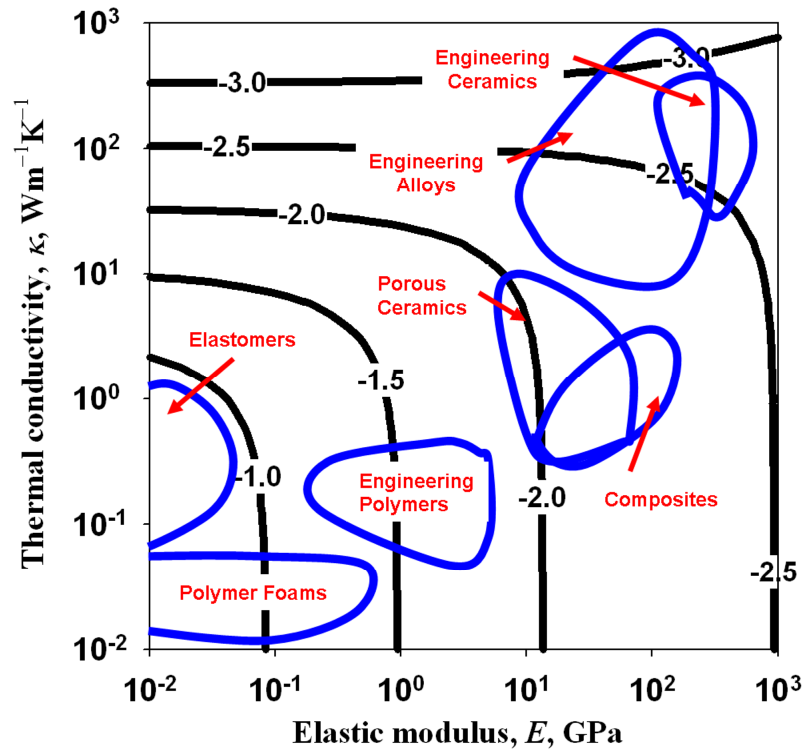
In order make an effective selection between the candidates, contours of equal response were plotted on an Ashby materials selection chart [17] in the domain of the governing properties. Materials which lie close to the contours indicating a high response were then considered for further detailed analysis.

The materials selection for BMET actuators is driven by the electrothermal and thermoelastic performances of the bimetals. Therefore, the performance of different classes of materials on silicon is evaluated on these considerations to identify novel material combinations. The electrothermal characteristics of different materials can be better understood if contours of  $P_1$  are plotted in the domain of relevant properties. Figure 3.3a shows contours of equal  $\log_{10}(P_1)$  plotted in the material domain ( $E$  vs.  $\kappa$ ) for silicon. It is evident that  $P_1$  for engineering polymers is greater than for engineering alloys/metals on silicon. Therefore, polymers require less power than metals to attain a given temperature. But the voltage required to attain a given temperature varies with the electrical resistance of the heating element which depends on the electrical resistivity of the substrate materials and the thickness ratio of the bimaterial layers. A parameter termed the electrothermal voltage index ( $V_1$ ) is defined by eliminating  $\dot{q}$  between equations (3.8) and (3.13):

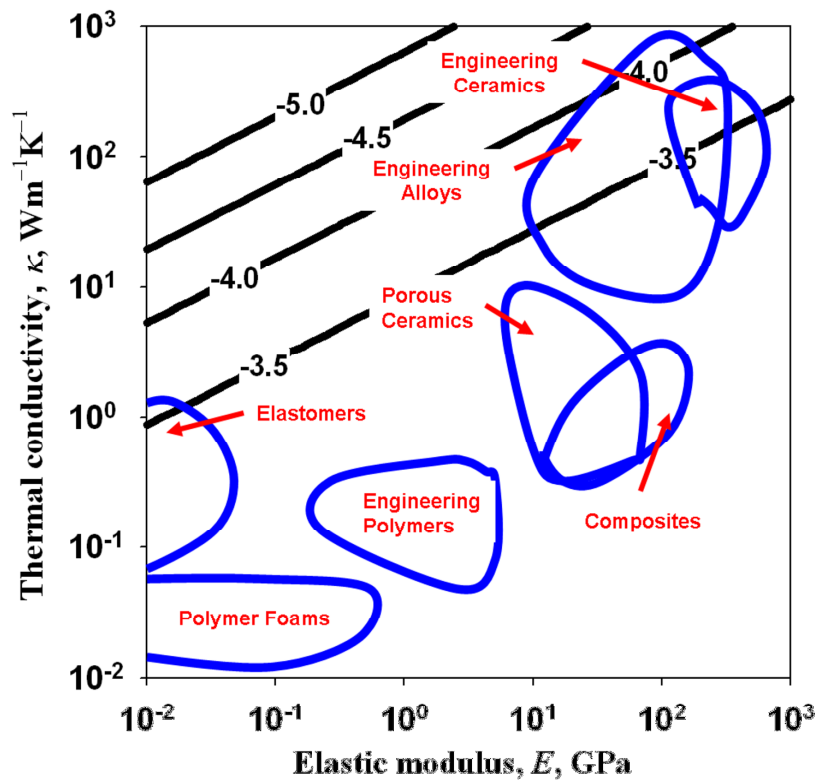
$$V^2 = \frac{(\Delta T)\rho_r}{V_1} \quad (3.29)$$

where  $V_1 = (12\kappa_{eq}(1+1/\xi_o))^{-1}$  is the voltage index of a material layer for a fixed heat source. The influence of  $V_1$  on the actuation voltage is small considering the range of variation in the electrical resistivity of different classes of materials ( $10^{-9}$  -  $10^{15}$   $\Omega\text{m}$ ).

Polymeric substrates would require much higher voltages than semiconductor and metallic substrates and therefore are not preferred heating elements. Furthermore, it is also possible to estimate the actuation voltage for a range of materials on a given heat source. Figure 3.3b shows contours of  $\log_{10}(V_1)$  plotted in the material domain ( $E$  vs.  $\kappa$ ) for silicon (which also acts as the heat source). It is clear from the plot that the actuation voltage required to attain a given temperature for different classes of materials on silicon varies only within an order of magnitude ( $V_1 \sim 10^{-3}$ - $10^{-4}$   $\text{mKW}^{-1}$ ) though the power required varies two orders of magnitude ( $P_1 \sim 10^{-1}$ - $10^{-3}$   $\text{mKW}^{-1}$ ). Figures 3.4a and 3.4b show similar contours of  $\log_{10}(P_1)$  for DLC and Poly-Methyl-MethAcrylate (PMMA) substrates respectively.

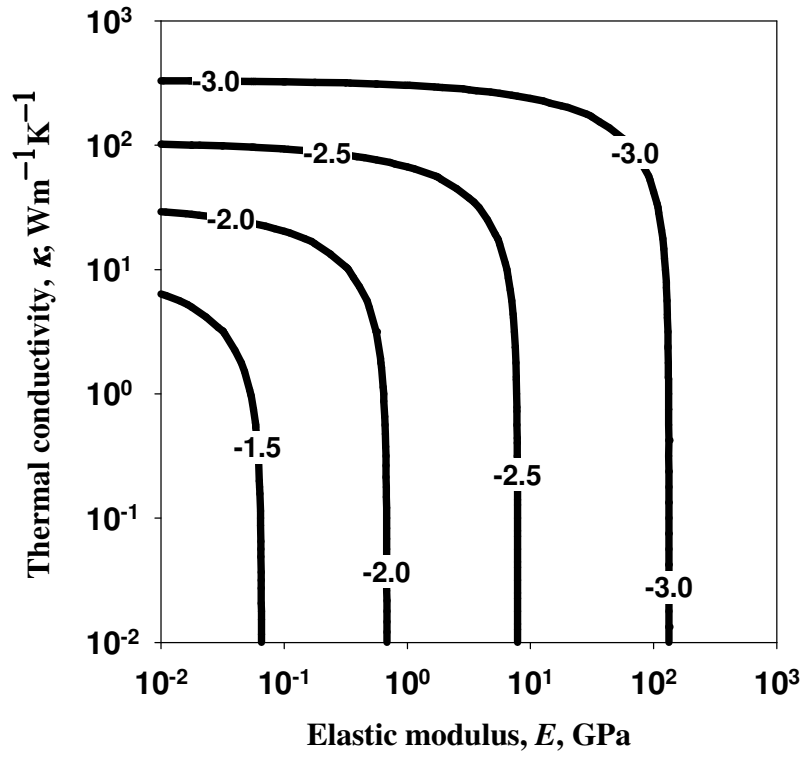


(a)

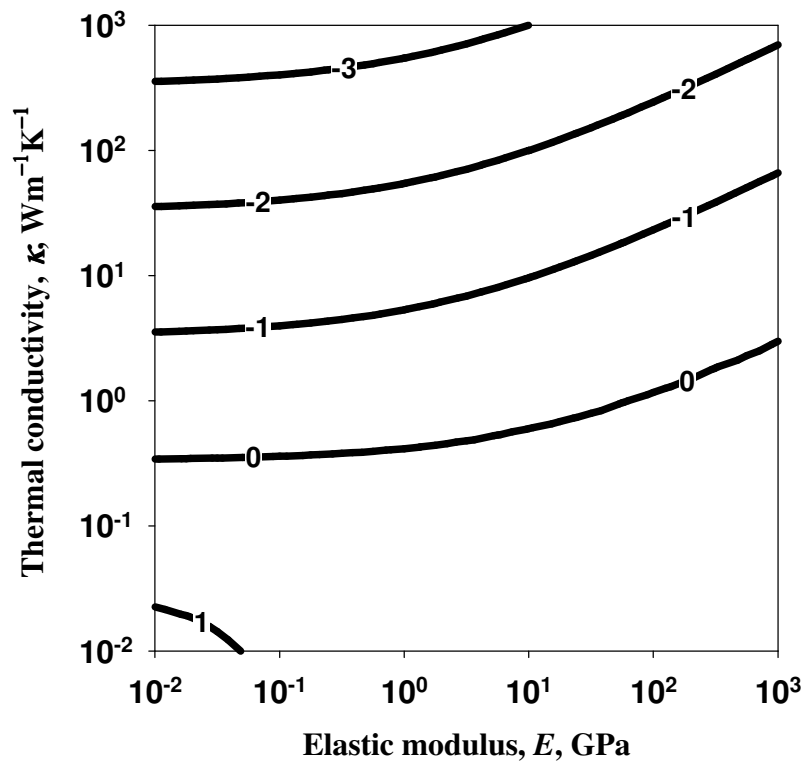


(b)

Figure 3.3 Contours of (a)  $\log_{10}(P_1)$ , (b)  $\log_{10}(V_1)$  for different classes of materials on silicon which acts as a heat source.



(a)



(b)

Figure 3.4 Contours of equal  $\log_{10}(P_1)$  for materials of different classes on (a) DLC, (b) PMMA substrates.

The achievable temperature for different material combinations due to Joule heating can be estimated from the isotherm contours plotted in the relevant material domains considering different modes of heat transfer. Figure 3.5 shows steady state isotherm contours (in Kelvin) obtained using equations (3.8) and (3.11) for different classes of materials on silicon for an optimal the thickness ratio,  $\xi_0$  considering heat dissipation due to conduction only. The voltage required for heating was assumed to be 5 volts considering the range of  $T_p$  preferred for microsystems applications.

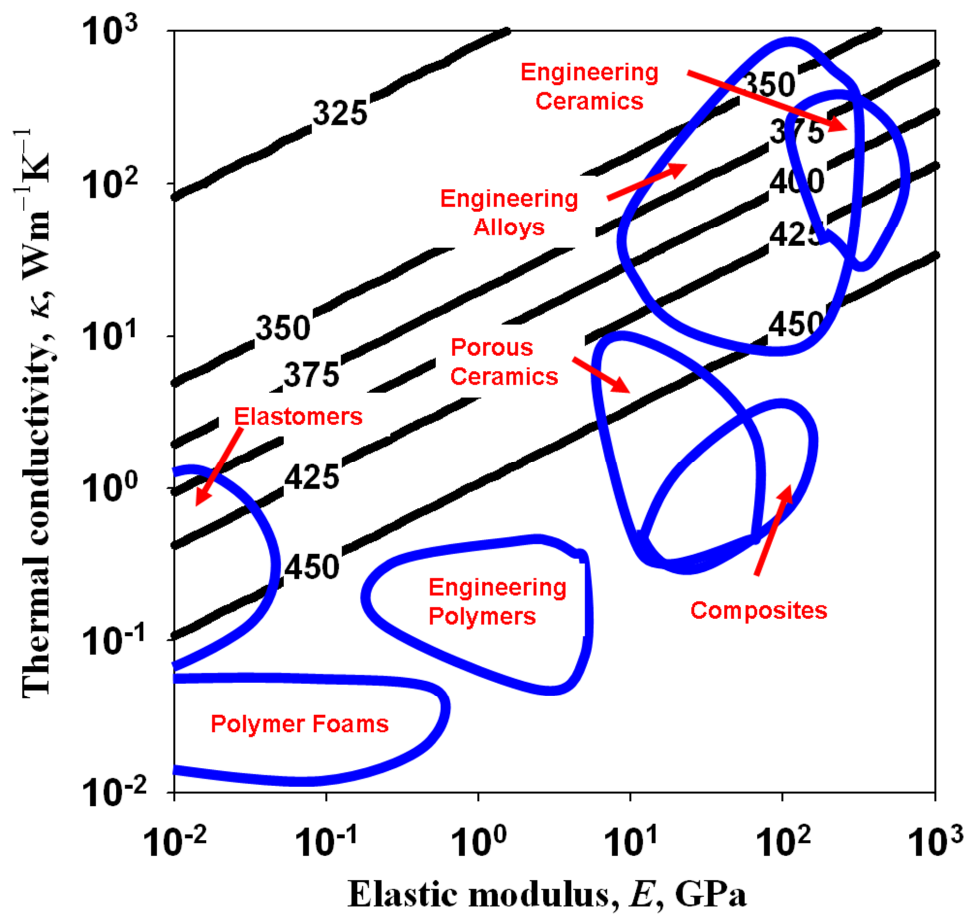


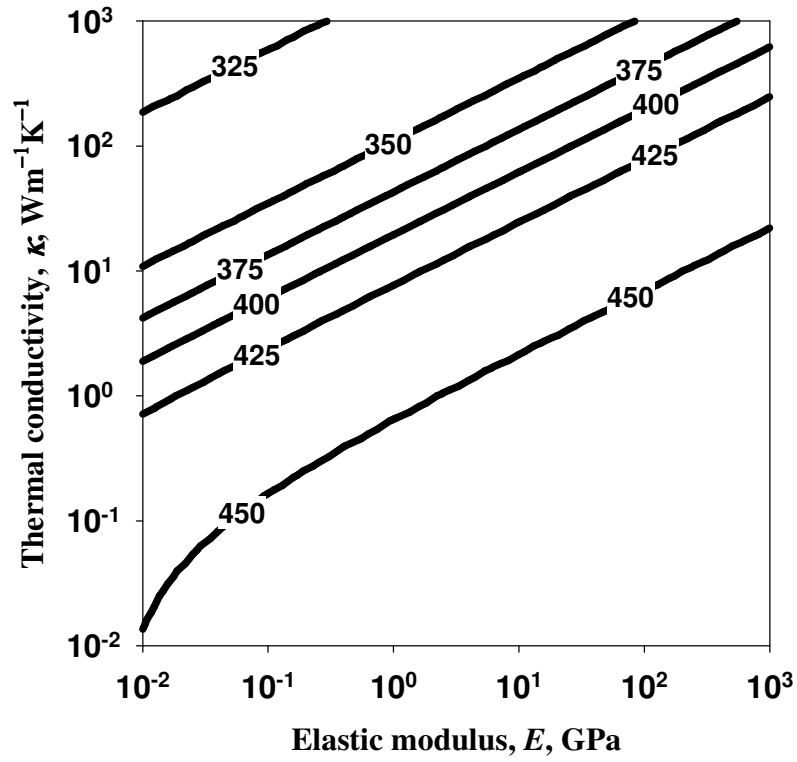
Figure 3.5 Comparison of the isotherms for different classes of materials on silicon with Ashby selection chart [17] considering heat dissipation due to conduction ( $V = 5$  volts).

Figures 3.6a and 3.6b show similar contours for Aluminium and PMMA substrates. Although the influence of materials choice on the achievable temperature is dictated by the power supplied, it is also limited further by the failure characteristics of the materials employed (e.g. yield/fracture stress and creep/melting temperature) which are not addressed in the present study. The effect of free convection on the isotherms

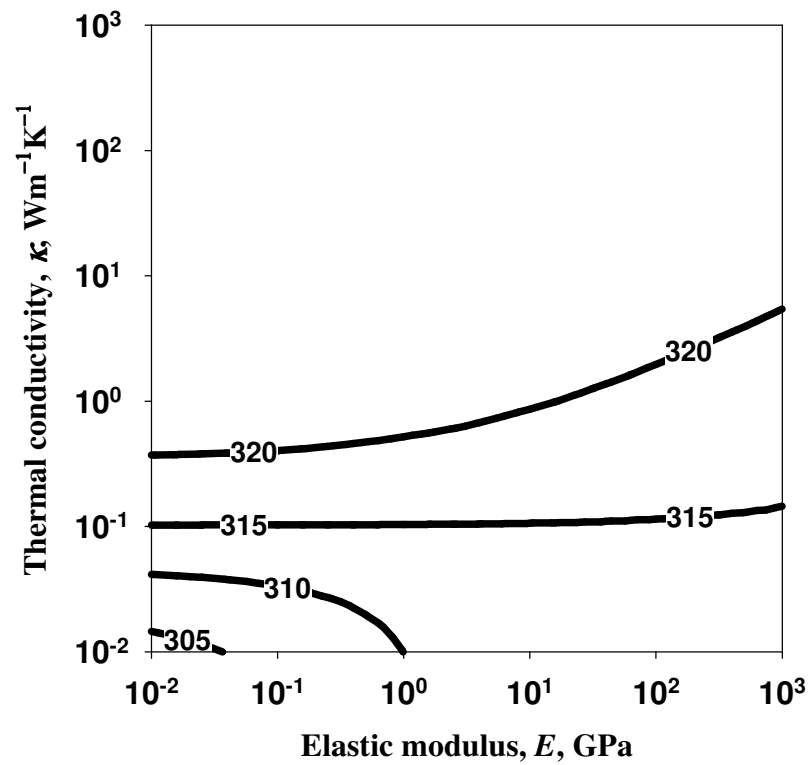
obtained using equations (3.8) and (3.12) for lengths,  $L = 100 \mu\text{m}$  and  $1 \text{ mm}$  are shown in Figures 3.7a and 3.7b respectively. A macroscale value of the convective heat transfer coefficient,  $h = 10 \text{ Wm}^{-2}\text{K}^{-1}$  was assumed. Figure 3.5 and 3.7(a) are almost identical which confirms that conduction is dominant at smaller scales ( $L < 1 \text{ mm}$ ). The effect of free convection becomes apparent at larger scales ( $L > 1 \text{ mm}$ ) as shown in Figure 3.7b. This is attributed to the decrease in the convection resistance accompanied by an increase in the Biot number due to large scales. However, even at this scale the variation in the isotherms is not very large. Hence the power dissipated due to convective currents is minimal at small scales which further confirm the applicability of the lumped heat capacity formulation.

The materials selection strategy for BMET actuators is based on complicated trade-offs between the electrothermal and thermomechanical performances. Therefore the overall selection criteria for promising candidates depend not only on the electrothermal response (achievable temperature difference for a given pair of materials due to Joule heating by constant voltage) but also on the thermomechanical response (effectiveness and efficiency). Establishing design trades based on the effectiveness is cumbersome due to the interaction between three material properties ( $E$ ,  $\alpha$ , and  $\kappa$ ). This complexity however, can be resolved if one of the governing properties is normalised (say  $(\Delta\alpha)$ ) and its effect is subsequently superimposed on the resulting response. It is evident from equation (3.25) that polymers on silicon are effective in delivering high displacement within a cycle for a given amount of electrical energy expended. Figure 3.8 shows contours of equal effectiveness indices for different classes of materials on silicon obtained using equations (3.26) and (3.27) by normalising with respect to  $(\Delta\alpha)$ .

It is surprising to note from Figures 3.8a and 3.8b that polymers are essentially equivalent to engineering alloys/ceramics for delivering high work or force per cycle considering their large thermal expansion coefficient. However, the large thickness required to compensate for the low Young's modulus may not be acceptable for many applications.



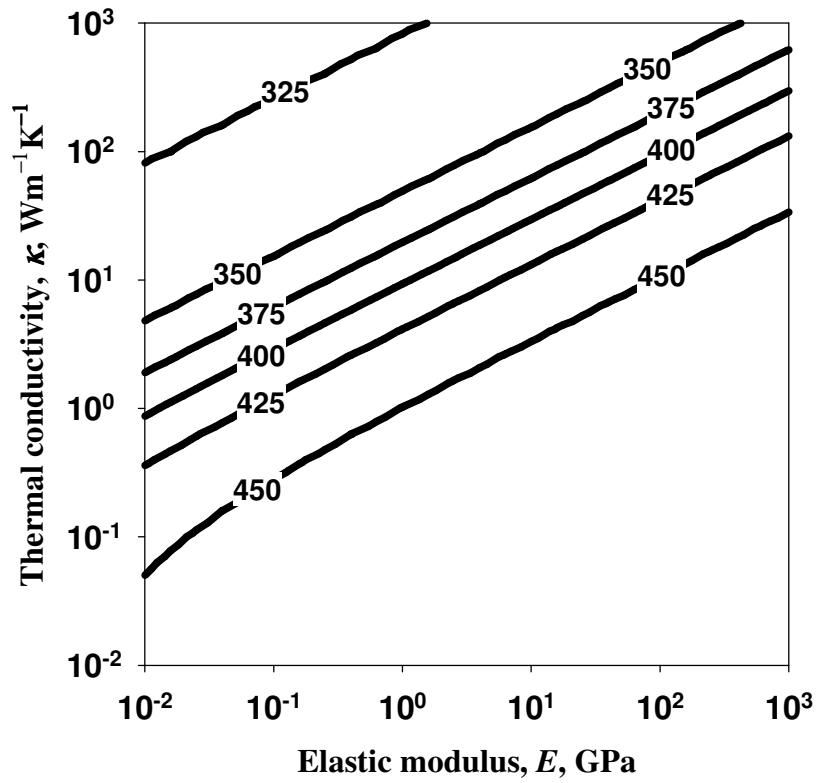
(a)



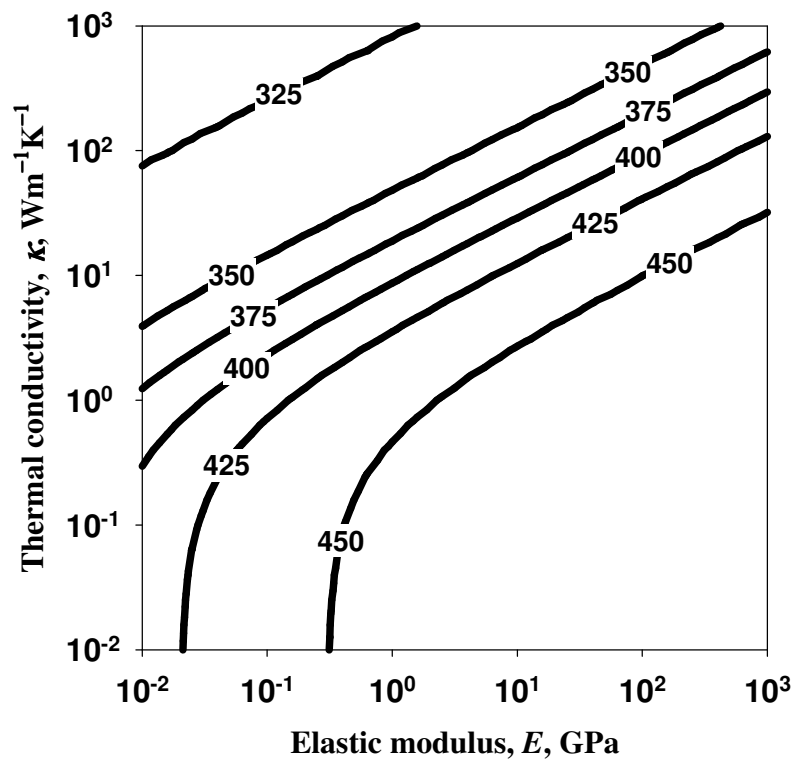
(b)

Figure 3.6 Steady state isotherms for different classes of materials on (a) Aluminium ( $V = 0.1$  volt), (b) PMMA ( $V = 5$  volts).



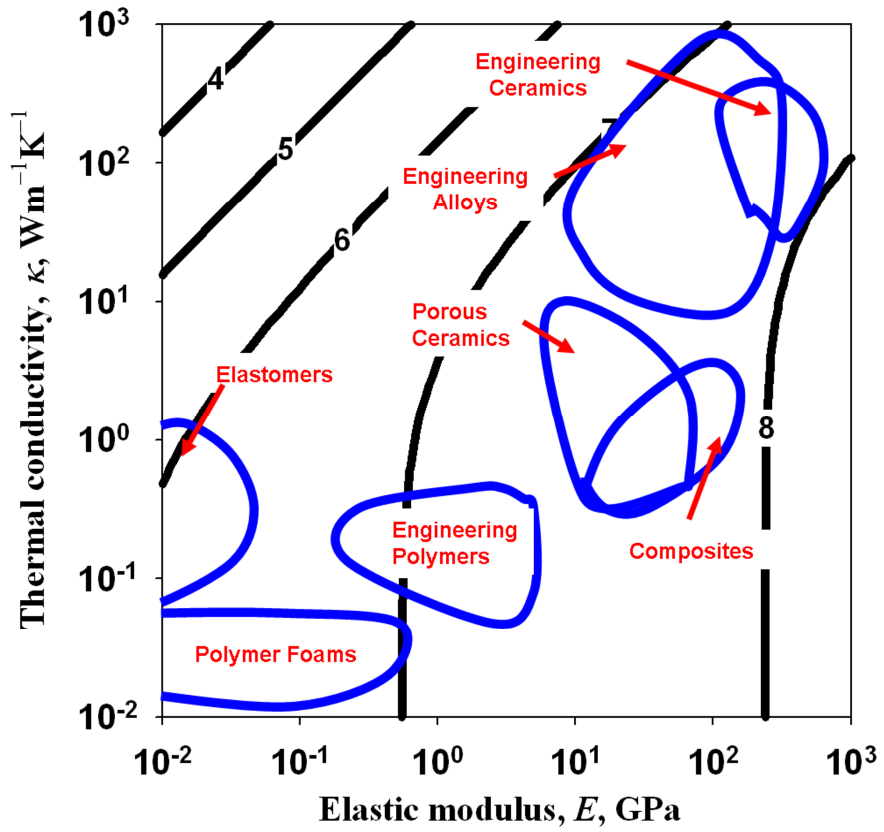


(a)

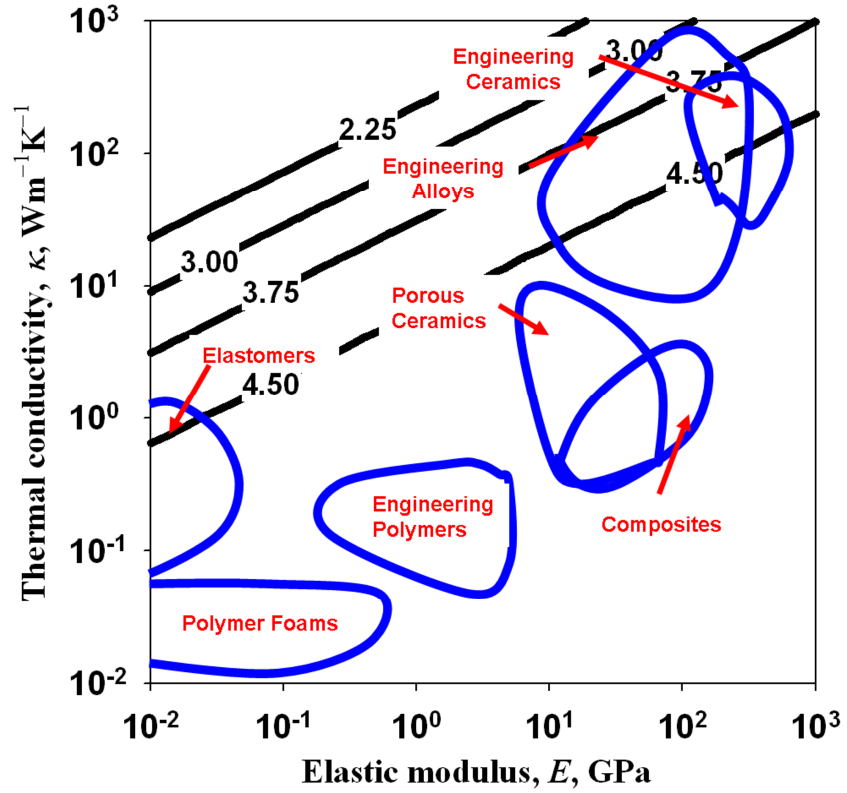


(b)

Figure 3.7 Isotherms for different classes of materials on silicon considering heat dissipation due to conduction and free convection for (a)  $L = 100 \mu\text{m}$ , (b)  $L = 1 \text{ mm}$ .



(a)



(b)

Figure 3.8 Contours of effectiveness indices normalised with respect to  $(\Delta\alpha)$  for different classes of materials on silicon (a) Contours of equal  $\log_{10}(M_{EI})$ , (b) Contours of equal  $\log_{10}(W_{EI})$ .

Another important target for materials selection is the electromechanical efficiency which depends on the maximum mechanical power output generated from a given amount of electrothermal power supplied as given by equation (3.28). Figure 3.9 shows a typical cooling curve for a bimaterial with the prescribed range of operating temperatures. Curve *a* represents a realistic transient thermal response of a bimaterial which is a monotonically decreasing non-linear function of time,  $t'$ . The area under the curve bounded by the temperature limits gives a measure of the achievable temperature difference for delivering the work per cycle for a given pair of materials.

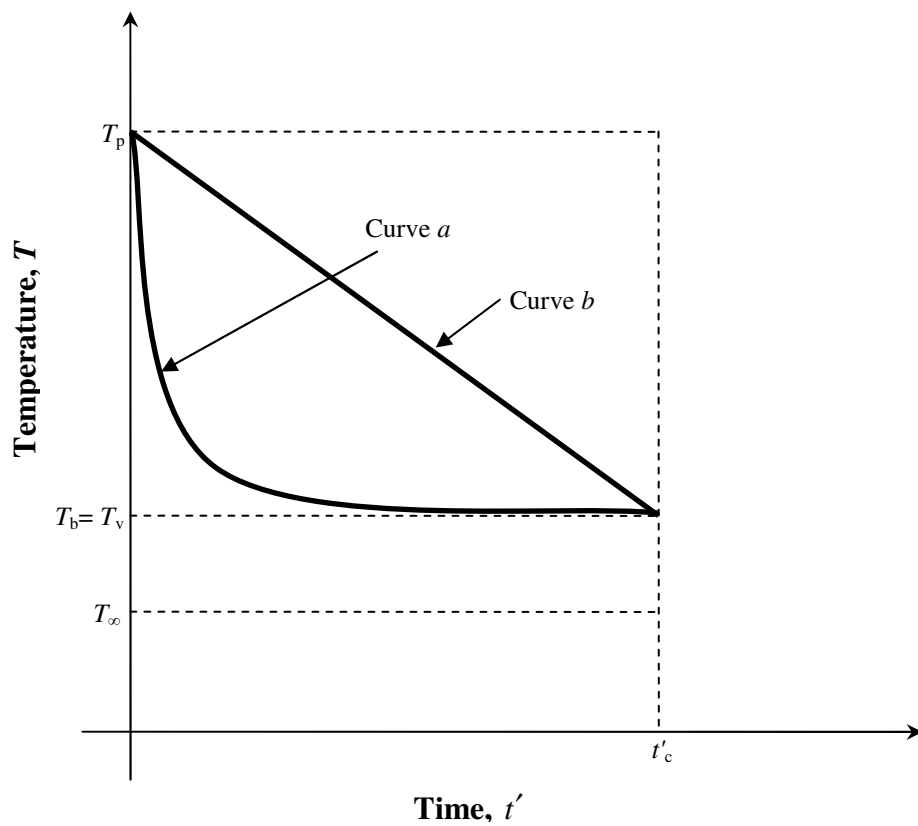


Figure 3.9 A typical transient cooling curve of a bimaterial approximated by linear response.

In order to evolve a relevant closed form solution for the efficiency metric which guides the materials selection, a linear transient cooling with an instantaneous heating (saw tooth response) is assumed. This assumption facilitates to comprehend the trade-off between the actuation frequency and the work per unit volume delivered per cycle in the preliminary design stage. The equation corresponding to curve *b* is given as

$$T = T_p - (T_p - T_v) f t'. \quad (3.30)$$

Substituting equation (3.30) in (3.28),  $\eta_{em}$  for a given material pairs can be obtained as

$$\eta_{em} = \frac{W_{no} (T_p + T_v - 2T_\infty)}{10(\rho C)_{eq}}. \quad (3.31)$$

The volume specific heat of different classes of materials is  $\sim 10^{6.5} \text{Jm}^{-3}\text{K}^{-1}$  [12] and therefore it can be assumed constant. Hence equation (3.31) further reduces to

$$\eta_{em} = \frac{W_{no} (T_p + T_v - 2T_\infty)}{10^{7.5}}. \quad (3.32)$$

Figure 3.10 shows contours of equal  $\log_{10}(\eta_{em})$  plotted in the domain of  $E-\alpha$  for the assumed values of operating temperatures. Since materials from different classes are clustered around  $\eta_{em} \sim 10^{-5}$ , it is evident that  $\eta_{em}$  for all these materials on silicon is almost constant.

The effect of temperature difference on the actuation frequency can be better understood if a relationship is established between the cooling rate and the operating temperature range. For a linear transient cooling curve from the initial temperature  $T_p$  to the final temperature  $T_v < T_b$ , a relationship can be evolved between the actuation frequency and the operating temperatures.

Substituting  $T^i - T^{i+1} = T_p - T_v$  and  $f = \frac{1}{\Delta t'}$ , equation (3-15) reduces to

$$(T_p - T_v) f = \left( \frac{K_{eq}}{(\rho C)_{eq} L^2} \right) ((T_v - T_b) + Bi (T_v - T_\infty)). \quad (3.33)$$

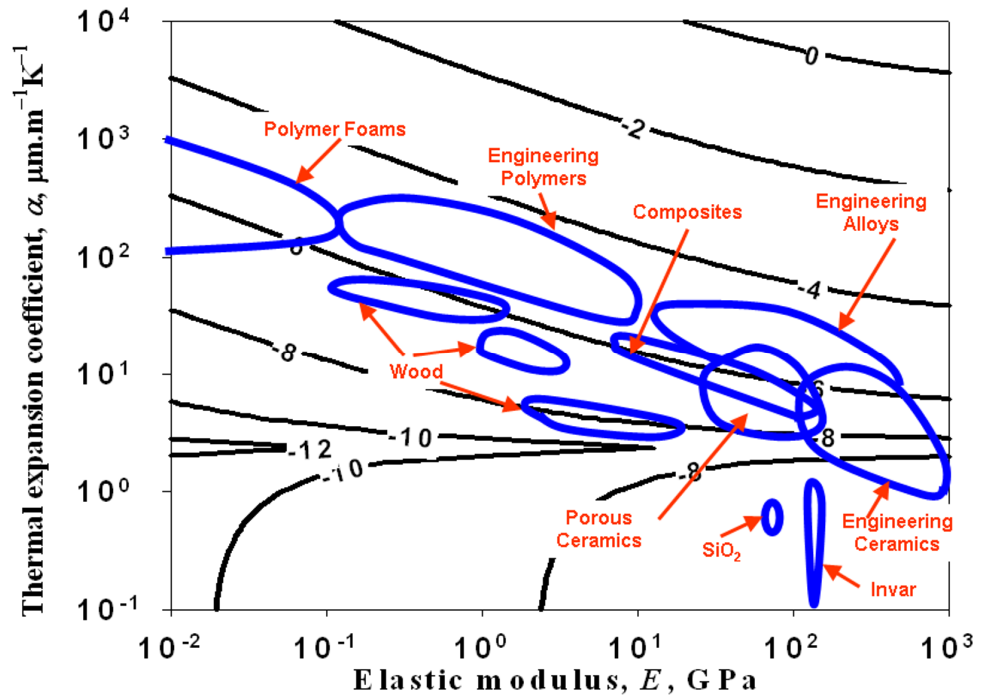


Figure 3.10 Contours of equal efficiency,  $\log_{10}(\eta_{em})$  for different bimaterial combinations with reference to a silicon substrate.

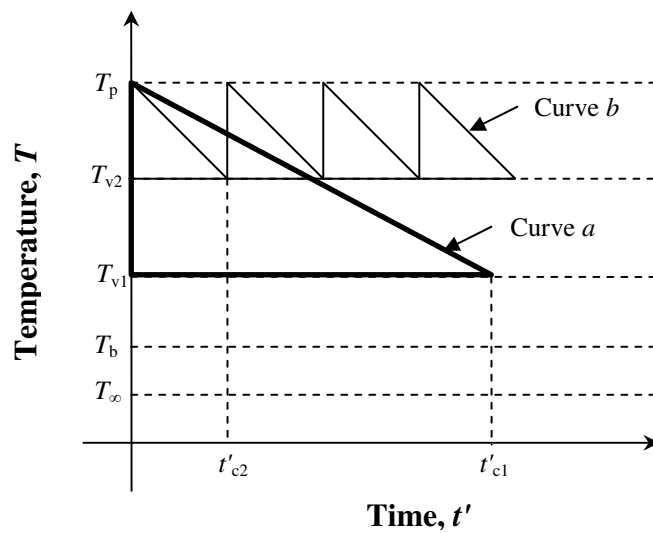
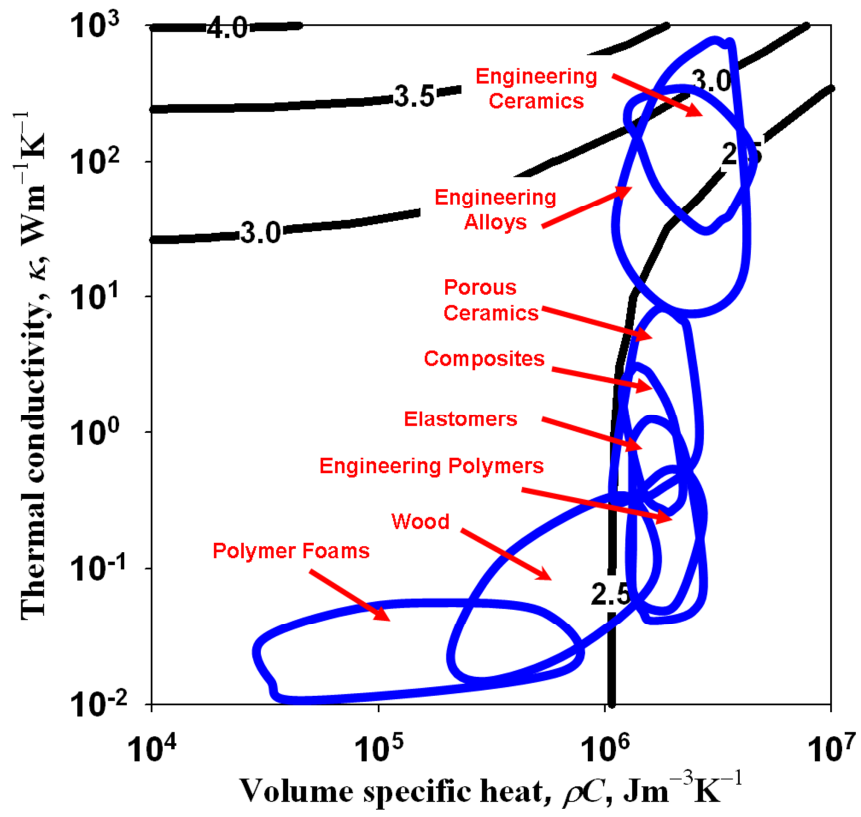
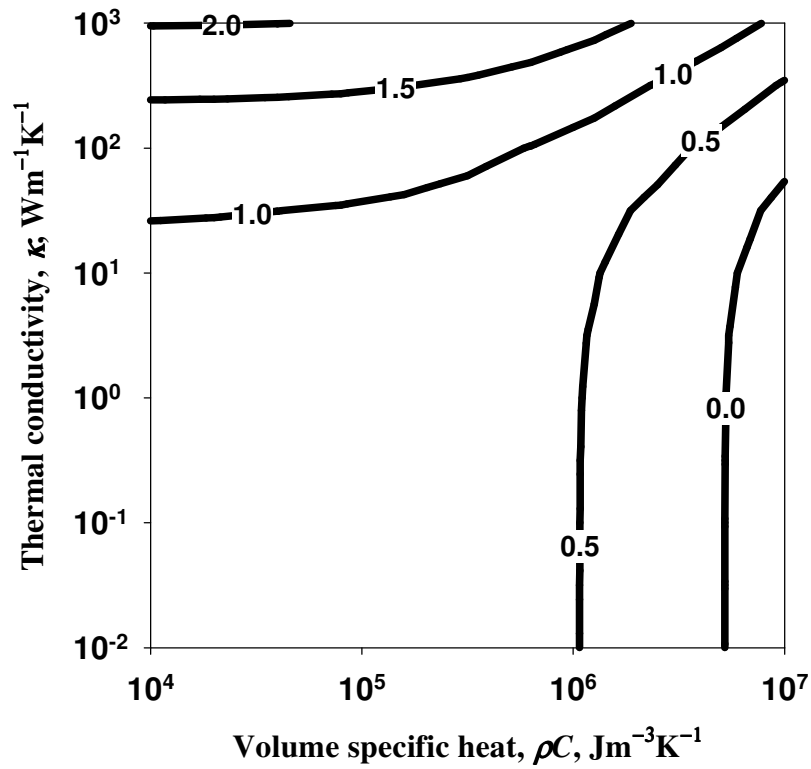


Figure 3.11 Effect of operating temperatures on the actuation frequency and the work per volume.

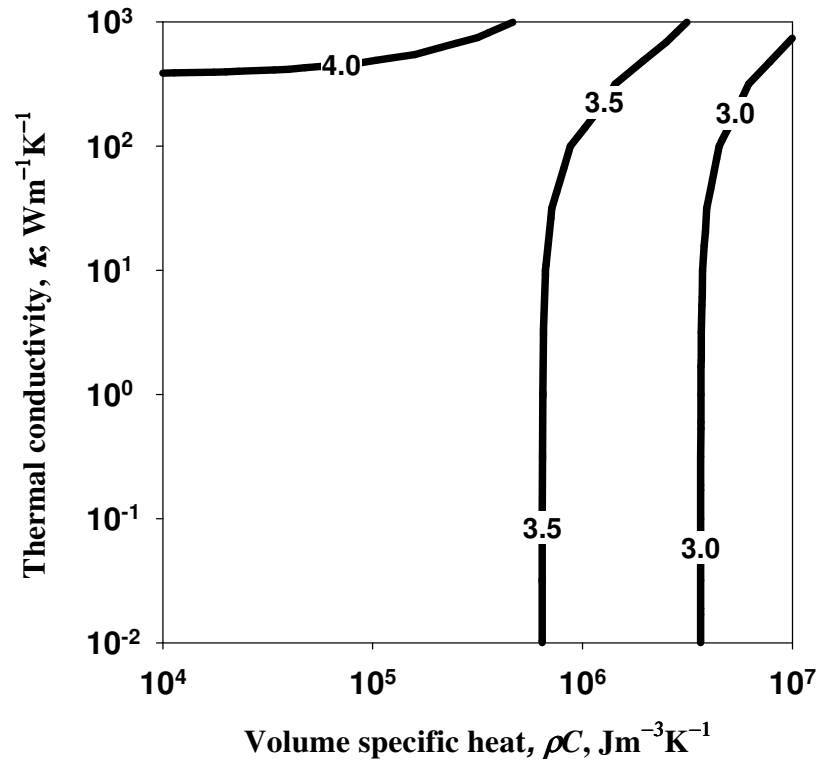


(a)

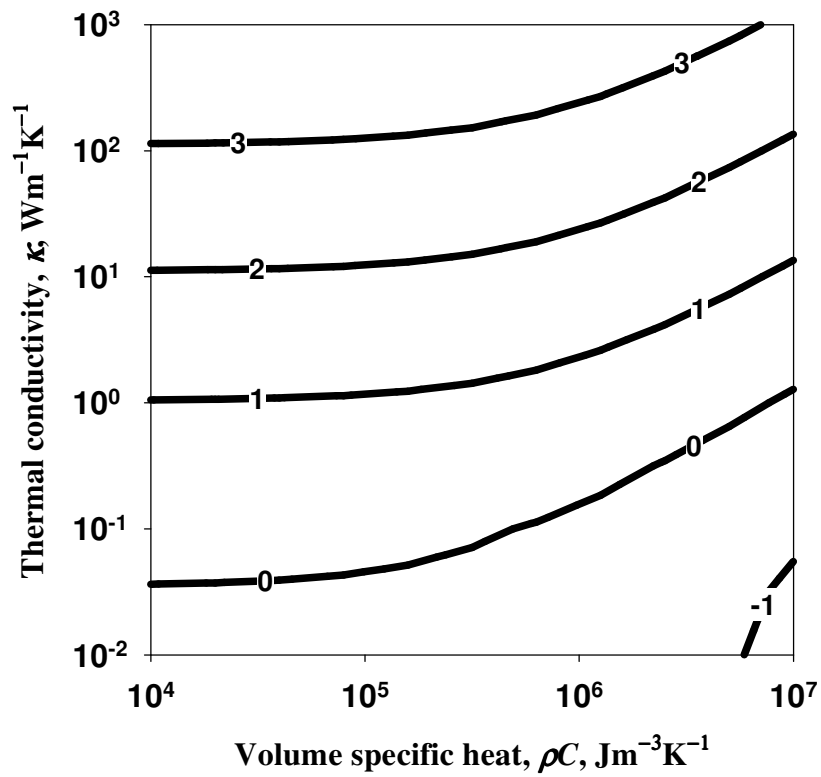


(b)

Figure 3.12 Contours of equal actuation frequency,  $\log_{10}(f)$  for different classes of materials on silicon for (a)  $L = 100 \mu\text{m}$ , (b)  $L = 1 \text{ mm}$  at  $\zeta = 0.5$ .



(a)



(b)

Figure 3.13 Contours of equal actuation frequency,  $\log_{10}(f)$  for different classes of materials on (a) DLC substrate, (b) PMMA substrate at  $\zeta = 0.5$ .

Figure 3.11 shows two curves *a* and *b* which correspond to two different lower operating temperatures  $T_{v1}$  and  $T_{v2}$  for a constant peak operating temperature  $T_p$ . The slope of the curves  $(-(T_p - T_v)f)$  depends on the thermal diffusivity of the materials chosen and the length scale for a given set of operating temperatures. It is also evident from equation (3.33) that the actuation frequency can be increased either by decreasing the operating temperature range or by decreasing the actuator's length. However, in either case the increase in frequency is compensated by a corresponding drop in the work per cycle as shown in Figure 3.11.

Figures 3.12a and 3.12b show contours of equal actuation frequency for a range of materials on silicon plotted in the domain of governing properties ( $\kappa$  vs.  $\rho C$ ) at small ( $L = 100 \mu\text{m}$ ) and large ( $L = 1 \text{ mm}$ ) scales respectively using equations (3.15) and (3.17). The initial average temperature at the instant  $t'_0 = 0$  was assumed to be 573 K and the actuator was allowed to cool down to 323 K due to conduction and free convection. It is clear from these plots that the actuation frequency increases with reducing scale as predicted by equation (3.33). Metals perform better than other classes of materials on silicon having a reasonably high actuation frequency  $\sim 1 \text{ kHz}$ . Figures 3.13a and 3.13b show similar contours for DLC and PMMA substrates respectively at small scale. Metals are capable of actuating at higher frequencies on DLC substrates compared to Si by about an order of magnitude.

### 3.8 Influence of thermal response on the materials selection

The achievable temperature difference is a system dependent design variable which affects the performance of different material combinations. Therefore, the design space available in the material domain can be better explored for a given temperature difference if a few promising candidates are considered for further analyses. The present study has not accounted for the effect of ambient temperature change on the actuator performance. For applications which involve a small finite ambient temperature change within a few degrees, the variation in the actuator performance is not appreciable and hence the materials selection decision is unaltered. However, if the actuators are to operate in an environment where the ambient temperature changes drastically, due



consideration to the relevant electrothermal properties of materials should be given in order to identify potential candidates.

Table 3.2 lists the properties of films from different material classes considered for the present study based on their optimal thermoelastic performance on silicon as discussed in chapter 2. Table 3.3 shows the heat transfer performance of these films on Si substrate while Table 3.4 shows similar such estimates on other promising substrates (DLC, invar and PMMA). The properties of these substrates are located at the extremes in the material domain (Young's modulus, thermal expansion coefficient and thermal conductivity) and as a result they provide an indication of the scope for exploration of novel candidates which can improve the performance.

S.No	Film Material -2	$E_2$	$\alpha_2$	$\rho_2$	$\kappa_2$	$C_2$
		GPa	$\mu\text{m.m}^{-1}\text{K}^{-1}$	$\text{kgm}^{-3}$	$\text{Wm}^{-1}\text{K}^{-1}$	$\text{Jkg}^{-1}\text{K}^{-1}$
1	Al	70	24	2700	237	925
2	Al <sub>2</sub> O <sub>3</sub>	370	7	3870	30	700
3	B	320	8	2470	27	1024
4	Be	303	12	1850	175	2178
5	BeO	345	7	1850	200	1850
6	Cl	165	12	7300	35	540
7	Cu	110	16	8960	398	385
8	DLC	700	1.2	3500	1100	518
9	Epoxies	2	55	1100	0.20	1500
10	Ge	102	6	5323	60	310
11	Invar	145	0.4	8100	13	510
12	Mg	45	26	1850	156	1015
13	Nb	105	7	8600	55	265
14	Ni	207	13	8900	91	445
15	Pb	14	29	11300	35	125
16	PDMS	4	60	970	0.2	1460
17	PMMA	2	75	1190	0.2	1500
18	PP	2	120	900	0.1	1900
19	PS	3	73	1045	0.1	1700
20	Si	165	2.5	2280	150	700
21	Si <sub>3</sub> N <sub>4</sub>	300	2.8	3184	30	840
22	SiO <sub>2</sub>	75	0.4	2150	1.2	725
23	Steel	207	13	7700	32	490
24	Ti	110	9	4540	22	535
25	W	400	4.3	19250	178	133
26	Zn	97	31	7140	120	390
27	Zr <sub>2</sub> O <sub>3</sub>	200	12	6050	2	430

Table 3.2 Properties of different materials considered based on their thermoelastic performance on silicon.

S. No	Thin Films - Material 2	Si Substrate – Material 1			
		$P_I \times 10^3$	$W_{no}$	$f$	$\log_{10}(\eta_{em})$
		mKW <sup>-1</sup>	Jm <sup>-3</sup> K <sup>-2</sup>	Hz	
1	Al	1.64	1.11	755	- 4.79
2	Al <sub>2</sub> O <sub>3</sub>	3.27	0.13	399	- 5.69
3	B	3.38	0.18	396	- 5.56
4	Be	2.08	0.42	488	- 5.31
5	BeO	1.96	0.11	581	- 5.84
6	Cast Iron	3.60	0.35	267	- 5.41
7	Cu	1.16	0.60	874	- 5.14
8	DLC	0.72	0.01	2205	- 6.65
9	Epoxies	22.14	0.42	73	- 5.10
10	Ge	3.35	0.03	489	- 6.22
11	Invar	4.20	0.02	218	- 6.76
12	Mg	2.17	1.01	690	- 4.75
13	Nb	3.43	0.07	392	- 5.96
14	Ni	2.73	0.49	360	- 5.26
15	Pb	5.47	0.56	335	- 4.93
16	PDMS	16.39	0.93	113	- 4.70
17	PMMA	20.06	0.98	75	- 4.77
18	PP	22.24	2.10	70	- 4.42
19	PS	18.59	1.07	82	- 4.72
20	Si	2.22	0.00	750	-
21	Si <sub>3</sub> N <sub>4</sub>	3.37	0.00	384	- 8.13
22	SiO <sub>2</sub>	5.45	0.01	310	- 6.67
23	Steel	3.53	0.49	287	- 5.24
24	Ti	4.19	0.13	309	- 5.70
25	W	2.07	0.02	651	- 6.53
26	Zn	2.51	2.40	468	- 4.48
27	Zr <sub>2</sub> O <sub>3</sub>	4.19	0.38	306	- 5.24

Table 3.3 Performance based on heat transfer analysis of different materials on Si substrate.

It is evident from Tables 3.3 and 3.4 that the materials selection has very little scope for the improvement of thermomechanical performance of the BMET actuators. Unlike fluids, the thermal diffusivity of different classes of solid state materials depends largely on their thermal conductivity since the constant volume specific heat is relatively constant ( $\sim 10^{6.5} \text{ Jm}^{-3}\text{K}^{-1}$ ). Therefore, DLC substrates can be considered for high frequency actuators owing to their large thermal conductivity but this has to be compensated for their power index which is an order of magnitude ( $\sim 10^{-4} \text{ mKW}^{-1}$ ) less than for silicon and invar substrates.

S. No	Thin Films - Material 2	DLC Substrate - Material 1				Invar Substrate - Material 1				PMMA Substrate -Material 1			
		$P_1 \times 10^4$	$W_{no}$	$f$	$\log_{10}(\eta_{em})$	$P_1 \times 10^3$	$W_{no}$	$f$	$\log_{10}(\eta_{em})$	$P_1 \times 10$	$W_{no}$	$f$	$\log_{10}(\eta_{em})$
		mKW <sup>-1</sup>	Jm <sup>-3</sup> K <sup>-2</sup>	Hz		mKW <sup>-1</sup>	Jm <sup>-3</sup> K <sup>-2</sup>	Hz		mKW <sup>-1</sup>	Jm <sup>-3</sup> K <sup>-2</sup>	Hz	
1	Al	7.50	1.97	1520	- 4.58	2.30	1.28	366	- 4.90	0.09	0.43	159	- 5.15
2	Al <sub>2</sub> O <sub>3</sub>	6.94	0.45	1644	- 5.22	17.05	0.25	44	- 5.66	1.35	0.91	11	- 4.82
3	B	7.25	0.54	1638	- 5.13	17.89	0.31	43	- 5.57	1.40	0.88	10	- 4.83
4	Be	6.15	1.10	1373	- 4.97	4.21	0.59	155	- 5.35	0.23	0.79	60	- 4.90
5	BeO	5.84	0.38	1653	- 5.37	3.85	0.22	179	- 5.75	0.21	0.92	66	- 4.83
6	Cast Iron	8.70	0.82	942	- 5.11	14.10	0.49	47	- 5.42	0.83	0.74	16	- 4.95
7	Cu	5.58	1.23	1597	- 4.90	1.52	0.76	464	- 5.20	0.06	0.61	208	- 5.03
8	DLC	3.03	0.00	4842	-	0.94	0.00	827	- 7.41	0.05	1.14	278	- 4.70
9	Epoxies	59.52	0.49	270	- 5.04	215.71	0.45	6	- 5.14	16.67	0.02	1	- 6.42
10	Ge	9.60	0.10	1635	- 5.72	8.64	0.08	111	- 6.04	0.40	0.84	37	- 4.83
11	Invar	9.44	0.00	827	- 7.41	25.64	0.00	25	-	1.98	1.02	7	- 4.81
12	Mg	9.61	1.67	1485	- 4.56	3.18	1.15	312	- 4.88	0.11	0.37	132	- 5.20
13	Nb	9.61	0.19	1288	- 5.56	9.34	0.14	91	- 5.86	0.44	0.81	32	- 4.87
14	Ni	7.47	1.16	1112	- 4.95	6.87	0.65	96	- 5.30	0.36	0.73	37	- 4.95
15	Pb	19.97	0.79	911	- 4.78	11.19	0.63	116	- 5.02	0.32	0.24	50	- 5.35
16	PDMS	43.04	1.12	428	- 4.62	168.33	0.98	9	- 4.77	18.73	0.02	1	- 6.50
17	PMMA	53.57	1.14	278	- 4.70	197.75	1.02	7	- 4.81	16.67	0.00	1	-
18	PP	59.60	2.39	260	- 4.37	226.19	2.15	6	- 4.47	21.13	0.11	1	- 5.73
19	PS	49.24	1.26	304	- 4.66	191.61	1.12	7	- 4.78	20.60	0.00	1	- 8.16
20	Si	7.24	0.01	2205	- 6.65	4.20	0.02	218	- 6.76	0.20	0.98	75	- 4.77
21	Si <sub>3</sub> N <sub>4</sub>	7.35	0.03	1550	- 6.45	16.69	0.03	45	- 6.61	1.24	1.03	12	- 4.77
22	SiO <sub>2</sub>	12.25	0.00	1340	- 7.33	54.32	0.00	19	- 10.35	9.41	0.93	2	- 4.78
23	Steel	8.17	1.16	1057	- 4.93	15.39	0.65	44	- 5.29	1.00	0.73	13	- 4.94
24	Ti	10.16	0.32	1161	- 5.35	18.72	0.22	44	- 5.67	1.09	0.77	13	- 4.89
25	W	5.80	0.12	2050	- 5.79	4.44	0.08	169	- 6.14	0.25	1.01	57	- 4.77
26	Zn	8.64	4.35	1221	- 4.27	4.64	2.62	169	- 4.62	0.20	0.33	70	- 5.27
27	Zr <sub>2</sub> O <sub>3</sub>	8.67	0.93	1319	- 4.91	41.98	0.54	18	- 5.31	8.75	0.75	2	- 4.90

Table 3.4 Performance based on heat transfer analysis for different films on DLC, Invar, and PMMA substrates.

S. No	Thin Films - Material 2	Si Substrate - Material 1		
		$\log_{10}(W_{EI})$	$\log_{10}(M_{EI})$	$\log_{10}(\Theta_{EI})$
		NW <sup>-2</sup>	NW <sup>-1</sup> m <sup>-1</sup>	mW <sup>-1</sup>
1	Al	- 5.52	2.66	- 7.28
2	Al <sub>2</sub> O <sub>3</sub>	- 5.84	2.68	- 7.62
3	B	- 5.69	2.74	- 7.53
4	Be	- 5.75	2.71	- 7.55
5	BeO	- 6.38	2.41	- 7.88
6	Cast Iron	- 5.34	2.85	- 7.29
7	Cu	- 6.09	2.43	- 7.61
8	DLC	- 8.20	1.55	- 8.85
9	Epoxies	- 3.69	2.97	- 5.76
10	Ge	- 6.45	2.24	- 7.79
11	Invar	- 6.54	2.24	- 7.87
12	Mg	- 5.32	2.70	- 7.12
13	Nb	- 6.08	2.43	- 7.61
14	Ni	- 5.44	2.82	- 7.36
15	Pb	- 4.78	2.79	- 6.66
16	PDMS	- 3.60	3.15	- 5.85
17	PMMA	- 3.41	3.16	- 5.66
18	PP	- 2.98	3.33	- 5.41
19	PS	- 3.43	3.18	- 5.71
20	Si	-	-	-
21	Si <sub>3</sub> N <sub>4</sub>	- 8.25	1.45	- 8.80
22	SiO <sub>2</sub>	- 6.49	2.18	- 7.77
23	Steel	- 5.22	2.94	- 7.25
24	Ti	- 5.63	2.66	- 7.39
25	W	- 7.09	2.06	- 8.25
26	Zn	- 4.82	3.05	- 6.97
27	Zr <sub>2</sub> O <sub>3</sub>	- 5.17	2.96	- 7.22

Table 3.5 Comparison of the effectiveness indices of different films on Si substrate.

S. No	Thin Films - Material 2	DLC Substrate - Material 1			Invar Substrate - Material 1			PMMA Substrate- Material 1		
		$\log_{10}(W_{EI})$	$\log_{10}(M_{EI})$	$\log_{10}(\Theta_{EI})$	$\log_{10}(W_{EI})$	$\log_{10}(M_{EI})$	$\log_{10}(\Theta_{EI})$	$\log_{10}(W_{EI})$	$\log_{10}(M_{EI})$	$\log_{10}(\Theta_{EI})$
		NW <sup>-2</sup>	NW <sup>-1</sup> m <sup>-1</sup>	mW <sup>-1</sup>	NW <sup>-2</sup>	NW <sup>-1</sup> m <sup>-1</sup>	mW <sup>-1</sup>	NW <sup>-2</sup>	NW <sup>-1</sup> m <sup>-1</sup>	mW <sup>-1</sup>
1	Al	- 5.95	2.54	- 7.59	- 5.17	2.82	- 7.09	- 4.48	2.60	- 6.17
2	Al <sub>2</sub> O <sub>3</sub>	- 6.66	2.43	- 8.19	- 4.13	3.52	- 6.74	- 1.78	3.99	- 4.86
3	B	- 6.55	2.47	- 8.11	- 4.01	3.57	- 6.67	- 1.76	3.99	- 4.85
4	Be	- 6.38	2.54	- 8.02	- 4.98	3.07	- 7.15	- 3.39	3.18	- 5.67
5	BeO	- 6.89	2.31	- 8.29	- 5.49	2.83	- 7.42	- 3.39	3.18	- 5.67
6	Cast Iron	- 6.21	2.55	- 7.85	- 4.01	3.50	- 6.61	- 2.29	3.71	- 5.11
7	Cu	- 6.42	2.38	- 7.89	- 5.75	2.58	- 7.44	- 4.61	2.55	- 6.25
8	DLC	-	-	-	- 8.41	1.42	- 8.93	- 4.49	2.64	- 6.23
9	Epoxies	- 4.76	2.46	- 6.32	- 1.68	3.97	- 4.75	- 1.24	3.97	- 4.30
10	Ge	- 7.02	2.07	- 8.18	- 5.21	2.85	- 7.16	- 2.87	3.42	- 5.38
11	Invar	- 8.41	1.42	- 8.93	-	-	-	- 1.40	4.16	- 4.65
12	Mg	- 5.81	2.54	- 7.44	- 4.93	2.88	- 6.91	- 4.34	2.65	- 6.09
13	Nb	- 6.75	2.21	- 8.05	- 4.92	3.00	- 7.01	- 2.80	3.45	- 5.35
14	Ni	- 6.19	2.59	- 7.87	- 4.51	3.27	- 6.88	- 3.02	3.36	- 5.47
15	Pb	- 5.50	2.48	- 7.08	- 4.10	3.12	- 6.32	- 3.61	2.95	- 5.66
16	PDMS	- 4.68	2.64	- 6.42	- 1.56	4.17	- 4.82	- 1.24	4.04	- 4.38
17	PMMA	- 4.49	2.64	- 6.23	- 1.40	4.16	- 4.65	-	-	-
18	PP	- 4.07	2.80	- 5.97	- 0.96	4.34	- 4.39	- 0.33	4.42	- 3.85
19	PS	- 4.51	2.67	- 6.28	- 1.39	4.20	- 4.68	- 2.77	3.25	- 5.11
20	Si	- 8.20	1.55	- 8.85	- 6.54	2.24	- 7.87	- 3.41	3.16	- 5.66
21	Si <sub>3</sub> N <sub>4</sub>	- 7.84	1.81	- 8.75	- 5.11	3.01	- 7.21	- 1.80	3.97	- 4.87
22	SiO <sub>2</sub>	- 8.44	1.31	- 8.84	- 7.95	1.44	- 8.49	- 0.08	4.80	- 3.98
23	Steel	- 6.11	2.63	- 7.84	- 3.81	3.62	- 6.53	- 2.14	3.80	- 5.03
24	Ti	- 6.48	2.35	- 7.92	- 4.11	3.40	- 6.62	- 2.04	3.83	- 4.97
25	W	- 7.40	2.07	- 8.57	- 5.79	2.69	- 7.58	- 3.19	3.28	- 5.57
26	Zn	- 5.49	2.82	- 7.41	- 4.25	3.32	- 6.67	- 3.88	2.91	- 5.88
27	Zr <sub>2</sub> O <sub>3</sub>	- 6.15	2.60	- 7.85	- 3.02	4.01	- 6.13	- 0.24	4.75	- 4.08

Table 3.6 Comparison of the effectiveness indices of different films on DLC, Invar, and PMMA substrates.

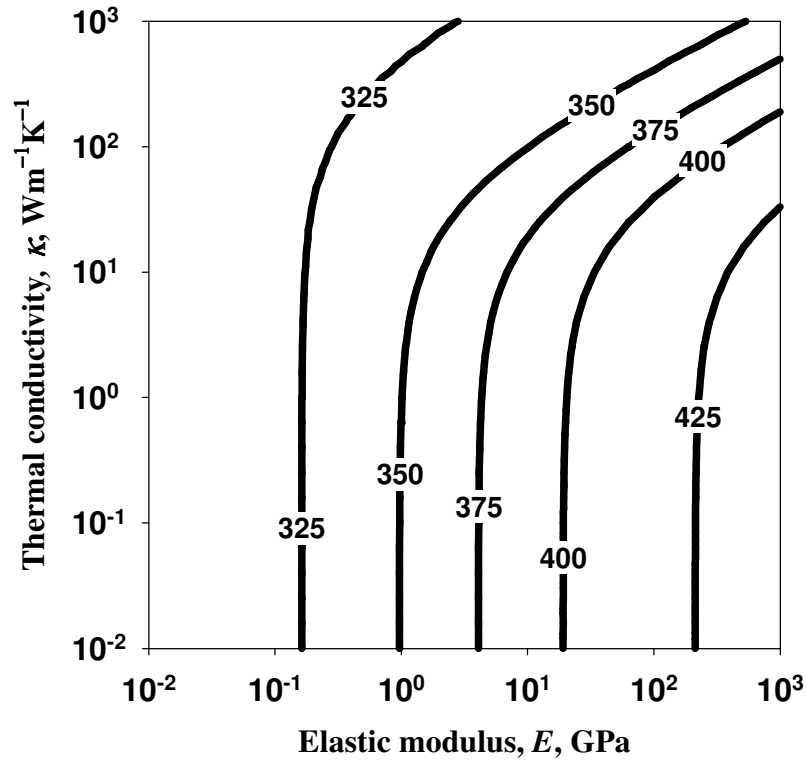
Zinc is the only candidate which significantly betters conventionally employed aluminium films with an effective and efficient performance irrespective of the substrates considered. Zinc films on DLC substrate have the potential to deliver high work at a high actuation frequency ( $W_0 \sim 4.35 \text{ Jm}^{-3} \text{ K}^{-2}$ ,  $f \sim 1.2 \text{ kHz}$ ) and these have not been considered so far for MEMS actuators. Zinc films up to a few microns thick can be grown on silicon by sputter deposition [35]. However, despite the potentially superior performance to aluminium, zinc films require cautious evaluation due to their chemically reactive nature (Electronegativity of 1.65 on Pauling scale).

The electromechanical efficiency of BMET actuators is inherently low ( $\eta_{em} \sim 10^{-5}$ ) due to excess heat dissipation and it is an order of magnitude lower than the efficiency of linear (uni-material) thermal expansion actuators [5]. This is due to inherently low work per unit volume,  $W_0$  associated with BMET actuators (equation (3-3)) compared to uni-material thermal expansion actuators by an order of magnitude for a constant temperature difference. Furthermore, the irreversibility associated with the electrothermal actuation is always greater when compared to any mechanical actuation. It is evident from Figure 3.10 that there is no appreciable variation in the electromechanical efficiency ( $\eta_{em} \sim 10^{-5} - 10^{-6}$ ) for all the films on the various substrates considered. However, their effectiveness varies significantly. Table 3.5 shows a comparison of the effectiveness indices of different films on Si substrate while Table 3.6 shows similar such estimates for other promising substrates (DLC, Invar, PMMA). Engineering polymers are very effective for high displacement actuators. Candidate materials such as PP, PMMA, PS and PDMS on Invar and  $\text{SiO}_2$  substrates and  $\text{Zr}_2\text{O}_3$  on PMMA substrate are capable of delivering high displacement per cycle per unit electrical energy consumed ( $\Theta_{EI} \sim 10^{-4} \text{ mW}^{-1}$ ). Thin polymeric films up to a few tens of microns can be achieved by spin coating which is a proven microfabrication route [37] for growing polymeric films on a substrate. For actuators to deliver a high force per cycle effectively material combinations such as  $\text{Zr}_2\text{O}_3$ , steel, Zn, Ni on PMMA/Si and  $\text{Zr}_2\text{O}_3$ , steel,  $\text{Al}_2\text{O}_3$ , Ti, Ni,  $\text{Si}_3\text{N}_4$  on Invar and Zn on DLC can be considered ( $M_{EI} \sim 10^3 - 10^4 \text{ NW}^{-1}\text{m}^{-1}$ ). It should be noted again that polymeric substrates require a large thickness to compensate for their low Young's modulus which may not be acceptable in some applications. Material combinations such as  $\text{SiO}_2$  on PMMA and  $\text{Zr}_2\text{O}_3$ , steel, Zn, Ni on Invar can be considered for actuators to deliver high work effectively ( $W_{EI}$

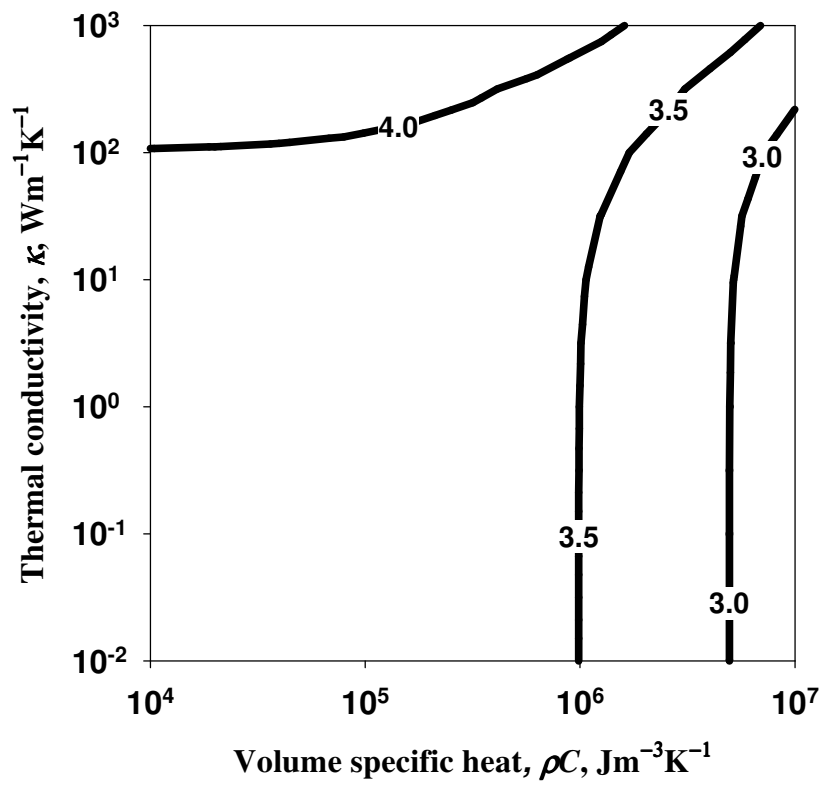
$\sim 10^{-0.1} - 10^{-4} \text{ NW}^{-2}$ ). It is noteworthy that the most commonly employed material combination: Al-Si is bettered by many others for effectiveness. This is due to the high thermal conductivity of aluminium which causes more heat dissipation despite its favourable mechanical properties.

However, for high frequency applications it essential to have high dissipation rate and therefore the candidate materials should possess a high thermal conductivity. The optimal material combinations in order to achieve high actuation frequency are DLC-Zn, DLC-Al, DLC-Cu, Si-Zn and Si-Al. Amorphous DLC films ( $sp^3$  bonded) up to a few microns thick can be prepared by pulsed laser deposition [43], magnetron sputtering with ion plating [44] or a filtered cathode vacuum arc [45]. A few micron thick aluminium films can be achieved by sputtering [46, 47] which is an established and proven microfabrication route. These material combinations could at the best yield  $\sim 1.2$  kHz for  $L = 100 \mu\text{m}$ , and are limited by the cooling rates achieved by conduction and natural convection at small scales. Frequencies can be further increased if the cooling rate is accelerated by forced convection.

Applications such as flow control require actuation at high frequencies up to a few kHz even at low free stream velocities ( $\sim 10\text{-}20 \text{ ms}^{-1}$ ). For a subsonic flow (Mach number,  $M = 0.5$ ), the Knudsen number,  $k_n$  evaluated at the atmospheric pressure and temperature for a characteristic length,  $L = 100 \mu\text{m}$  is  $\sim 10^{-4}$  ( $< 10^{-2}$ ) which ensures that rarefied gas effects can be neglected in the flow analysis [48]. Using von Karman closed form solutions [49], the average heat transfer coefficient due to forced convective currents can be evaluated for the bimaterial actuator. Figure 3.14a and 3.14b show isotherms and contours of equal actuation frequency for a range of materials on silicon considering heat dissipation due to conduction and forced convection. Although there is a marginal drop in the steady state isotherms ( $\sim 25 \text{ K}$ ), the actuation frequency increases by almost an order of magnitude  $\sim 7 \text{ kHz}$ . Frequencies of the order of  $\sim 10 \text{ kHz}$  can be achieved for engineering alloys/metals if either the scale is reduced to  $60\mu\text{m}$  or if the temperature range is restricted to  $423\text{-}573 \text{ K}$ . In either case, the work per unit volume delivered by the actuator per cycle is reduced. Figures 3.15a and 3.15b show the contours of equal actuation frequency for the two cases;  $L = 60 \mu\text{m}$  and for  $L = 100 \mu\text{m}$  with the operating temperature range of  $\sim 423\text{-}573 \text{ K}$  respectively.



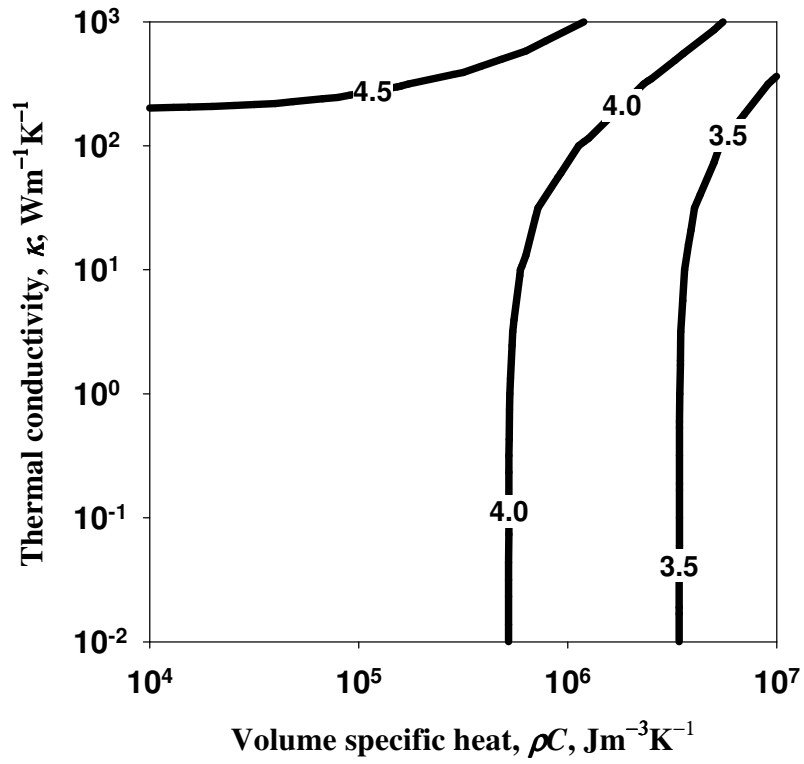
(a)



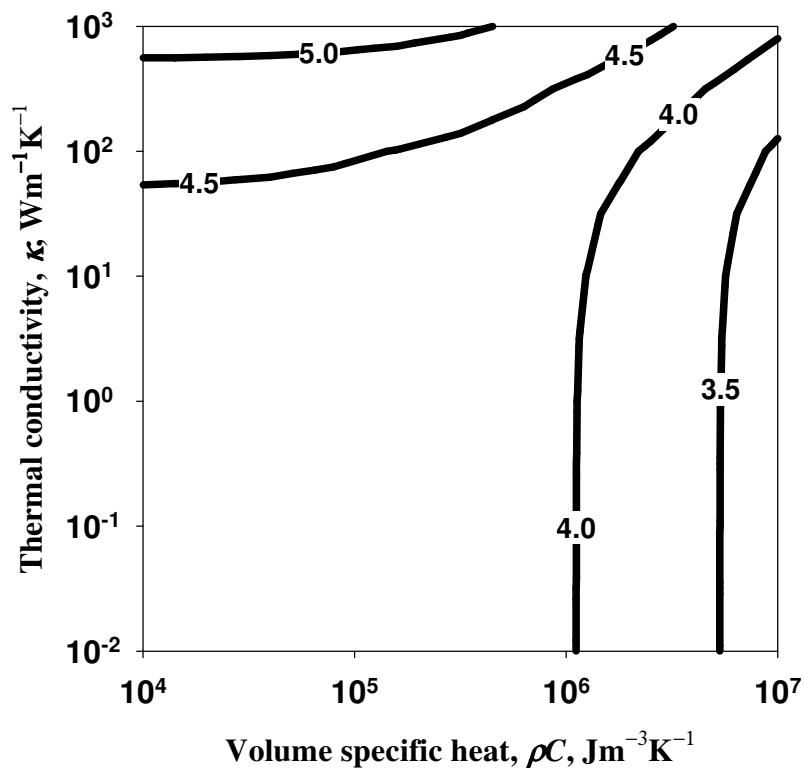
(b)

Figure 3.14 Effect of forced convection on the (a) steady state isotherms (in Kelvin); (b) actuation frequency,  $\log_{10}(f)$  for different classes of materials on silicon at small scale ( $L = 100 \mu\text{m}$ ).





(a)



(b)

Figure 3.15 Increase in the actuation frequency,  $\log_{10}(f)$  accomplished by (a) reducing the scale ( $L = 60 \mu\text{m}$ ); (b) reducing the operating temperature range (573 K - 423 K) for different materials on Si.

Hitherto, piezoelectric actuators [50, 51] and electrostatic actuators [52] have been preferred for applications such as boundary layer flow control devices which operate at high frequencies of the order  $\sim 10$  kHz. The results presented herein suggest the point at which electrothermal actuators might be considered as viable alternatives.

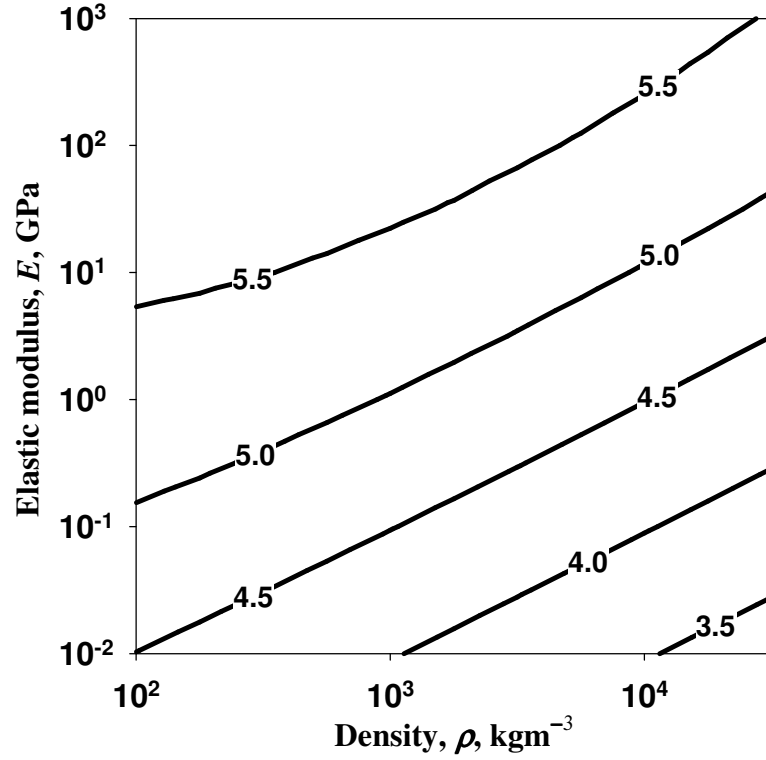


Figure 3.16 Contours of equal resonant frequency (fundamental flexural mode),  $\log_{10}(f_s)$  for different materials on silicon for an optimal thickness ratio at small scale ( $L = 100 \mu\text{m}$ ).

The ability to achieve mechanical resonance is enabling for many sensor applications although it may be detrimental for actuator structures. Electrostatic and piezoelectric devices are often operated at resonance. The structural frequencies of bimaterial structures are therefore estimated using the Euler-Bernoulli relation to compare with the thermal actuation frequencies. The fundamental structural frequency,  $f_s$  (flexural mode) for a bimaterial structure with an optimal geometry is given as

$$f_s = \frac{1}{2\pi} \left( \frac{1.8751}{L} \right)^2 \sqrt{\left( \frac{E_1 t^2}{3\lambda(\rho_1 \xi_0 + \rho_2)(\xi_0 + 1)} \right)} \quad (3.34)$$

where  $\rho_1$  and  $\rho_2$  are the densities of the materials in bi-layers. Figure 3.16 shows contours of equal structural frequency (fundamental flexural mode) for range of materials on silicon plotted in the domain of governing material properties ( $E$  vs.  $\rho$ ) for  $L = 100 \mu\text{m}$  at optimal thickness ratio.

It is evident that the structural resonant frequencies are approximately an order of magnitude greater than the thermal actuation frequencies for different classes of materials at optimal configuration. Thermal actuation frequencies were found to be always less than the structural resonant frequencies for realistic values of the scales and thickness ratios. The length scale (a few tens of nanometers) at which thermal actuation frequency is equal to the structural resonant frequency cannot be realised using the present microfabrication routes. If electrothermal actuation was to be considered for high frequency applications it would have to be achieved either by using a triggering mechanism or by exploiting non-linear structural behaviour. It should also be noted that both structural resonant frequency and the thermal actuation frequency are inversely proportional to the square of the actuator length.

### 3.9 Summary

The competition between the different modes of heat transfer was studied at various scales using a simple lumped heat capacity model for a BMET actuator. The choice of materials has a significant effect on functional effectiveness and actuation frequencies for the specified temperature limits. BMET actuators have the potential to operate at actuation frequencies  $\sim 10$  kHz at scales less than  $100 \mu\text{m}$  with optimal choices of engineering alloys/metals on Si substrates. DLC substrate can be considered for high frequency applications such as micromirror positioners, microcage device and fibre optic switches in which high power consumption is permissible. The potential of Invar as a substrate for high force or work at low frequency requiring relatively low power is yet to be realised in microsystems even though it is promising and should therefore be considered for further research studies. Although polymeric substrates are promising for high displacement, low frequency applications their time dependent non-linear response requires further consideration. The influence of materials choice on the electromechanical efficiency is very small for BMET actuators and the overall efficiency is inherently very low irrespective of the substrates. Thermally induced

mechanical resonance cannot be directly achieved using bimaterial structures with realistic thickness ratios. In addition to the specific results presented herein, the general framework for the selection of materials for microsystems is an important outcome of the present analysis. Applying rational engineering criteria for the selection of materials for new systems and the development of new materials and processes is important to allow the potential of MEMS technology to be fully realised.

The realisation of high performance MEMS devices is governed by the ability to design actuators at microscales which delivers large work per volume at high frequencies. Although electrothermal actuators in bimaterial architecture deliver a reasonably large work per volume ( $\sim 10^4 - 10^5 \text{ Jm}^{-3}$ ), further improvement in the performance of out-of-plane actuation can be achieved by different actuator configurations. Chapter 4 discuss the preliminary design of one such configuration where actuation is achieved by Electrothermal Buckling (ETB) mode.

# Chapter 4

## Design of Electrothermal Buckling Microactuators

### 4.1 Design configuration for an improved performance

The ability to achieve high performance (displacement, blocked moment, work per volume, frequency and efficiency) from a simple structural design determines the practical realisation of successful MEMS actuators. As micromachining is usually done by in-plane selective patterning of wafers using masks and physical/chemical etchants, it is essential to minimise the complexities involved in the device features normal to the wafer plane. Hence the constraints imposed by the micromachining processes on the design are significant challenges in the realisation of high performance, and reliable MEMS devices. This chapter discusses the design guidelines for electrothermal buckling (ETB) of microscale structures since such configurations are attractive for realising MEMS actuators capable of delivering a large work per volume at high frequencies. Some areas of application of ETB actuators include: adaptive flow control valves [53], microrelays [54] and microswitches for pneumatic control [55].

Although the mechanism of electrothermal buckling actuation has been employed in a few research applications such as flow control devices [53] and bidirectional relays [56], it is far less prevalent than BMET actuation. This may be attributed to the challenges posed by the stability issues which are inherent to the buckling of beam structures. Some of the ETB actuators demonstrated previously include; in-plane buckling response of silicon micromachined beams under resistive heating [57] and vertically driven silicon microactuators by electrothermal buckling effects [58]. The performance of specific MEMS structures has been evaluated and analysed. However, significant attention has not been focussed on improving the performance and the actuation authority. This chapter focuses on the improvement in performance of an out-of-plane ETB actuator achieved by various design modifications.

This chapter is organised as follows. Section 4.2 discusses the mechanics of the out-of-plane ETB actuator. Section 4.3 discusses the estimation of the critical temperature for ETB actuation. Section 4.4 discuss on the limiting value of slenderness ratio for

different candidates of ETB actuators. The performance metrics relevant to the ETB actuator structure are presented in Section 4.5. Section 4.6 discusses the transient thermal response and the actuation efficiency of the ETB structure. The influence of pre-stress on the performance of the actuator is discussed on Section 4.7 and Section 4.8 discusses the promising candidates for ETB actuator structures. Section 4.9 summarises the key inferences drawn from this analysis.

## 4.2 Mechanics of an out-of-plane electrothermal buckling actuator

Figure 4.1a shows the buckling of a statically indeterminate fixed-fixed beam of uniform cross section subjected to a uniform temperature greater than the ambient temperature,  $T_{\infty}$ . Figure 4.1b shows the equivalent free body diagram of the system shown in Figure 4.1a. The elastic modulus of the material is  $E$  and its thermal expansion coefficient is  $\alpha$ . The beam length is  $L$  and its width and thickness are  $b$  and  $t$  respectively. Applying Euler's buckling theory; the out-of-plane deflection across any section along the length of the beam at the onset of buckling corresponding to the fundamental mode is given as

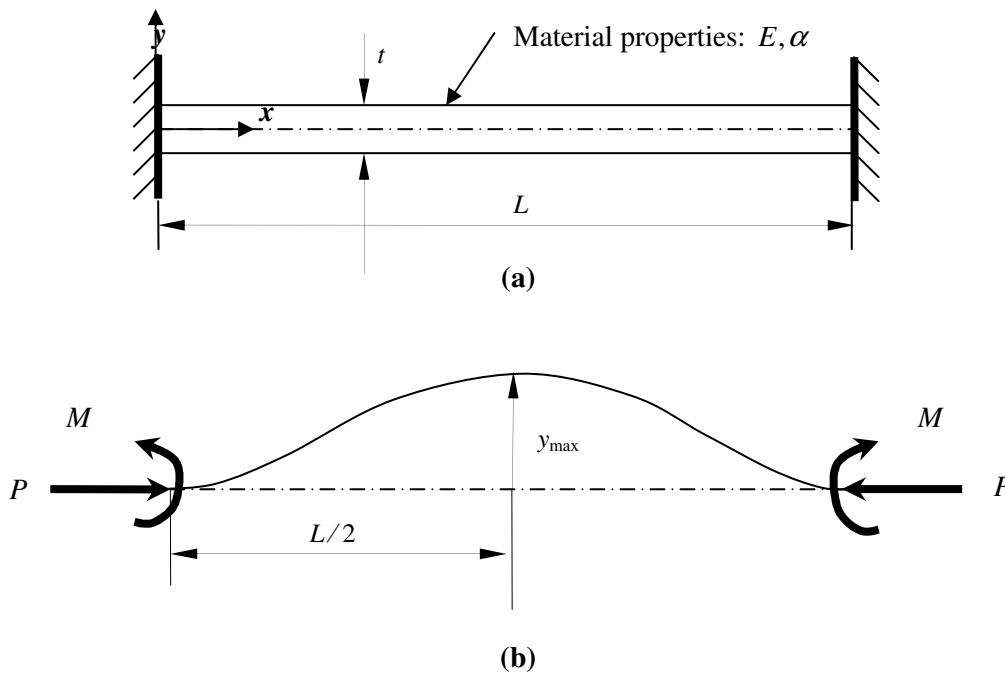


Figure 4.1 (a) Schematic of the fixed-fixed beam structure subjected to electrothermal buckling; (b) Free body diagram of the structure subjected to equivalent system of forces and moments.

$$y = \frac{y_{\max}}{2} \left( 1 - \cos \left( \frac{2\pi x}{L} \right) \right). \quad (4.1)$$

The out-of-plane actuation due to buckling occurs when the axial load developed due to thermal expansion is equal to the fundamental crippling load,  $P_c$  required to buckle the beam. The critical temperature difference required to buckle the structure is given as

$$P_c = \frac{4\pi^2 E b t r_g^2}{L^2} = E \alpha b t (\Delta T)_c \quad (4.2)$$

where  $r_g = \sqrt{\frac{t^2}{12}}$  is the radius of gyration of the beam and  $(\Delta T)_c = T_c - T_\infty$  is the critical temperature difference at which the beam buckles in the fundamental mode. The temperature profiles vary with the actuator geometries when subjected to joule heating. However, the present analysis considers the nominal temperature of the actuator for the purpose of materials selection.

#### 4.3 Estimation of the critical temperature difference for ETB actuation

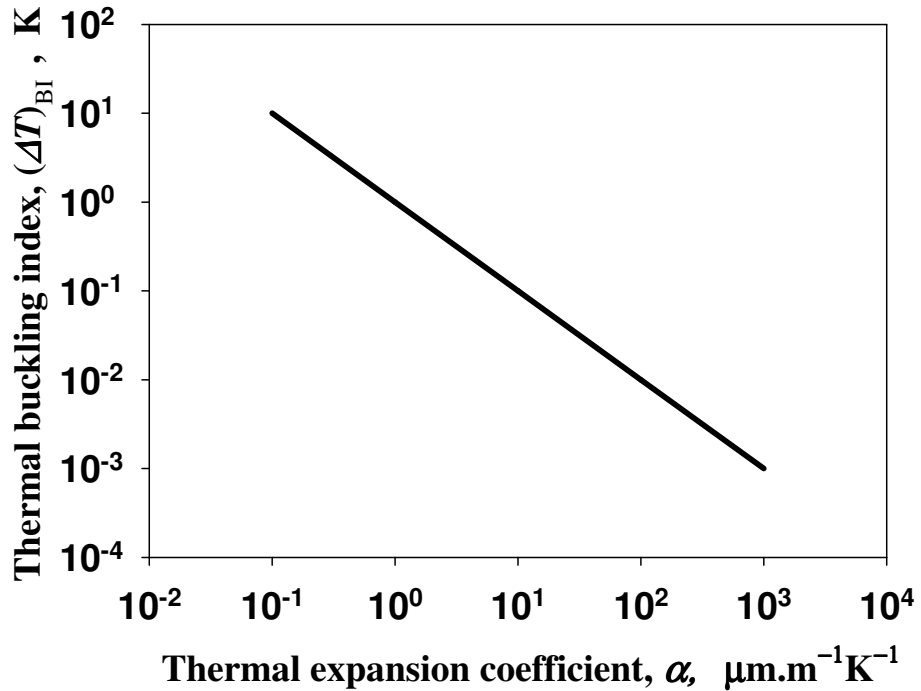


Figure 4.2 Variation of the thermal buckling index with the thermal expansion coefficient of the material.

Using equation (4.2), the thermal buckling index,  $(\Delta T)_{\text{BI}}$  is defined as

$$(\Delta T)_{\text{BI}} = \frac{(\Delta T)_c L^2}{4 r_g^2 \pi^2} = \frac{1}{\alpha} \quad (4.3)$$

Since the actuation is achieved by self expansion of the structure due to Joule heating, the thermal strain corresponding to the critical temperature difference should be equal to the critical buckling strain which depends only on the geometry of the actuator structure. Hence  $(\Delta T)_{\text{BI}}$  depends only on  $\alpha$  of the actuator material and is independent of  $E$ .  $(\Delta T)_{\text{BI}}$  is a critical design parameter because it determines the temperature difference required for the actuation of ETB structures for a fixed geometry.

Figure 4.2 shows the plot of thermal buckling index for variation in thermal expansion coefficient of the material obtained using equation (4.3). It is evident from the plot that for an actuator with a fixed geometry, the thermal buckling index (hence the critical temperature difference,  $(\Delta T)_c$ ) is inversely proportional to the thermal expansion coefficient of the material. Hence, the higher the thermal expansion coefficient of the material, the lower the critical actuation temperature required to buckle the structure.

#### 4.4 Failure characteristics of an ETB actuator structure

The failure criteria for the design of ETB actuator structure can be obtained by equating the axial stresses developed due to the combined buckling and compression and the failure strength of the material. The limiting value of the slenderness ratio of an ETB structure is given as

$$\frac{L}{r_g} \geq 2(\sqrt{6} + 1)^{1/2} \pi \sqrt{\frac{E}{\sigma_f}} = 3.71 \pi \sqrt{\frac{1}{\sigma_{\text{nf}}}} \quad (4.4)$$

where  $\sigma_f$  and  $\sigma_{\text{nf}}$  are the failure strength and normalised strength (failure strain) of the ETB actuator material. Figure 4.3 shows the contours of the limiting value of



$\log_{10}(L/r_g)$  for different classes of materials plotted on an Ashby's selection map ( $E$  vs.  $\sigma_f$ ) obtained using equation (4.4). It is evident that the limiting values of  $L/r_g$  for most promising materials are  $\geq 100$ .

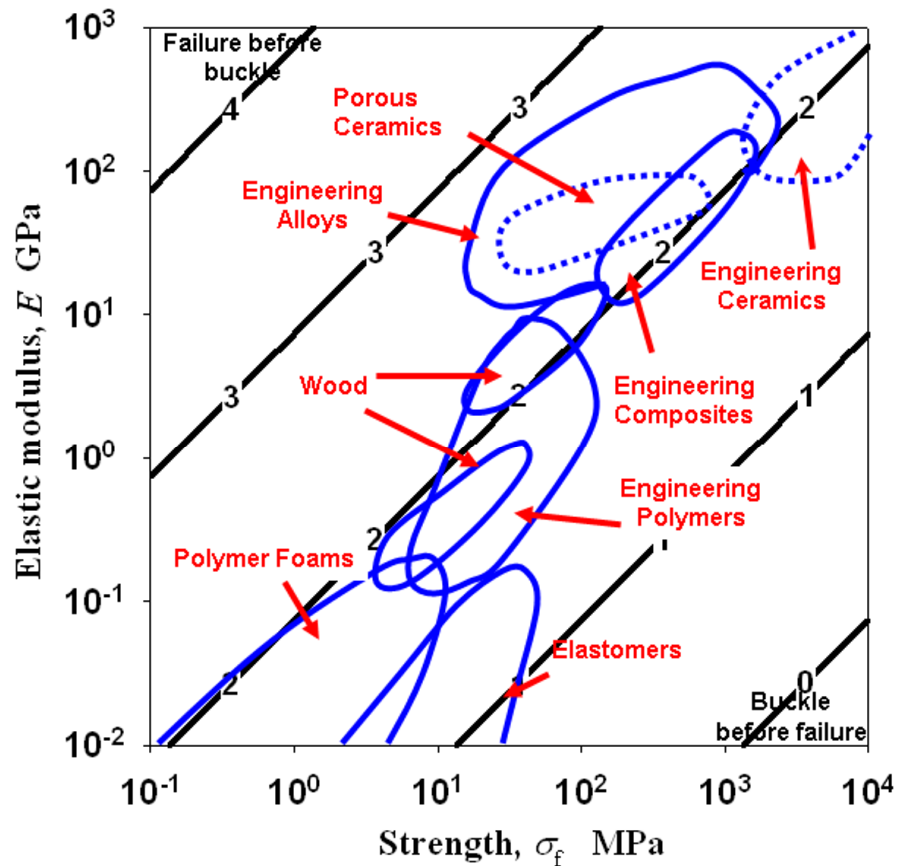


Figure 4.3 Contours of limiting value of  $\log_{10}(L/r_g)$  for different classes of materials on Ashby's  $E$  vs.  $\sigma_f$  selection map.

Although polymeric substrates are promising for ETB actuator structures owing to their high normalised strength (about an order of magnitude greater than engineering alloys/metals), the blocked force, work per volume and the actuation frequency associated with such structures are very low due to their low elastic modulus and thermal conductivity. Hence a large thickness is required to compensate for their low elastic modulus and this may not be a feasible design for some applications.

## 4.5 Evaluation of the performance metrics of ETB actuator structure

### 4.5.1 Maximum deflection, $y_{\max}$

From equation (4.1) it is evident that the maximum deflection occurs at the centre of the beam. In reality, the deflection in a buckled structure is an indeterminate quantity since the system transforms from the stable equilibrium to an unstable equilibrium. However, the present analysis considers the amplitude of the deflected shape obtained by equating the strain energy in the post buckled state corresponding to the fundamental critical load to the compressive strain energy stored at the onset of buckling due to temperature difference.

$$\frac{EI}{2} \int_0^L \left( \frac{d^2 y}{dx^2} \right)^2 dx = \frac{1}{2} E (\alpha (\Delta T)_c)^2 Lbt \quad (4.5)$$

Substituting equation (4.1) and (4.2) in equation (4.5) gives

$$y_{\max} = 2\sqrt{2} r_g \quad (4.6)$$

It is clear from equation (4.6) that the maximum deflection of the ETB actuator at the critical load depends only on the radius of gyration. However, the critical temperature required to actuate the structure depends on the thermal expansion coefficient of the material.

### 4.5.2 Blocked force, $F_b$ and the maximum work per volume, $W$

Unlike BMET bending actuators, the achievable forces and displacements delivered by an ETB actuator against external mechanical impedance is not linear. This is due to the non-linear buckling response of an ETB actuator structure. Figure 4.4a shows a schematic of an ETB actuator structure working against an external mechanical spring with constant spring stiffness,  $k_s$ . Figure 4.4b shows an equivalent free body diagram of the system shown in Figure 4.4a. The buckling response of the ETB structure can be

obtained by solving the governing differential equation in the domains  $0 \leq x_1 \leq L/2$  and  $0 \leq x_2 \leq L/2$  which is given as

$$EI \frac{d^4 y_i}{dx_i^4} + P \frac{d^2 y_i}{dx_i^2} = 0 \quad (4.7)$$

where the free indices  $i=1, 2$  correspond to the responses in the domains  $x_1$  and  $x_2$  respectively. The general solution to equation (4.7) is a function of the variable  $x_i$  which is given as

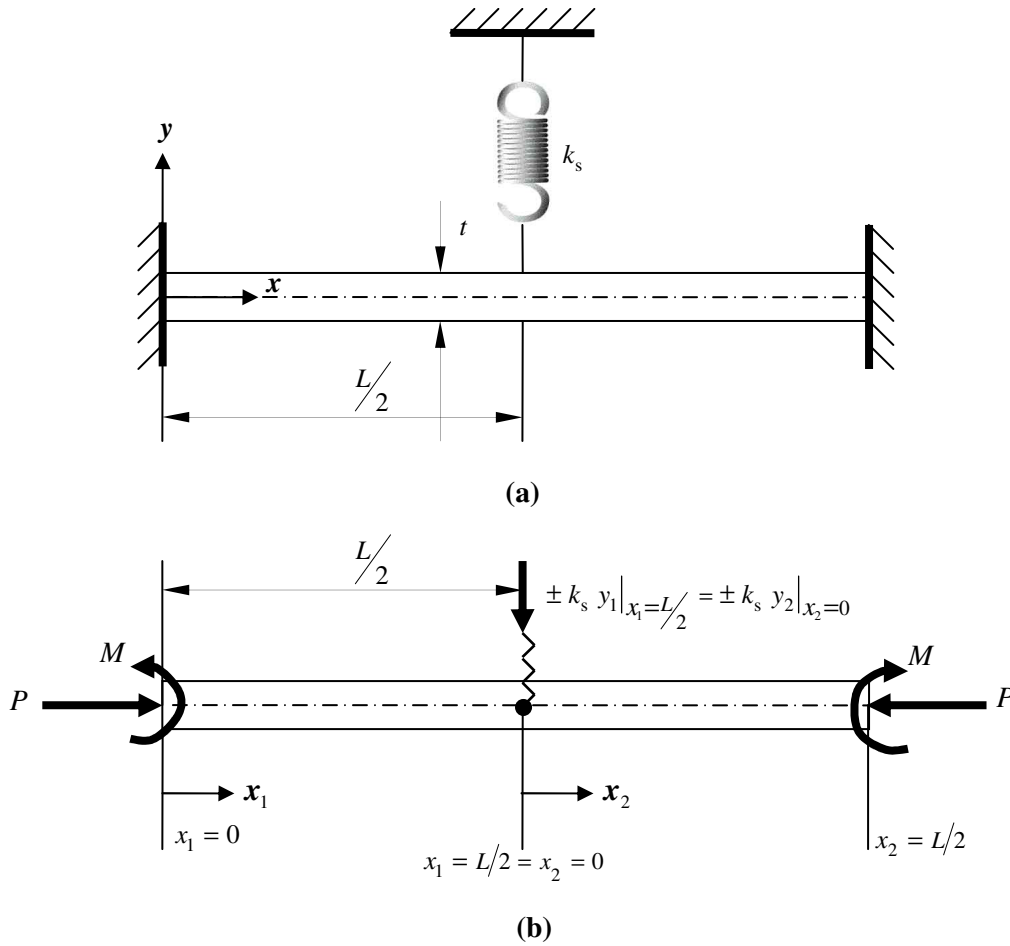


Figure 4.4 (a) Schematic of an ETB structure actuating an external lateral spring of stiffness,  $k_s$ ; (b) Free body diagram of an ETB actuator structure actuating the external spring.

$$y = A_i \cos(k^\theta x_i) + B_i \sin(k^\theta x_i) + C_i x_i + D_i \quad (4.8)$$

where  $A_i, B_i, C_i$  and  $D_i$  are constants,  $k^0 = \sqrt{P/EI}$  and  $I$  is the second moment of area of the cross section. Equation (4.8) is a system of equations involving eight constants which are obtained from the following boundary conditions.

$$\left. \begin{aligned} & @ x_1 = 0; y_1 = 0, dy_1/dx_1 = 0, @ x_2 = L/2; y_2 = 0, dy_2/dx_2 = 0, \\ & @ x_1 = L/2 \text{ or } x_2 = 0; y_1|_{x_1=L/2} = y_2|_{x_2=0}, (dy_1/dx_1)|_{x_1=L/2} = (dy_2/dx_2)|_{x_2=0}, \\ & (d^2 y_1/d^2 x_1)|_{x_1=L/2} = (d^2 y_2/d^2 x_2)|_{x_2=0}, \\ & EI(d^3 y_1/d^3 x_1)|_{x_1=L/2} = EI(d^3 y_2/d^3 x_2)|_{x_2=0} \pm k_s y_1|_{x_1=L/2} \end{aligned} \right\} \quad (4.9)$$

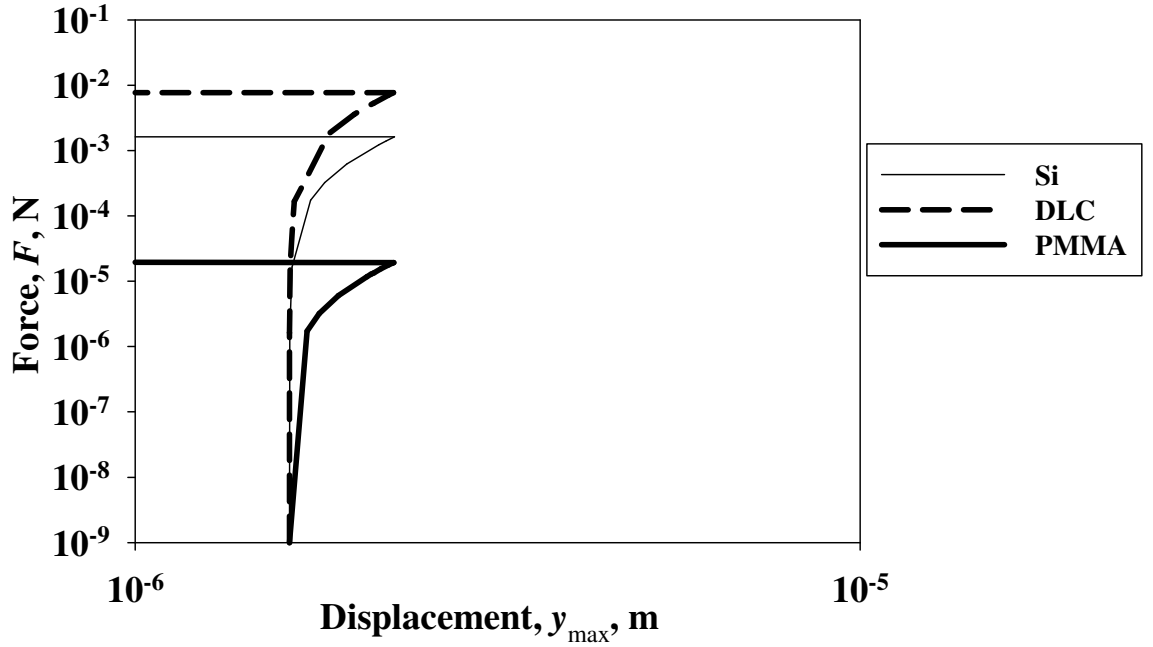


Figure 4.5 Operating characteristics of an ETB actuator ( $L/t \sim 60; b = 62 \mu\text{m}; t = 2 \mu\text{m}$ ). The constant value of  $y_{\text{max}}$  irrespective of the materials chosen is attributed to the fixed buckling strain for a given geometry.

Substituting equation (4.9) in equation (4.8) and solving for the non-trivial solution gives the critical buckling load as a function of the spring stiffness,  $k_s$  which is given by

$$k_s = \frac{(16EI/L^3)\theta^3(-S^4 - 2S^2C^2 - 2S^2 - 1 + 4CS\theta + 2C^2 - C^4)}{(4S^3 - 8CS + 4S + 4C^2S - 4C^3\theta - 4S^2\theta + 4CS\theta^2 - 4C\theta - 4S^2C\theta + 8C^2\theta)} \quad (4.10)$$

where  $\theta = k^0 L/2$ ;  $S$  and  $C$  are sine and cosine functions of  $\theta$  respectively.

The trade-off between the achievable force and the displacement between the bounding limits can be obtained by varying the spring constant,  $k_s$  between 0 and  $\infty$ . Hence the critical load required to buckle the structure varies with the value of  $k_s$ . It is evident from equation (4.10) that  $P$  corresponds to the fundamental critical load for a fixed-fixed structure of length  $L$ ; i.e.  $\theta = \pi$  if  $k_s \rightarrow 0$ . When  $k_s \rightarrow \infty$ ,  $P$  corresponds to the fundamental critical load for a fixed-pinned structure of length  $L/2$ ; i.e.  $\theta \sim 4.493$ . For any arbitrary finite values of  $k_s$ , the value of  $P$  is in between these bounding limits. The eigenvector associated with a particular  $\theta$  (hence  $P$ ) is obtained by solving equation (4.8) for linearly independent vector components.

Figure 4.5 shows the operating characteristics of an ETB actuator in the log-log domain for Si, DLC and PMMA candidates. The trend in the tradeoffs between the force and displacement delivered for different materials as  $k_s$  varies between 0 and  $\infty$  is plotted. The aspect ratio of the beam,  $L/t \sim 60$ . The width of the beam,  $b = 62 \mu\text{m}$  and the thickness,  $t = 2 \mu\text{m}$ . The curves are obtained by using solving for the fundamental eigenpair using equations (4.10) and (4.8) for different values of  $k_s$  for each of the materials considered. The displacement amplitude corresponding to an eigenpair is obtained by energy conservation considering the spring effects.

$$\frac{EI}{2} \int_0^L \left( \frac{d^2 y}{dx^2} \right)^2 dx + \frac{k_s}{2} (y|_{L/2})^2 = \frac{1}{2} E (\alpha (\Delta T)_c)^2 Lbt \quad (4.11)$$

An estimate of the work per volume delivered can be obtained by evaluating the enclosed area between the bounding limits. It is also obvious from the plot that DLC is superior to Si and PMMA for high force/work per volume actuators. The work per volume delivered by an ETB structure is greater than that of a BMET structure at least by an order of magnitude for realistic values of the slenderness ratios  $L/r_g \sim 10^2$ .

#### 4.5.3 Electromechanical efficiency, $\eta_{em}$

The work per volume delivered depends on the compressive strain energy per unit volume,  $E_s$  developed at the onset of buckling due to thermal expansion. Hence

efficiency metric for the actuation is defined here as the ratio of the compressive strain energy per unit volume,  $E_s$  at the onset of buckling to the internal energy per volume,  $U_t$  associated with the critical temperature difference,  $(\Delta T)_c$

$$\eta_{em} = \frac{E_s}{U_t} = \frac{E\alpha^2(\Delta T)_c^2}{2\rho C(\Delta T)_c} = \left(\frac{2r_g^2\pi^2}{L^2}\right)\left(\frac{E\alpha}{\rho C}\right) \quad (4.12)$$

where  $\rho C$  is the volume specific heat of the material. Since  $\rho C$  remains almost constant ( $\sim 10^{6.5} \text{ Jm}^{-3}\text{K}^{-1}$ ) for different classes of materials, materials with large values of  $E\alpha$  are promising for efficient ETB actuator structures. The efficiency of ETB actuator structures is, therefore, an order less than the uni-material linear in-plane actuators ( $\sim 10^{-3} - 10^{-4}$ ) for realistic slenderness ratios ( $L/r_g > 10$ ). However, the work per volume delivered by ETB structures is greater than that of the uni-material actuators.

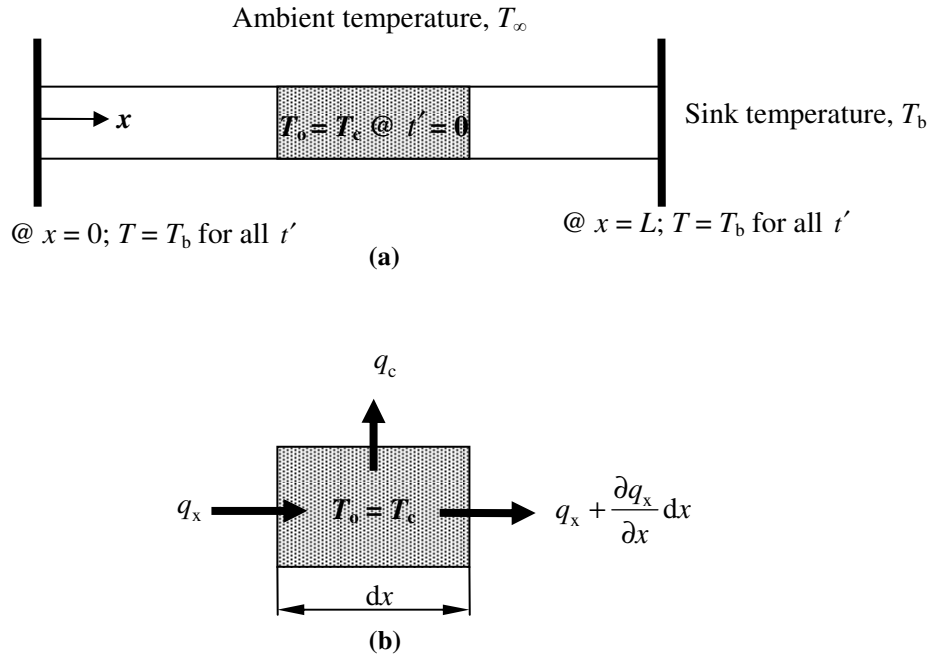
#### 4.6 Transient thermal response of an ETB actuator structure

Actuation frequency depends on the time taken by the actuator to cool between the prescribed operating temperature limits. Figures 4.6a and 4.6b show a one dimensional transient thermal model of the ETB actuator structure and the energy flow across the control volume considered. The thermal conductivity of the material is  $\kappa$  and its volume specific heat capacity is  $\rho C$ . The actuator is assumed to be a heat source maintained at an initial temperature  $T_o$  which is equal to the critical temperature  $T_c$ . The heat sinks on either end are maintained at the temperature  $T_b$ .

The heat generated by the actuator is dissipated by conduction to the heat sink and convection to the environment. The effect of radiation is neglected in the estimation of the transient thermal response of the actuator. This is because the heat dissipated due to radiation is of the same order as the convective heat transfer even for a unit emissivity.

The actuation frequency depends on the time taken by the actuators to heat and cool alternately between the prescribed operating temperatures ( $T_b$  and  $T_c$ ). The time taken

by the actuators to be heated to a given temperature is usually rapid and can be controlled to a certain extent by altering the electrical resistivity of the heating element (e.g. silicon) by doping. The cooling phase is usually uncontrolled, and it depends on the thermal properties of the materials. If  $T_c$  and  $T_b$  are the operating temperatures of the actuator with  $T_c > T_b$ , then the time corresponding to the cooling phase ( $t'_c$ ) can be obtained by solving the implicit transient thermal model by numerical integration



$q_x$  - heat loss by conduction,  $q_c$  - heat loss by convection

Figure 4.6 (a) One dimensional transient thermal model of an ETB actuator structure; (b) Energy transfer across the control volume considered.

$$T^{i+1} = \frac{T^i + F_o(4T_b + Bi.T_\infty)}{1 + F_o(Bi + 4)} \quad (4.13)$$

where  $T^i$  and  $T^{i+1}$  are the temperatures of the bimaterial at successive instants  $t'$  and  $t' + \Delta t'$ ,  $F_o = \kappa \Delta t' / (\rho C) L^2$  is the Fourier number,  $Bi = 2h(b+t)L^2 / \kappa bt$  is the Biot number and  $h$  is the heat transfer coefficient. The characteristic actuation frequency is defined here as

$$f = \frac{1}{t'_c} \quad (4.14)$$

It should be noted that the actuation frequency of the ETB actuator structure is higher than that of the cantilever BMET actuator due to the reduced thermal path to the heat sinks associated with the fixed-fixed architecture. Furthermore, the maximum allowable operating temperature limits are governed by the materials used for the actuators.

#### 4.7 Influence of pre-stress on the performance of ETB actuator

The ability of certain materials to be grown as thin films in a pre-stressed state at microscales presents an opportunity to improve the performance (efficiency and actuation frequency) of the ETB actuator structures. If the material is under compressive pre-stress,  $\sigma_c$  then the critical temperature difference required to buckle the pre-stressed structure,  $(\Delta T)_c^p$  is given as

$$(\Delta T)_c^p = \frac{1}{\alpha} \left( \frac{4\pi^2 r_g^2}{L^2} - \frac{\sigma_c}{E} \right) \quad (4.15)$$

It is evident from equation (4.15) that an increase in the compressive stress leads to a corresponding drop in the critical temperature difference for structures under pre-stress. For instance, a pre-stress of about  $\sim 595$  MPa reduces  $(\Delta T)_c^p$  down to about  $\sim 20^\circ\text{C}$  for silicon structures with  $L/t = 30$ . The decrease in the critical temperature difference due to compressive pre-stress will in turn improve the actuation frequency and the efficiency.

The efficiency of an ETB actuator under pre-stress can be evaluated as the ratio of the work per volume delivered,  $W$  to the internal energy,  $U_t^p$  associated with the critical temperature difference under pre-stress,  $(\Delta T)_c^p$ . The work per volume delivered by the actuator under pre-stress is same as that without pre-stress and hence corresponds to the compressive strain energy at the onset of buckling without pre-stress. The actuation efficiency of ETB structures under pre-stress,  $\eta_{em}^p$  is therefore given as



$$\eta_{em}^p = \frac{E_s}{U_t^p} = \frac{E\alpha^2(\Delta T)_c^2}{\rho C(\Delta T)_c^p} = \eta_{em} (1 - \varepsilon')^{-1} \quad (4.16)$$

where  $\varepsilon' = (\sigma_c/E)/(4\pi^2 r_g^2/L^2)$  is the dimensionless strain which is defined as the ratio of the strain corresponding to the pre-stress to the critical buckling strain. The condition  $\eta_{em}^p \rightarrow \infty$  as  $\varepsilon' \rightarrow 1$  signifies that the structures are in the buckled state without being subjected to electrothermal actuation.

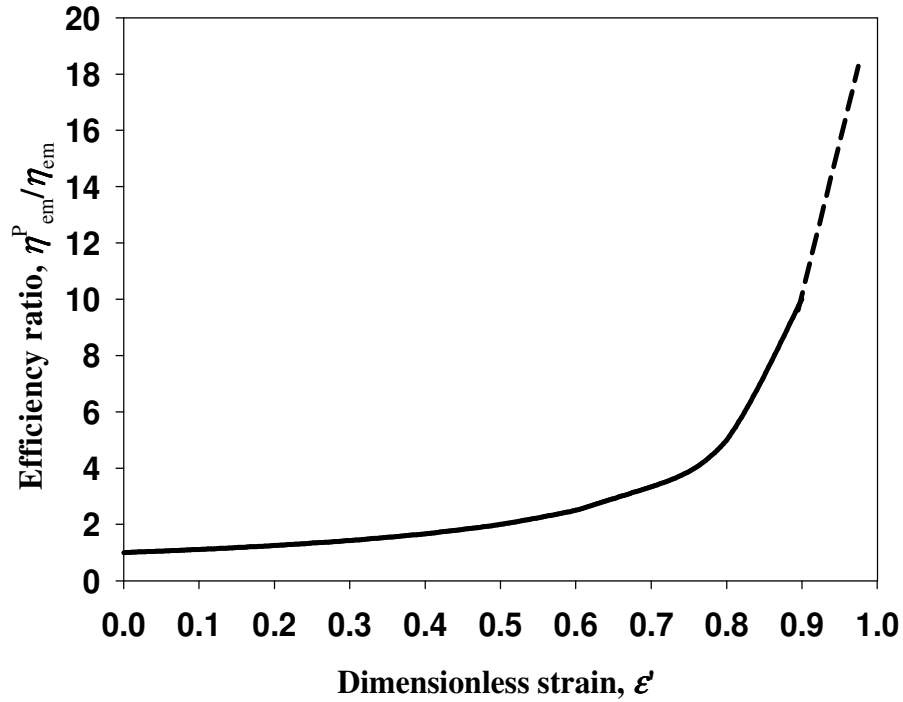


Figure 4.7 A plot of efficiency ratio,  $\eta_{em}^p / \eta_{em}$  as a function of dimensionless strain,  $\varepsilon'$ .

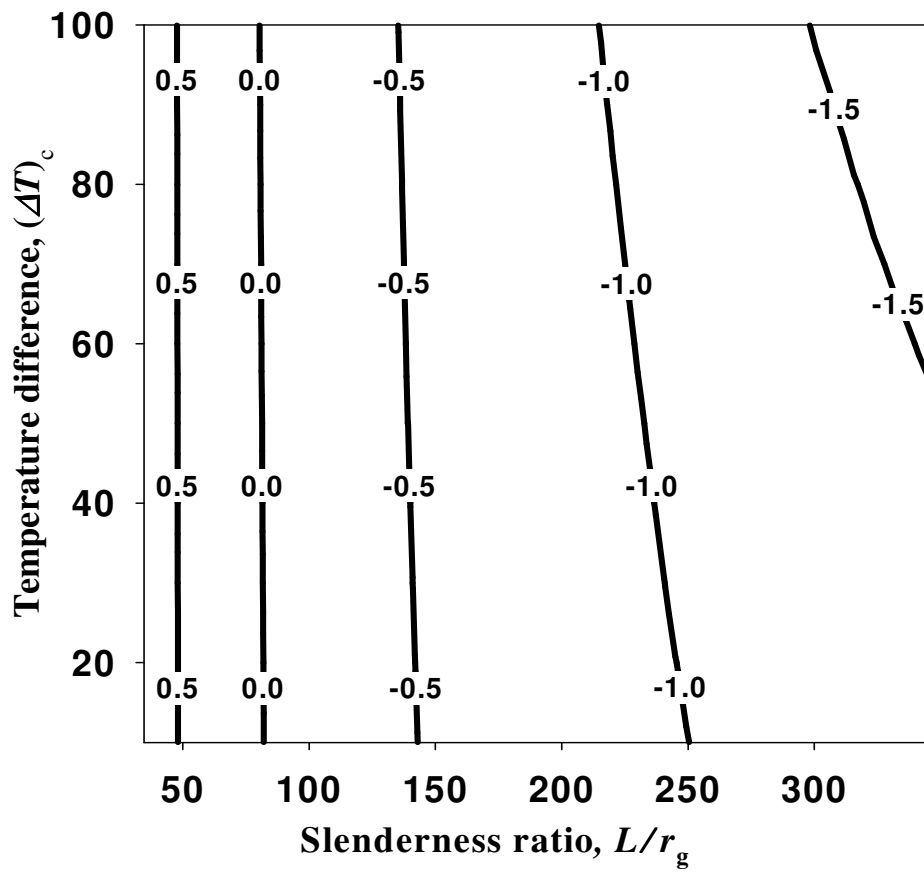
Figure 4.7 shows a plot of efficiency ratio,  $\eta_{em}^p / \eta_{em}$  as function of  $\varepsilon'$ . It is evident from the plot that the actuation efficiency can be improved at most by an order by controlling the pre-stress. For instance, a compressive pre-stress of  $\sim 450$  MPa in a silicon structure with  $L/r_g \sim 100$  is efficient than a similar structure without pre-stress by a factor of 4. Compressive pre-stress of that order can be achieved in *a*-Si layers by low pressure CVD process [59]. The required pre-stress to achieve the same efficiency for DLC structures having same values of  $L/r_g$  and  $\varepsilon'$  is about  $\sim 2.7$  GPa which can be achieved

in thin film DLC grown by pulsed laser deposition [60] although wafer handling issues associated with the bow formation requires further consideration.

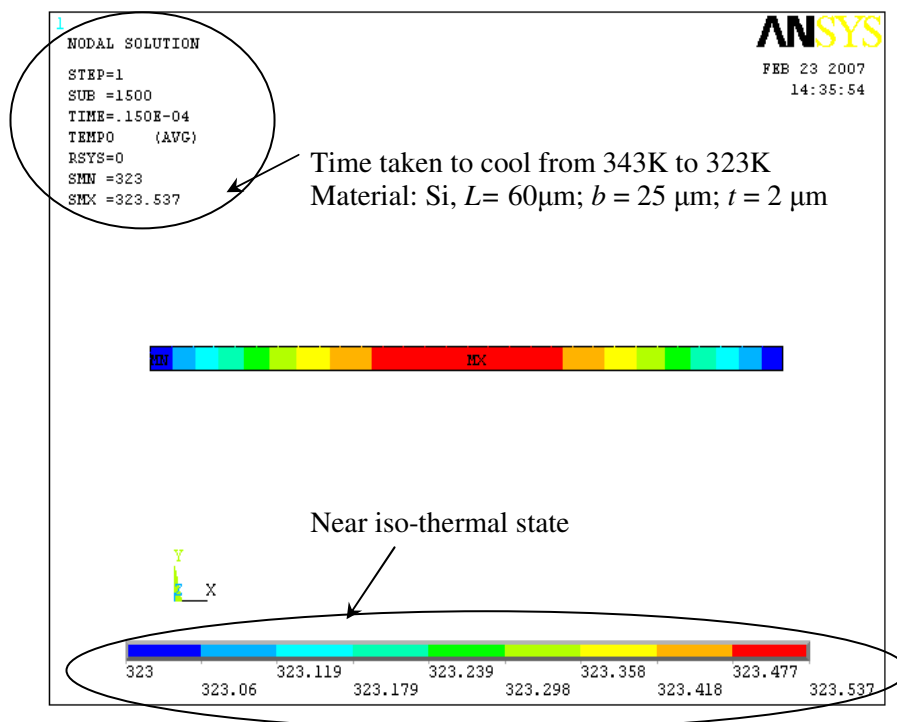
#### 4.8 Candidate materials for ETB actuators

It is evident from equations (4.2) and (4.12) that materials with large values of  $E\alpha$  and a small critical temperature difference,  $(\Delta T)_c$  have a significant bearing on the actuation efficiency and frequency. Candidates such as Al, Zn, Cu, Ni, Mg,  $\text{Al}_2\text{O}_3$ ,  $\text{Zr}_2\text{O}_3$ ,  $\text{Si}_3\text{N}_4$ , DLC and Si possess high values of  $E\alpha$  ( $\sim 1.0 \text{ MPaK}^{-1}$ ) and are therefore promising for ETB actuator structures [17]. Candidates such as Cu require careful consideration based on corrosion resistance before further analysis. Although engineering ceramics deliver large work per volume, their low electrical resistivities pose problems in actuating them electrothermally. A few of these candidates in particular, polycrystalline Si [61] and DLC [62, 63] are capable of being grown as thin films with high intrinsic compressive stress and are therefore promising for ETB microactuator structures. Polycrystalline Si films with a thickness of a few microns can be grown by chemical vapour deposition (CVD) which is a proven fabrication route. The CVD process involves decomposition of silane ( $\text{SiH}_4$ ) with hydrogen as a gaseous by-product. The process variables associated with the CVD process (substrate temperature, pressure, furnace temperature, silane concentration, etc.) can be controlled to the extent that compressive pre-stress levels varying from 100 MPa - 1 GPa can be achieved despite the intrinsic tensile stress which results from the dopant diffusion during the doping process [64].

Figure 4.8a shows a plot relating  $(L/r_g)$ ,  $\log_{10}(\sigma_c)$  and  $(\Delta T)_c$ , for silicon. It is evident from the plot that for a structure with  $L/r_g$  varying from 80-150, the critical temperature difference,  $(\Delta T)_c$  can be brought down to a few tens of degrees if the intrinsic compressive stress is suitably varied between 1 GPa - 100 MPa. Figure 4.8b shows model results for the transient thermal response of an ETB actuator structure made of silicon by finite element analysis using ANSYS. The near iso-thermal state is assumed to be attained when there is no variation in the zeroth order of the estimated temperatures. Frequencies of up to  $\sim 50 \text{ kHz}$  could be achieved for a temperature difference of  $20 \text{ }^\circ\text{C}$ .



(a)



(b)

Figure 4.8 (a) Iso-stress contours,  $\log_{10}(\sigma_c)$  in GPa for Si ETB structure for a range of slenderness ratios and critical temperature differences; (b) Transient thermal response of a Si ETB actuator structure. All temperature values are in Kelvin.

Although DLC structures have a limited success when compared to silicon for the commercial MEMS devices, the performance of DLC is better than silicon for ETB actuators. DLC films can be grown either by sputter/pulsed laser deposition of graphite/polycarbonate [43, 65] or a CVD using hydrocarbon source gas [66, 67] with plasma enhancement [68, 69]. The quality of the films in terms of properties is governed by the relative proportions of  $sp^2/sp^3$  sites and hydrocarbon content which are dependent on the process employed to grow the films [70, 71]. The non-diamond impurities ( $sp^2$  sites and hydrogen content) are found to be responsible for the development of intrinsic compressive stresses in DLC films [72]. Recently, *Sandia National Laboratory, U.S.A* has developed a successful process to control the intrinsic compressive stresses in tetrahedrally bonded amorphous carbon films grown by pulsed laser deposition. Their process provides flexibility in controlling the intrinsic compressive stress levels ranging from  $\sim 5 \times 10^{-3}$  - 6 GPa by periodic annealing of the substrate [60, 73]. Hence the development of large intrinsic compressive stresses in DLC films during growth process can be exploited for the design of high performance ETB actuator structures. High actuation frequencies of the order  $\sim 400$  kHz are potentially achievable for ETB actuators made of DLC owing to their large thermal conductivity.

#### **4.9 Summary**

The thermoelastic and electrothermal performance of ETB actuator structures have been evaluated using Euler buckling theory and lumped thermal models respectively. Si and DLC are promising candidates for ETB structures since the processes for controlling the residual stresses for these materials are well established. The work per unit volume delivered by ETB structures is large compared to BMET structures by an order of magnitude. The low temperature difference ( $\sim 20$ -40 K) required for actuating ETB structures results in relatively high frequency ( $\sim 400$  kHz) actuation. The pre-stress required for such structures is less than  $\sim 350$  MPa for  $(L/t) > 40$ . However other issues such as robustness of the device when subjected to environmental temperature changes would have to be addressed in order to realise reliable actuators. This might be achieved by employing an active control strategy using integrated sensors. Furthermore,

issues such as oxidation/corrosion of the actuator material in the operating environment which have a bearing on the performance of a device also need to be addressed.

A generalised comparison between various actuation schemes based on their performance metrics reveals that electrothermal actuation is competitive with piezoelectric actuators [6]. Preliminary design and analysis is therefore essential to estimate the performance limits achievable using piezoelectric actuator structures to identify promising material combinations in different configurations. The comprehensive data evolved from such a design study are not only useful for the selection of actuators but also serve as guidelines for identifying the suitable material choices. Chapter 5 discusses the design guidelines for selecting promising candidates for bimaterial piezoelectric microactuators.

# Chapter 5

## Materials selection for Bimaterial Piezoelectric Microactuators

### 5.1 Introduction on the piezoelectric microactuators

The performance limits for different actuation mechanisms have a significant bearing on the selection of actuation schemes for particular applications. It was found earlier that the BMET actuator structures can compete with bimaterial piezoelectric (BMPE) actuators for applications which require frequencies of the order of  $\sim 10$  kHz at small scales ( $L < 100 \mu\text{m}$ ). In order to obtain a more detailed comparison on the performance limits of BMET and BMPE actuator structures, optimal performances achieved from these actuation schemes need to be estimated. The optimal performances of BMET actuators have been evaluated and discussed in detail already in chapters 2 and 3. The present chapter focuses on the materials selection strategy for BMPE actuator structures in order to achieve the maximum performance.

Piezoelectric microactuators, in general, are capable of delivering relatively large forces (0.01-1mN) but are limited to small displacements (0.1-10  $\mu\text{m}$ ). Present generation microsystems have generally preferred ferroelectric piezoceramics such as BaTiO<sub>3</sub>, PZT, PZN-PT, PMN-PT and PYN-PT due to their high  $d$  coefficients and reasonably high Curie temperatures, which are compatible with most transducer applications. Despite their promising characteristics, applications of piezoelectrics in commercial microsystems are not widely prevalent but do include the important case of inkjet printer heads [12] and non-contact AFM probes [74]. However, a much wider range of research or prototype applications of piezoelectrics in MEMS include linear micromotors [11, 75, 76], high power transformers [77], micropumps [78, 79] and power generators [80].

The optimal selection of a suitable active material for a given elastic substrate is of great importance from the MEMS perspective considering the need to develop reliable devices with high performance. This challenge is equally supported by the growing interest in developing thin films of arbitrary materials on various substrates

thereby improving the capability of existing microfabrication routes. Therefore, guidelines for optimal materials selection in the preliminary design stage become essential. These have not yet been established for microsystems despite the hitherto limited available choices of active materials [81-83] . This chapter focuses on identifying and ranking promising candidate materials for BMPE structures, properly accounting for the discrete nature of the properties of engineering materials. The performance metrics considered are the same as defined previously for BMET structures i.e. tip slope (displacement), blocked moment (force), work per unit volume and frequency. The influence of materials selection on the quality factor ( $Q$ ) and the electromechanical impedance of actuators are also discussed.

The present analysis assumes linear elastic material behaviour for the actuator design in the estimation of the performance. This assumption restricts the applicability of the results, however, in practice the majority of piezo-devices operate within the linear range. Furthermore, this study does not take into account the effect of thin film stresses developed during deposition and issues such as depoling and aging of active materials which significantly degrade their performance. Also a particular, simple, actuator design is chosen in order to allow a straightforward comparison of the choices of material combinations. Detailed design clearly requires more refined models for the material and actuator geometry. Nevertheless, the estimates obtained from this study are sufficiently accurate to facilitate materials selection decisions in the preliminary design of actuators. The conclusions regarding the ranking of the material combinations are sufficiently clear cut that they will not be altered by introducing more refined models.

This chapter is organised as follows. Section 5.2 discusses the mechanics of BMPE actuators. Section 5.3 focuses on the estimation of performance limits of BMPE actuators. Section 5.4 discusses the process of identifying suitable material combinations for BMPE actuators for various functional requirements. Section 5.5 summarises the key inferences drawn from this analysis.

## 5.2 Mechanics of a BMPE actuator structure

Although the mechanics of uni-material and bimaterial piezoelectric actuator structures are well documented, little attention has been given to the materials selection process. This chapter focuses on identifying promising materials for BMPE actuator structures applying mechanics relations developed previously [84-86]. Figure 5.1 shows a schematic of an ideal bimaterial cantilever piezoelectric actuator. The actuator structure consists of a piezoelectric layer and an elastic substrate referred to by subscripts 1 and 2 respectively. The layers corresponding to the electrodes are neglected in the present analysis. The actuator length and width are given by  $L$  and  $b$  respectively. The layer thicknesses are denoted by  $t_1$  and  $t_2$  and  $t$  is the total thickness. The Young's moduli of the bimaterials are denoted by  $E_1$  and  $E_2$ . The ratio of the Young's moduli of the bimaterials is defined as,  $\lambda = E_1/E_2$  and the ratio of the thicknesses of the bi-layers,  $\xi = t_1/t_2$ .

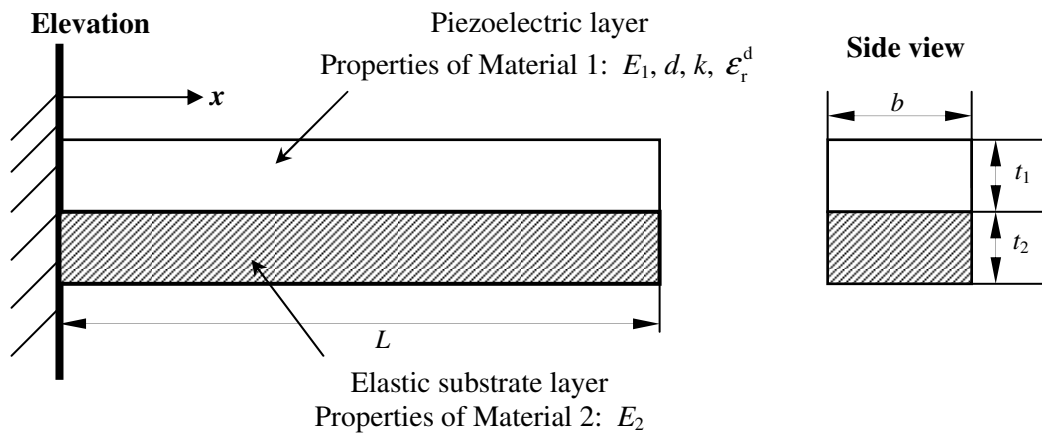


Figure 5.1 Schematic of a bimaterial cantilever piezoelectric actuator structure.

Actuation in piezoelectric bilayers can be achieved either in  $d_{31}$  mode or  $d_{33}$  mode (using an inter-digitated configuration) as shown in Figures 5.2a and 5.2b. The compliance relations for BMET and BMPE actuator structures are the same except that the thermal strain is replaced by the piezoelectric strain. The tip slope, blocked moment and maximum work per volume of the BMPE actuator in  $d_{31}$  mode can therefore be given as



$$\Theta_f = \frac{6E_p d_{31} L}{t} \left( \frac{\lambda \xi (\xi + 1)^2}{(\lambda \xi^3 + 1)(1 + \lambda \xi) + 3\lambda \xi (\xi + 1)^2} \right) \quad (5.1)$$

$$M_{\text{blk}} = \frac{E_1 b t^2 E_p d_{31}}{2} \left( \frac{\xi}{(1 + \lambda \xi)(\xi + 1)} \right) \quad (5.2)$$

$$W = \frac{3E_1 (E_p d_{31})^2}{8 \left( 3(\lambda \xi + 1) + \left( \frac{(1 + \lambda \xi)^2 (1 + \lambda \xi^3)}{\lambda \xi (\xi + 1)^2} \right) \right) \left( \frac{\xi + 1}{\xi} \right)} \quad (5.3)$$

where  $E_p = V/t_1$  is the electric field parallel to the polarised orientation in  $\text{Vm}^{-1}$  and  $d_{31}$  is the piezoelectric strain coefficient of the piezoelectric layer in  $\text{mV}^{-1}$  or  $\text{CN}^{-1}$ . The condition pertaining to optimal performance for a given pair of materials under a constant electric field is given by equation (2.14) since the compliance relations for BMPE actuators are the same as that of BMET actuators. Substituting equation (2.14) in equations (5.1), (5.2) and (5.3) and normalising the geometric parameters ( $L$ ,  $b$  and  $t$ ) gives optimised critical performance metrics for a constant electric field which serves as a basis for selection between candidate materials.

$$\Theta_{\text{no}} = \frac{\Theta_f t}{E_p L} = \frac{6d_{31}}{4} \quad (5.4)$$

$$M_{\text{no}} = \frac{M_{\text{blk}}}{b t^2 E_p} = \frac{E_1 d_{31}}{2 \left( \frac{\xi_o + 1}{\xi_o} \right)^2} \quad (5.5)$$

$$W_{\text{no}} = \frac{W}{E_p^2} = \frac{3E_1 (d_{31})^2}{32 \left( \frac{\xi_o + 1}{\xi_o} \right)^2} \quad (5.6)$$

where  $\Theta_{\text{no}}$ ,  $M_{\text{no}}$  and  $W_{\text{no}}$  are material parameters which correspond to optimal slope, moment and work normalised with respect to geometry and electric field.

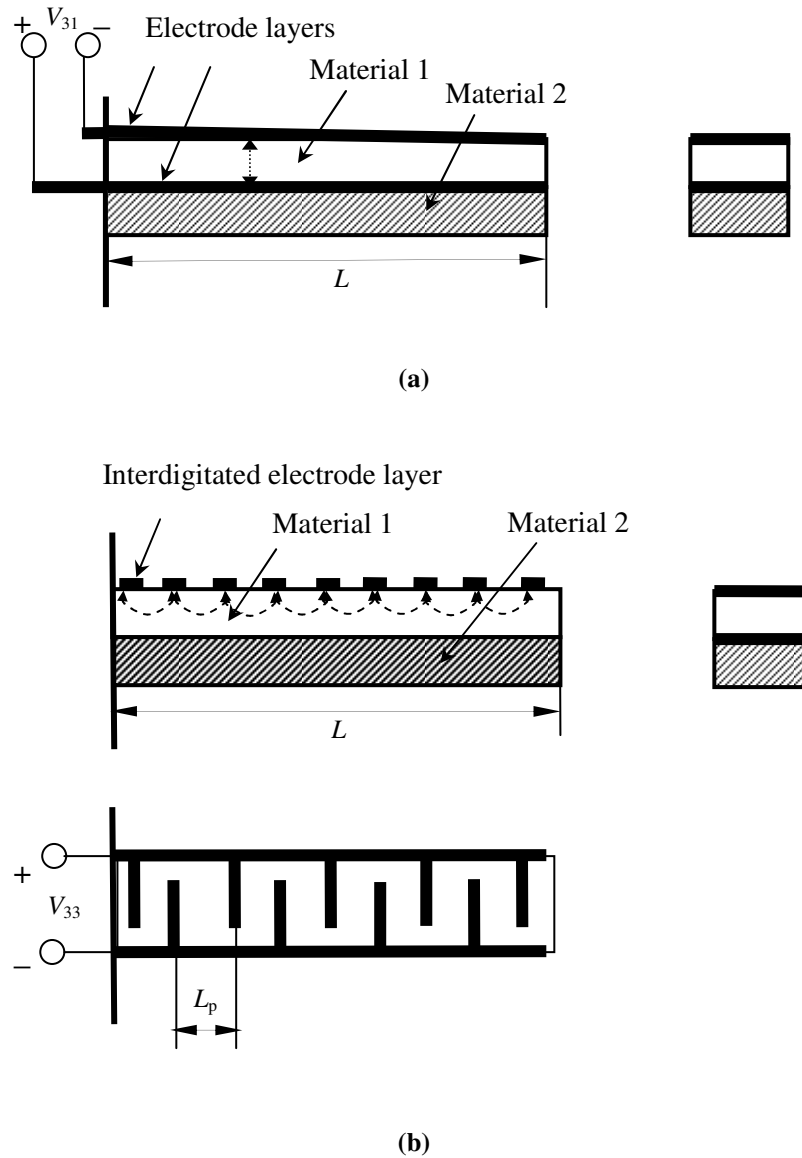


Figure 5.2 Schematic of a cantilever BMPE actuator (a) actuation in  $d_{31}$  mode, (b) actuation in  $d_{33}$  mode.

Actuation in  $d_{33}$  mode can be obtained by depositing inter-digitated electrodes parallel to the polarised direction as shown in Figure 5.2b. The actuation voltage for such a configuration has to be increased by a factor of  $\sim 5$  in order to achieve the same performance as that obtained in  $d_{31}$  mode considering the distance between the electrode fingers,  $L_p \sim 10t_1$ . Hence the  $d_{33}$  mode configuration is more appropriate for sensor applications than for actuator structures [87]. The present materials selection process considers only  $d_{31}$  mode actuation which is commonly preferred in MEMS devices.

### 5.3 Performance limits of BMPE actuator structures

The promising active/substrate material combinations are to be identified and ranked for various performance metrics. Tables 5.1 and 5.2 show the properties of a few available choices of the piezoelectric active materials which might be considered for MEMS applications. The properties are obtained from the sources cited in the last column of each tables. Active materials for which sufficient data are available are only considered to allow for consideration in a practical actuator design. Both thin film and bulk properties of piezoelectric materials are presented, to indicate the variation in property values and to provide realistic estimates of what might be achieved via present and future microfabrication processes.

The materials selection strategy is based on plotting performance contours in the domain of governing active material properties for different substrate materials. Silicon is the most commonly used substrate material in MEMS devices. Therefore the materials selection strategy is primarily illustrated using Si ( $E = 165$  GPa) substrates, but other substrates could be considered using the appropriate properties in conjunction with equations (5.4), (5.5) and (5.6). Figure 5.3a shows contours of equal slope ( $\log_{10}(\theta_{no})$ ), blocked moment ( $\log_{10}(M_{no})$ ) and work per volume ( $\log_{10}(W_{no})$ ) plotted in the domain of governing properties ( $d$  vs.  $E$ ) for a range of active materials on silicon. Similar plots are generated at the extremities of the range of substrate properties, i.e. for DLC ( $E = 700$  GPa) and PMMA ( $E = 2.5$  GPa) to provide an indication of the practical limits on performance. Figure 5.3b and 5.3c shows performance contours for DLC and PMMA substrates respectively. The variation in blocked moment and work per volume are within an order of magnitude of that for Si, while the variation in tip slope is relatively small.

S.No	Active Materials	$E_{11}$	$E_{22}$	$E_{33}$	$d_{11}$	$d_{12}$	$d_{14}$	$d_{15}$	$d_{21}$	$d_{22}$	$d_{23}$	$d_{25}$	$d_{26}$	$d_{31}$		$d_{33}$		References	
														Film	Bulk	Film	Bulk		
		GPa			pCN <sup>-1</sup>									pCN <sup>-1</sup>					
1	BaTiO <sub>3</sub> (unpoled)	125		64										8	35	15	86	[81, 88-91]	
2	BaTiO <sub>3</sub> (poled)	110		105											-78	42	190	[81, 92]	
3	PbTiO <sub>3</sub>																		
4	PZT	70		53										(-30) - (-70)	-180	190 - 250	360	[81, 88, 93-95]	
5	LiNbO <sub>3</sub>	202		240											-1		6	[88, 96, 97]	
6	SBT														6			[88]	
7	YMnO <sub>3</sub>																		
8	KH <sub>2</sub> PO <sub>4</sub>	57					1.3					1.3						[88, 98]	
9	NaNO <sub>2</sub>																		
10	Pb <sub>5</sub> Ge <sub>3</sub> O <sub>11</sub>																		
11	GeTe																		
12	PVDF	9		4										3	20	23	30	[83, 88, 89, 99]	
13	ZnO	127		144										-3.4	-5.4	6.8	10.7	[81, 100]	
14	AlN	340		355										-2	-2.8	4	5.8	[81, 101, 102]	
15	PMZT	70														30 - 50		[103]	
16	CdS	48		60											-5.2		10.3	[81, 98]	
17	$\alpha$ - Quartz	87		107	-2.31	2.3	-0.73					0.67	4.6					[81, 104]	
18	$\beta$ -Quartz	87		107			0.54												
19	RSALT	42	51	62			345		700	2200	2100	54						[98, 105]	
21	PMNPT	14		8											-1330	84	2820	[106, 107]	
22	PZNPT	15	149	7											-1154		2000	[108-110]	
23	PYNPT							1700							500		2500	[111-113]	

■ Data not available; PMZT - Mn doped PZT; PMNPT- Mg based Piezoceramics; PZNPT - Zn based Piezoceramics; PYNPT- Yb based Piezoceramics; RSALT- Rochelle salt

Table 5.1 Elastic and piezoelectric properties of some active materials which might be considered for the BMPE actuator structures.

S.No	Active Materials	$E_C^P$	$E_{IC}^P$	$\epsilon_r^d$	$\rho$	$k_{31}$		$k_{33}$		$T^C$	References
						Film	Bulk	Film	Bulk		
				$\epsilon_{ii}^d, i = 1,2,3$							
		MVm <sup>-1</sup>			kgm <sup>-3</sup>					°C	
1	BaTiO <sub>3</sub> (unpoled)	1 - 5	98	2920, 2920, 168	5800	0.07	0.32	0.10	0.56	120	[81, 88-91]
2	BaTiO <sub>3</sub> (poled)			1450, 1450, 1700			0.21	0.11	0.50		[81, 92]
3	PbTiO <sub>3</sub>									~ 490	[88]
4	PZT	5 - 10	107	1475, 1475, 1300	7500	0.17	0.44	0.54	0.77	~ 370	[81, 88, 93-95]
5	LiNbO <sub>3</sub>	4	465	84, 84, 30	4700		0.03		0.18	1210	[88, 96, 97]
6	SBT									570	[88]
7	YMnO <sub>3</sub>									~ 640	[88]
8	KH <sub>2</sub> PO <sub>4</sub>		163	42, 42, 21	2338					-150	[88, 98]
9	NaNO <sub>2</sub>									164	[88]
10	Pb <sub>5</sub> Ge <sub>3</sub> O <sub>11</sub>									180	[88]
11	GeTe									400	[88]
12	PVDF	55	333	~ 12 - 14	1780	0.03	0.17	0.13	0.16	~ 120	[83, 88, 89, 99]
13	ZnO		282	~ 11	5680	0.12	0.20	0.26	0.41		[81, 100]
14	AlN		537	~ 9	3300	0.13	0.18	0.27	0.39	> 1000	[81, 101, 102]
15	PMZT										[103]
16	CdS			10	4820		0.12		0.27		[81, 98]
17	$\alpha$ - Quartz			4.5	2650		0.00			~ 573	[81, 104]
18	$\beta$ -Quartz				2650						
19	RSALT			205, 9.5, 9.5	1767					-18 ; 24	[98, 105]
21	PMNPT	8	35	1000 -1500	8060		0.73		0.94	~ 150 - 160	[106, 107]
22	PZNPT	1		3100, 3100, 5200	8310		0.66		0.78	~ 150 - 160	[108-110]
23	PYNPT	2 - 5		1030			0.76		0.9	~ 300 - 400	[111-113]

■ - Data not available; PMZT - Mn doped PZT; PMNPT- Mg based Piezoceramics; PZNPT - Zn based Piezoceramics; PYNPT- Yb based Piezoceramics; RSALT- Rochelle salt

Table 5.2 Electromechanical properties of some active materials which might be considered for the BMPE actuator structures.

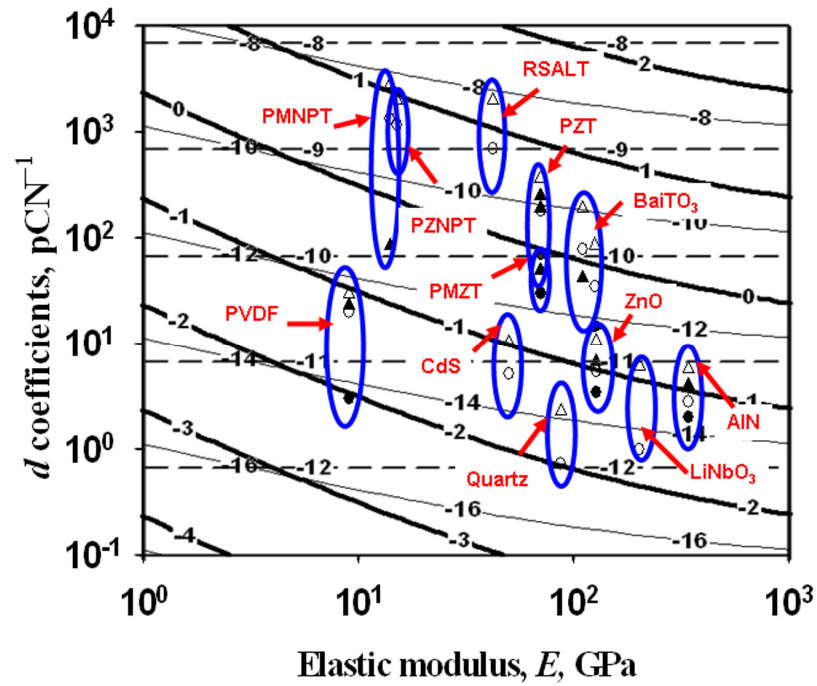
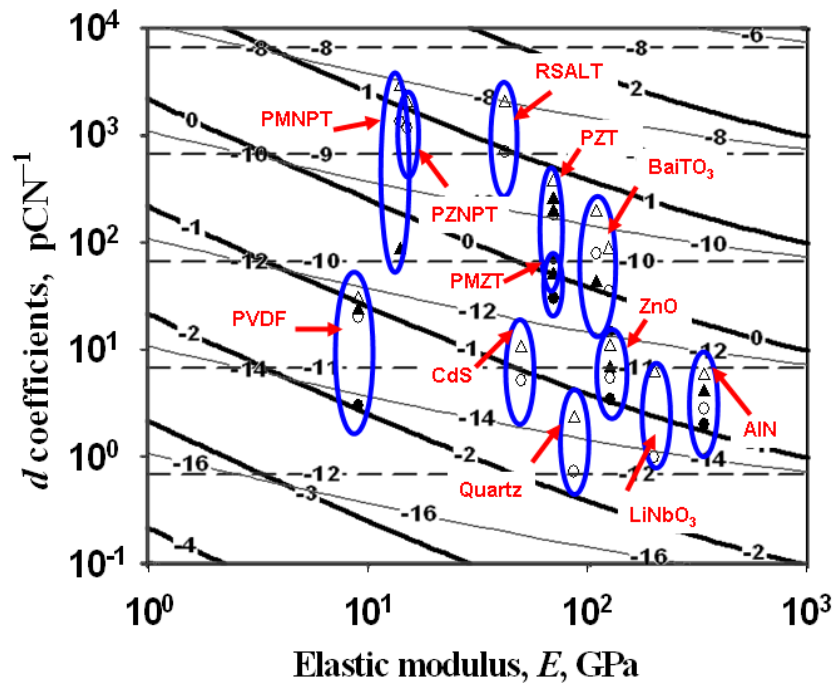
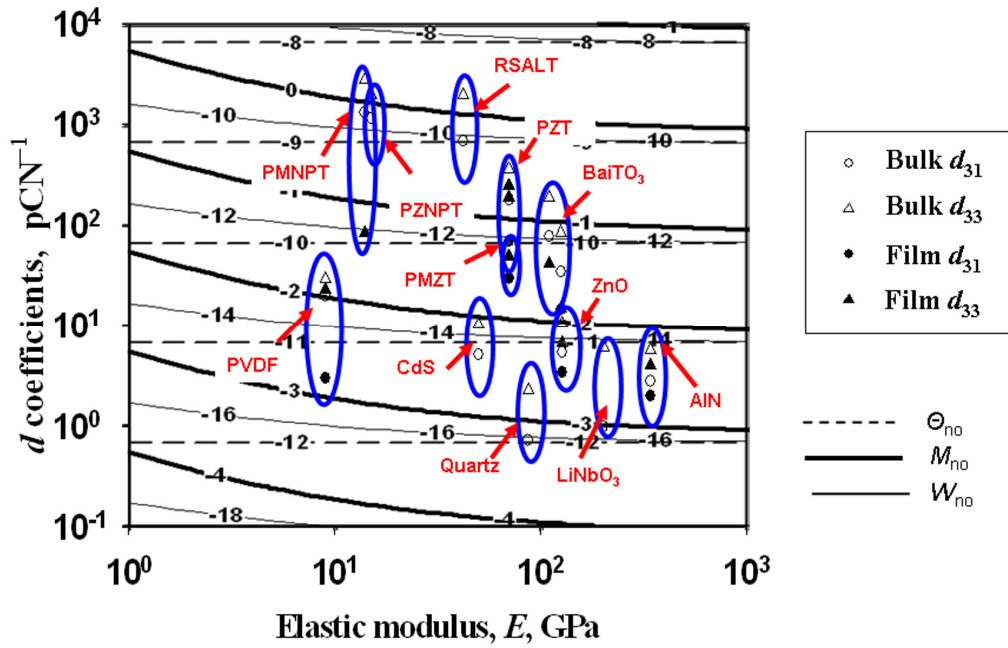


Figure 5.3a Contours of equal tip slope ( $\log_{10}(\Theta_{no})$ ), blocked moment ( $\log_{10}(M_{no})$ ) and work per volume ( $\log_{10}(W_{no})$ ) for a range of piezoelectric materials on Si substrate.



(b)

Figure 5.3b Contours of equal tip slope ( $\log_{10}(\Theta_{no})$ ), blocked moment ( $\log_{10}(M_{no})$ ) and work per volume ( $\log_{10}(W_{no})$ ) for a range of piezoelectric materials on DLC substrate.



(c)

Figure 5.3c Contours of equal tip slope ( $\log_{10}(\Theta_{no})$ ), blocked moment ( $\log_{10}(M_{no})$ ) and work per volume ( $\log_{10}(W_{no})$ ) for a range of piezoelectric materials on PMMA substrate.

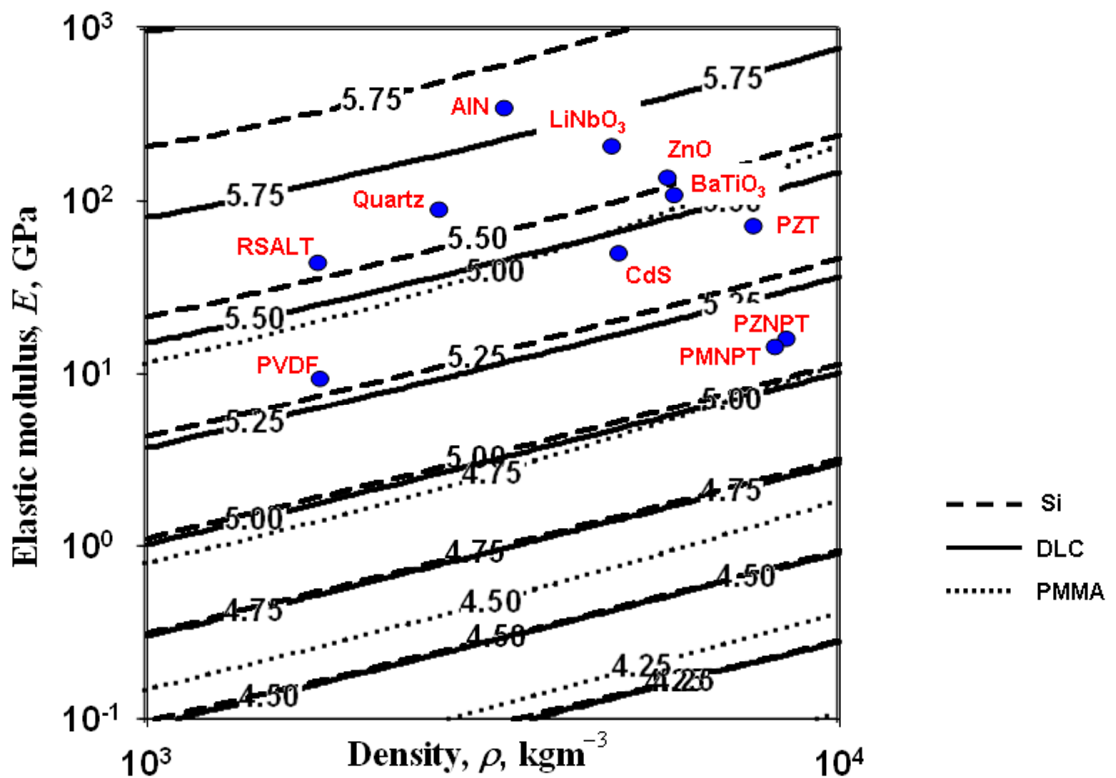


Figure 5.4 Contours of equal actuation frequency ( $\log_{10}(f_s)$ ) for different piezoelectric materials on Si, DLC and PMMA substrates ( $L = 100 \mu\text{m}$ ;  $L/t = 30$ ).

Actuation frequency is another important performance metric governed partly by materials selection. BMPE actuators typically operate close to mechanical resonant frequencies. The fundamental flexural frequency of a bimaterial can be estimated using Euler-Bernoulli beam theory as given by equation (3.34). Figure 5.4 shows contours of equal actuation frequency for different material combinations with respect to silicon, DLC and PMMA substrates for a length scale of  $100\ \mu\text{m}$  and  $L/t = 30$ . The influence of materials selection on actuation frequency is relatively small because the densities of the active materials only vary within an order of magnitude ( $\sim 10^3\text{-}10^4\ \text{kgm}^{-3}$ ).

Another important target for materials selection is the electromechanical efficiency,  $\eta_{\text{em}}$ . Actuation efficiency is defined here as the ratio of mechanical work done per unit volume ( $W$ ) to the input electrical energy per unit volume ( $E'_s$ ) supplied.

$$\eta_{\text{em}} = \frac{W}{E'_s} \quad (5.7)$$

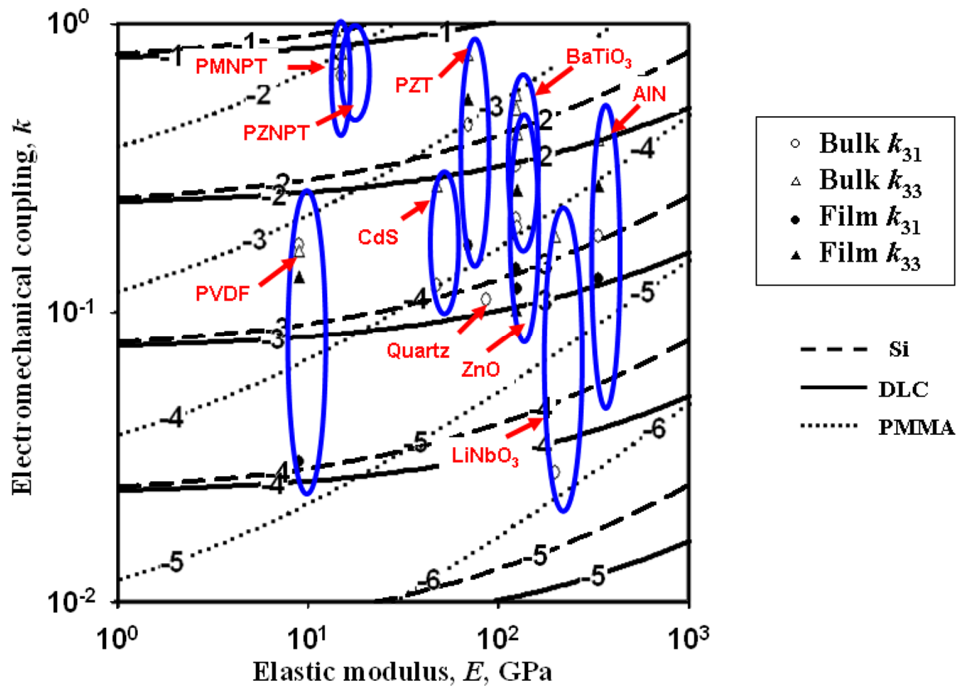


Figure 5.5 Contours of electromechanical efficiency,  $\log_{10}(\eta_{\text{em}})$  for different piezoelectric materials on Si, DLC and PMMA substrates.



The electrical energy supplied is assumed to be equal to the dielectric energy stored in the parallel plate capacitor, thereby ignoring electrical losses in the external circuitry (which are independent of any material selection decision). Therefore the energy per volume supplied,  $E'_s$  is given as

$$E'_s = \frac{CV^2}{2At_1} = \frac{\epsilon_r^d E_p^2}{2} \quad (5.8)$$

where  $\epsilon_r^d$  is the relative dielectric constant of the active material employed. Substituting equations (5.6) and (5.8) in (5.7) gives efficiency in terms of material properties.

$$\eta_{em} = \frac{3E_1 d_{31}^2}{16\epsilon_r^d \left(\frac{\xi_o + 1}{\xi_o}\right)^2} = \frac{3k^2}{16\left(\frac{\xi_o + 1}{\xi_o}\right)^2} \quad (5.9)$$

where  $k$  is the electromechanical coupling factor of the piezoelectric material. Figure 5.5 shows the contours of equal efficiency for various piezoelectric materials plotted in the domain of governing active material properties ( $k$  vs.  $E$ ) for three different substrates considered. Actuation efficiency varies over three orders of magnitude ( $\eta_{em} \sim 10^{-3} - 10^{-1}$ ) for the given range of material combinations considered.

The overall size of the integrated components for piezoelectric MEMS actuators is dependent on the off-chip voltage and power amplifier requirements which are prone to make the system bulky. The higher the actuation voltage, the larger the amplifier required. Hence a comparison is made of the voltage requirements for a constant electric field with variation in active material properties over the range of substrates considered. The voltage required for actuating different BMPE actuators for a constant electric field can be quantified by a parameter termed the electromechanical voltage index ( $V_I$ ).

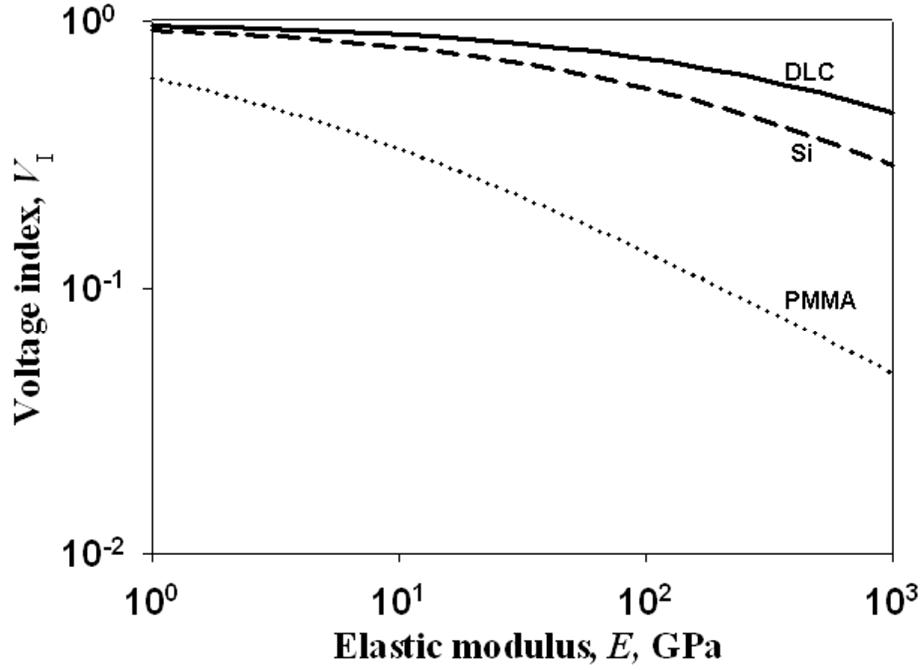


Figure 5.6 Effect of different material combinations on the actuation voltage for an optimal performance under a constant electric field.

$$V_I = \frac{V}{E_p t} = \frac{1}{\left(1 + \left(\frac{1}{\xi_0}\right)\right)} \quad (5.10)$$

Figure 5.6 shows the variation in  $V_I$  for a range of piezoelectric materials on the three different substrates considered previously. It is clear from the plot that the voltage required for a constant electric field varies by about an order of magnitude ( $V_I \sim 10^{-1} - 10^0$ ) for the range of material combinations considered.

The candidate materials selected strongly influence the quality factor (hence the loss coefficient) of the actuators. The loss coefficient,  $\chi$  associated with the material damping is predominantly governed by the energy dissipation mechanisms in the lattice structures. The mechanism of energy dissipation is governed by the chain sliding motion in engineering polymers whereas in metals this is dictated by the dislocation movements within the crystal lattice. Consequently, material damping is very sensitive to ambient temperature variations. The present study therefore restricts to the estimation of loss coefficients based on the elastic modulus [114] for

materials selection in the preliminary design. These estimates are a reasonably good first approximation for most material combinations, except those prone to deformation by twinning (such as magnesium alloys, zinc alloys, quartz, etc.). A more detailed discussion on the damping mechanisms in different classes of engineering materials can be found elsewhere [115].

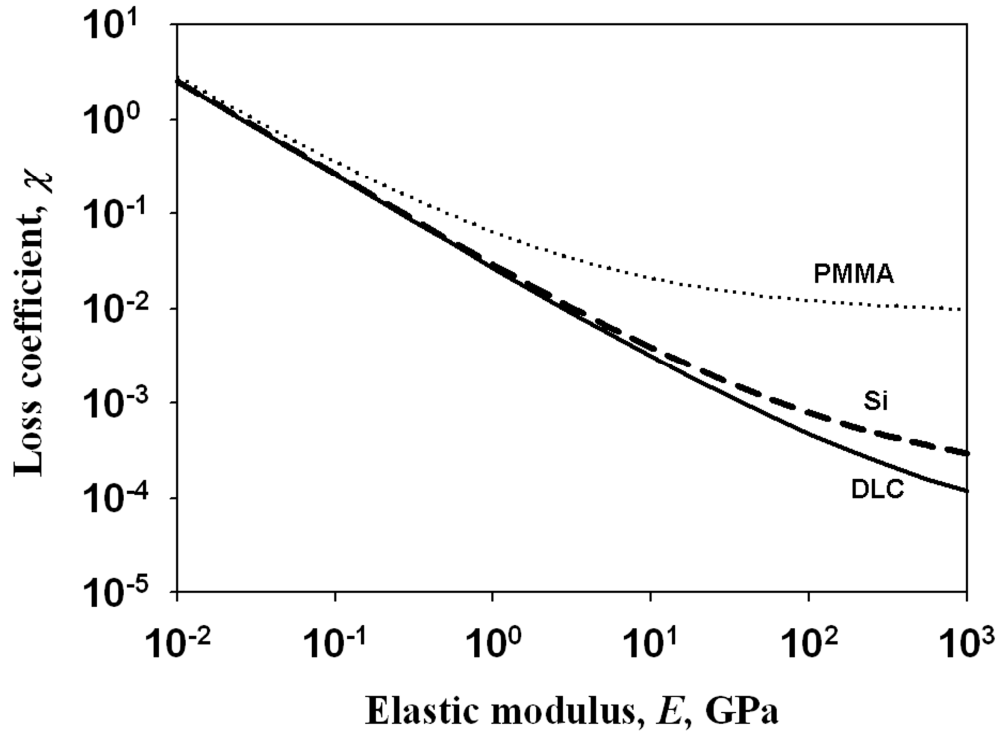


Figure 5.7 Effect of material combinations on the loss coefficient (hence the  $Q$ -factor) of BMPE actuators for a range of substrates considered.

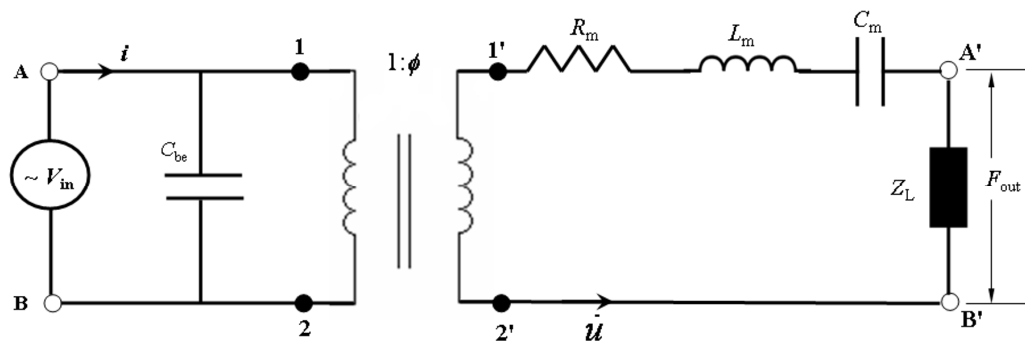
The loss coefficient based on elastic moduli of the bimetals is given by

$$\chi = \frac{0.1}{E_{\text{eq}}} \quad (5.11)$$

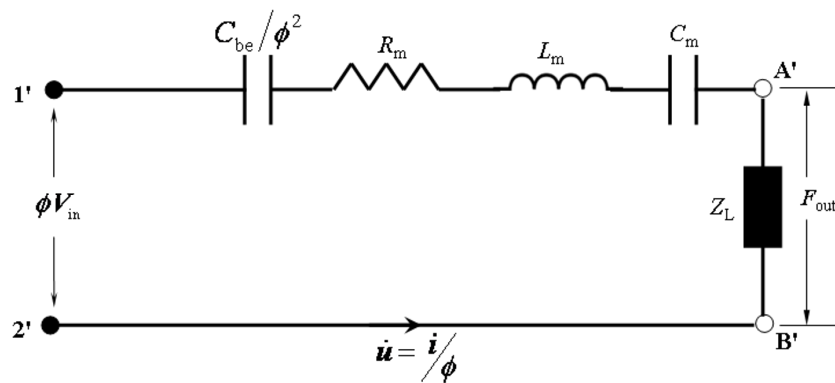
$$\text{where } E_{\text{eq}} = \frac{E_1 I_1 + E_2 I_2}{I} = \frac{4E_1}{\left(\frac{\xi_0 + 1}{\xi_0}\right)^2}$$

is the elastic modulus in GPa of an equivalent beam with rectangular cross section whose width is identical to that of the bi-layer ( $b$ ) with thickness equal to the total thickness,  $t$ .  $I_1$ ,  $I_2$  are the second moments of area of each of the bilayers about the

centroidal axis of the actuator structure and  $I$  is the second moment of area of the equivalent beam about its centroidal axis. Figure 5.7 shows a plot of the loss coefficient of the actuator as a function of the elastic modulus of the piezoelectric material for the range of substrates considered. BMPE actuator structures made of polymeric substrates have a lower  $Q$ -factor compared to those made of metallic or ceramics substrates. This is due to the viscous damping effects which are predominant in polymeric substrates compared to other classes of materials.



(a)



(b)

Figure 5.8(a) Ideal electromechanical transduction circuit for BMPE actuators; (b) Equivalent circuit of the ideal transduction obtained by applying Thevenin and Norton theorems.

A possibly more realistic material selection strategy for an optimal dynamic response can be evolved by establishing a suitable condition for electromechanical oscillation matching the required external impedance. Figure 5.8a shows an ideal electromechanical transduction circuit for BMPE actuator structures. An input electrical signal ( $V_{in}$ ) applied across the terminals AB is transformed into an output mechanical signal ( $F_{out}$ ) across terminals A'B' to drive the external load. The

dissipation due to the leakage charges in the electrical capacitor is ignored and the input circuit therefore includes only a capacitor corresponding to the blocked electrical capacitance,  $C_{be}$  parallel to the voltage source. The output circuit is the electrical analogue of a lumped mechanical model for a damped vibration system.  $L_m$ ,  $C_m$  and  $R_m$  correspond to the mass, the bending stiffness and the mechanical damping constant of the bimaterial actuator structure respectively.  $\phi$  is the transduction ratio of the circuit. The parameters relevant to the electromechanical transduction are given as

$$C_{be} = \frac{(1-k^2)\epsilon_r^d Lb}{t_1} = \left( \frac{(1-k^2)\epsilon_r^d (1+\xi_o)}{\xi_o} \right) \left( \frac{Lb}{t} \right) \quad (5.12)$$

$$\phi = k_b d_{31} = \left( \frac{16M_{blk}}{3L^2 \Theta_f} \right) d_{31} = \left( \frac{16E_1 b t^3 \xi_o^2}{9L^3 (\xi_o + 1)^2} \right) d_{31} \quad (5.13)$$

where  $k_b$  is the bending stiffness of the bimaterial cantilever evaluated based on the average energy of the bimaterial bounded by extreme compliant conditions (fixed-free and fixed-fixed). Using the Thevenin and Norton [116] theorems, an equivalent electrical circuit of the electromechanical transduction circuit is obtained as shown in Figure 5.8b. The total impedance of the equivalent circuit,  $Z_T$  is given by

$$Z_T = (R_m + Z_L') + j \left( \omega L_m - \frac{1}{\omega C_m} - \frac{\phi^2}{C_{be} \omega} + Z_L'' \right) \quad (5.14)$$

where  $\omega$  is the frequency of the input signal and  $Z_L'$  and  $Z_L''$  are the real and imaginary parts of the external impedance respectively. The output force required to overcome the external impedance is given by

$$F_{out} = \phi V_{in} \frac{|Z_L|}{|Z_T|} \quad (5.15)$$

Neglecting the mechanical damping effects in the electromechanical system, the transfer function,  $G$  for the electromechanical system is given as

$$G = \frac{F_{\text{out}}}{V_{\text{in}}} = \frac{\phi Z_L'' \omega C_m C_{\text{be}}}{C_{\text{be}} \left( \left( \frac{\omega}{\omega_n} \right)^2 - 1 \right) + Z_L'' \omega C_m C_{\text{be}} - \phi^2 C_m} \quad (5.16)$$

where  $\omega_n$  is the undamped natural frequency of the actuator structure. It is evident from equation (5.16) that the frequency of the input signal has to be tuned for a given material combination in order to match the required external impedance. The external impedance depends on the nature of the system utilising the work delivered by the actuator and this typically can be modelled as a spring-mass system under free or forced vibration. The physical significance of equation (5.16) is illustrated by considering a simple application such as a fibre optic switch, where the external impedance can be modelled as a spring mass system under free vibration. For instance, a large  $F_{\text{out}}$  at high  $\omega_n$  can be attained for a given input voltage  $V_{\text{in}}$  only if the signal frequency  $\omega$  is increased which in turn requires a large integrated power amplifier unit. A reduction in the requirements for an amplifier could be achieved if optimal materials were to be selected which would require evaluation of the limiting value of  $G$  at  $\omega = \omega_n$ . Therefore substituting  $\omega = \omega_n$  in equation (5.16) gives

$$G = \frac{F_{\text{out}}}{V_{\text{in}}} = \frac{Z_L''}{\left( \frac{Z_L''}{\phi} - \frac{\phi}{C_{\text{be}} \omega_n} \right)} \quad (5.17)$$

Electromechanical oscillation occurs as  $G \rightarrow \infty$ , i.e., the denominator of equation (5.17) should tend to zero in order to obtain a large  $F_{\text{out}}$  for an infinitesimally small  $V_{\text{in}}$ . Therefore equation (5.17) reduces to

$$Z_L'' = \frac{\phi^2}{C_{\text{be}} \omega_n} \quad (5.18)$$

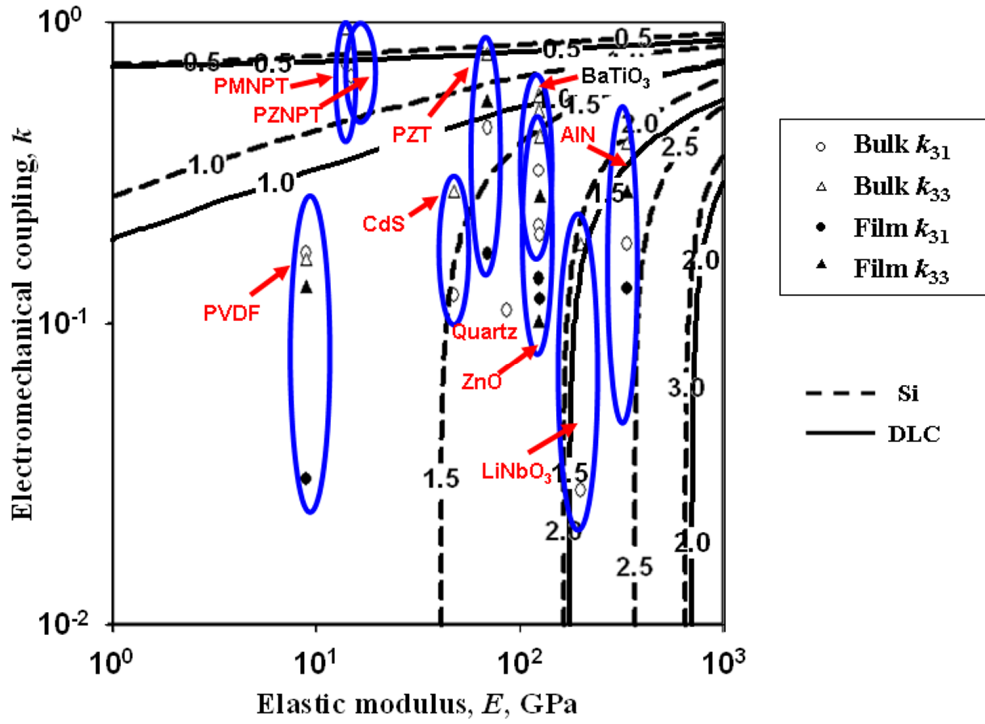


Figure 5.9 Contours of blocked capacitance index,  $[C_{bc}]_t$ , for different active materials on Si and DLC substrates.

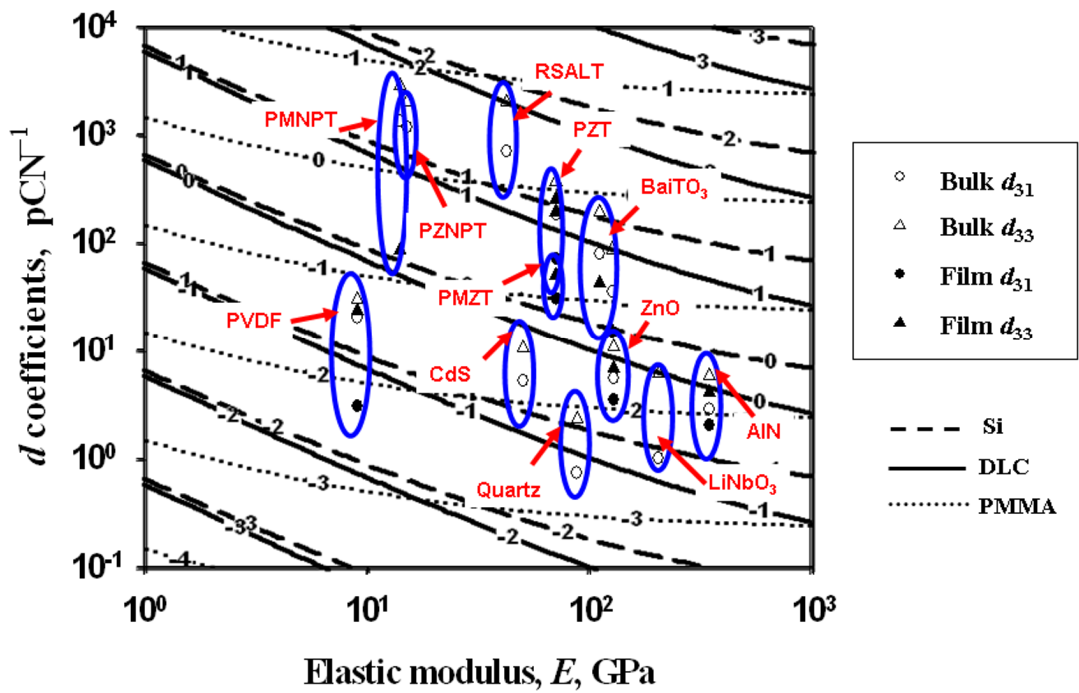


Figure 5.10 Contours of equal electromechanical transduction index,  $\log_{10}((\phi)_t)$  for different materials on the range of substrates considered.

Equation (5.18) is the relevant performance metric for selecting optimal material combinations to match the external impedance. Material combinations with a large  $\phi$  and a small  $C_{be}$  are desirable to overcome a large load impedance considering the variation in  $\omega_n$  bounded within an order of magnitude. Using equations (5.12) and (5.13) performance indices are obtained by normalising  $\phi$  and  $C_{be}$  with respect to the geometry and dielectric constant.

$$[C_{be}]_I = C_{be} \left( \frac{t}{Lb\epsilon_r^d} \right) = \left( \frac{(1-k^2)(1+\xi_o)}{\xi_o} \right) \quad (5.19)$$

$$\phi_I = \frac{\phi L^3}{bt^3} = \left( \frac{16E_1\xi_o^2}{9(\xi_o+1)^2} \right) d_{31} \quad (5.20)$$

where  $[C_{be}]_I$  and  $\phi_I$  are the capacitance index and transduction index respectively. Figures 5.9 and 5.10 show contours of equal  $[C_{be}]_I$  and  $\log_{10}(\phi_I)$  for different piezoelectric materials on the range of substrates considered. For performance metrics described as a function of many variables, relevant non-dimensional indices which dictate the materials selection can be formulated by applying the Buckingham  $\pi$  theorem.

#### 5.4 Materials selection process for BMPE actuators

Selection of suitable actuation for an application requires estimation of the performance limits achieved from different actuation methods. Piezoelectric actuation in general, is particularly promising for high force applications. It is evident from the contours shown in Figure 5.3, that BMPE actuators are more applicable for high force/work ( $M_{no} \sim 10 \text{ Nm}^{-1}\text{V}^{-1}$ ,  $W_{no} \sim 10^{-8} \text{ NV}^{-2}$ ) applications than for large displacement applications ( $\Theta_{no} \sim 10^{-8} \text{ mV}^{-1}$ ). Although the work per unit volume,  $W$  delivered by piezoelectric actuation [5, 6, 117] is  $\sim 10^5 \text{ Jm}^{-3}$ , the drop in the  $d$  co-efficient at microscales by an order of magnitude reduces  $W$  by two orders of magnitude ( $\sim 10^3 \text{ Jm}^{-3}$ ) which is evident from the results presented herein.



Also from Figure 5.4 it is clear that an actuation frequency of  $\sim 100$  kHz can be attained for an actuator length of  $100 \mu\text{m}$  with  $L/t = 30$ . Furthermore, the maximum efficiency of BMPE structures is  $\eta_{\text{em}} \sim 0.1$ , which is an order of magnitude less than the efficiency of uni-material active structures estimated previously [5]. This reflects the internal strain energy locked within the bimaterial that is not available for performing external work.

It is apparent from Figure 5.3 that ferroelectric piezoceramics dominate in performance compared to other active materials over the entire range of practical substrate materials. Quartz, traditionally used for macroactuators and sensors is not suitable for MEMS actuators due to its low piezoelectric constants [104, 118, 119]. Despite its very high piezoelectric constants, Rochelle salt ( $\text{NaKC}_4\text{H}_4\text{O}_6 \cdot 4\text{H}_2\text{O}$ ) is unlikely to be practical for microactuators due to its unstable nature and low transition temperature [105, 120, 121]. Material combinations such as PMNPT, PZNPT, PZT and  $\text{BaTiO}_3$  on Si, DLC or other high stiffness substrates are promising candidates for large force/work actuators with high transduction indices and reasonable efficiency ( $\eta_{\text{em}} \sim 0.1$ ). AlN on Si or DLC substrates is marginally superior to other material combinations for high frequency applications ( $> 100$  kHz) by virtue of the relatively high modulus of AlN. Although polymeric substrates exhibit a lower  $Q$ -factor than other classes of materials due to viscous damping effects, the actuation voltage required by the active materials when combined with polymers in all cases is less for a given electromechanical strain.

The present material selection strategy has certain limitations. Variations in thin film properties of materials due to processing routes, temperature and substrate effects have not been captured in the present analysis. The processing routes strongly influence the electromechanical properties of piezoceramics. For example, thin film PZT grown by sol-gel has a relatively high remnant polarisation ( $\sim 0.57 \text{Cm}^{-2}$ ) and a lower coercive field compared to films grown by a pulsed laser deposition process [93]. Furthermore, the electromechanical properties are very sensitive to stoichiometric variation of the piezoceramic constituents [108] which are not taken into account in the present work although the materials selection decision is not greatly influenced by this variation.

The operating temperature significantly affects the performance of the actuator structure. The electrical properties of the active materials are sensitive to temperature variation although the change in elastic modulus is generally not significant. The active materials selected for BMPE actuator structure should possess Curie temperatures greater than the operating ambient temperature. Hence an accurate estimate of the operating temperature is essential especially for applications involving drastic temperature fluctuations so that piezoelectric to paraelectric transformation at Curie temperature can be avoided. The influence of Curie temperature on the materials selection process can be better understood from the data presented in Table 5.1. The Curie temperatures for most of the active materials considered are above 200°C except for Rochelle salt (−18 °C and 24 °C) and KH<sub>2</sub>PO<sub>4</sub> (~ −150 °C) which make these materials suitable only for low temperature applications. LiNbO<sub>3</sub> and AlN can be considered for harsh environment applications where operating temperature exceeds ~ 1000 °C. A reasonably high Curie temperature of PZT (~ 370 °C) makes it a promising candidate for most applications.

The present materials selection strategy has not accounted for the variation in coercive field of the piezoelectric materials which further restricts actuator response. A desirable active material selected should possess a large coercive field while also having a high  $d$  coefficient. Although the  $d$  coefficients increase at the stoichiometric combinations corresponding to the morphotropic phase boundary (tetragonal-rhombohedral transition) for ferroelectric piezoceramics, this is accompanied by a drop in the coercive field [88, 122]. Furthermore, the applied electric field on the active materials reaches the maximum achievable value only if the coercive field,  $E_C^P$  is as high as the intrinsic coercive field,  $E_{IC}^P$ . However, this is feasible only at nano scales considering the inverse dependence of the coercive field on the film thickness [89, 94] which thereby reduces the work done per cycle. For polymeric films,  $E_C^P$  approaches  $E_{IC}^P$  only at Langmuir-Blodgett scales [89] which are beyond the capability of the present microfabrication processes and results in actuators with very low absolute values of work or force delivered. For ferroelectric piezoceramic films, values of  $E_C^P$  up to a few MVm<sup>−1</sup> can be achieved at the microscale given the present

capability of microfabrication. This is smaller than  $E_{IC}^P$  by an order of magnitude. Although the coercive field of piezoelectric polymers ( $E_C^P$  of PVDF  $\sim 55 \text{ MVm}^{-1}$ ) is greater than that of the ferroelectric piezoceramics by an order of magnitude, piezoelectric polymers require a large thickness to compensate for their low elastic modulus to deliver optimal performance. This is unlikely to be acceptable for many applications.

## 5.5 Summary

An approach to the optimal materials selection for BMPE actuators has been presented. Critical performance metrics are obtained applying the mechanics of bimaterial piezoelectric actuator structures developed in earlier work. Using performance maps optimal material combinations are identified for various functional requirements. Material combinations such as PMN-PT, PZN-PT, PZT and BaTiO<sub>3</sub> on Si or DLC are promising for large force/work actuators with high transduction indices and efficiency ( $\eta_{em} \sim 0.1$ ). AlN on Si or DLC substrates performs better than other alternative candidates for high frequency applications ( $\sim 600 \text{ kHz}$ ). A condition for electromechanical oscillation is obtained which serves as a useful basis for materials selection to achieve matching of the external impedance. Polymeric substrates offer higher material damping due to viscous effects compared to other classes of materials. The potential of active materials could be realised for MEMS applications if better control over the properties of thin films could be achieved during microfabrication. This can be accomplished only by enhancing our understanding of the process-property relationships from further research studies.

A generalised study identifying promising materials choices for various actuation schemes at microscales would set up an agenda for future development. The ranking of the candidates obtained based on the performance limits are useful data for the designers to select directly the potential candidates. The materials selection process for BMET and BMPE actuators has been discussed so far. Similar studies for other actuation schemes at microscales could be beneficial to the designers in realising high performance devices. Chapter 6 discuss the design guidelines and the relevant potential candidates for thermo-pneumatic and phase change microactuators.

# Chapter 6

## Materials selection for Thermally Actuated Pneumatic and Phase Change Microactuators

### 6.1 Introduction on thermo-pneumatic and phase change microactuators

The preference for commonly employed actuation schemes such as electrostatic [18], electrothermal [123], piezoelectric [86] and shape memory [124] actuation in MEMS can be attributed to their acceptable performance, ease of fabrication and long term reliability. The diverse application areas of MEMS e.g.: automotive, aerospace, consumer products and bio-medical present a wide range of functional requirements. Identifying the most suitable actuation scheme and their associated material choices for a given set of functional requirements and operating conditions is the key step in defining the system. Following the analyses on electrothermal and piezoelectric microactuators discussed in chapters 2-5, this chapter primarily focuses on the achievable performance limits of two related actuation schemes namely, thermo-pneumatic and phase change actuators.

Thermo-pneumatic actuation in MEMS is achieved by the deformation of a diaphragm (a structural member) due to volume expansion accompanied by a pressure rise in the fluid (usually air or a gaseous mixture) contained in a closed cavity by a small rise in temperature. Joule heating is generally preferred for increasing the temperature of the fluid due to its simplicity of implementation. The actuation cycle consists of a volume expansion due to the pressure increase caused by electrothermal heating followed by contraction due to a pressure drop aided by ambient cooling. Earlier studies relevant to thermo-pneumatic actuation include: demonstrations of thermo-pneumatic microvalves using silicon [125] and PDMS [126] diaphragms for flow control in bio-chips used for integrated blood examination and the experimental characterisation of the performance of polyimide diaphragm thermo-pneumatic actuators for micropumps with improved long term durability [127]. Unlike microelectrothermal actuators which are capable of delivering a large work per volume ( $\sim 10^4 - 10^5 \text{ Jm}^{-3}$ ), the performance of thermo-pneumatic actuators

is relatively low owing to the design constraint associated with the inefficient conversion of thermal energy to pneumatic energy. Although the frequencies achieved (30-100 Hz) by this actuation scheme are less than that of electrostatic, electrothermal and piezoelectric actuators they may still be adequate for certain microfluidic applications such as fluid handling and mixing in integrated bio-chips for DNA analysis [128].

Unlike thermo-pneumatic actuators which depend on the temperature amplitude to achieve a volume change, phase change actuators utilise the change in specific volume of a substance due to a change in the form of matter (e.g. solid to liquid, liquid to gas or solid to gas). Phase changes are usually accompanied by the absorption or release of thermomechanical energy (latent heat) depending on whether the reaction is endothermic or exothermic. This passive energy transfer accompanied by absorption/liberation of latent heat due to the phase change has been widely exploited in many energy storage/transfer applications [129]. Commercial applications based on phase change mechanisms include memory discs [130] and protective thermal outfits [131]. However, the use of such materials for microscale actuator structures has been limited owing to the difficulties involved in realising reliable devices. Most research on phase change actuators have focussed on working materials capable of undergoing phase transformations (sublimation/fusion/vaporisation) close to ambient conditions. Some earlier works relevant to phase change actuators at the microscale includes: development of thermally driven microactuators using methanol/Freon-11 as the working fluid [132] for flow control applications and characterisation of a phase change membrane actuator using Perfluorocarbon (3M<sup>TM</sup> PF-5060DL) [133]. Although most saturated hydrocarbons (alkanes) have desirable properties and attractive characteristics for phase change actuation, the suitability of long chain saturated hydrocarbons (paraffin waxes) is mainly attributed to their stability during phase changes at near ambient conditions (~ 40-70°C). Paraffin actuators have been considered for many macroscale applications such as endoscopic surgical attachments for tissue extraction [134, 135] and thermostats [136]. However, their application in MEMS devices has been limited [117, 137]. It should be noted that shape memory alloys/polymers which undergo phase changes due to a change in crystal symmetry are also phase

change actuators. However, the categorisation of actuation schemes based on phase change is generally restricted only to those mechanisms involving a change in the form of matter (solid, liquid and gas) within the MEMS literature and hence shape memory actuators do not fit into the present modelling framework.

The key objectives of this study are: to quantitatively assess the influence of engineering materials for diaphragm/substrate structures on the achievable pressure-volume tradeoffs in thermo-pneumatic actuators and to briefly review the materials issues constraining the performance limits of phase change actuators. Since materials selection studies are usually performed in the preliminary design stage, a generic axisymmetric model is considered to obtain the relevant performance metrics. A detailed design is essential for complicated diaphragm shapes and fixity conditions with compliant effects which would affect the performance. However, the accuracy of the performance limits estimated using the present models is sufficient to make the materials selection decision and for ranking the candidates. A comparison of the performance with other preferred MEMS actuation schemes is also discussed in this chapter.

This chapter is organised as follows. Section 6.2 discusses the mechanics of a thermally actuated pneumatic actuation system. Section 6.3 discusses the mechanical design of the diaphragm structure and its effect on the actuator performance. Section 6.4 focuses on the thermal performance of thermo-pneumatic actuators using lumped heat capacity models. Section 6.5 discusses promising materials and working fluids for thermo-pneumatic actuators. Section 6.6 assesses the performance of promising materials for phase change actuators. Section 6.7 discuss the achievable performance limits of thermo-pneumatic and phase change actuators acknowledging the limitations. Section 6.8 summarises the inferences drawn from this study.

## **6.2 Mechanics of a thermally actuated pneumatic actuator**

Figure 6.1 shows a schematic of a thermally actuated pneumatic actuator. The actuator consists of a flexible diaphragm sealing a rigid chamber subjected to internal pressure. The pressure increase in the cavity is achieved by raising the

temperature of the gas it contains using Joule heating, thereby causing out of plane deformation of the diaphragm. The constraints associated with the achievable maximum operating temperature, limits the volume expansion and the pressure in the cavity.

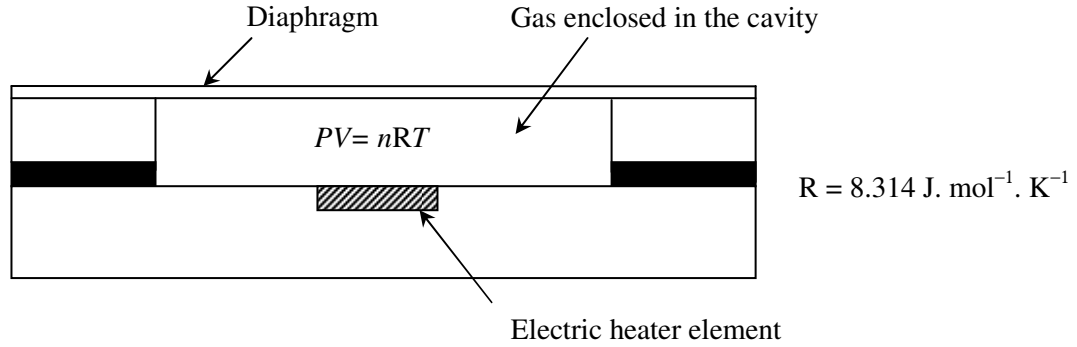


Figure 6.1 Schematic of a thermo-pneumatic actuator structure.

The maximum operating temperature is usually restricted by the thermal budget of the heater element for the allowable current densities ( $\sim 10^9 - 10^{10} \text{ Am}^{-2}$ ). Although engineering ceramics and a few alloys such as W and Pt can withstand high temperatures up to  $\sim 1000^\circ\text{C}$ , the voltage required to achieve such temperatures is very high owing to their high electrical resistivities. The preference for engineering alloys (such as Al, Cu and Au) as heater elements in most MEMS devices can be attributed to their low electrical resistivities and their compatibility to micromachining routes. The maximum permissible temperature for engineering alloys is constrained by the phase transformation temperature or the melting point of the material and this does not exceed a nominal value of  $\sim 673 \text{ K}$  for commonly used engineering alloys in MEMS devices. Assuming the ambient temperature to be  $\sim 293 \text{ K}$  and the process to be adiabatic, the practical maximum temperature ratio of the gas is:

$$(T_r)_{\max} = \frac{(T_2)_{\max}}{T_1} = \frac{673}{293} \approx 2 \quad (6.1)$$

where  $T_1$  and  $T_2$  correspond to the temperature of the initial and final states of the thermodynamic system. The maximum pressure ratio  $(P_r)_{\max} = (P_2)_{\max}/P_1$  cannot

exceed  $(T_r)_{\max}$  achievable from an isochoric process assuming the gas to be ideal which is a reasonably good approximation considering the small deviation in compressibility at sub-critical pressure ratios [138]. Therefore the governing equation of state is given as

$$\frac{P_r V_r}{T_r} = 1 \quad (6.2)$$

where  $P_r = P_2/P_1$ ,  $V_r = V_2/V_1$  and  $T_r = T_2/T_1$  are the pressure, volume and temperature ratios respectively. The initial state usually corresponds to the ambient condition, i.e.  $P_1 = 1 \text{ atm}$ . and  $T_1 \sim 293 \text{ K}$ .

The pressure and the volume maintained within the cavity during the temperature rise depend on the compliance of the diaphragm which is dictated by the elastic properties of the material for a given geometry and boundary conditions. Hence the synergy between the material, geometry, boundary conditions and temperature ratio determine the performance of the actuator.

### 6.3 Mechanical design of the diaphragm structure

The diaphragm structure is idealised as an axi-symmetric plate with a pre-tension due to process-induced residual stresses. Thin film pre-stress in a few microfabricatable materials such as Si, DLC and PMMA can be controlled only to about  $\sim 5 \text{ MPa}$ . Hence the assumption of plate structure for the actuator is ideal. Nevertheless, this assumption allows estimating the maximum achievable performance which serves as the bounding limits for the actuator design. The design guidelines for the aspect ratio of the diaphragm structures made of arbitrary materials and the permissible operating temperature ranges need to be established to achieve the best performance. The maximum attainable thermo-pneumatic pressure ( $< 2 \text{ atm}$ .) ensures the applicability of linear theory in the constitutive modelling of plate/membrane structures since at such low pressures the allowable deflection can be assumed to be less than the thickness of the diaphragm, for a given diaphragm stiffness. This assumption is clearly violated for extremely compliant diaphragms



with very large aspect ratios due to geometric non-linear effects. However in the preliminary design stage, the assumption of linearity allows exploration of most of the available design space with acceptable accuracy. In this spirit, the effect of a central boss on the performance of the actuator is also considered.

### 6.3.1 Diaphragm structure as an axi-symmetric plate

The present analysis evaluates the achievable performance limits of a thermo-pneumatic actuation system for the cases of a diaphragm designed as either a plate or a membrane. Figure 6.2 shows a schematic of a thermo-pneumatic actuation system. A rigidly clamped circular diaphragm of external radius  $R$ , is subjected to a differential pressure,  $\Delta P$ . The thickness of the diaphragm and the height of the cavity are denoted by  $t_d$  and  $w_c$  respectively. Considering the diaphragm as an ideal axi-symmetric plate structure, the out-of-plane deflection in the  $z$  direction,  $w_p(r)$  as function of radial location  $r$  due to uniform internal pressure can be obtained using the linear plate theory [139] which gives:

$$w_p(r) = \frac{\Delta P}{64D} (R^2 - r^2)^2 \quad (6.3)$$

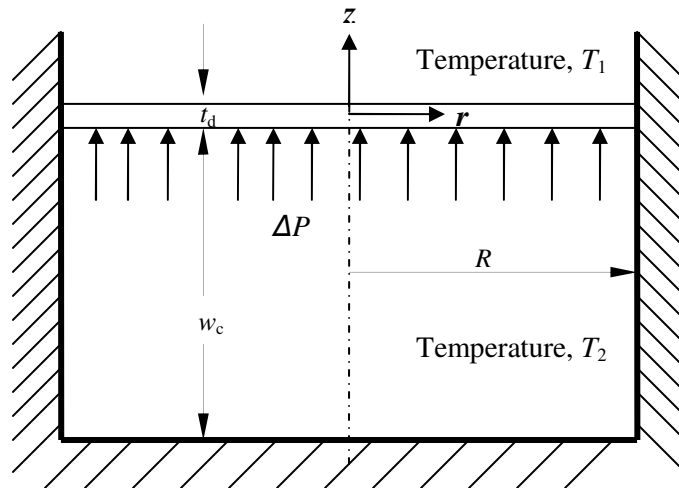


Figure 6.2 Schematic of a circular axi-symmetric clamped diaphragm actuated thermo-pneumatically.

where  $D = Et_d^3/12(1-\nu^2)$  is the flexural rigidity of an isotropic plate with elastic modulus,  $E$  and Poisson ratio,  $\nu$ . If the initial volume,  $V_1 = \pi R^2 w_c$  then the change in the average volume ( $\Delta V = V_2 - V_1$ ) due to a small incremental change in the internal pressure ( $\Delta P = P_2 - P_1$ ) is given by:

$$\Delta V = \int_{r=0}^{r=R} 2\pi r w_p(r) dr = \frac{\Delta P \pi R^6}{192D} = \frac{\Delta P}{k_s^f} \quad (6.4)$$

where  $k_s^f = 192D/\pi R^6$  is the volumetric stiffness of the fluid cavity which depends principally on the structural compliance of the diaphragm. If the expansion process is assumed to be adiabatic, then by invoking the principle of energy conservation, the change in the internal energy of the system will be equal to the potential energy stored in the flexible diaphragm.

$$\frac{k_s^f (\Delta V)^2}{2} = m C_v (T_2 - T_1) = \frac{P_2 V_2 - P_1 V_1}{\gamma - 1} \quad (6.5)$$

Where  $m$  is the mass of the fluid,  $C_v$  is the specific heat capacity of the fluid at constant volume and  $\gamma$  is the adiabatic index. Equation (6.5) can be expressed in dimensionless form as:

$$M_p (V_r - 1)^2 = \frac{P_r V_r - 1}{\gamma - 1} \quad (6.6)$$

where  $M_p = 128 E' V' / \beta^4$ , the material index of the plate which determines the achievable pressure and volumetric expansion,  $E' = E/(1-\nu^2)P_1$  is the dimensionless modulus defined as the ratio of plate modulus to the initial pressure,  $V' = V_1/V_d = w_c/t_d$  is the ratio of the cavity volume to the diaphragm volume and  $\beta = 2R/t_d$  is the aspect ratio of the diaphragm structure. Eliminating  $P_r$  between equations (6.6) and (6.2) gives a relation between  $V_r$  as a function of  $T_r$  and  $M_p$ .

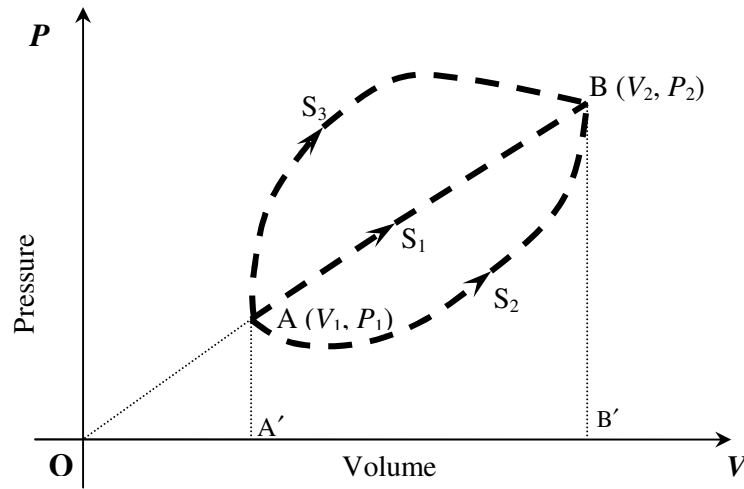


Figure 6.3 Operating characteristics of thermo-pneumatic actuator.

$$V_r = \sqrt{\frac{(T_r - 1)}{M_p(\gamma - 1)}} + 1 \quad (6.7)$$

Equations (6.7) and (6.2) together provide the pressure and volumetric expansion associated with a material index for a given temperature ratio,  $T_r$ .

The work delivered by the actuator can be obtained from the bounding operating limits of pressure and volumetric expansion. Figure 6.3 shows the operating limits of a thermo-pneumatic actuator in the  $P$ - $V$  domain. The expansion is an irreversible and non-equilibrium thermodynamic process due to the rapid change in temperature. Hence the work done by the actuator varies with the path between the initial and final states for a given change in the internal energy. Although the work done by an irreversible process is a thermodynamically indeterminate quantity, the present study considers an estimate of the useful work done by the actuator against a linear elastic spring through the shortest direct route connecting the initial and final states due to a small temperature rise. The work done by the actuator is signified by a parameter termed the work ratio,  $W_r$  corresponding to the path  $S_1$  and is defined as

$$W_r = \frac{\oint_{S_1} P dV}{P_1 V_1} = \frac{(P_r V_r - 1) - (P_r - V_r)}{2} \quad (6.8)$$

It is evident from equation (6.8) that in order to obtain maximum useful work, the condition to be satisfied is given as:

$$P_r = V_r = \sqrt{T_r} \quad (6.9)$$

This suggests that the vector components corresponding to the initial and final states should form geometrically similar triangles in order to deliver maximum work i.e. triangles OAA' and OBB' should be geometrically similar. Substituting equation (6.9) in (6.8) gives the maximum work,  $(W_r)_m$  achievable from the system along the path  $S_1$ .

$$(W_r)_m = \frac{(V_r^2 - 1)}{2} = \frac{(P_r^2 - 1)}{2} = \frac{(T_r - 1)}{2} \quad (6.10)$$

The optimal material index,  $M_{po}$ , corresponding to the maximum work, can be obtained by substituting equation (6.9) in (6.6)

$$M_{po} = \frac{(\sqrt{T_r} + 1)}{(\sqrt{T_r} - 1)(\gamma - 1)} \quad (6.11)$$

Figure 6.4 shows the plot of  $M_{po}$  as a function of  $T_r$  obtained using equation (6.11). The curve tends to become asymptotic ( $(M_p)_o \rightarrow \infty$ ) when  $T_r = 1$  thereby indicating  $V_r = 1$  when the work done is zero. Equation (6.11) also reveals that the optimal material index varies with the temperature ratio. Since the temperature varies sharply within the operating range in a cycle, it is desirable to operate in a range at which  $M_p$  is least sensitive to  $T_r$  in order to achieve the best performance. This is can be accomplished by the deformation of an extremely compliant diaphragm structure at high operating temperatures ( $T_r \geq 1.6$ ) which is the preferred design configuration

for high performance MEMS devices. However, there is a practical difficulty in realising such configurations owing to the low thermal conductivity of commonly employed fluids within the cavity. A heater temperature between ~150 - 200 °C is at least required even to achieve a temperature of ~ 50-70 °C within the air cavity in the steady state provided the heater volume is 20% of the cavity volume.

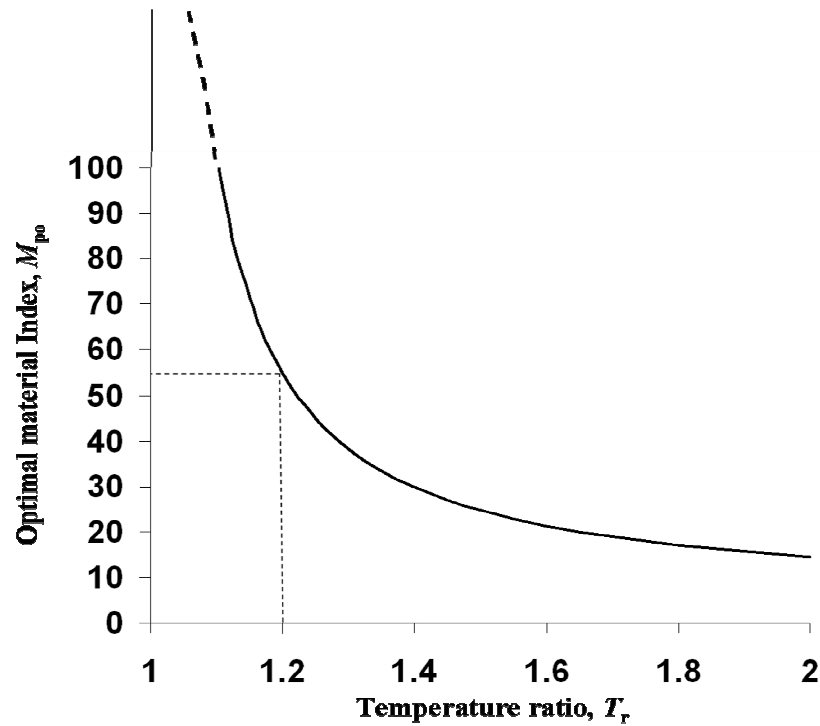


Figure 6.4 A Plot of optimal material index,  $M_{po}$  as a function of  $T_r$ .

The present study considers the performance evaluated within the small displacement regime at the limit of attainable cavity temperatures i.e. for  $T_r \leq 1.2$  for materials selection process. Hence the design guidelines provided in this analysis can be applied directly for the structures which deliver small displacements in order to meet the required functional requirements. The performance estimated using the present models is reasonably accurate as long as the following condition is met.

$$V_r \leq 1 + \frac{8}{15V'} \quad (6.12)$$

However, for actuators which deliver a large deflection (greater than the diaphragm thickness), the effect of geometric non-linearity and the membrane effects require

further consideration in the performance evaluation which does not have a significant bearing on the materials selection process.

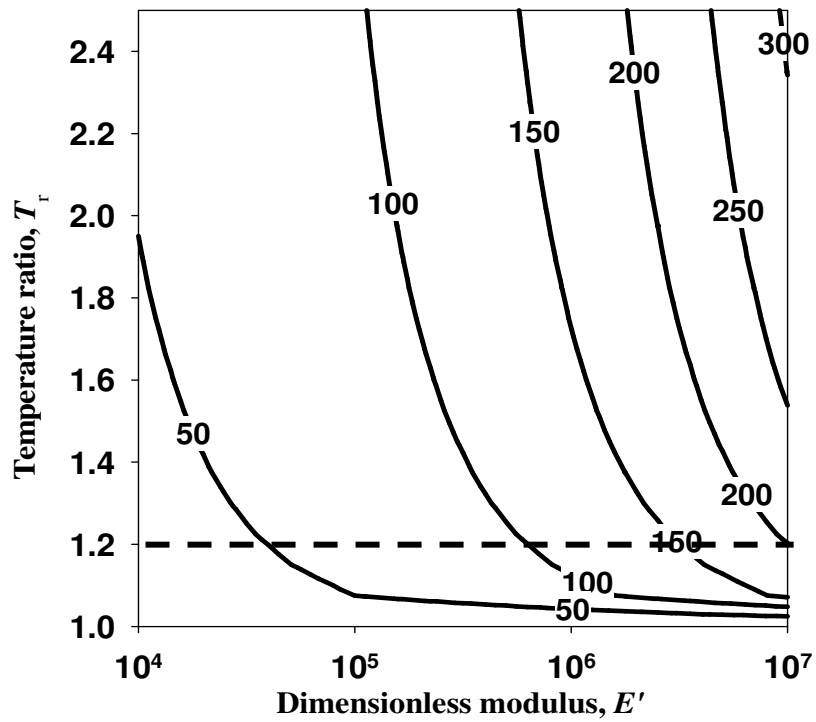
A more appropriate parameter to characterise the irreversibility of a system is the change in entropy. The change in specific entropy of a system for an ideal gas is given as:

$$\left. \begin{aligned} \int_1^2 ds &\geq \int_1^2 \frac{c_v dT}{T} + \int_1^2 \frac{PdV}{T} \\ s_2 - s_1 &\geq \frac{(c_p + c_v) \ln(T_r)}{2} \end{aligned} \right\} \quad (6.13)$$

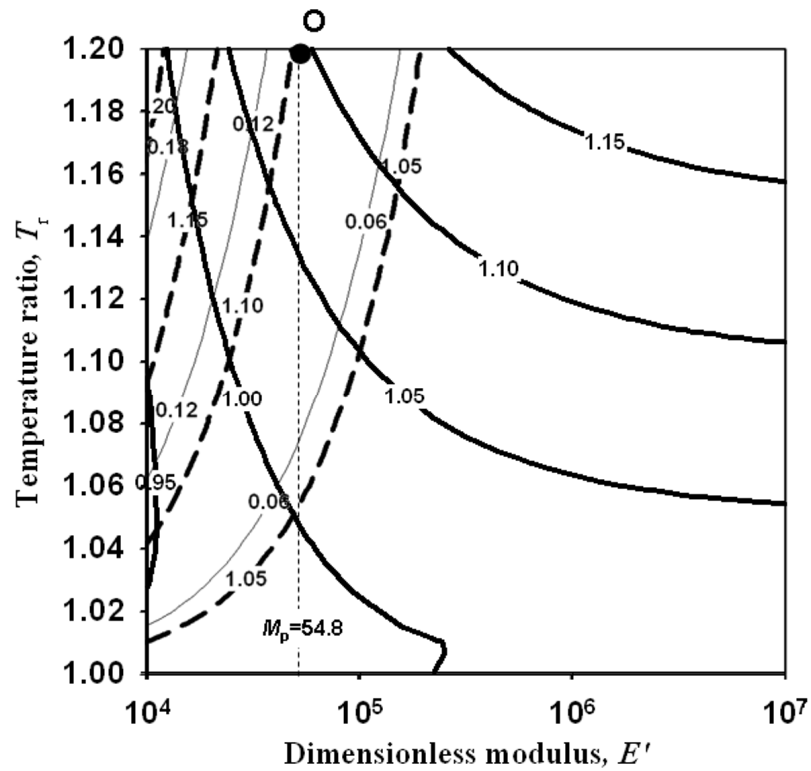
It is evident from equation (6.13) that the change in specific entropy of the system,  $(s_2 - s_1)$  is very low for small values of  $T_r$ . Although the variation of  $M_{po}$  is very small at large values of  $T_r$ , the effect of irreversibility is very high thereby reducing the low overall efficiency. A trade off between the maximum work and the degree of irreversibility can be obtained using equations (6.11) and (6.13).

Figure 6.5a is a plot of equal aspect ratios for optimal performance. For the values of  $T_r \leq 1.2$  the optimal aspect ratios for polymers (40-60) are smaller than those for engineering alloys/ceramics (100-200) by a factor of  $\sim 3$ . For polymeric diaphragms, the allowable optimal thickness is about  $\sim 2-3 \mu\text{m}$  for  $R = 50 \mu\text{m}$  while for engineering alloys / ceramics the thickness has to be reduced to less than  $1 \mu\text{m}$ . Current microfabrication technology can easily create thin polymeric films, a few microns thick by spin coating [37].

Although established processing routes for growing thin films of engineering alloys/ceramics with thicknesses between  $\sim 0.5 - 1 \mu\text{m}$  are available for some promising candidates (e.g. Si, Al, Cu, Ni, DLC), the wafer handling associated with the stress-free release of thin film structures from the substrate could be a critical issue. Furthermore, any flexibility in the design enabled by increasing the diaphragm thickness has to be compensated by a corresponding increase in the radius,  $R$  which



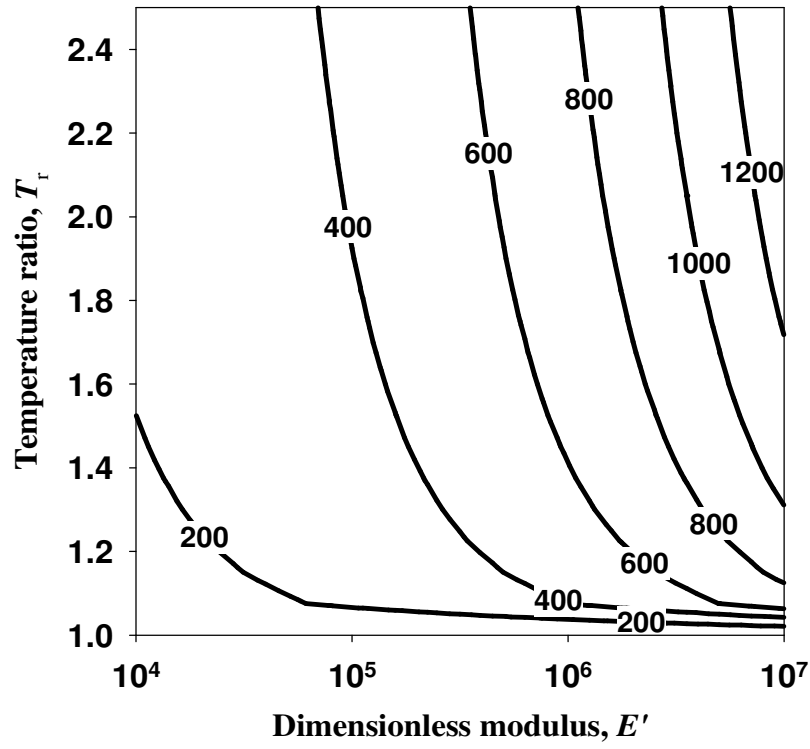
(a)



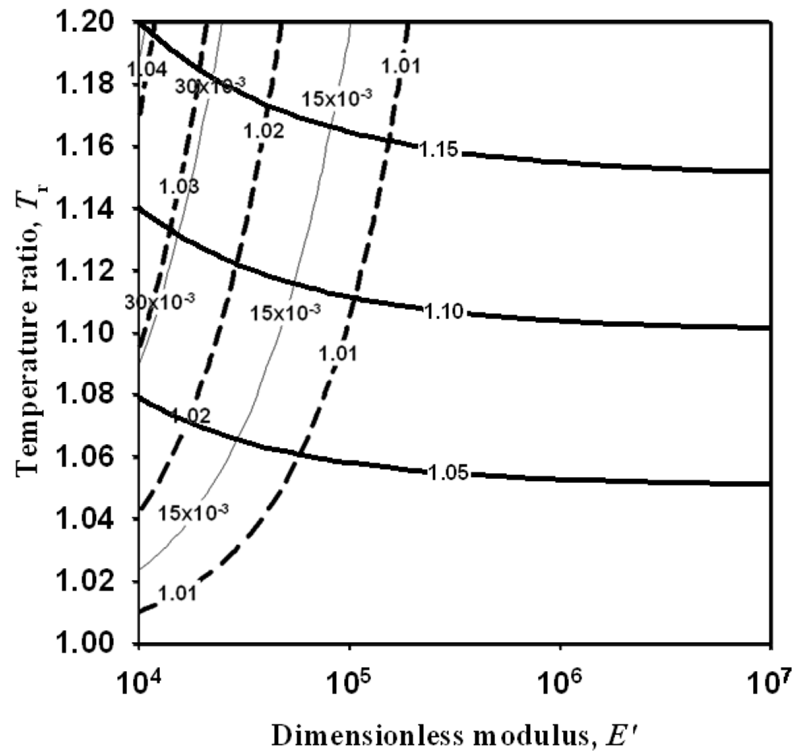
— Pressure ratio      - - - Volume ratio      — Work ratio

(b)

Figure 6.5 (a) Contours of optimal aspect ratios of an axi-symmetric plate for a range of dimensionless moduli within the temperature range considered; (b) Contours of  $P_r$ ,  $V_r$  and  $W_r$  as a function of  $E'$  and  $T_r$  for an axi-symmetric plate structure ( $V' = 50$ ;  $\beta = 50$ ).



(a)



— Pressure ratio      - - - Volume ratio      ..... Work ratio

(b)

Figure 6.6 (a) Contours of optimal aspect ratios of an axi-symmetric membrane for a range of dimensionless moduli within the temperature range considered; (b) Contours of  $P_r$ ,  $V_r$  and  $W_r$  as a function of  $E'$  and  $T_r$  for an axi-symmetric membrane structure ( $V' = 50$ ;  $\beta = 50$ ;  $k_m = 100$ ).



in turn results in more power consumption to maintain the cavity at a given temperature.

Figure 6.5b shows contours of dimensionless parameters  $P_r$ ,  $V_r$  and  $W_r$  plotted as a function of  $E'$  and  $T_r$  for  $V' = 50$  and  $\beta = 50$  obtained using equations (6.7) and (6.2). Point O corresponds to the optimal performance for this configuration. Although the achievable  $V_r$  for low values of the dimensionless modulus is high, the over-estimation of the out-of-plane deflection by linear theory results in very low pressure ratios ( $P_r < 1$ ) which are inadmissible. However, the applicability of this particular result for  $P_r \geq 1$  suggest that the optimal performance for the configuration considered is obtained by selecting materials such that  $E' \sim 10^{4.7}$ .

### 6.3.2 Effect of pre-tension on the actuator performance

The diaphragm analysed previously assumed the structure as an axi-symmetric plate without any pre-stress. Any compressive pre-stress in a high aspect ratio membrane introduces the possibility of buckling thereby rendering the actuator ineffective. The principal effect of pre-tension is to alter the pressure/volume trade-offs. Since pre-stress levels for different thin film materials and processes can vary widely, the present analysis considers the actuator performance at extreme pre-tension levels causing the diaphragm to act as a membrane structure. The out-of-plane deflection of a pure axi-symmetric membrane in the  $z$  direction,  $w_m(r)$  as function of radial location  $r$  due to uniform internal pressure is given as [139]

$$w_m(r) = \left( \frac{3 \Delta P R^2}{E t_d^3 k_m^2} \right) (1 - \nu^2) (R^2 - r^2) \quad (6.14)$$

where  $k_m = \sqrt{N_o R^2 / D}$  is a non-dimensional pre-tension parameter associated with the initial radial tensile load per unit length,  $N_o$ . For membrane structures  $k_m$  is usually greater than 20 [139]. Following the same thermodynamic formulations presented in the previous section, the material index parameter for an axi-symmetric membrane,  $M_m$  is obtained.

$$M_m = \frac{16E'V'k_m^2}{3\beta^4} \quad (6.15)$$

Figure 6.6a is a plot of the optimal aspect ratios corresponding to maximum performance for pre-tension parameter,  $k_m = 100$ . This corresponds to an in-plane radial stress of  $\sim 570$  MPa in a Si diaphragm of  $1 \mu\text{m}$  thick and  $500 \mu\text{m}$  radius. It is obvious from these plots that the optimal aspect ratios for membranes at this stress level are greater than those of plates by a factor of  $\sim 4$ . Hence the thickness of the diaphragm has to be reduced down to a few tens to hundreds of nanometers for most classes of materials if realised as pre-tensioned membranes. Growing stand-alone thin films with thicknesses varying between a few tens to hundreds of nanometers under severe stress would be challenging with existing MEMS fabrication routes. Figure 6.6b shows the contours of dimensionless parameters  $P_r$ ,  $V_r$  and  $W_r$  plotted as a function of  $E'$  and  $T_r$  for  $V' = 50$ ,  $\beta = 50$  and  $k_m = 100$ . The contours are obtained using equations (6.7) and (6.2) by replacing  $M_p$  by  $M_m$ . It is clearly evident that tensile membrane stresses are detrimental to the actuator performance. The achievable work is an order of magnitude less than that of the stress-free plate structures. This is attributed to the high fraction of the thermo-pneumatic energy developed which becomes trapped in the form of internal strain energy thereby resulting in a significant reduction in the out-of-plane deflection.

### 6.3.3 Effect of boss size on the actuator performance

The effect of boss size on the response of the diaphragm is also considered in the present study. The use of a central boss is often required if the actuator is required to act as a piston or to achieve sealing in flow control.

Figure 6.7 shows a schematic of a clamped diaphragm structure with a boss subjected to a differential pressure. The inner and outer radii of the boss are  $R_o$  and  $R_i$  respectively. Using linear theory the out-of-plane deflection for the pure plate member in a bossed configuration under internal pressure is given as [140]

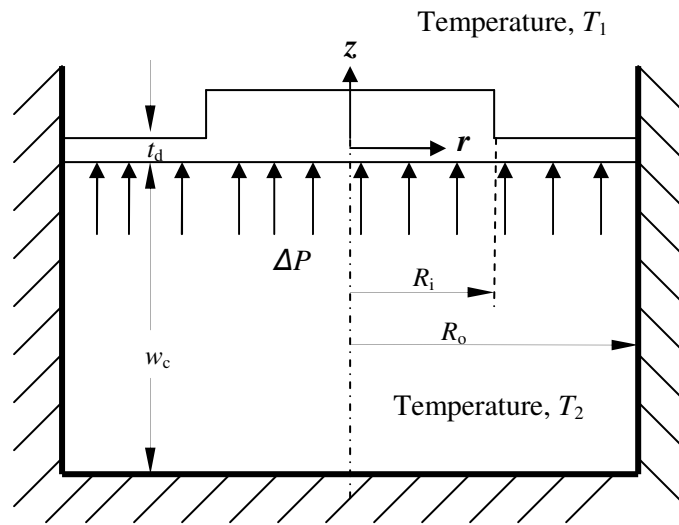


Figure 6.7 Schematic of a circular axi-symmetric clamped diaphragm with boss actuated thermo-pneumatically.

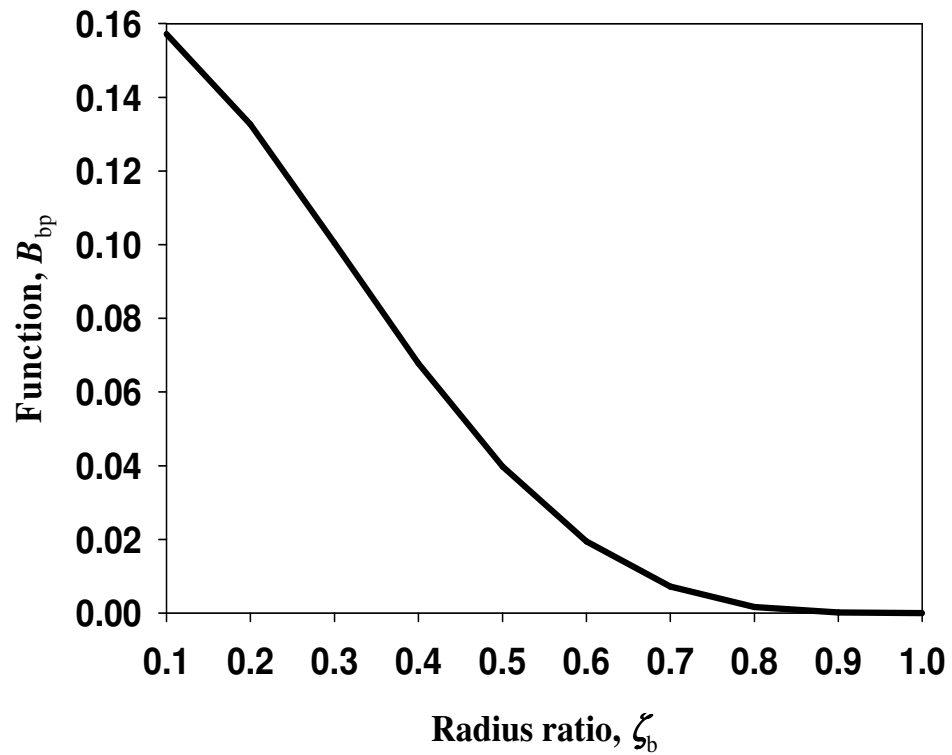
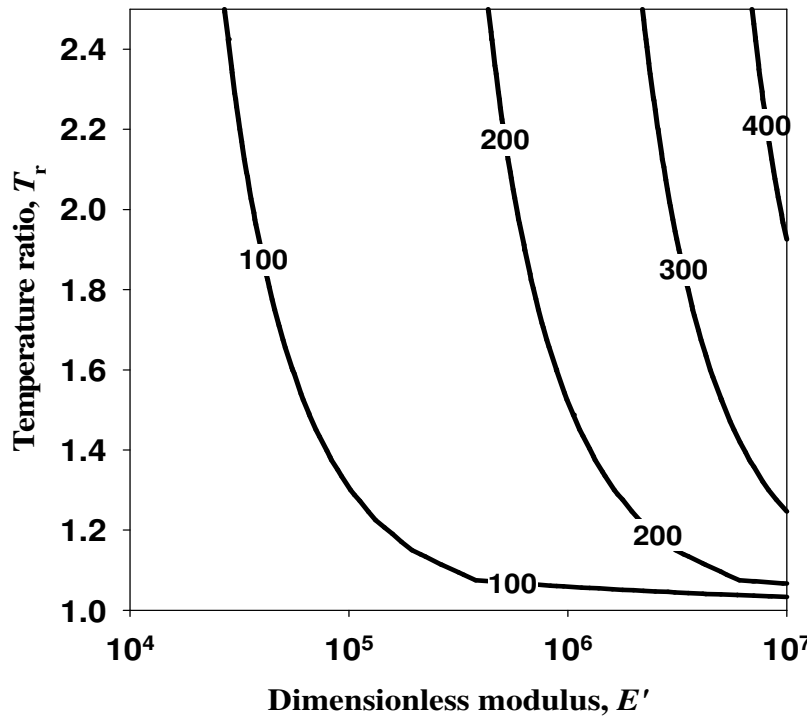
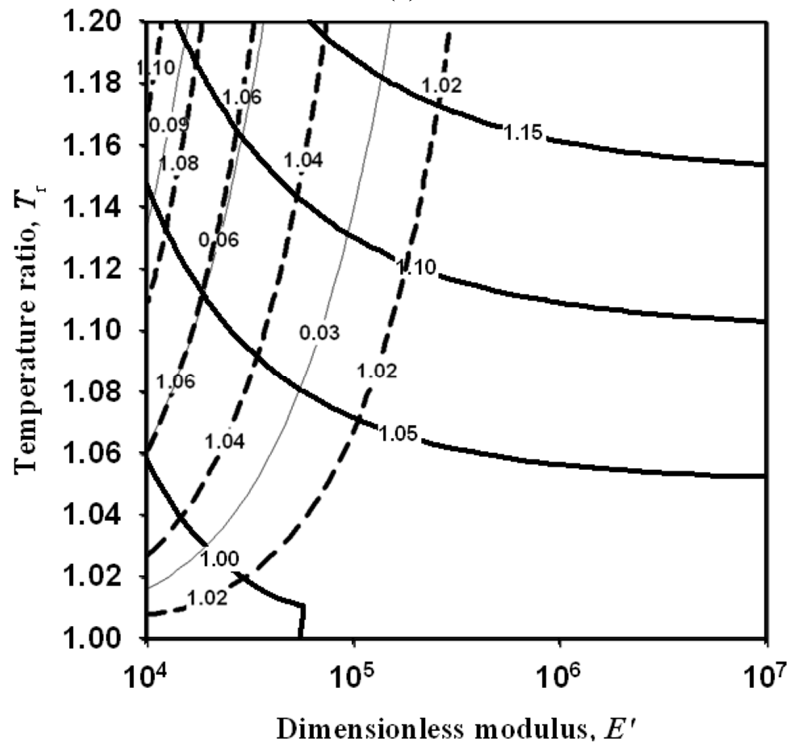


Figure 6.8 Variation in  $B_{bp}$  with respect to the ratio of boss radii,  $\zeta_b$ .



(a)



— Pressure ratio      - - - Volume ratio      ..... Work ratio

(b)

Figure 6.9 (a) Contours of optimal aspect ratios of axi-symmetric plate with boss for a range of dimensionless moduli within the temperature range considered ( $\zeta_b = 0.5$ ); (b) Contours of  $P_r$ ,  $V_r$  and  $T_r$  as function of  $E'$  and  $T_r$  for axi-symmetric plate with a boss feature ( $V' = 50$ ;  $\beta_o = 50$ ;  $\zeta_b = 0.5$ ).

$$w_{bp} = \left( \frac{3 \Delta P R_o^4}{16 E t_d^3} \right) \left( (1 - \zeta^2)(1 - \zeta^2 + 2\zeta_b^2) + 4\zeta_b^2 \log \zeta \right) \quad (6.16)$$

where  $\zeta = r/R_o$  is the ratio of any radial location to the external radius and the boss ratio,  $\zeta_b$  is the value of  $\zeta$  at  $r = R_i$ . Following the thermodynamic formulations presented earlier, the material index for the bossed diaphragm in the pure plate configuration,  $M_{bp}$  is obtained:

$$M_{bp} = \frac{64 E' V'}{3 \beta_o^4 (1 - \nu^2) B_{bp}} \quad (6.17)$$

where  $V' = w_c/t_d$  for the bossed plate structure,  $\beta_o = 2R_o/t_d$  is the aspect ratio and

$$B_{bp} = \frac{1}{6} - \zeta_b^2 + \frac{\zeta_b^2}{2} (1 - 4 \log \zeta_b) + \frac{\zeta_b^6}{3}$$

is a function of boss ratio,  $\zeta_b$  for  $0 < \zeta_b < 1$ .

Figure 6.8 shows the variation in function  $B_{bp}$  with respect to the parameter  $\zeta_b$  which follows the trend of normalised centre deflection estimated by linear theory [140]. It is evident from the plot that the variation in  $B_{bp}$  is about an order of magnitude over the range of  $\zeta_b$ . Figure 6.9a shows the contours of the optimal aspect ratios for bossed plates for a range of  $T_r$  and  $E'$ . The influence of the boss on the aspect ratio of the structure is not significant. Figure 6.9b shows contours of  $P_r$ ,  $V_r$  and  $W_r$  plotted as a function of  $E'$  and  $T_r$  for  $V' = 100$ ,  $\beta_o = 100$  and  $\zeta_b = 0.5$ . The contours are obtained using equation (6.7) and (6.2) by replacing  $M_p$  by  $M_{bp}$ . It is evident from the plot that  $W_r$  achievable with a boss ( $\zeta_b = 0.5$ ) is only 50% of that achievable without a boss. The effect of pre-stress is not considered here but can be calculated as discussed previously [141].

#### 6.4 Thermal performance of thermo-pneumatic actuator

The actuation mechanisms of a thermo-pneumatically actuated diaphragm structure are analysed assuming the process to be a temperature dependent quasi-static. A lumped capacity thermal model is therefore used to evaluate the transient thermal

response of the actuator structure in the preliminary design stage. Since the fluid cavity is very thin compared to the bulk substrate, the heat transfer within the layer can also be assumed to be due to conduction. This assumption provides a reasonably good estimate useful in the preliminary design stage for the selection of materials (for diaphragm and substrate) and for the choice of fluids in order to realise high performance MEMS actuators. This assumption in the thermal modelling is manifested by the predominance of conductive heat transfer at microscales due to the small Biot numbers inherent to MEMS structures as discussed in Chapter 3. The influence of convective heat transfer effects on the temperature of the fluid within the cavity and the effect of external impedance on the actuator response require consideration in the detailed actuator design.

Figures 6.10a and 6.10b show an axi-symmetric, one-dimensional heat transfer model in a cylindrical structure and the energy transfer across the control volume considered respectively. A closed form solution for the thermal resistance of a cylinder with an annular cross section is used to evaluate the equivalent thermal resistance. The thickness of the substrate is denoted by  $t_s$ . The equivalent thermal properties (conductivity,  $\kappa_{eq}$ , specific heat,  $(\rho C)_{eq}$  and thermal diffusivity,  $\alpha_{eq}^d$ ) of the actuator structure are obtained as

$$\kappa_{eq} = \frac{\kappa_d t_d + \kappa_f w_c + \kappa_s t_s}{t_d + w_c + t_s} \quad (6.18)$$

$$(\rho C)_{eq} = \frac{(\rho C)_d t_d + (\rho C)_f w_c + (\rho C)_s t_s}{t_d + w_c + t_s} \quad (6.19)$$

$$\alpha_{eq}^d = \frac{\kappa_{eq}}{(\rho C)_{eq}} \quad (6.20)$$

A macroscale heat transfer co-efficient of  $h = 10 \text{ Wm}^{-2}\text{K}^{-1}$  is assumed in this study between the peripheral layer and the ambient surroundings. The time taken to cool,  $t_c$  from an initial average temperature,  $T_{av}^i$  at the instant  $t' = 0$  to the final average temperature,  $T_{av}^f$  is obtained by solving the transient heat transfer model.

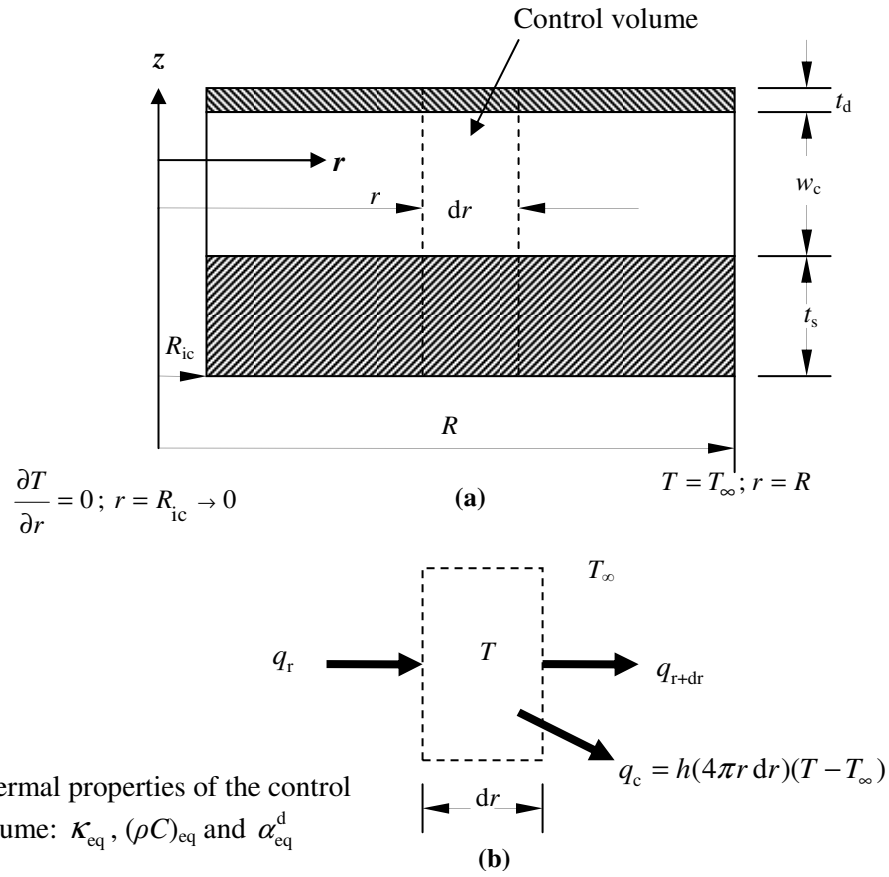


Figure 6.10 (a) one dimensional heat transfer model for transient thermal response; (b) Energy transfer across the control volume considered.

$$T^{i+1} = \frac{T^i + T_\infty F_o}{F_o + 1} \quad (6.21)$$

$$F_o = \frac{2\alpha_{eq}^d (\Delta t') \left( \frac{1}{\ln\left(\frac{R}{R_{ic}}\right)} + \frac{h(R^2 - R_{ic}^2)}{k_{eq}(t_d + w_c + t_s)} \right)}{R^2 - R_{ic}^2} \quad (6.22)$$

where  $F_o$  is the Fourier number,  $T^i$  and  $T^{i+1}$  are the average temperatures at the instant  $t'$  and  $t' + \Delta t'$  respectively. The actuation frequency can be estimated as:

$$f = \frac{1}{t'_c} \quad (6.23)$$

Frequencies estimated by lumped capacity thermal models correspond to the characteristic length scale equal to the diffusion length for the temperature amplitude considered.

## 6.5 Candidate materials for thermo-pneumatic actuators

Identifying promising materials for various functional requirements is critical for the design of microsystems. It is evident from the plots shown in Figures 6.5, 6.6 and 6.9 that engineering polymers are promising diaphragm materials for large displacements although the maximum achievable pressure rise ( $\sim 0.2$  atm.) delivers a small force. The thermo-pneumatic energy generated for the maximum achievable pressure ratio  $(P_r)_{\max} = T_r$  makes polymeric diaphragms attractive for delivering large work although the work per unit volume delivered is lower than that achieved by direct electro-thermal actuation by two orders of magnitude. Table 6.1 shows the properties of materials and gases considered for the design of thermo-pneumatic actuators in the present study. The properties of gases are representative values at ambient conditions (1 atm., 293 K). Table 6.2 shows the achievable actuation frequencies for different substrate materials for a polymeric diaphragm actuator structure at different scales. It is found that the choice of cavity gas (air, He and Ar) does not greatly influence the actuation frequencies. However, the substrate materials do affect the rate at which heat is lost according to their thermal diffusivity. The achievable frequencies for a temperature difference of  $\sim 150$  °C vary between a few tens to a few thousand Hertz as the radius;  $R$  varies from 50  $\mu\text{m}$  to 250  $\mu\text{m}$ . Frequencies in this range are suitable for applications such as micropumps used for particle counting and fluid mixing in bio-chips [142].

S.No	Materials/gases	Thermal conductivity, $\kappa$ , $\text{Wm}^{-1}\text{K}^{-1}$	Density, $\rho$ , $\text{kgm}^{-3}$	Specific heat capacity, $C$ , $\text{Jkg}^{-1}\text{K}^{-1}$
1	Si	150	2280	700
2	DLC	1100	3500	518
3	Glass	1.2	2450	780
4	PMMA	0.2	1190	1500
5	Air	0.03	1.2	1006
6	He	0.15	0.2	5200
7	Ar	0.02	1.8	577

Table 6.1 Properties of materials and gases considered in this study. All properties are representative values at ambient condition (1 atm., 20 °C).



S.No	Substrate materials	Diaphragm radius, $R$ , $\mu\text{m}$	Actuation frequency, $f$ , Hz
1	Si	50	~ 800
		250	~30
2	Glass	50	~ 5
		250	-
3	DLC	50	~ 4850
		250	~42
4	Hf	50	~ 90
		250	~ 5

Table 6.2 Effect of substrate materials on the actuation frequencies of a polymeric (PMMA) diaphragm ( $t_d = 2 \mu\text{m}$ ,  $w_c = 100 \mu\text{m}$  and  $t_s = 250 \mu\text{m}$ ) thermo-pneumatic actuator for a heater temperature difference of  $\sim 150 \text{ }^\circ\text{C}$ .

## 6.6 Candidate materials for phase change actuators

A simple phase change actuator can be realised by replacing the gaseous cavity shown in Figure 6.1 by substances capable of undergoing a phase change at near the ambient conditions. Some essential engineering requirements of phase change materials for microactuators are: chemical inertness, phase change temperatures close to the ambient conditions, low latent heat, low viscosity, good phase stability and availability. The preferred ranking of the available mechanisms for realising high performance phase change actuators is: sublimation, evaporation and fusion. Sublimation is preferred due to its inherently high volumetric change. Substances such as dry ice (solid  $\text{CO}_2$ ), Naphthalene ( $\text{C}_{10}\text{H}_8$ ) and Iodine ( $\text{I}_2$ ) sublime under atmospheric conditions but pose difficulties in controlling the sublimation rate in addition to other critical issues such as toxicity, flammability and chemical reactivity.

Phase transition temperature	~ 72 $^\circ\text{C}$
Allowable volumetric strain, $\epsilon_{\text{rec}}$	~ 15% against 0 pressure [114]
Thermal conductivity, $\kappa$	~ 0.2 $\text{Wm}^{-1}\text{K}^{-1}$ [114]
Bulk modulus of liquid, $K$	~ 1.6 GPa [143]
Elastic modulus of solid, $E$	~ 3 GPa
Latent heat of fusion	~ 150 - 200 $\text{kJkg}^{-1}$ [129]

Table 6.3 Properties of Paraffin wax.

The performance metrics of phase change actuators are evaluated by applying relevant mechanics relations. The average out-of-plane deflection,  $\delta_{\text{av}}$  is obtained by

equating the strain energy associated with dilatation of the phase change material and the strain energy associated with the deformation of the diaphragm. The blocked force,  $F_b$  is obtained from the pressure developed when the volume expansion is negated. The maximum work per unit volume,  $W$  is associated with bounding limits of the operating characteristics of the actuator defined by  $\delta_{av}$  and  $F_b$ . Assuming the diaphragm structure to be an ideal plate, the performance metrics of phase change actuator are estimated as:

$$\delta_{av} = \left( \sqrt{\frac{2K}{E}} \right) \left( \frac{\varepsilon_{rec} R^2}{8 t_d} \right) \quad (6.24)$$

$$F_b = \pi R^2 \varepsilon_{rec} K \quad (6.25)$$

$$W = \frac{F_b \delta_{av}}{8 \pi R^2 w_c} \quad (6.26)$$

where  $\varepsilon_{rec}$  and  $K$  are the recoverable volume strain and the bulk modulus of the phase change material respectively. Although the work per volume delivered by phase change actuators is higher than the other actuation schemes, not many choices of materials are available beyond paraffin. Table 6.3 shows the representative values of the thermo-physical properties of paraffin considered for the present study. A large work per volume ( $\sim 10^7 \text{ Jm}^{-3}$ ) at relatively low frequencies ( $\sim 300 \text{ Hz}$  for a Si substrate) [117] can be obtained using paraffin based phase change actuators.

### 6.7 Performance limits of thermo-pneumatic and phase change actuators

The present study is intended as a means of assessing and comparing actuation schemes and for identifying optimal material choices in preliminary design. In order to achieve these aims, limitations are accepted regarding the capability of the models. In particular, the effect of the temperature change associated with the thermo-pneumatic energy on the material properties and hence the structural response of the diaphragm is not taken into consideration. Furthermore, the effect of

ambient temperature fluctuation on the performance of the actuator requires further consideration in the detailed design. Also, the elastic moduli of different classes of materials considered for the diaphragm are assumed to be isotropic. Nevertheless, these assumptions have no significant bearing on the materials selection considering the comparison of the performance estimates in an order of magnitude.

A comparison between the estimated performances obtained from the analytical solutions with the experimental values reported in the literature is made to justify the suitability of the models for the materials selection decision. For a temperature difference of 70 °C, the maximum achievable centre deflection of the diaphragm and the corresponding pressure difference are 120 µm and 10 kPa respectively for an optimal material index ( $M_{po} \sim 54$ ). These values are of the same order as the experimental values ( $\sim 250$  µm and  $\sim 7.5$  kPa) reported in the literature [144]. The deviation in the centre deflection values by a factor of  $\sim 2$  can be attributed to the compliant nature of the polymeric diaphragm in the experimental device due to a large aspect ratio ( $\beta = 1250$ ). The associated material index of the compared experimental structure ( $M_p \sim 1.5 \times 10^{-4}$ ) is very low and hence require validation by the non-linear large deformation theory. However, the materials selection and the ranking of the candidates based on performance are unchanged. Although performance of the actuators varies depending on the topology of the diaphragm structure, the materials selection decision is unaltered. Hence the candidates identified and ranked are promising for rectangular diaphragms as well.

Furthermore, the estimated frequencies listed in the Table 6.2 are also of the same order as the experimental values ( $\sim 20$  Hz) quoted in the literature [127] for relevant scales and substrate materials. The achievable frequencies can be improved by using either high conductivity substrates or by reducing the operating temperature range. However, this has to be compensated by a corresponding increase in the heat dissipation (hence a decrease in the efficiency) or a decrease in the work per volume delivered.

It is found that the maximum achievable work per volume,  $W$  by thermo-pneumatic actuation ( $\sim 10^4$  Jm<sup>-3</sup>) is two orders of magnitude less than the value quoted in the

literature [117]. This may be attributed to referring the  $W$  to the cavity volume in the present work instead of the diaphragm volume, given that  $V' \sim 10 - 100$ . The increase in the work per volume delivered mainly depends on the achievable deflection of the diaphragm since the achievable pressure rise is much less sensitive to materials selection. Also, the presence of a boss on the diaphragm results in drop in the work per volume by  $\sim 50\%$ . However, such configurations are often necessary for applications such as flow control valves in micropumps. Also, the actuation frequencies for thermo-pneumatic and phase change actuators are relatively low and vary between a few tens to few hundreds of Hertz depending on the substrates (Si, Glass, DLC) and scales ( $50 \mu\text{m} < R < 250 \mu\text{m}$ ). For reference, the resonant frequency due to Helmholtz oscillation of the fluid medium is estimated as  $f_h \sim 500 \text{ kHz}$ , which is of the same order of magnitude as the structural resonant frequencies of piezoelectric microactuators.

The performance limits of phase change actuators are constrained due to the lack of promising materials beyond the choice of paraffin waxes. The stiffness of the diaphragm structure and the low thermal conductivity of paraffin restrict the achievable average volumetric strain to less than 5% even though the allowable limit is 15% under free expansion. Nonetheless, phase change actuators are superior to other actuation schemes when high force ( $\sim 1 \text{ N}$ ) or work is the primary requirement in low frequency applications ( $\sim 300\text{-}400 \text{ Hz}$ ).

On the basis of efficiency, phase change actuators are superior ( $\eta_{em} \sim 0.07$ ) to other actuation schemes owing to their high volumetric strain. Although the mechanical efficiency of the thermo-pneumatic actuators is high ( $\eta_m \sim 0.15$ ) and of the same order as macroscale pneumatic actuators [5], their overall efficiency is of the same order as electro-thermal actuators ( $\eta_{em} \sim 10^{-4}$ ) due to the inherently low conversion from electro-thermal energy to pneumatic energy. Diaphragm materials with high dimensionless moduli and membrane stresses can further reduce the efficiency of thermo-pneumatic actuators by an order of magnitude.

The results presented herein provide guidelines for the selection of MEMS actuators and their associated materials choices based on performance. Although a detailed analysis specific to particular microsystems is required for further development, the present generalised study serves as a good tool for the selection of materials in order to realise high performance reliable MEMS devices.

## 6.8 Summary

Design guidelines for the optimal selection of materials are presented for thermo-pneumatic and phase change actuators. Engineering polymers are very promising diaphragm materials for high work per unit volume ( $\sim 10^4 \text{ Jm}^{-3}$ ), low frequency ( $\sim 200 \text{ Hz}$ ) applications. The actuation frequency can be improved by employing substrates with high thermal conductivity such as DLC at the expense of efficiency. The influence of a boss and the presence of tensile membrane stress are both detrimental to the actuator performance in terms of work per volume and efficiency. Paraffin waxes are promising candidates for realising high force ( $\sim 0.6 \text{ N}$ ) and high work per volume ( $\sim 10^7 \text{ Jm}^{-3}$ ) phase change microactuators at a few hundred Hertz.

The performance limits of different actuators and the ranking of associated material choices have been evolved from the fundamental governing mechanisms of relevant actuation schemes. These would serve as useful basis for the selection of actuators for various applications besides providing practical insight for realising high performance devices. However, for identifying a suitable actuation scheme for an application, a more comprehensive understanding of the critical functional requirements of the microsystems is essential which requires system level analyses. Chapter 7 discusses the selection of microactuators for a few applications by comparing the achievable performance limits of different actuation schemes.

# Chapter 7

## Selection of Microactuators Based on Performance

### 7.1 Transition in the design philosophy of MEMS

The applications of MEMS actuators at the research level are vast. However, their applications in commercial products are very few. An electrostatically actuated micromirror device developed by *Texas Instruments Inc.* [7] and piezoelectrically actuated variable droplet inkjet printer heads developed by *Epson* [12] are the two most notable commercial applications. Although promising materials beyond silicon and other CMOS/MOSFET materials are available, the process capability for growing thin films of arbitrary materials is not sufficiently mature to realise commercial acceptance. Nevertheless, there is a gradual transition in the design philosophy from process-centric design to performance-centric design. The analyses carried out in this thesis have identified some potential candidates for commonly employed MEMS actuation schemes. This provides further research opportunities in exploring the feasibility of individual actuation schemes and their associated materials choices for realising high performance devices.

This chapter is organised as follows. Section 7.2 discusses the selection of microactuators based on performance in accordance with the primary functional requirements relevant to different applications. Section 7.3 discusses a particular case study; assessing the suitability of BMET actuators against the commonly preferred BMPE actuators for a boundary layer flow control application. Section 7.4 discusses the design of masks and microfabrication processes to create representative devices of Al-Si<sub>3</sub>N<sub>4</sub> BMET actuators. Section 7.5 summarises the outcomes of the analyses performed in this chapter.

### 7.2 Comparison of the performance limits of microactuators

Selection of actuators for a given application determines the performance of MEMS devices. A generalised comparison between various actuation schemes based on performance is presented in Table 7.1.

<b>Actuation method</b>	<b>BMET</b>	<b>BMPE</b>	<b>BMSM</b>	<b>ETB</b>	<b>Thermo-pneumatic</b>	<b>Phase change</b>
Material combinations	Al-Si	PZT-Si	NiTi-Si	DLC	PMMA/air/Si	PMMA/Paraffin/ Si
Actuator dimension	125 $\mu\text{m} \times 62 \mu\text{m} \times 2 \mu\text{m}$				$R = 50 \mu\text{m}; t_d = 2 \mu\text{m}; w_c = 10 \mu\text{m}; t_s = 250 \mu\text{m}$	
Temperature difference, in $^{\circ}\text{C}$	$\sim 150$	-	$\sim 30\text{-}40$	$\sim 112$	$\sim 55$	$\sim 55$
Compressive pre-stress, in MPa	-	-	-	$\sim 500$	-	-
Electric field, $E_p$ in $\text{MVm}^{-1}$	-	5	-	-	-	-
Recoverable strain, $\epsilon_{\text{rec}}$	-	-	0.8 %	-	-	$\sim 5 \%$ (average volume strain)
Power dissipated, $P$ in W	$\sim 10^{-1}$	$\sim 0$	$\sim 10^{-2}$	$\sim 1$	$\sim 10^{-3}$	$\sim 10^{-2}$
Dielectric energy/volume stored, $E_s$ in $\text{Jm}^{-3}$	-	$\sim 0.14$	-	-	-	-
Tip deflection, $\delta_t$ in $\mu\text{m}$	$\sim 19$	$\sim 2$	$\sim 46$	-	-	-
Blocked moment, $M_b$ in Nm	$\sim 10^{-8}$	$\sim 10^{-9}$	$\sim 2.5 \times 10^{-8}$	-	-	-
Average out-of-plane deflection, $\delta_{\text{av}}$ in $\mu\text{m}$	$\sim 6.3$	0.7	15	1.6	$\sim 2$	$\sim 10$
Blocked force, $F_b$ in N	$\sim 3 \times 10^{-4}$	$\sim 3 \times 10^{-5}$	$\sim 6 \times 10^{-4}$	$\sim$	$\sim 10^{-4}$	$\sim 0.6$
Maximum work per unit volume, $W$ in $\text{Jm}^{-3}$	$\sim 3 \times 10^4$	$\sim 293$	$\sim 10^5$	$\sim 10^5$	$\sim 10^4$	$\sim 9 \times 10^6$
Actuation frequency, $f$ in Hz	$\sim 3 \times 10^3$	$\sim 9 \times 10^4$	$\sim 10^3$	$\sim 10^4$	$\sim 2 \times 10^2$	$\sim 2 \times 10^2$
Loss coefficient, $\chi$	-	$\sim 10^{-3}$	-	-	-	-
Mechanical efficiency, $\eta_m$	0.05	-	-	-	$\sim 0.15$	-
Overall electromechanical efficiency, $\eta_{\text{em}}$	$\sim 10^{-4}$	$\sim 0.1$	$\sim 10^{-3}$	$\sim 10^{-3}$	$\sim 10^{-4}$	$\sim 0.07$

Table 7.1 Comparison of the performance of different actuation schemes at the microscale.

The in-plane area and the thickness for all actuator structures under comparison are maintained constant even though their basic geometric configurations are different (bimaterial cantilevers and axi-symmetric plates). Although a blocked moment is a more appropriate performance metric for bimaterial cantilever structures, the present work also evaluated the blocked force (the average uniformly distributed load required to negate the average deflection of the structure) for the purpose of comparison.

A comparison of the performances of BMET (Al-Si) and BMPE (PZT-Si) cantilever actuator structures for sensible limits on temperature ( $\Delta T = 150^\circ\text{C}$ ) and electric field ( $E_p = 5\text{MVm}^{-1}$ ) respectively is shown in Table 7.1. The tip deflection, blocked moment and work/volume delivered by the BMET actuators are greater than those of the BMPE actuators for a fixed geometry ( $125\ \mu\text{m} \times 62\ \mu\text{m} \times 2\ \mu\text{m}$ ). However, the actuation frequency of the BMPE actuators is greater than that of the BMET actuators by an order of magnitude. Although the force delivered by the BMPE actuator structures could be improved without an appreciable drop in the actuation frequency at large scales ( $\sim 10\ \text{kHz}$  can be attained even for  $L \sim 2 \times 10^{-3}\ \text{m}$  and  $L/t = 30$ ), the displacement and the work per volume which could be achieved are consistently lower than those for the BMET actuators corresponding to the assumed scale. For applications such as arrays of small flap actuators for boundary layer flow control [50, 145], it is necessary for the actuator structures to operate at high frequencies ( $\sim 10\ \text{kHz}$ ) and to deliver a high work per cycle. Since the BMPE actuators operate at mechanical resonance, an actuation frequency of  $\sim 100\ \text{kHz}$  can be achieved even for a cantilever length of a few hundred microns, however the work/volume per cycle is relatively small. On the other hand, BMET actuators have the ability to actuate at  $\sim 10\ \text{kHz}$  only if their length is less than  $100\ \mu\text{m}$  (Figure 3.15a), however, the work per volume per cycle is larger than that of the BMPE actuator. Unlike BMET actuators which are characterised by high losses due to the Joule heating effect, the losses associated with BMPE actuators due to charge leakage are very small. As a result, the actuation efficiency of BMET actuators is less than that of BMPE actuators by four orders of magnitude. However, a large amount of input electrical energy is stored within the blocked electrical capacitor without being utilised for transduction in BMPE actuators. Also, the ability of



BMPE actuator structures to operate at resonant frequencies can lead to energy losses due to damping effects (material, and/or fluid) which are very low in BMET actuators. The BMPE actuators are also prone to depoling and aging issues which degrade their performance.

The performance of electrothermal actuators can be improved in ETB configuration using DLC substrates. The work per volume delivered and the actuation efficiency of ETB actuators are an order of magnitude greater than that of the BMPE actuators. However, controlling high compressive stresses in the actuator structure is a critical issue which need to be addressed for realising high performance devices.

Unlike BMPE actuators, BMET actuators require relatively simple microfabrication steps involving sputtering or evaporation of Al on Si wafers followed by etching. This involves comparably few mask patterns. BMPE actuators require relatively complicated fabrication routes involving sputtered electrode deposition, spin coating of the seed layer, and sol-gel deposition of the piezoceramic followed by pyrolysis and sintering [93]. Furthermore, the range of variation in the electromechanical properties (such as  $d$  coefficients, coercive field, and saturated polarisation) with scale is greater than that of the mechanical and thermal properties. On balance this analysis suggests that BMET actuators are (perhaps) surprisingly competitive with BMPE devices, unless very high frequency and/or efficiency are the primary design drivers.

For bimaterial shape memory (BMSM) actuators, Nitinol (nickel titanium Naval Ordnance Laboratory), an alloy of nickel and titanium is a promising candidate compared to other shape memory alloy systems. This is attributed to its large actuation strain ( $\sim 6\%$  in bulk) over a small temperature range close to ambient conditions. For a NiTi-Si combination the actuation due to the shape memory effect is more pronounced than that due to the thermal expansion effect within the transformation temperature range ( $\sim 40\text{-}80\text{ }^\circ\text{C}$ ). Since one of the material properties governing the performance of electrothermal ( $\alpha$ ) and shape memory ( $\epsilon_{\text{rec}}$ ) actuators is not common, a uniform basis need to be established to compare the performance.

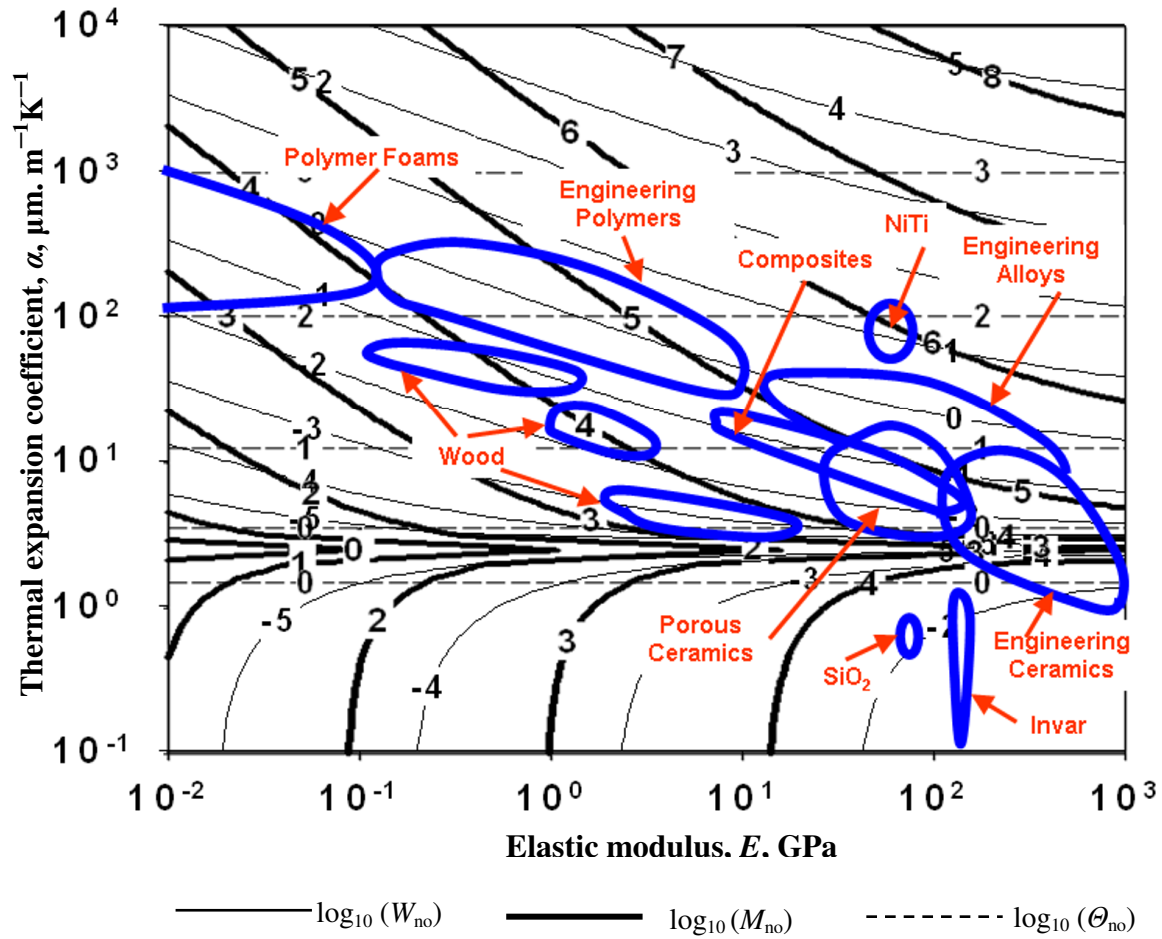


Figure 7.1 Comparison of the performance of NiTi shape memory alloy with different classes of engineering materials with respect to silicon substrates.

This is feasible if the actuation strain due to phase change at microscales in NiTi ( $\epsilon_{\text{rec}} = 0.4\text{-}0.8\%$ ) is represented as an equivalent strain due to thermal expansion corresponding to the temperature limits associated with the austenite-martensite phase transformation as shown in Figure 7.1. It should be noted that Figure 7.1 can be used for comparing the performance so long as the peak actuation temperatures are less than  $80^{\circ}\text{C}$ . This is a reasonably valid representation considering the operating temperature difference of most electrothermal actuators ( $\sim 100\text{-}200^{\circ}\text{C}$ ). However, for peak actuation temperatures greater than  $80^{\circ}\text{C}$ , the work per unit volume beyond  $80^{\circ}\text{C}$  would be contributed by thermal expansion ( $\alpha_{\text{NiTi}} \sim 11 \mu\text{m.m}^{-1}\text{K}^{-1}$ ) thereby leading to a slight drop in the performance. Hence the region corresponding to NiTi in Figure 7.1 would slightly descend along the ordinate in accordance with the temperature difference beyond the austenitic finish temperature.

Although the work per volume,  $W$  of thermo-pneumatic actuators is very low compared to electrothermal, shape memory and phase change actuators, it is on par with that of bimaterial piezoelectric microactuators. On the other hand, phase change actuators are superior to other actuation schemes when high force ( $\sim 1 \text{ N}$ ) or work is the primary requirement in low frequency applications ( $\sim 300\text{-}400 \text{ Hz}$ ). Actuators delivering performance in that range are very promising for applications such as flow control microvalves employed in particle counters and biochips.

Unlike electrothermal/piezoelectric actuators, there is a critical length scale for shape memory actuators which is dependent on the grain size of the alloy system. There has been a wide disagreement on this limiting scale associated with the shape memory effect [146-148] which depends on the processing routes. Hence electrothermal actuation could be a better alternative at such scales. Generally piezoelectric actuation has been preferred for applications such as boundary layer flow control [50, 51] due to its ability to operate at mechanical resonance ( $\sim 100 \text{ kHz}$ ). The results presented herein suggest that electrothermal actuators at small scales ( $\leq 100 \mu\text{m}$ ) are competitive with piezoelectric actuators at  $\sim 10 \text{ kHz}$ .

## 7.3 Detailed design of microactuators for boundary layer flow control\*

### 7.3.1 Role of MEMS technology in flow control

The design of fuel efficient aircraft is a long standing problem and researchers have been trying to increase the fuel efficiency by various means. One of the possible approaches is to improve the aerodynamic performance by increasing the lift to drag ratio of the vehicle moving through the fluid medium. The total drag is the sum of two components namely, skin friction drag and form (pressure) drag. Skin friction drag occurs due to the resistance offered to the motion of a body by the frictional forces that arise when fluid flows over its surface (skin). This depends on the wall shear stress developed and the wetted area exposed to the fluid medium. Form drag occurs due to the development of adverse pressure gradients which are attributed to flow separation. Form drag depends mainly on the shape of the vehicle. Traditional flow control characterised by sleekness in the shape of the vehicle by rigorous fluid dynamics studies over years has resulted a significant reduction in the form drag. With the recent advent of MEMS technology, it is now possible to manipulate the surface dynamically using an array of sensors and microactuators thereby reducing the skin friction drag as well.

The recent trends in boundary layer flow control using MEMS technology has motivated the present study which focuses on assessing the feasibility of a design for a proposed distributed flow control facility at the *University of Southampton, U.K.*. Such a facility could be very useful for conducting demonstration experiments relevant to fluid dynamics research. Some of the published works on boundary layer flow control include: Active control of laminar stream wise vortices similar to the wall region eddies in the turbulent zone using piezoelectric stainless steel cantilever actuators [50], reduction of separated wakes in the flow past circular cylinder by Au-Si electrostatic actuation [149] and application of dielectric elastomers [150] in dimple actuators for the flow control using electrostatic actuation. Although laboratories around the world have achieved a considerable success recently in drag reduction by boundary layer control, an effective practical solution to this problem

---

\* The contribution of Prof. Sergei Chernyshenko, *Imperial College, London*, in the fluid dynamics studies relevant to turbulent flow control is gratefully acknowledged.

has not been obtained. This is mainly attributed to a lack of understanding of the implementation of turbulent flow control by actuators and sensors. The purpose of the present analysis is to assess the performance of bimaterial MEMS structures for boundary flow control by relevant analytical, numerical and experimental studies.

### 7.3.2 Introduction on distributed flow control

A fundamental understanding on the boundary layer theory is essential in order to successfully implement a desirable flow control using MEMS technology. A detailed analysis focussing exclusively on the boundary layer theory for flow past different geometries is already well documented [151]. This section therefore discusses the relevant flow parameters that influence the microactuator design for boundary layer flow control applications.

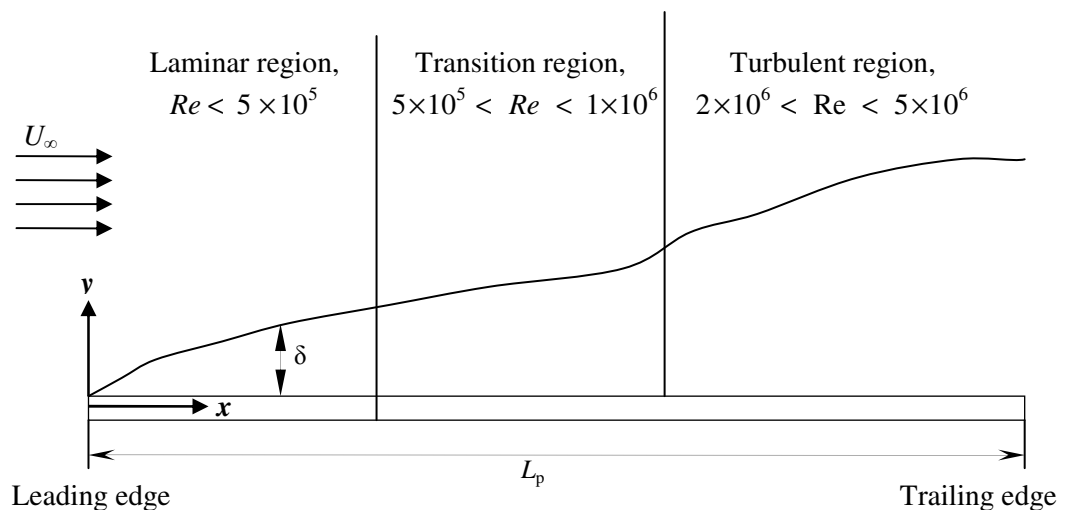


Figure 7.2 A fully developed boundary layer over a flat plate[151].

Figure 7.2 shows a fully developed boundary layer when a fluid flows over a flat plate. The length of the plate is  $L_p$  and the free stream velocity of the fluid along the  $x$  direction is  $U_\infty$ . As the fluid flows over the flat plate, a thin layer of fluid called the boundary layer is developed near the wall within which the velocity varies from zero to the free stream velocity normal to the plate surface due to viscous effects. The flow field within the boundary layer is characterised by the non-dimensional

Reynolds number,  $Re$ , which is defined as the ratio of the inertial force to the viscous force and is given as

$$Re = \frac{l_c U_\infty}{\nu_f} \quad (7.1)$$

where  $\nu_f$  is the kinematic viscosity of the fluid and  $l_c$  is the characteristic length which is equal to the length of the plate,  $L_p$  for a flow over flat plate.

Depending on the values of  $Re$ , the flow field within the boundary layer is characterised as laminar ( $Re < 5 \times 10^5$ ), transition ( $5 \times 10^5 < Re < 1 \times 10^6$ ) or turbulent ( $2 \times 10^6 < Re < 5 \times 10^6$ ). Assuming a no slip boundary condition at the wall, the shear stress distribution for a Newtonian fluid is inversely proportional to the square root of the plate length in the laminar region. Hence the skin friction drag is reduced as the Reynolds number increases within the laminar region. However, when the flow becomes turbulent ( $Re > 2 \times 10^6$ ) random mixing of the fluid particles occurs. This is characterised by the formation of near wall low speed streaks and vortices which contribute to skin friction. The span wise dimensions of these streaks are such that they can be effectively controlled either by an external disturbance due to perturbation [50] or by controlled removal of low speed streak layers at a prescribed frequency as described in this work.

The present study discusses a particular flow control mechanism achieved by the removal of low speed streaks at prescribed frequencies by means of boundary layer suction controlled by valve actuators. The quantity of fluid removed is very small because only fluid particles in the vicinity of the wall are sucked into the plenum. Figure 7.3 shows the schematic of a simple active open loop flow control. An array of sensors and actuators integrated in a single wafer is flush mounted on a flat plate. The sensors are deployed upstream of the actuators which operate against a constant plenum pressure in the turbulent region of the flow field. The communication between the sensors and the actuators is established via external control electronics through a computer as shown in the Figure 7.3.

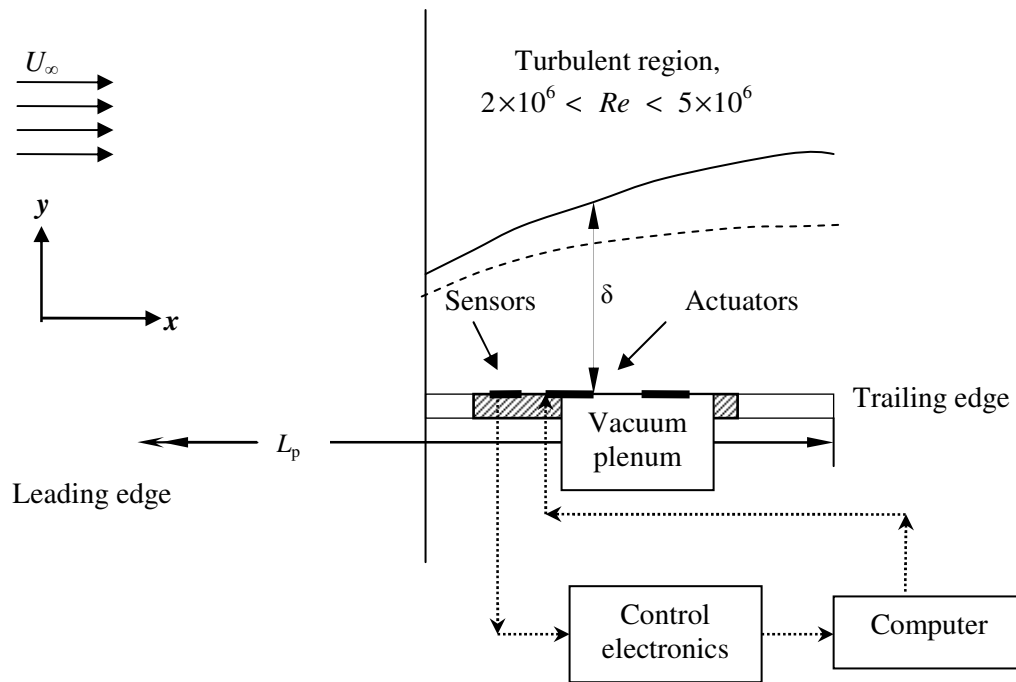


Figure 7.3 Schematic of an active open loop flow control implementation.

The thickness of the turbulent boundary layer,  $\delta$  for a flow over a flat plate is given as [151]:

$$\delta = 0.037 L_p Re^{-0.2} \quad (7.2)$$

If air at atmospheric pressure, flows over a flat plate of length,  $L_p = 0.5$  m at a free stream velocity,  $U_\infty = 15 \text{ ms}^{-1}$ , the thickness of the turbulent boundary layer developed is  $\delta \sim 0.01$  m. Using boundary layer relaxation theory [151], the distance over which the control has to be felt can be estimated, which is approximately 10 times the turbulent boundary layer thickness. Hence the dimension of the wafer flush mounted into a flat plate has to be  $\sim 0.1$  m (4").

The actuators have to operate against a differential pressure of 100 kPa in order to remove the low speed streaks near the wall at some prescribed frequencies. Typical dimensions of near wall low speed streaks are 100 wall units in the span wise direction and 1000 wall units in the longitudinal direction respectively. A wall unit is

a characteristic length scale defined in terms of fluid properties and the flow parameters and it is given as:

$$l = \frac{V_f}{V^*} = \frac{V_f}{(\tau_w / \rho_f)^{0.5}} \quad (7.3)$$

where  $V^*$  is the frictional velocity,  $\tau_w$  is the shear stress near the wall and  $\rho_f$  is the density of the fluid. The expression for the frictional velocity,  $V^*$  for a turbulent flow over a flat plate is given as

$$V^* = U_\infty (0.5 \times 0.058 \times Re^{-0.2})^{0.5}. \quad (7.4)$$

The low speed streaks evolve and die out at a particular frequency called the bursting frequency,  $f_b$  [50] which is given as:

$$f_b = \frac{V^{*2}}{250 V_f}. \quad (7.5)$$

For air,  $f_b$  is approximately  $\sim 100$  Hz at atmospheric conditions with the assumed flow parameters. Hence the actuation frequency,  $f$  has to be at least 10 times greater than the bursting frequency for controlling the fluid flow through the valves whose total cross-sectional dimensions is about 10% of a streak dimensions. Depending on the degree of autonomy required, sophisticated control algorithms to coordinate between the responses of sensors and actuators are essential in order to realise a closed-loop adaptive control implementation.

The flow control technology has been demonstrated only at low speeds ( $10-30 \text{ ms}^{-1}$ ) so far by laboratory experiments. However, the real success depends primarily on the demonstration of this technology at high speeds besides addressing other issues such as net payload gain, reliability and effect of global shift in the flow parameters. Although demonstration at high speeds ( $75 \text{ ms}^{-1}$ ) has been done at laboratory scale



using plasma actuators [152], the implementation in commercial applications is still a long term goal.

The achievement of an effective boundary layer flow control is dictated by the performance of the actuators which depends on the selection of suitable materials for the given fluid properties and flow parameters. This is because the suction flow rate per streak and the flow velocity through valves are governed by the actuator design. The following sub-section assesses the suitability of BMET actuators for boundary layer flow control application by comparing the performance with the commonly proposed BMPE actuators. Using closed form solutions, the suitability of BMET actuators for flow control demonstration at the laboratory scale is assessed.

### 7.3.3 Mechanics of a bimaterial flow control actuator

Figure 7.4 shows a schematic of a cantilever bimaterial valve actuator operating against a pressure difference for controlling the boundary layer flow. Assuming operation in the linear, small displacement regime, the valve opening,  $y$  can be expressed as:

$$y = y_{ps} + y_p - y_a \quad (7.6)$$

where  $y_{ps}$  is the deflection due to pre-stress,  $y_p$  is the deflection due to pressure difference and  $y_a$  is the deflection due to actuation.

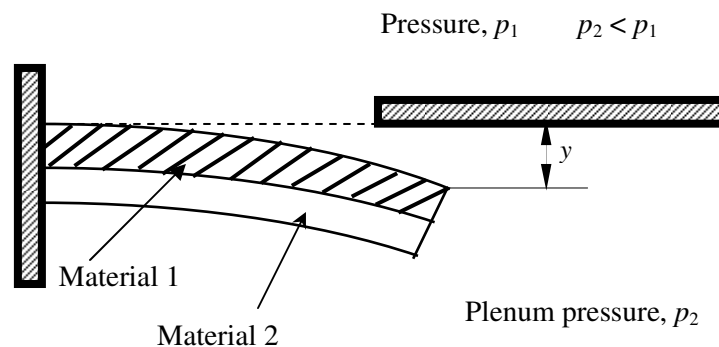


Figure 7.4 Schematic of a bimaterial cantilever valve actuator operating against a pressure difference.

The effect of pre-stress is expressed in terms of residual moment,  $M_{ps}$ . Using simple beam theory, the actuation strain required for complete valve closure for an actuator with an optimised geometry is given by

$$\varepsilon_a = \frac{(1 + \xi_o)^2}{E_1 \xi_o^2} \left\{ \frac{(\Delta p) \beta^2}{2} + \frac{2M_{ps}}{bt^2} \right\} \quad (7.7)$$

where  $\xi_o$  is the optimal thickness ratio of the bimaterial actuator as given by equation (2.14),  $\beta = L/t$  is the aspect ratio of the beam and  $\Delta p = p_1 - p_2$  is the pressure difference. The actuation strain  $\varepsilon_a$  is  $(\Delta\alpha)(\Delta T)$  and  $d_{31}V_1/t_1$  for BMET and BMPE actuators respectively.

#### 7.3.4 Analysis of the design space for flow control microactuators

In order to realise an effective flow control implementation, performance charts are constructed in the domain of design variables considered (actuator length scale and plenum pressure) for bimaterial structures subjected to electrothermal and piezoelectric actuations. An Al-Si bimaterial combination is considered for the BMET actuator structure. The effect of residual stress has to be considered in the actuator design in order to achieve the required valve opening for the removal of fluid streaks. The residual stresses developed generally depend on the process conditions, film thickness and the substrate materials. The flow stress in a 1.1  $\mu\text{m}$  thick polycrystalline Al film, deposited by magnetron-sputtering on Si at 450°C is  $\sim 180$  MPa [153]. The present analysis therefore assumes a residual stress of  $\sim 150$  MPa for a 1.35  $\mu\text{m}$  thick Al layer which is a reasonably good estimate for the preliminary design. For the BMPE actuator on the other hand, a PZT-Si combination is considered. The residual stress in thin film PZT deposited by pulsed laser deposition on Si was found to vary from  $\sim 75$ -25 MPa as the film thickness increases from 0.05-1  $\mu\text{m}$  [154]. A conservative estimate of 70 MPa was assumed in this study.

Figures 7.5a shows the performance contours corresponding to BMET actuators for a turbulent boundary layer control. The design charts consist of contours of tip

displacement ( $\log_{10}(y)$ ), actuation frequency ( $\log_{10}(f)$ ), power dissipated per streak ( $\log_{10}(P)$ ), temperature difference required for valve closure ( $\Delta T$ ) and the number of actuators per streak ( $\log_{10}(n)$ ), plotted in the domain of pressure difference and the actuator length scale. The contours corresponding to  $\Delta T$  were obtained using equation (7.7) assuming the actuation strain is caused by differential expansion due to Joule heating. It is clear from the Figure 7.5a that an increase in the pressure difference corresponds to an increase in the temperature difference and it is independent of the actuator length. This is because the valve closure is a position which corresponds to the negation of tip displacement of the actuator due to pre-stress and pressure loads by an equivalent electrothermal expansion. The contours of equal tip deflection ( $\log_{10}(y)$ ) were obtained by using equation (2.15) corresponding to the value of  $\Delta T$  required for the valve closure. It is evident from the plot that achievable tip deflection increases with the actuator length which would result in an increase flow rate through the valve. Contours of equal actuation frequency ( $\log_{10}(f)$ ) are obtained by solving the transient thermal model given by equations (3.15) and (3.17) for the achievable temperature difference,  $\Delta T$  corresponding to the valve closure. Unlike tip displacement, actuation frequency increases with decreasing actuator length and it is independent of the pressure difference. For a total valve cross section equal to 1% of streak area, the number of actuators per streak ( $\log_{10}(n)$ ) is obtained by dividing total valve cross section with the cross-sectional area of an actuator assuming  $L/t = 35$  and  $b = 0.5L$ . The power dissipated per streak ( $\log_{10}(P)$ ) is obtained by using equation (3.13) for the total number of actuators per streak which is a function of the total number of actuators per streak,  $n$  and the actuator length,  $L$ .

It is evident from Figure 7.5a that for a given actuator length the temperature difference required for the valve closure increases with the pressure difference thereby decreasing the actuation frequency. On the other hand, a decrease in the actuator length results in the high actuation frequency with a corresponding drop in the tip displacement of the valve. Hence the boundaries of the allowable operating space depend on the actuation frequency and the tip displacement for sensible temperature limits.

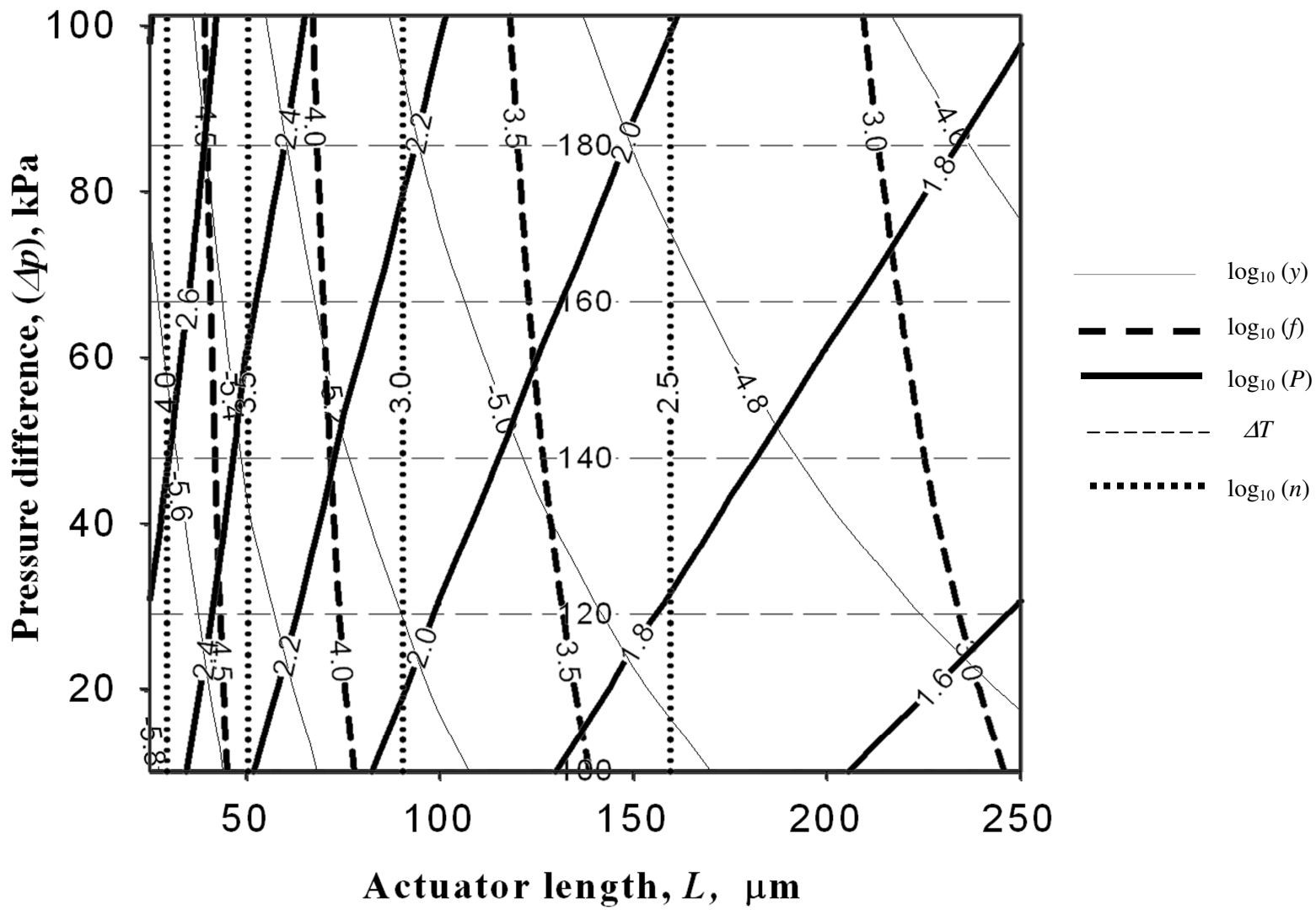


Figure 7.5a Performance of Al-Si BMET actuators for turbulent boundary layer flow control.

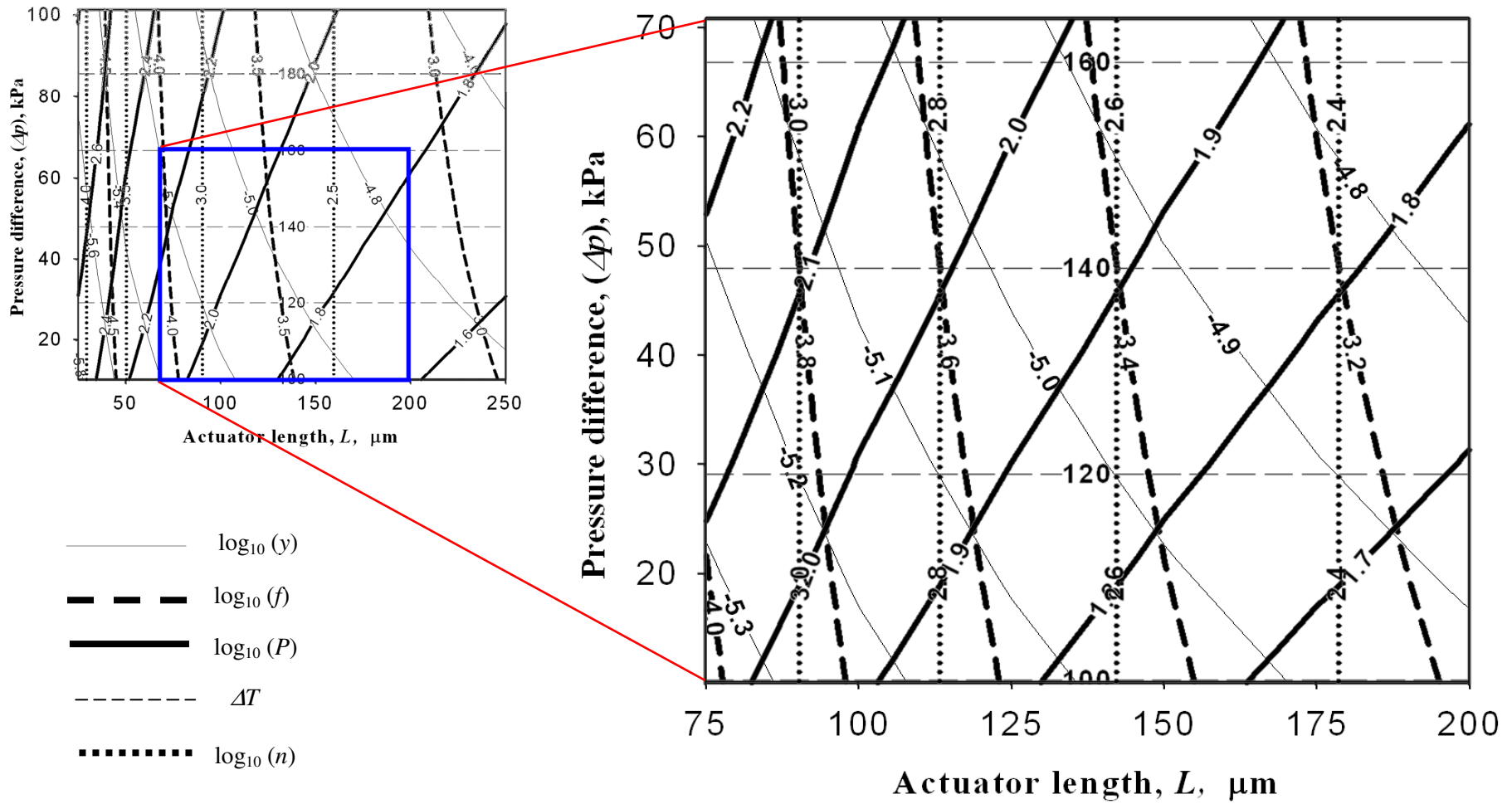


Figure 7.5b Design envelope for Al-Si BMET actuator structures for turbulent boundary layer control.

Figure 7.5b shows the allowable operating space for the BMET actuator which is indicated by the blue region on the performance chart. The design envelope is obtained based on the sensible limits on the achievable temperature ( $\leq 200^\circ\text{C}$ ) difference and the design constraint on the actuator length so that the flow velocity through the valves do not reach the sonic velocity at the prescribed actuation frequencies ( $\sim 1\text{-}10\text{ kHz}$ ).

Figure 7.6a shows similar such performance contours for BMPE actuators. The performance metrics considered are same as that for BMET actuators except for the temperature difference,  $\Delta T$  which is replaced by the actuation voltage,  $V$ . Using equation (7.7) contours of equal actuation voltage,  $V$  for BMPE actuator are obtained assuming the actuation strain is due to the converse piezoelectric effect. The required actuation strain negates the tip displacement due to differential pressure and the pre-stress. Unlike BMET actuators, BMPE actuators operate at mechanical resonance. Hence the actuation frequency,  $f$  is obtained using the Euler-Bernoulli relation for flexural vibration as given in equation (3.34). The tip displacement is obtained using equation (5.4) for the achievable electric field required for the valve closure. Furthermore, the power dissipation in BMPE actuators due to charge leakage is very small compared to heat dissipation due to Joule heating in BMET actuators. Hence the contours of equal power,  $P$  correspond to the dielectric power stored in the electrical capacitor which is obtained by using equation (5.8) for the achievable actuation frequencies.

Figure 7.6b shows the operating space for BMPE actuator structures for turbulent boundary layer control. The operating space of the BMPE actuator is smaller than that of the BMET actuator. This is attributed to the small variation in plenum pressure due to the constraints imposed by the coercive field of PZT layers ( $\sim 8\text{-}10\text{ MVm}^{-1}$ ) on the achievable deflection for the complete valve closure and the voltage requirements ( $< 100\text{ V}$ ). Although the tip displacement can be increased by increasing the actuator length, meeting the frequency requirements, there is a corresponding increase in the actuation voltage as well.

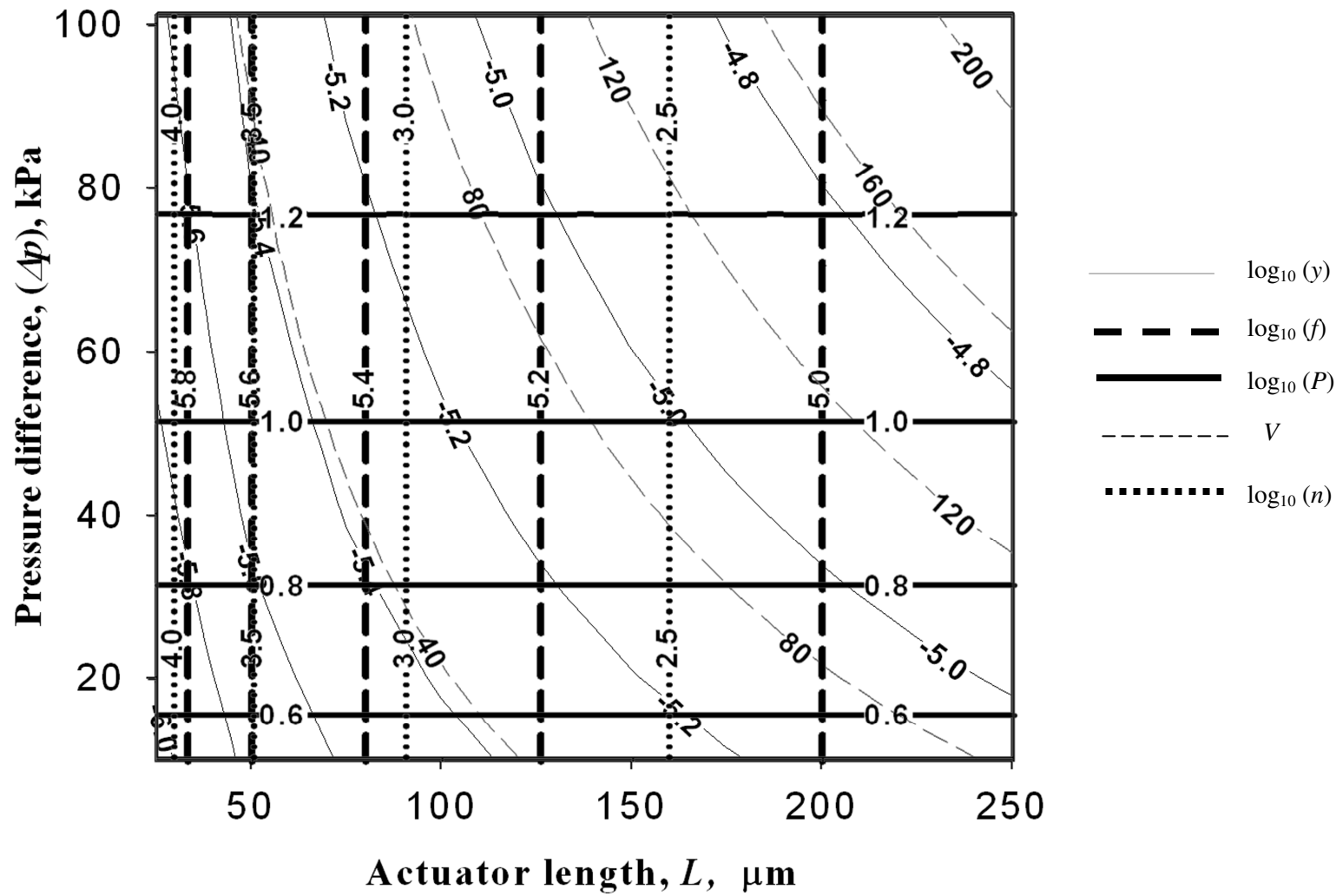


Figure 7.6a Performance of PZT-Si BMPE actuators for turbulent boundary layer flow control.

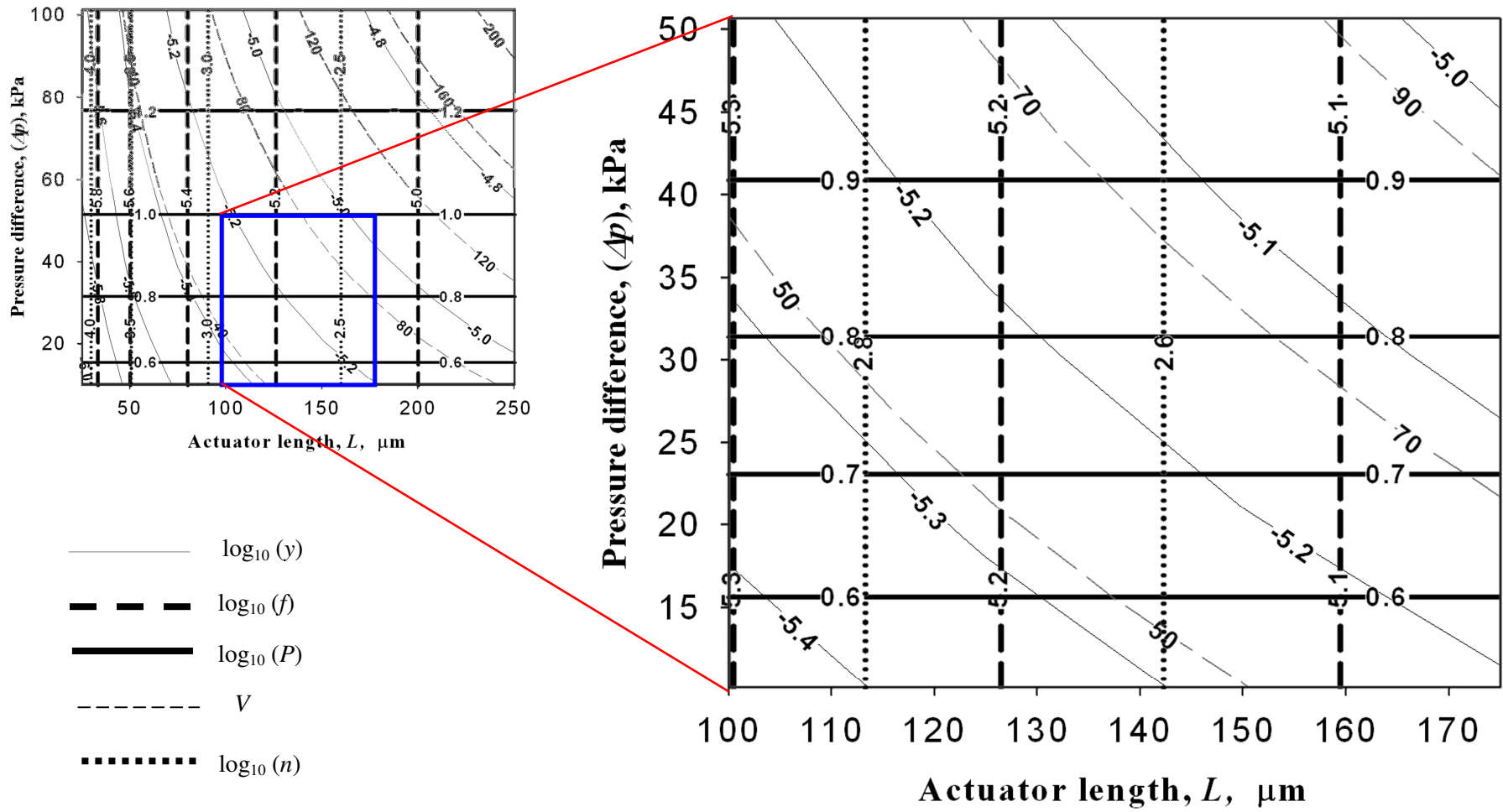


Figure 7.6b Design envelope for PZT-Si BMPE actuator structures for turbulent boundary layer control.



The small operating space of the BMPE actuators compared to that of the BMET actuators further reiterates the fact that the specific work associated with the BMET structures is more than that of BMPE structures. The ability of BMPE structures to operate at mechanical resonance results in an actuation frequency higher than that achieved from BMET actuators by an order of magnitude. However, issues associated with damping which affects the  $Q$ -factor of the actuator require further consideration. Furthermore, the inherent quality of BMET structures to dissipate power may affect the flow locally within the boundary layer if the temperature amplitude is not appropriately controlled thereby rendering the flow control ineffective. Hence, the influence of heat transfer on the temperature of the fluid needs to be evaluated to ensure the applicability of BMET structures for flow control applications.

The increase in the local temperature of the fluid due to heat transfer can be evaluated based on heat transfer through the turbulent boundary layer [151] which is given as

$$\frac{\hat{q}}{(\Delta T)_f} = \frac{c_p \tau_w}{(U_\infty - U_o)} \quad (7.8)$$

where  $\hat{q}$  is the heat flux through the boundary layer,  $U_o$  is the velocity of the wall and  $(\Delta T)_f$  is the increase in the temperature of the fluid.

The number of streaks within the area to be controlled is dictated by the turbulent cone spread angle,  $\theta_t$  which is approximately  $\sim 10$  degrees. For a boundary layer thickness,  $\delta \sim 0.01\text{m}$  (604  $l$ ), the total number of streaks,  $n_s$  within the area to be controlled is given as:

$$n_s = \frac{1}{2} \times \frac{2\delta}{100l} \times \frac{10\delta}{1000l} \sim 40 \quad (7.9)$$

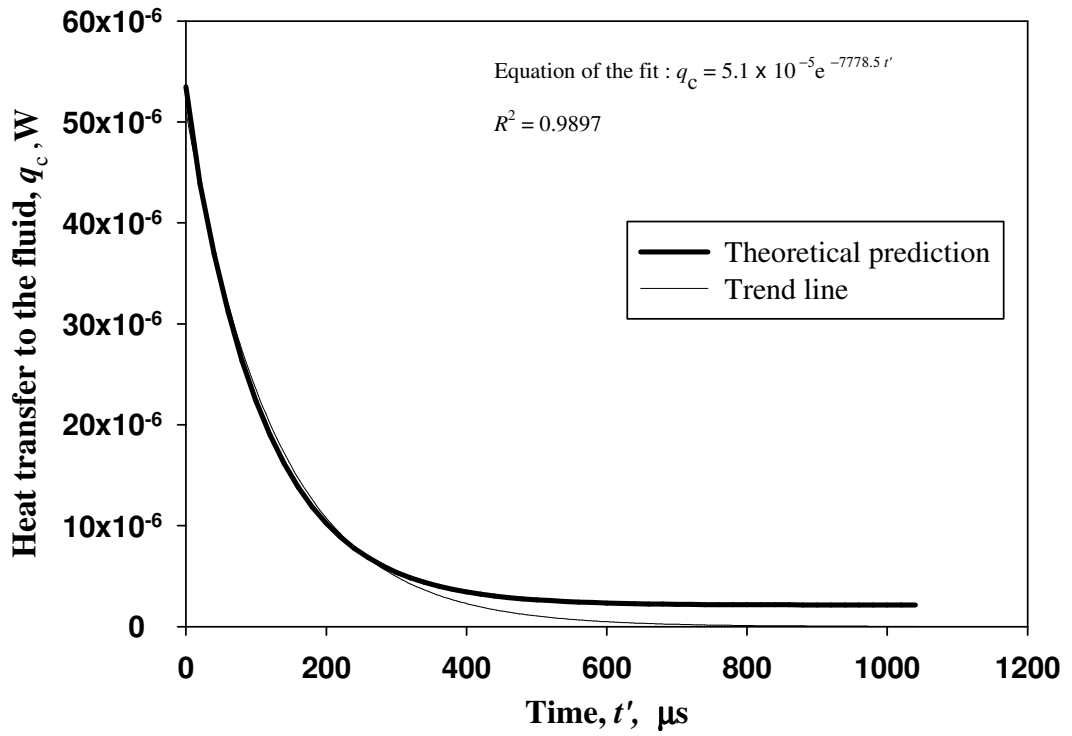


Figure 7.7 Transient heat transfer loss per cycle to the ambient for temperature difference of 125°C.

The number of streaks within the wafer area is about ~ 200. A total of 630 valves is required to remove 10% of a streak volume for an actuator length of,  $L = 100\mu\text{m}$ . Assuming the flow through each valve is controlled by an actuator, a total of  $126 \times 10^3$  actuators are required within the wafer area. The average heat transfer to the ambient fluid per cycle is estimated to be  $\sim 7 \mu\text{W}$  from the transient thermal response of a BMET actuator shown in Figure 7.7. Hence the total heat flux transferred to the boundary layer from the wall with a 4" flush mounted wafer is given by

$$\hat{q} = \frac{(126 \times 10^3 \times 7 \times 10^{-6})}{\pi \left(\frac{0.1}{2}\right)^2} \approx 112 \text{Wm}^{-2}. \quad (7.10)$$

Substituting the values of relevant fluid properties, flow parameters and the value of heat flux,  $\hat{q}$  in equation (7.8) gives a value of  $(\Delta T)_f \sim 3^\circ\text{C}$ . Hence the rise in local temperature of the fluid due to heat transfer through the boundary layer is about  $3^\circ\text{C}$

even for a structural temperature difference,  $\Delta T = 125^\circ\text{C}$ . Overall, BMET structures are competitive with BMPE structures for low speed flow control actuation based on this preliminary analysis. Detailed design and analysis on flow physics and effective control strategies are essential for further development.

### *7.3.5 Finite element analysis of a BMET actuator structure*

The analytical solution discussed in the previous sub-section assumes a uniform nominal temperature difference for the actuator structure. However, in reality, the temperature field of the actuator structure due to Joule heating varies with the geometry. Hence a detailed finite element simulation was performed to estimate the thermoelastic and electrothermal performances of BMET structures considering the variation in the thermal field. Three dimensional finite element models were built using SOLID45 and SOLID70 brick elements implemented in ANSYS® to simulate the mechanical and heat transfer analyses respectively. The actuator is a bimaterial cantilever structure of length,  $L = 60\ \mu\text{m}$  and its width,  $b = 25\ \mu\text{m}$ . The thicknesses of the Al and Si layers are  $1\ \mu\text{m}$  and  $650\ \text{nm}$  respectively. These values are obtained from the optimality condition given by equation (2.14). Figure 7.8 shows the deflection contours of a cantilever actuator structure due to pre-stress and pressure difference. A tip deflection of  $\sim 4.0\ \mu\text{m}$  was obtained from the finite element simulation for a pre-stress of  $150\ \text{MPa}$  in the Al layer against a differential pressure of  $50\ \text{kPa}$ . This is close to the estimated value of  $\sim 3.9\ \mu\text{m}$  obtained from the closed form solution using simple beam theory. A total compressive stress of  $300\ \text{MPa}$  is developed in the pre-stressed Al layer on application of the pressure load.

Figure 7.9 shows the steady state temperature field required for valve closure. The thermal boundary condition was defined by a constant fixed sink temperature of  $323\ \text{K}$  at the mechanically clamped end of the cantilever structure. A macroscale convective heat transfer coefficient of  $\sim 10\ \text{Wm}^{-2}\text{K}$  was assumed for the simulation. A constant power generation of  $\sim 4 \times 10^{13}\ \text{Wm}^{-3}$  within the Si layer is required to negate the tip deflection of  $4.0\ \mu\text{m}$  caused by the combined effect of pre-stress and differential pressure.

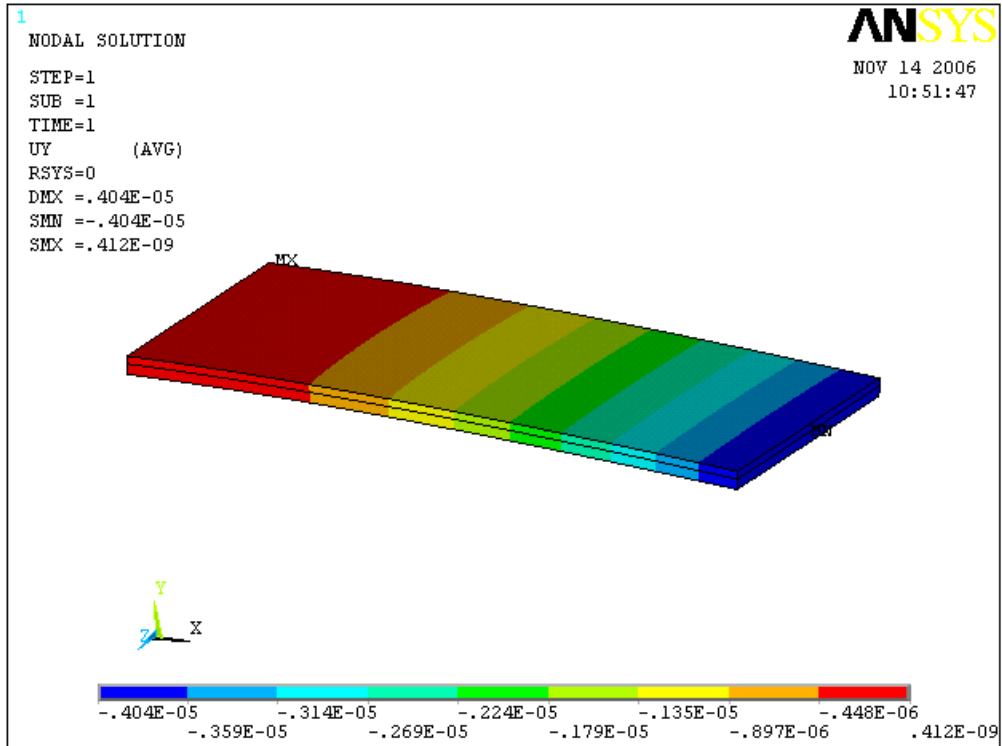


Figure 7.8 Vertical deflection of the actuator structure due to pre-stress and pressure difference. All deflections are in m.

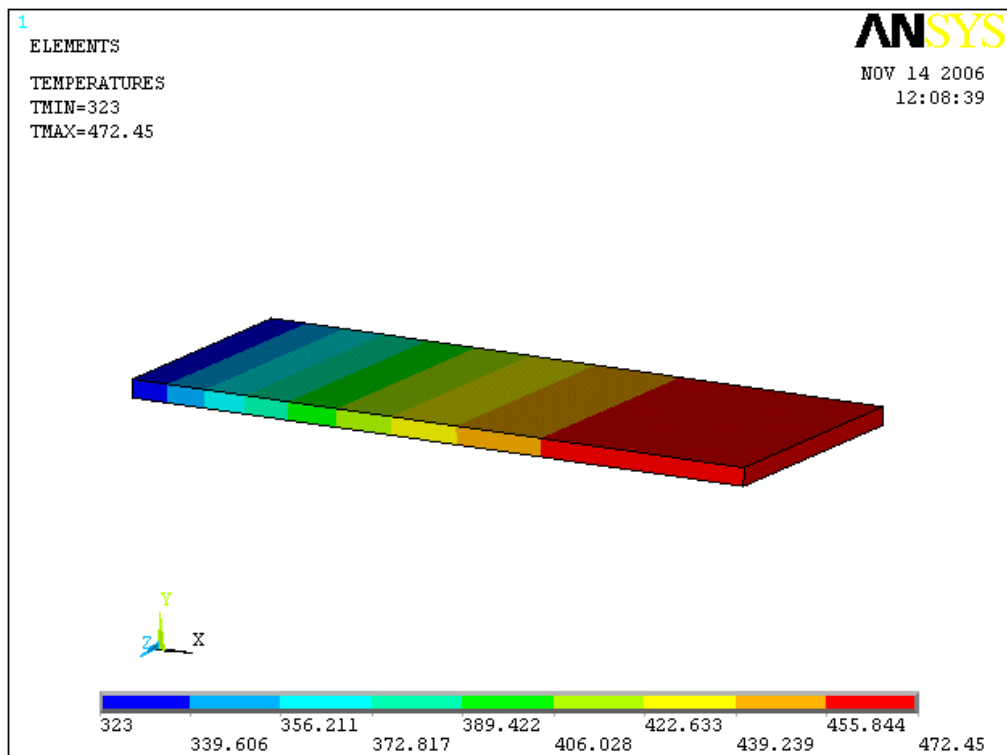


Figure 7.9 Steady state temperature field for a BMET actuator corresponding to valve closure. All temperatures are in Kelvin.

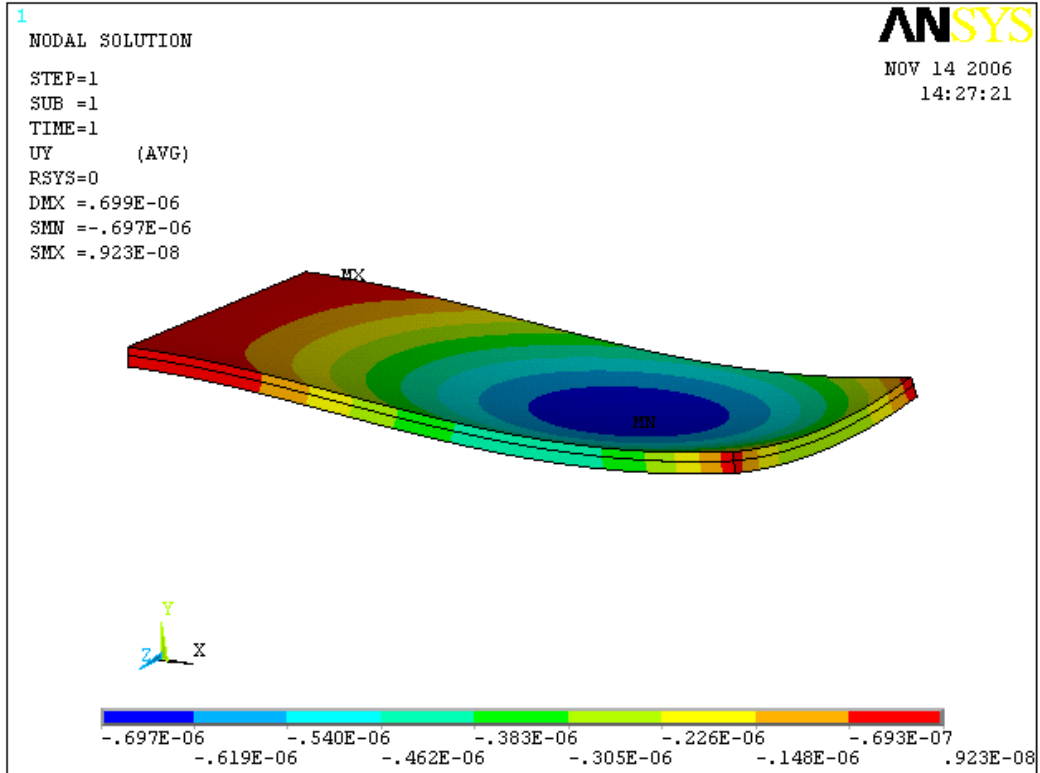


Figure 7.10 Vertical deflection of the BMET structure at the valve closure position. All deflections are in m.

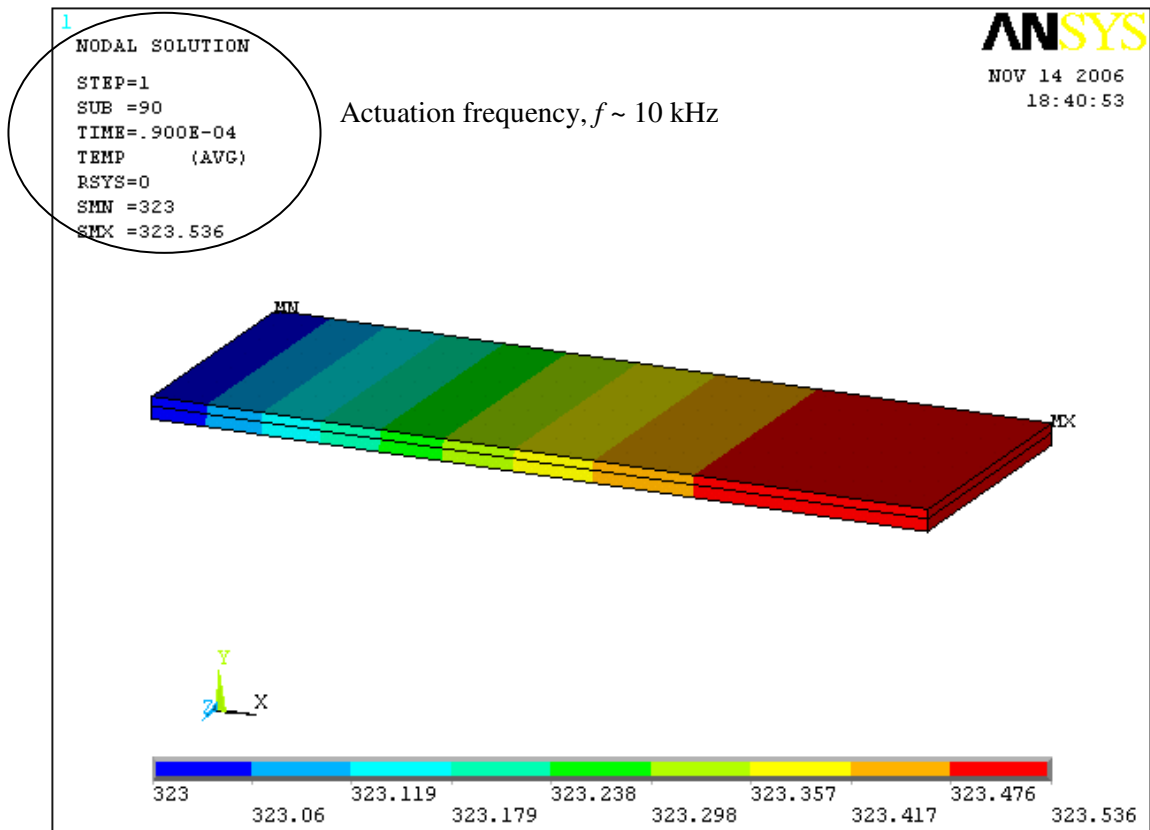


Figure 7.11 Near iso-thermal state in the transient thermal response of the BMET actuator structure. All temperatures are in Kelvin.




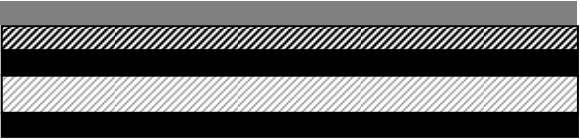
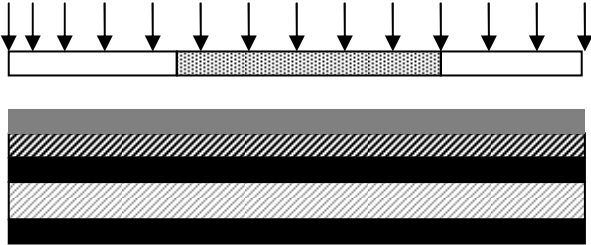
Figure 7.10 shows the vertical deflection contours of the actuator structure in the valve closure position. A gap which could result in a localised leakage corresponding to 600 nm vertical deflection at approximately one-third of the beam length from the free-end is observed besides a gap at the free-end due to synclastic curvature resulting in 300 nm deflection at the mid of the cross section.

Figure 7.11 shows the transient thermal response of the BMET actuator. The initial condition corresponds to the temperature field in valve closure position as shown in Figure 7.9. An actuation frequency of  $\sim 11$  kHz was achieved with the present configuration. The time taken for valve closure can be reduced to an order of magnitude less than the time taken for valve opening by increasing the power generation in the Si layer to  $\sim 10^{14}$  Wm<sup>-3</sup> which is achievable with the typical current densities employed in IC circuits ( $\sim 10^9$  Am<sup>-2</sup>)

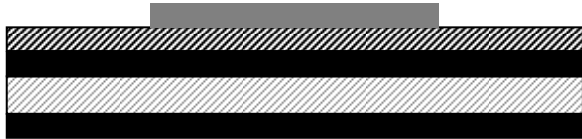
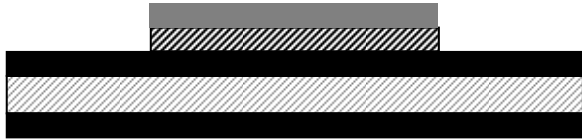


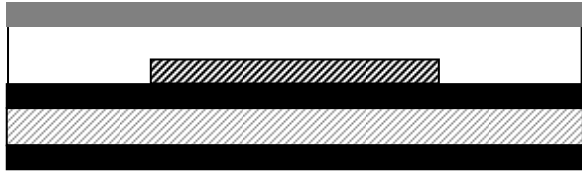
The performance of BMET actuator structures could be further improved by employing a Zn-DLC combination which can deliver four times the work per volume of Al-Si. However, as noted in chapter 3, the capability for fabricating thin film Zn alloys is not sufficiently mature in order to realise microscale structures. Al-Si<sub>3</sub>N<sub>4</sub> is another promising combination which outperforms Al-Si by a factor of 2. Thin films of Al can be deposited on Si<sub>3</sub>N<sub>4</sub> substrates by sputtering which is an established processing route. Detailed micromachining processes and the design of suitable masks to create representative devices of Al-Si<sub>3</sub>N<sub>4</sub> BMET actuator structures in cantilever and clamped configurations have been developed, and these are discussed in detail in the following section.

#### **7.4 Micromachining of Al-Si<sub>3</sub>N<sub>4</sub> BMET microactuators**

Representative devices of Al-Si<sub>3</sub>N<sub>4</sub> BMET actuator structures were fabricated by the *Interdisciplinary Microsystems Group at the University of Florida, Gainesville, U.S.A.* Figure 7.12 shows the process flow sequence to micromachine the BMET actuators. Two different configurations will be fabricated in bimaterial architectures namely, the cantilever and the clamped configurations.

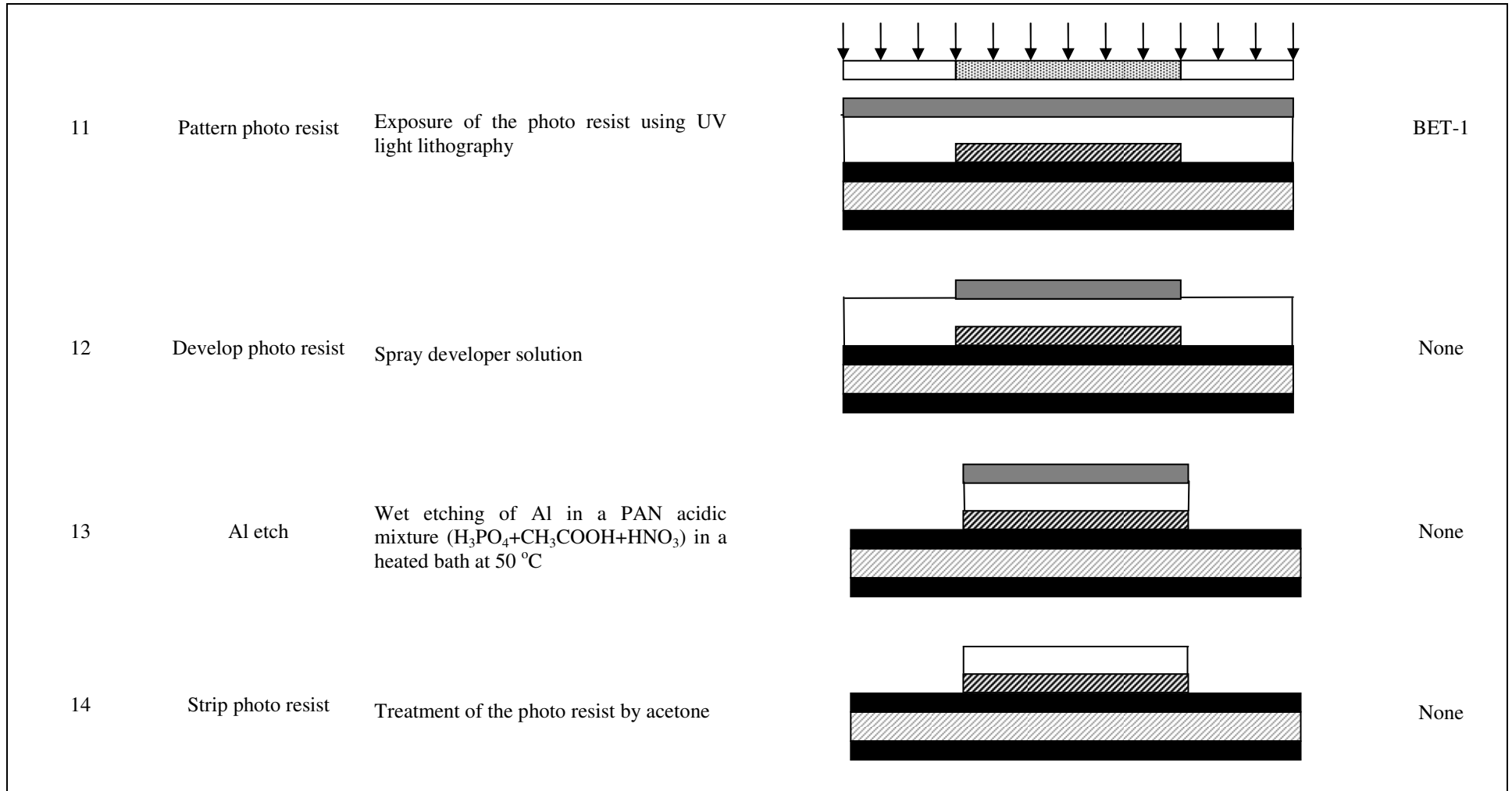
Process No.	Process	Description	Sketch	Masks
1	Plain wafer	-		None
2	Deposit oxide	Plasma enhanced chemical vapour deposition (PECVD) using oxidation of SiH <sub>4</sub> for a layer thickness of ~ 200 nm		None
3	Deposit nitride	PECVD using SiH <sub>2</sub> Cl <sub>2</sub> +NH <sub>3</sub> for a layer thickness of ~ 650 nm		None
4	Apply photo resist	Spin coating of photo resist followed by low temperature baking		None
5	Pattern photo resist	Exposure of the photo resist using UV light lithography		BET-1

Contd...


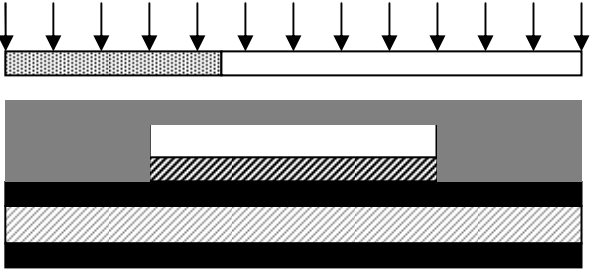
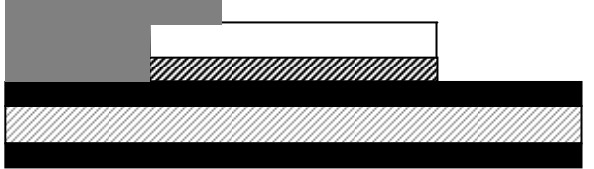
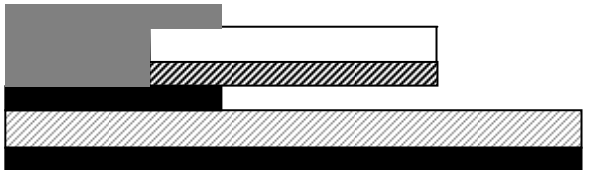
6	Develop photo resist	Spray developer solution		None
7	Nitride etch	Plasma dry etching using $\text{CF}_4/\text{O}_2$ etch gas		None
8	Strip photo resist	Treatment of the photo resist by acetone		None
9	Deposit Al	Sputter deposition. Device layer thickness is $\sim 1.35 \mu\text{m}$		None
10	Apply photo resist	Spin coating of photo resist followed by low temperature baking		None

Contd...





Contd...

15	Apply photo resist	Spin coating of photo resist followed by low temperature baking		None
16	Pattern photo resist	Exposure of the photo resist using UV light lithography		BET-2
17	Develop photo resist	Spray developer solution		None
18	Oxide etch	Wet etch using buffered HF acid		None

Contd...

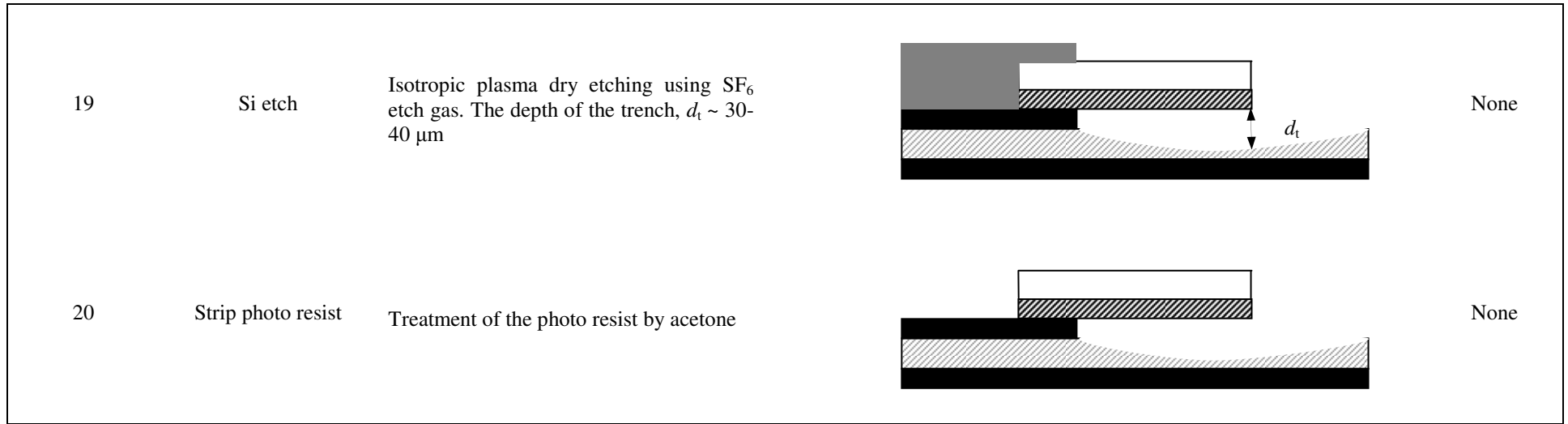


Figure 7.12 Process flow sequence to micromachine Al- $\text{Si}_3\text{N}_4$  BMET actuator structures.

Due to a significant slippage in the microfabrication schedule these devices were not available to test prior to completion of this thesis.

Figures 7.13a and 7.13b show the layout of the masks (BET-1 and BET-2) used for microfabricating the actuators. The masks were created by *Photosciences Inc., U.S.A.* Each actuator structure is accompanied by a pair of bond pads besides the peripheral pads to facilitate testing of the devices. Distinctive alignment marks were made along the horizontal and vertical directions to improve the alignment accuracy. The photolithographic process was carried out using MA6 mask aligner system with a dimensional tolerance of  $\sim 2 \mu\text{m}$ . The masks were designed such that the length of the actuator structures,  $L$  vary from 40-200  $\mu\text{m}$  for constant width ( $b = 30 \mu\text{m}$ ) and thickness ( $t = 2 \mu\text{m}$ ). The distance between the U-shaped conducting paths is 10  $\mu\text{m}$  and the size of the bond pads are  $400 \mu\text{m} \times 400 \mu\text{m}$ .

Preliminary analysis on electromigration reveals that the electrical resistance of the microfabricated structures drop by about 3% for 1hr operation at nominal current densities ( $\sim 10^{10} \text{Am}^{-2}$ ) if 99.999 % pure Al is used. The achievable temperature difference at such current densities is between  $\Delta T = 125 - 200^\circ\text{C}$ . However, commercial Al alloys (Al with 0.5 wt % of Cu) commonly preferred in the microfabrication industry has improved the resistance to electromigration due to the presence of Cu. The drop in electrical resistance is only about 1% for 3 hrs operation under similar conditions if commercial Al alloys are used [155] for microfabricated structures. The mean time to failure (MTTF) estimated from Black's analysis [156] is about  $\sim 161$  hrs for structures made of pure Al. Hence the effect of electromigration on the performance of the actuators should not be a concern during the experimental investigation considering the actual testing time associated with the actuator structures.

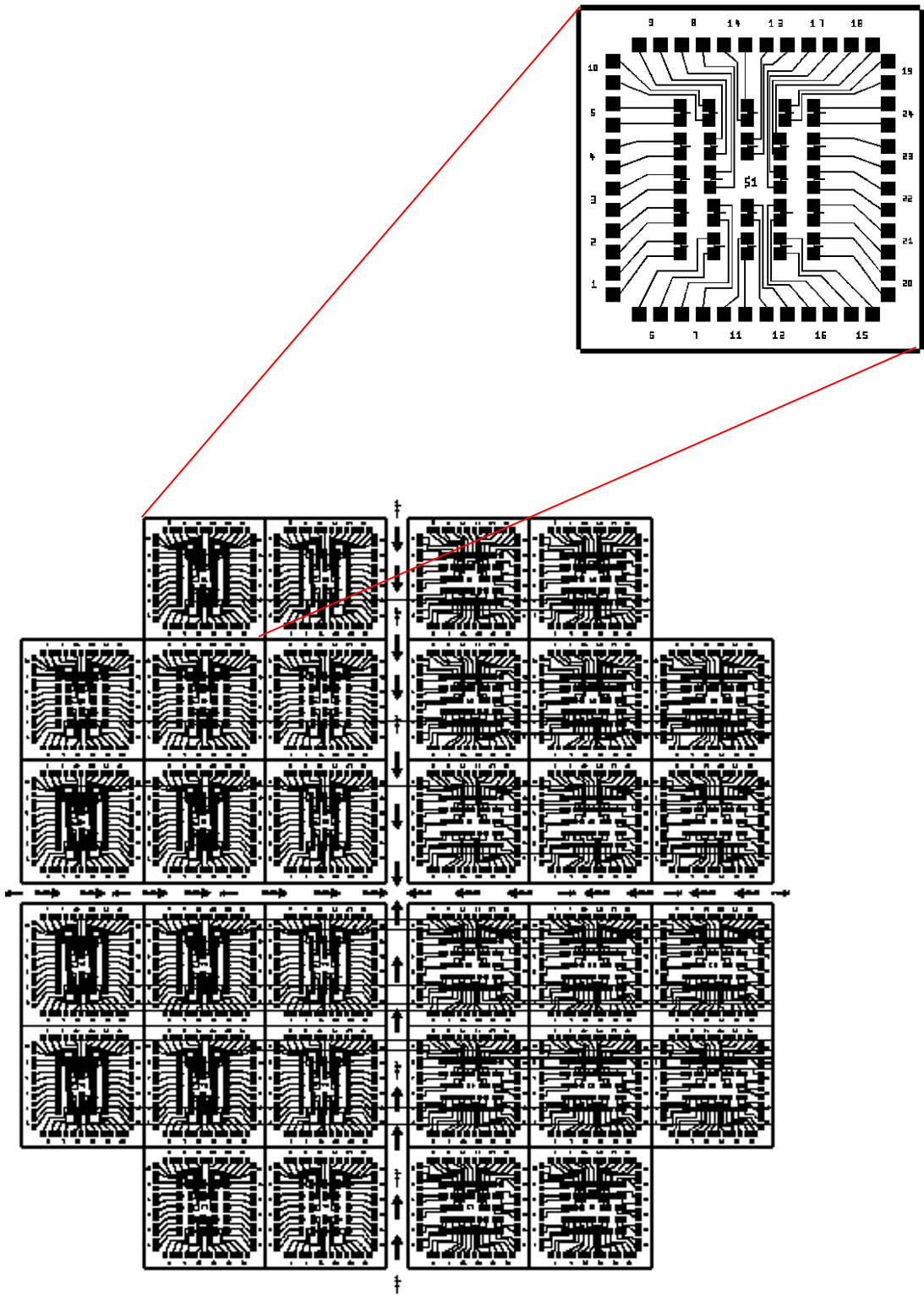


Figure 7.13a Layout of BET-1 mask used in processing steps 5 and 11. The shaded region represents the chrome coated opaque area.

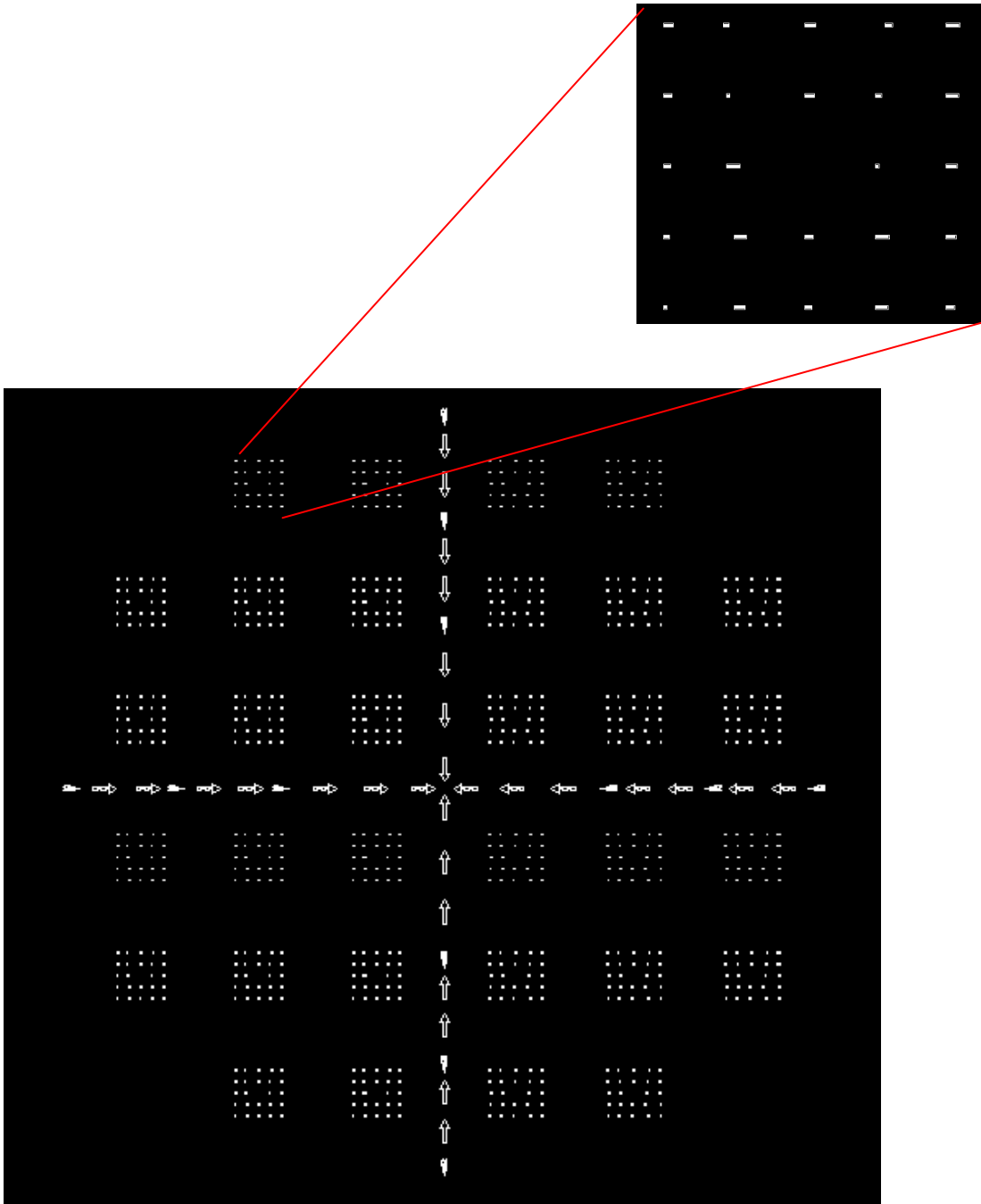
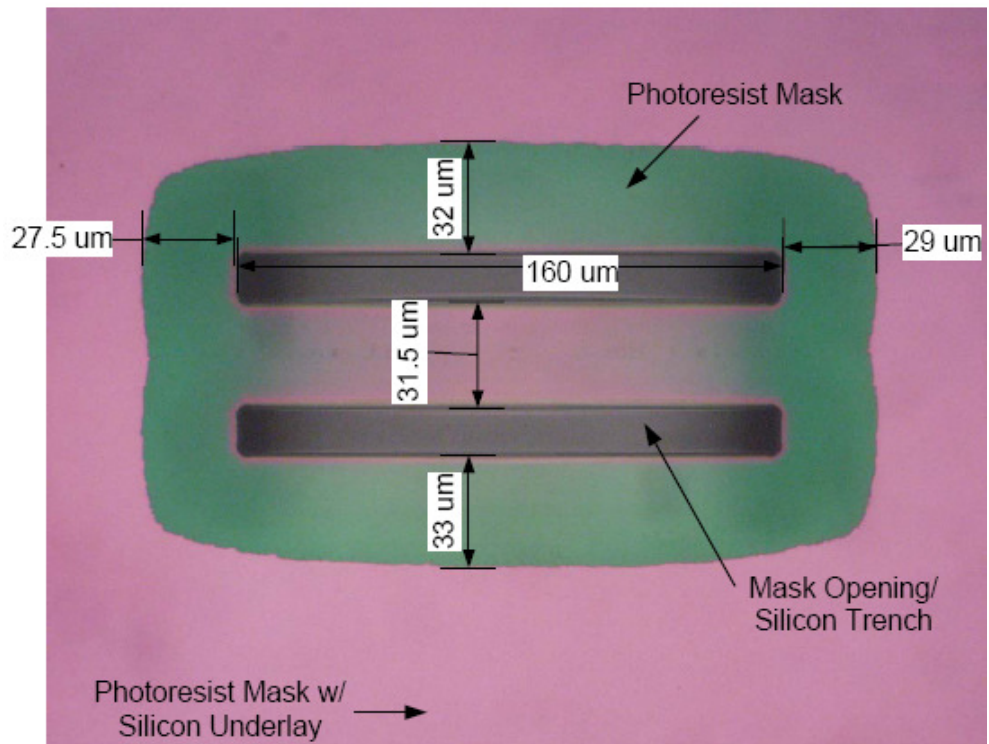
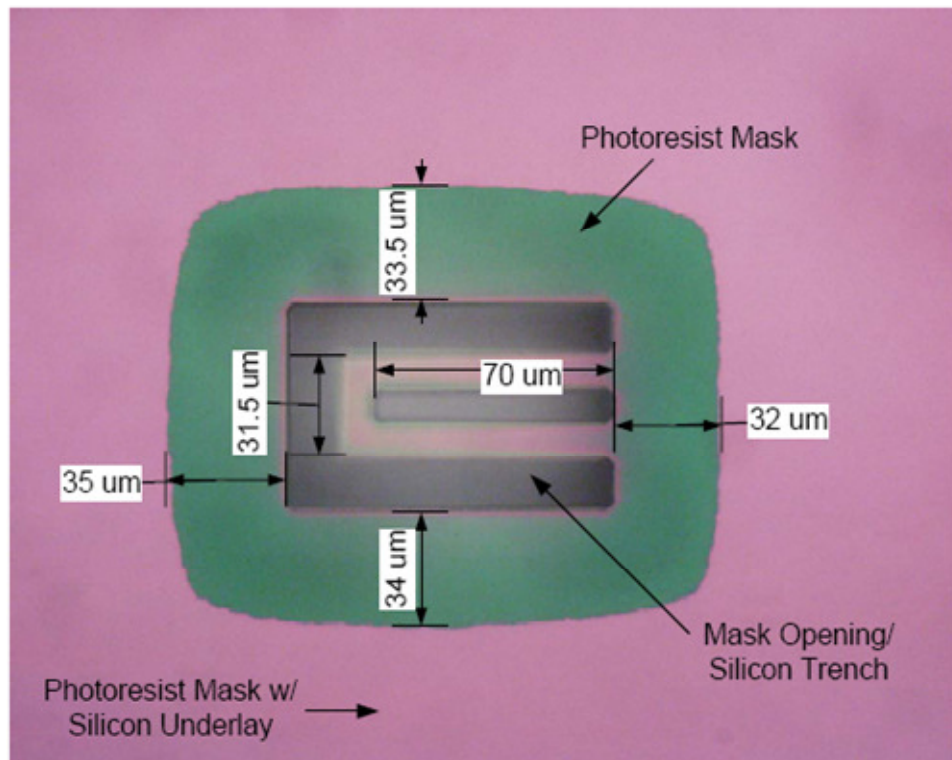


Figure 7.13b Layout of BET-2 mask used in processing step 16. The shaded region represents the chrome coated opaque area.

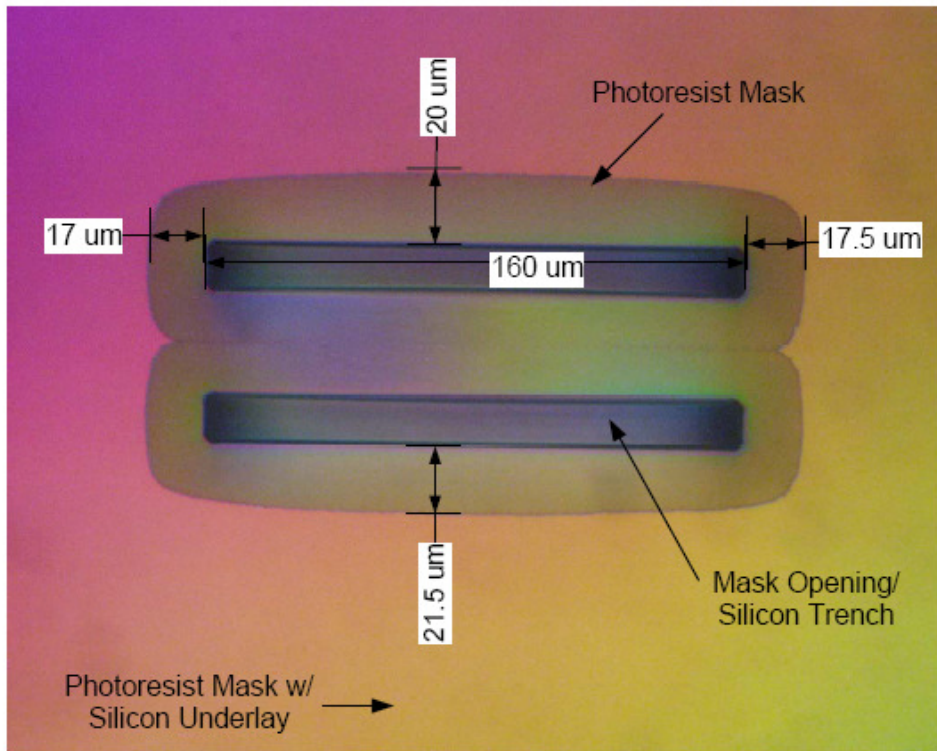


(a)

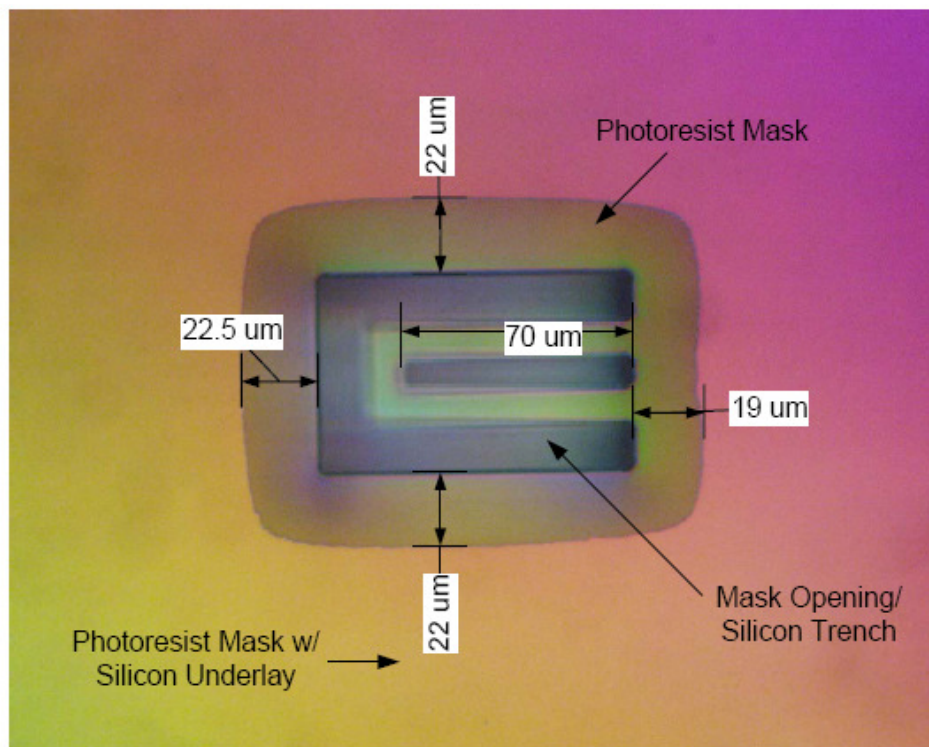


(b)

Figure 7.14 Effect of etch time on the undercut of (a) clamped structure (b) cantilever structure. (No. of cycles = 33, etching/passivation time = 12/7 s, RF platen power = 13 W, etch duration = 16 min 30 s).



(a)



(b)

Figure 7.15 Effect of etch time on the undercut of (a) clamped structure (b) cantilever structure. (No. of cycles = 18, etching/passivation time = 12/7 s, RF platen power = 13 W, etch duration = 9 min 5 s).



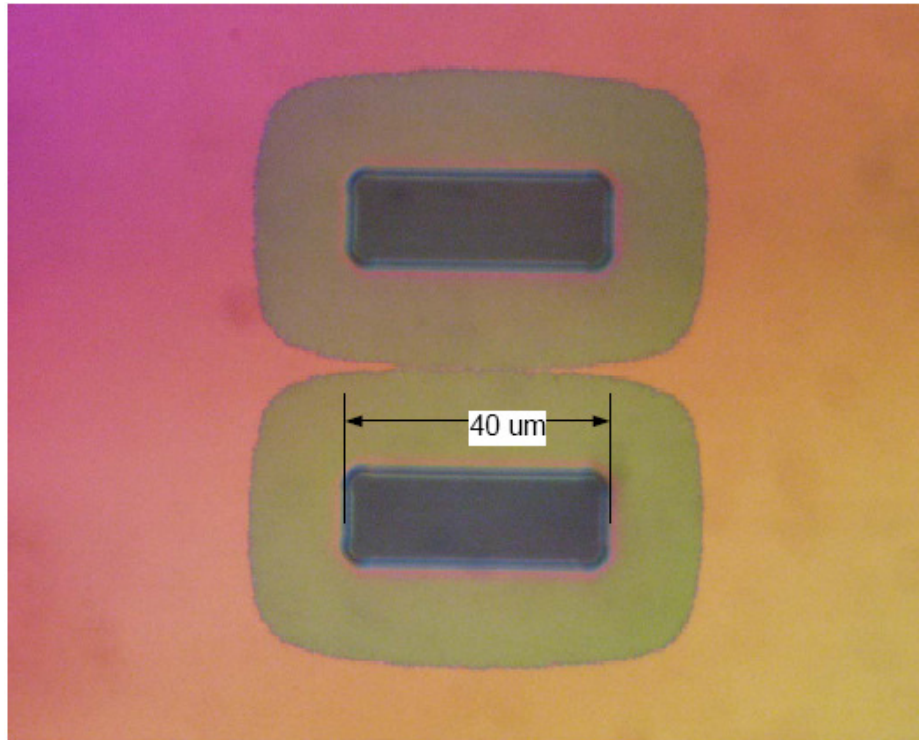
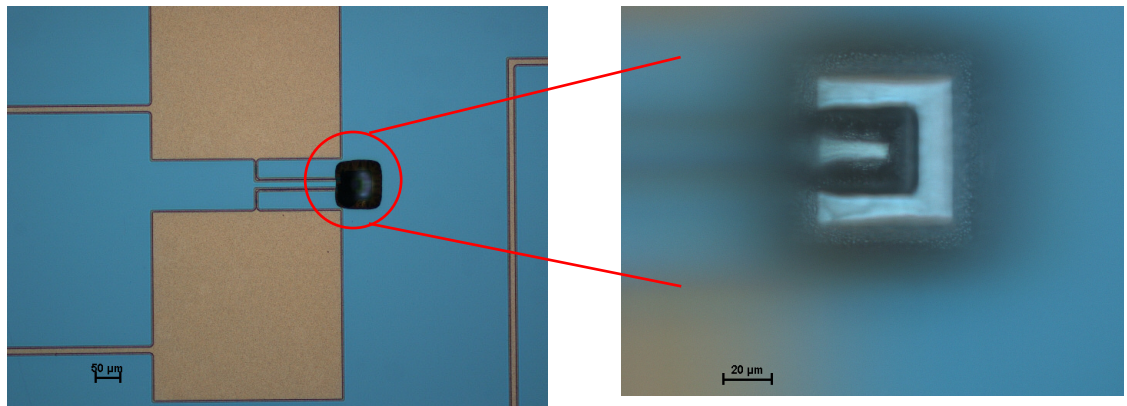
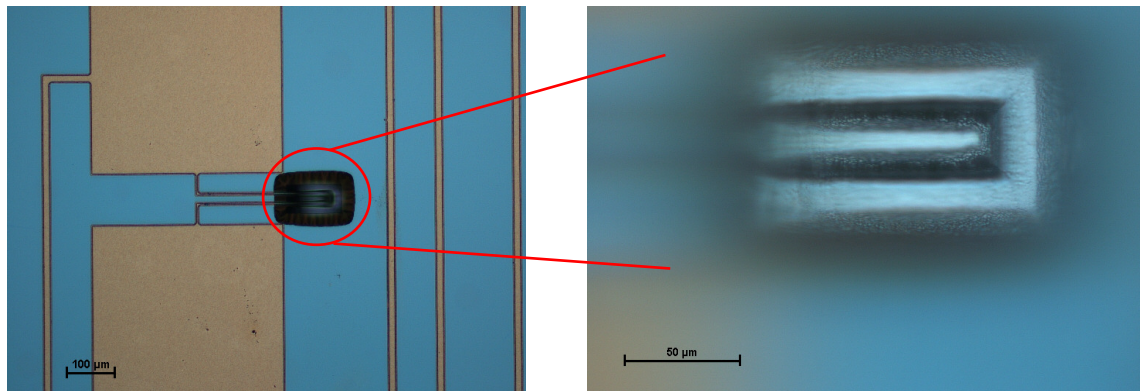


Figure 7.16 Unreleased clamped structure for the reduced etch time (No. of cycles = 18, etching/passivation time = 12/7 sec, RF platen power = 13 W, etch duration = 9 min 5 s).

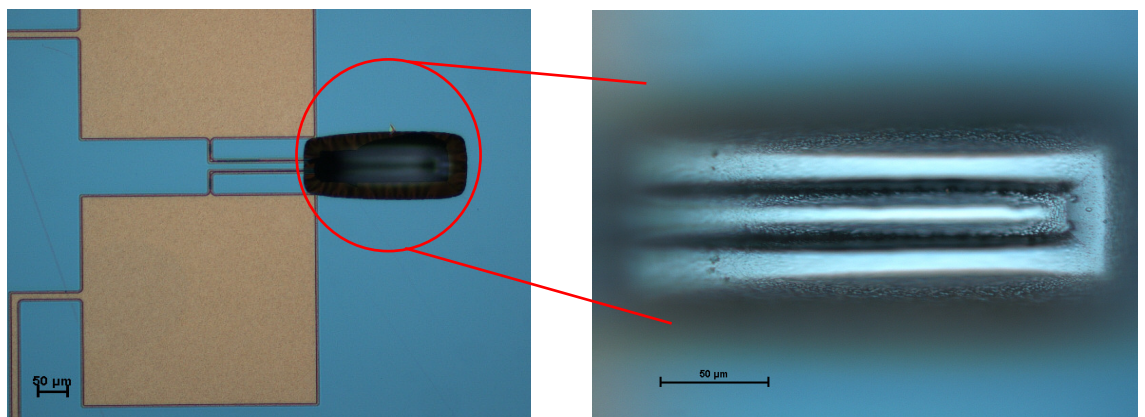
Studies relevant to the preparation of suitable dry etch recipes (Process no. 19) and the effect of etch time on the undercut of silicon were initially performed to maximise the yield of devices. Figures 7.14 and 7.15 show the effect of etch time on the undercut of silicon underneath the clamped and cantilever structures in one of the iterative studies on the test wafers. The structures were obtained by isotropic dry etching of silicon protected by a polymer mask patterned by the optical mask BET-2. The greenish tint along the periphery of the trench gives an indication of the depth of undercut. For an etch duration of 16 min 30 s, the undercut was about  $\sim 30 \mu\text{m}$  and the corresponding depth of the trench was about  $\sim 100 \mu\text{m}$ . A trench depth of at least  $\sim 30 \mu\text{m}$  beneath the tip of the largest cantilever structure ( $L = 200 \mu\text{m}$ ) is required to facilitate the testing of the structures. Although the undercut depth ( $\sim 20 \mu\text{m}$ ) and the trench depth ( $\sim 55 \mu\text{m}$ ) were reduced for an etch time of 9 min 5 s, a few structures at small length scales ( $L = 40, 80 \mu\text{m}$ ) were not released completely. Figure 7.16 shows one of the unreleased clamped structures of length,  $L = 40 \mu\text{m}$ . The thin demarcation between the periphery of the undercut along the middle of the clamped structure clearly indicates that the structure was unreleased. This is attributed to the reduction in the available plasma to etch the silicon at small scales as the etch time is reduced.



(a)

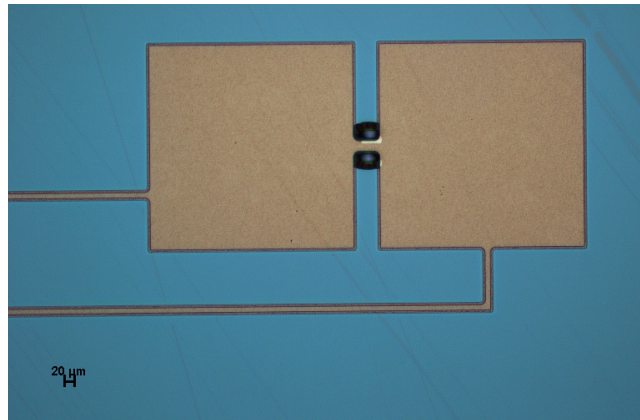


(b)

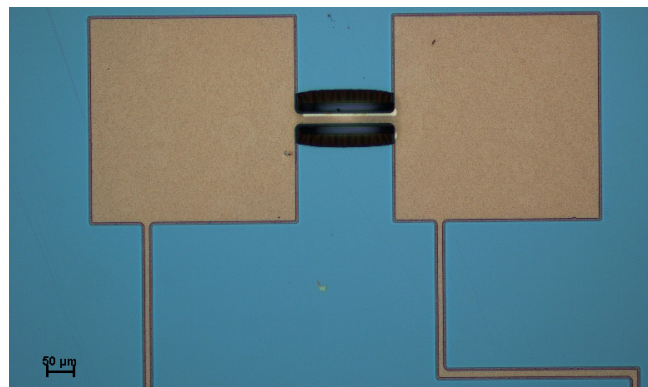


(c)

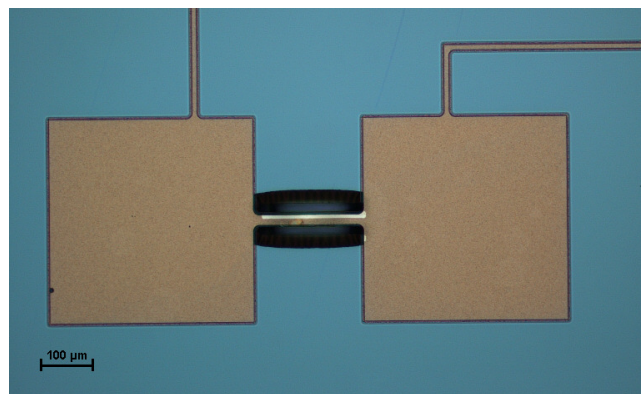
Figure 7.17 Optical microscopic images of microfabricated Al-Si<sub>3</sub>N<sub>4</sub> cantilever bimaterial actuators of length (a)  $L = 40 \mu\text{m}$ , (b)  $L = 100 \mu\text{m}$ , and (c)  $L = 200 \mu\text{m}$ .



(a)



(b)



(c)

Figure 7.18 Optical microscopic images of microfabricated Al-Si<sub>3</sub>N<sub>4</sub> fixed-fixed bimaterial actuators of length (a)  $L = 40 \mu\text{m}$ , (b)  $L = 180 \mu\text{m}$ , and (c)  $L = 200 \mu\text{m}$ .

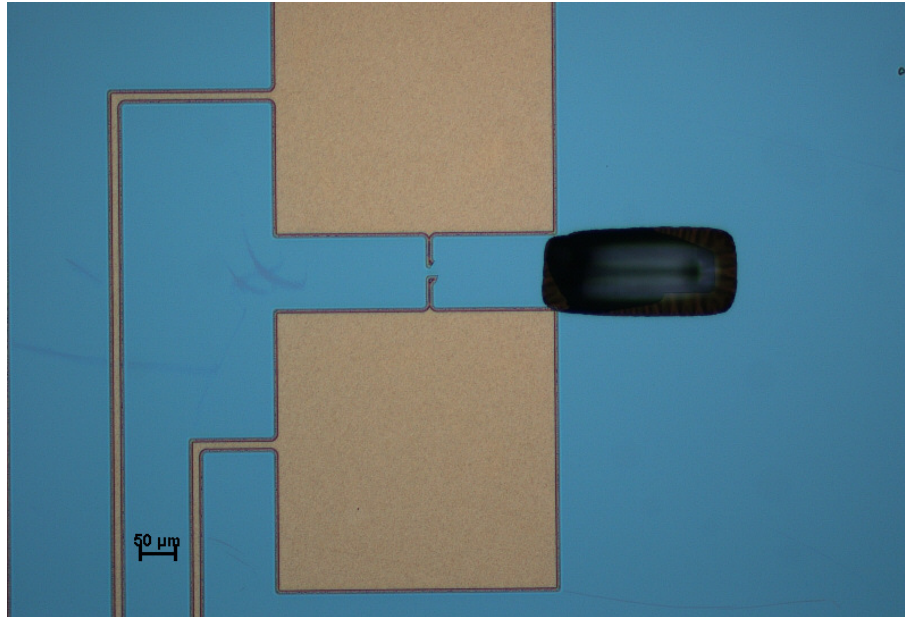


Figure 7.19 Optical microscopic image of Al-Si<sub>3</sub>N<sub>4</sub> cantilever bimaterial actuator of length,  $L = 200 \mu\text{m}$  with damaged electrical contacts due to over etch.

Further studies were carried out to determine an optimal etch time which would yield the maximum number of devices with the minimum possible undercut. Also the inability of the buffered oxide etch solution ( $\text{H}_2\text{O} + \text{HF} + \text{NH}_3\text{F}$ ) to seep completely through the thin oxide layer due to surface tension effects could have resulted in the formation of Al-Si<sub>3</sub>N<sub>4</sub>-SiO<sub>2</sub> tri-layer instead of Al-Si<sub>3</sub>N<sub>4</sub> bimaterial. Further investigations to confirm the presence of the oxide layer if any have to be carried so that it can be appropriately accounted in the detailed finite element simulations.

A total of 3 device wafers (WF-1, WF-2 and WF-4) were processed to ensure availability of sufficient number of structures for experimentation. Figures 7.17 and 7.18 are the optical microscopic images of microfabricated actuators at different length scales in cantilever and clamped configurations respectively. A visual microscopic examination reveals that more than 75 % of devices are available for experimentation in WF-1 and WF-2. However, the Al layer was over etched in WF-4 due to which the electrical contacts of few cantilever structures were broken. Figure 17.19 shows one such structure from WF-4 in which the aluminium conducting path was over etched perhaps during wet etching processes (Process no. 13 and 18).

The final microfabricated structures will be tested in a probe station to evaluate their mechanical performance (displacement, blocked force, work per volume). The

thermal performance (actuation frequency) will be evaluated using a laser vibrometer. The performance metrics evaluated experimentally will provide baseline data for further research studies relevant to flow control applications. Furthermore, metrological studies correlating the actual device features and their undercuts to the relevant process parameters will be documented which could serve as best practice for further research work.

Unlike the solid cross section of layer-2 defined in the analytical models previously (Figure 3.1), the layer-2 topology of the fabricated structure follows the profile of the conducting path. This deviation in the topology is attributed to the cost considerations associated with the number of masks employed. Nevertheless, the topology of the resultant fabricated structure is sufficiently accurate to obtain good estimates of the performance in the preliminary design stage ( $\leq 10\%$  accuracy). The deviations in the experimental results, if any will be corroborated by a detailed finite element simulation considering the realistic dimensions of the actuator structure and accounting for the compliance effect at the anchor locations of the actuators.

## **7.5 Summary**

A comparison of the performance limits of different MEMS actuation schemes is presented, ranking the potential candidate materials. It is found that electrothermal actuation is promising for applications requiring large specific work at frequencies of a few hundred Hertz. Piezoelectric actuators are promising for applications requiring a relatively large force at high frequency. Shape memory actuators (NiTi on Si) are capable of delivering high work per volume at relatively low frequencies ( $<1$  kHz). Although the work per volume delivered by BMET actuators is lower than that of the BMSM by an order of magnitude, electrothermal actuators are capable of actuating at  $\sim 10$  kHz at scales less than  $100\ \mu\text{m}$ . Phase change actuators are superior to other actuators in delivering large work per volume. However, the achievable frequencies are relatively very low. The results presented herein provide guidelines for the selection of MEMS actuators by comparing the best achievable performance from the various actuation schemes. Although a detailed analysis specific to a particular microsystem with due consideration to application specific constraints is required for

further development, the present comparative study would provide an indication of what best could be achieved with the present capability in microfabrication routes.

The suitability of BMET actuators for low speed flow control is discussed by comparing its performance to commonly preferred BMPE actuators. A detailed microfabrication process has been developed with relevant masks design to micromachine Al-Si<sub>3</sub>N<sub>4</sub> BMET actuators. Further research is still in progress evaluate the electrothermal and thermoelastic performance of the microfabricated structures experimentally.

# Chapter 8

## Conclusions and recommendations

“There’s plenty of room at the bottom”

– **Richard P. Feynman**, *American Physical Society*, Caltech., U.S.A, 1959

The ability to process thin films made of novel materials at the microscale has opened doors for new opportunities to enhance the performance limits of MEMS devices. It has also introduced significant challenges which need to be overcome from the micromachining standpoint. This is clearly evident from the novel candidates which are not traditional CMOS materials, identified for various functional requirements for different actuator structures. Further research on the processes which directly result in high quality thin films is required in order to realise MEMS devices made of these materials. Nevertheless, the analyses carried out in this thesis relevant to various MEMS structures serve as useful design guidelines for materials selection which forms the overall aim of the present research.

This chapter is organised as follows. Section 8.1 discusses and summarises the inferences drawn from the analyses performed in the previous chapters. Section 8.2 lists the specific contributions made based on the research outcomes. Section 8.3 highlights the scope for further research studies. Section 8.4 concludes the thesis with closing remarks.

### **8.1 Discussion and summary**

The possibility of realising high performance MEMS devices is dictated by the fundamental change in the design philosophy of MEMS i.e., from process-centric to performance-centric. This transformation relies on continuing research into process development activities relevant to novel thin film materials so that the population of the MEMS materials set can be expanded. The present research is a preliminary work adapting this new design trend by identifying and ranking potential candidate materials for realising high performance MEMS devices. Further detailed studies

specific to various microsystems are essential in order to derive the maximum benefits.

A strategy for selecting novel material combinations for high performance BMET actuators has been developed by understanding the associated physical mechanisms. Using simple beam theory and lumped heat capacity models in conjunction with the relevant 'Ashby' selection map, optimal candidate materials were identified and ranked based on the maximum achievable performance for various functional requirements. The resulting few promising candidates identified beyond the CMOS materials set, however require further research to assess their suitability for MEMS structures. BMET actuators have the potential to operate at actuation frequencies  $\sim 10$  kHz at scales less than  $100 \mu\text{m}$  with optimal choices of engineering alloys/metals on Si/DLC substrates. Zn on DLC substrate deliver the highest achievable work per unit volume compared to other combination at very high frequencies. The most commonly preferred material combination (Al on Si) is bettered by some promising combinations such as Zn on DLC and Al on  $\text{Si}_3\text{N}_4$  for high work per unit volume at high frequencies. Although, Invar is a very promising substrate for high work per unit volume at low frequencies due to its low thermal expansion coefficient, its suitability for MEMS devices requires further research.

The performance limits of ETB actuators were obtained using Euler's buckling theory and lumped capacity thermal models. An analytical framework for materials selection was developed and promising candidates for various functional requirements were identified by plotting iso-performance contours in the domain of material properties. The influence of intrinsic compressive stress on the improvement of actuator performance (actuation frequency and efficiency) was also studied for silicon and DLC substrates. High frequencies between  $\sim 10$ - $100$  kHz could be achieved from ETB structures made of Si and DLC at the microscale.

Unlike electrothermal actuators, the choice of active materials for piezoelectric actuators is very limited. Piezoceramics such as PMN-PT, PZN-PT, PZT and  $\text{BaTiO}_3$  on Si or DLC are promising for large force/work actuators with high transduction indices and efficiency ( $\eta_{\text{em}} \sim 0.1$ ). AlN on Si or DLC substrates



performs better than other alternative candidates for high frequency applications (~ 600 kHz). The suitability of other active materials on different substrates for an actuator design can be assessed by applying impedance matching studies as described in chapter 5. Furthermore, the variation of electromechanical properties of active materials with processing routes demands better understanding on the process-property relationships in order to improve the performance.

For shape memory alloy actuators, NiTi, on Si is a promising combination for high work/volume at frequencies less than ~1 kHz due to its high recovery strains (~ 6% in bulk) over a small temperature change (~ 30-35 °C). However, there is disagreement in the literature regarding the threshold scaling limit for sustenance of the shape memory effect. This is attributed to the dependence of the limiting scale on the processing routes of thin film shape memory alloys.

Polymers are leading potential candidates for the diaphragm materials of thermo-pneumatic actuators. The maximum achievable work per volume by thermo-pneumatic actuators is comparable to that of BMPE actuators at the microscale, although the actuation frequencies are only a few hundred Hertz. Furthermore, there is a limitation on the achievable temperature rise within the cavity thereby making the materials selection for such diaphragms almost insensitive to the maximum achievable pressure.

Although phase change actuators are superior to other actuation schemes in regard to large work per volume delivered, not many choices of materials are available beyond paraffin. Also, the low thermal conductivity of paraffin restricts the actuation frequency of phase change actuators which are close to that achievable by thermo-pneumatic actuators. The suitability of paraffin for reliable MEMS devices requires further research.

## **8.2 Key contributions of the research**

The focus on materials selection for realising high performance MEMS devices with due consideration to length scales and processing routes has led to the following

outcomes beneficial to the research and technical community which are the key contributions of this work.

- i) A strategy for selecting potential candidate materials for commonly employed MEMS actuation schemes has been developed analytically applying mechanics and thermodynamics relations.
- ii) Design guidelines for selecting optimal materials for various functional requirements were provided for BMET, BMPE, BMSM, thermo-pneumatic and phase change microactuator structures.
- iii) Promising candidates for various functional requirements were identified and ranked based on performance for various actuation schemes which could serve as useful basis for further research.
- iv) Selection of microactuators for an application has been illustrated by detailed comparison of the performance limits achievable from different actuation schemes and by a case study on a flow control application.
- v) Effect of processing routes on the variation of thin film properties which thereby affect the performance was illustrated by multiscale performance maps for BMPE actuators.
- vi) A need for transition in the design philosophy (from process-centric to performance-centric design) to realise high performance structures at the microscale has been identified in order to make MEMS technology more mature.

### **8.3 Future scope and recommendations**

The present work has made significant advances in the field of MEMS technology from the materials perspective by understanding the relevant physical mechanisms of the device structures. Further work is essential to translate the preliminary design of the MEMS structures to a promising application. The key tasks itemised as below serve as a short term plan of the present research

- i) Thermoelastic and electrothermal performance of the BMET actuator structures will be evaluated experimentally using a probe station and laser vibrometer.

- ii) The variations in the geometry of the microfabricated structure due to undercuts and alignment errors will be determined from appropriate metrological studies and a realistic finite element model considering the thin film properties will be built and analysed.
- iii) A detailed comparison between the experimentally evaluated performances with the theoretical estimates will be made which would serve as baseline data for further design improvements of flow control actuators.

The present work has left immense scope for further research opportunities which will serve as a long term plan of the on-going research. Some promising directions which could bring significant advancement in the field of MEMS technology are:

- i) The present work has provided a clear indication on the advancements required in the microfabrication routes to process novel thin film materials beyond CMOS candidates. Hence any effort to populate the MEMS materials set with these novel candidates requires a rigorous fundamental research on the relevant physical chemistry. Although the process for developing thin film Zn alloys on metallic substrates such as steel (galvanisation) and copper is established, the ability to extend for processing on other substrates requires a significant effort. The improvements in the capability of the processing routes for thin film layered structures would also have an influence on the MEMS-CMOS integration if the required thermal budget can be met.
- ii) The recent advent of Hafnium, Hf substrates in the microelectronics industry has given an opportunity to realise MEMS structures which deliver better performance than Si substrates. Although the thermoelastic properties of Hf ( $E \sim 138\text{-}144\text{ GPa}$ ;  $\alpha \sim 6 \times 10^{-6}\text{ m.m}^{-1}\text{K}^{-1}$ ) are comparable to that of the Si, its low electrothermal properties ( $\kappa \sim 22\text{-}23\text{ Wm}^{-1}\text{K}^{-1}$ ;  $\rho_r \sim 35 \times 10^{-8}\text{ }\Omega\text{m}$ ) would make it a potential candidate better than Si for high performance, low power electrothermal actuators. Hence assessing the suitability of Hf substrates for MEMS structures could be another promising direction.
- iii) The candidate materials which deliver the best performance in the bi-layered configuration could be a good starting point to realise multilayered composite structures. The materials identified and ranked for different actuation

schemes in this study are promising candidates which can be considered for designing multilayered MEMS structures.

- iv) The ability to realise nanocomposite structures using carbon nanotubes (CNT) has led to the development of new materials with tailored elastic and thermal properties. Hence assessing the performance of thin film layered structures made of CNT based nanocomposites would be an exciting direction to explore further.
- v) The development of NiTi shape memory alloy actuators for MEMS applications is not as advanced as electrothermal and piezoelectric actuators. Hence characterising the properties of thin film NiTi structures considering the effect of scaling and stoichiometric variations is another important step towards development.
- vi) The ability to realise thin film structures made of different materials would provide a significant advantage in designing actuators to work against a range of external mechanical impedances. This would in turn lead to development of novel MEMS devices in different areas of application.

#### **8.4 Closing remarks**

A materials selection strategy has been developed considering the mechanics of actuation in order to identify and rank potential candidates for realising high performance MEMS devices. Apart from the results presented herein, it is believed that the systematic material selection process described here would underscore the importance of performance-centric design philosophy to the MEMS community.

## REFERENCES

1. P. J. Gilgunn, J. Liu, N. Sarkar and G. K. Fedder, "CMOS-MEMS Lateral electrothermal actuators", *Journal of Microelectromechanical Systems*, vol. 17, no. 1, pp.103-114, 2008.
2. D. Pasini, "Shape and materials selection for optimising flexural vibrations in multilayered resonators", *Journal of Microelectromechanical Systems*, vol. 15, no. 6, pp.1745-1758, 2006.
3. G. K. Lau, T. Chu Duc, J. F. L. Goosen, P. M. Sarro and F. van Keulen, "An in-plane thermal unimorph using confined polymers", *Journal of Micromechanics and Microengineering*, vol. 17, pp. S174 - S183, 2007.
4. K. S. Teh, Y. T. Cheng and L. Lin, "Nickel nano-composite film for MEMS applications", *The 12<sup>th</sup> International Conference on Solid State Sensors, Actuators and Microsystems, Boston, U.S.A.*, pp.1534-1537, 2003.
5. J. E. Huber, N. A. Fleck and M. F. Ashby, "The selection of mechanical actuators based on performance indices", *Proceedings of Royal Society A, London*, vol. 453, no. 1965, pp. 2185 - 2205, 1997.
6. D. J. Bell, T. J. Lu, N. A. Fleck and S. M. Spearing, "MEMS actuators and sensors: Observation on their performance and selection for purpose", *Journal of Micromechanics and Microengineering*, vol. 15, pp. S153-164, 2005.
7. L. J. Hornbeck, "Digital light processing and MEMS: Timely convergence for a bright future", *SPIE Micromachining and Microfabrication, Austin, Texas*, 1995.
8. J. K. Luo, A. J. Flewitt, S. M. Spearing, N. A. Fleck and W. I. Milne, "Three types of planar structure microspring electrothermal actuators with insulating beam constraints", *Journal of Micromechanics and Microengineering*, vol. 15, pp. 1527-1535, 2005.
9. J. Singh, T. Gan, A. Agarwal, M. Raj and S. Liw, "3D free space thermally actuated micromirror device", *Sensors and Actuators A*, vol. 123-124, pp. 468-475, 2005.
10. Y. Takahashi and M. Suzuki, "Piezoelectric inkjet printer using laminated piezoelectric actuator", *United States Patent*, Patent no. 5402159, 1995.
11. S. Dong, S. P. Lim, K. H. Lee, J. Zhang, L. C. Lim and K. Uchino, "Piezoelectric ultrasonic micromotor with 1.5mm diameter", *IEEE Transactions on Ultrasonics, Ferroelectrics and Frequency Control*, vol. 53, no. 4, pp. 810-816, 2003.

12. J. Boyd, "Epson's next-generation micro piezo print head boasts macro potential", in *Technology Newslines*, 2007.
13. S. G. Kim and K. H. Hwang, "Thin-film micromirror array (TMA) for large information-display systems", *Journal of the Society for Information Display*, vol. 8, no. 2, pp. 177-181, 2000.
14. S. M. Spearing, "Materials issues in microelectromechanical systems (MEMS)", *Acta Materialia*, vol. 48, pp.179-196, 2000.
15. N. D. Mankame and G. K. Ananthasuresh, "Topology synthesis of electrothermal compliant mechanisms using line elements", *Structural and Multidisciplinary Optimization*, vol. 26, no. 3 - 4, pp. 209-218, 2004.
16. A. C. H. Leung, D. D. Symons and S. D. Guest, "Actuation of kagome lattice structures", *Proceedings of the 45<sup>th</sup> AIAA/ASME/ASCE/AHS/ASC Structures, Structural Dynamics & Materials Conference, Palm Springs, CA, U.S.A*, pp. AIAA-2004-1525, 2004.
17. M. F. Ashby, "*Materials selection in mechanical design*", 1<sup>st</sup> ed., Pergamon press, Oxford, U.K, 1993.
18. V. T. Srikar and S. M. Spearing, "Materials selection for microfabricated electrostatic actuators", *Sensors and Actuators A*, vol. 102, pp. 279-285, 2003.
19. J. K. Luo, J. H. He, Y. Q. Fu, A. J. Flewitt, S. M. Spearing, N. A. Fleck, and W. I. Milne, "Fabrication and characterization of diamond-like-carbon/Ni bimorph normally closed microcages", *Journal of Micromechanics and Microengineering*, vol. 15, pp. 1406-1413, 2005.
20. N. T. Nguyen, S. S. Ho and C. L. N. Low, "A polymeric microgripper with integrated thermal actuators", *Journal of Micromechanics and Microengineering*, vol. 14, pp. 969-974, 2004.
21. M. Y. Aioubi, V. Djakov, S. E. Huq and P. D. Prewett, "Deflection and load characterisation of bimorph actuators for bio MEMS and other applications", *Microelectronic engineering*, vol. 73-74, pp. 898-903, 2004.
22. J. S. Lee, D. S. Park, A. K. Nallani, G. S. Lee and J. B. Lee, "Submicron metallic electrothermal actuators", *Journal of Micromechanics and Microengineering*, vol. 15, pp. 322-327, 2005.
23. D. Bullen, X. Wang, J. Zou, S. W. Chung, C. A. Mirkin and C. Liu, "Design, fabrication and characterization of thermally actuated probe arrays for dip pen nanolithography", *Journal of Microelectromechanical Systems*, vol. 13, no. 4, pp. 594-602, 2004.
24. A. J. Brook, S. J. Bending, J. Pinto, A. Oral, D. Ritchie, H. Beere, A. Springthorpe, and M Henini, "Micromachined III-V cantilevers for AFM-

- tracking scanning Hall probe microscopy", *Journal of Micromechanics and Microengineering*, vol. 13, pp. 124-128, 2003.
25. M. Hopcroft, T. Kramer, G. Kim, K. Takashima, Y. Higo, D. Moore, and J. Brugger, "Micromechanical testing of SU-8 Cantilevers", *Intl. Conf. on Advanced Technology in Experimental Mechanics, JSME-MMD*, pp. 1-6, 2003.
  26. R. R. A. Syms, H. Zou, J. Yao, D. Uttamchandani and J. Stagg, "Scaleable electrothermal MEMS actuator for optical fibre alignment", *Journal of Micromechanics and Microengineering*, vol. 14, pp. 1633-1639, 2004.
  27. L. A. Field, D. L. Burriesci, P. R. Robrish and R. C. Ruby, "Micromachined  $1 \times 2$  optical fibre switch", *Sensors and Actuators A*, vol. 53, pp. 311-315, 1996.
  28. P. Kopka, M. Hoffmann and E. Voges, "Coupled U-shaped cantilever actuators for  $1 \times 4$  and  $2 \times 2$  optical fibre switch", *Journal of Micromechanics and Microengineering*, vol. 10, pp. 260-264, 2000.
  29. M. Hoffmann, P. Kopka and E. Voges, "Bistable micromechanical fibre optic switches on silicon with thermal actuators", *Sensors and Actuators A*, vol. 78, pp. 28-35, 1999.
  30. X. X. Qu, Q. X. Zhang, Q. B. Zou, N. Balasubramanian, P. Yang and K. Y. Zeng, "Characterization of Ti-Al alloy films for potential application in MEMS bimorph actuators", *Material Science in Semiconductor Processing*, vol.5, pp. 35-38, 2002.
  31. V. T. Srikar and S. M. Spearing, "Material selection in Micromechanical design", *Journal of Microelectromechanical Systems*, vol. 12, pp. 3-10, 2003.
  32. S. M. Spearing, "Design diagrams for layered materials", *AIAA Journal*, vol. 35, pp. 1638-44, 1997.
  33. S. Timoshenko, "Analysis of bimetal thermostats", *Journal of the Optical Society of America*, vol. 11, pp. 233-255, 1925.
  34. R. G. Budynas, "Advanced Strength and Applied Stress Analysis", 2<sup>nd</sup> ed., McGraw-Hill Intl., Singapore, pp. 302-309, 1999.
  35. G. Perluzzo, C. K. Jen and E. L. Adler, "Characteristics of reactive magnetron sputtered ZnO films", *Ultrasonics Symposium Proceedings, IEEE*, pp. 373-376, 1989.
  36. Y. Zhu, H. Wang and P. P. Ong, "Composite zinc/silicon nanocrystalline thin film: preparation, structures and the effect of oxidation on their photoluminescence", *Journal of Physics: Condensed Matter*, vol. 13, pp. 787-795, 2001.

37. L. Tan, Y. P. Kong, L. R. Bao, X. D. Huang, L. J. Guo, S. W. Pang, and A. F. Yee, "Imprinting polymer film on patterned substrates", *Journal of Vacuum Science and Technology B*, vol. 21, no. 6, pp. 2742-2748, 2003.
38. H. Sehr, I. S. Tomlin, B. Huang, S. P. Beeby, A. G. R. Evans, A. Brunnschweiler, G. J. Ensell, C. G. J. Schabmueller, and T. E. G. Niblock, "Time constant and lateral resonances of thermal vertical bimorph actuators", *Journal of Micromechanics and Microengineering*, vol. 12, pp. 410-413, 2002.
39. L. H. Han and S. Chen, "Wireless bimorph microactuators by pulsed laser heating", *Sensors and Actuators A*, vol. 121, pp. 35-43, 2005.
40. W. P. King, "Design analysis of heated atomic force microscope cantilevers for nanotopography measurements", *Journal of Micromechanics and Microengineering*, vol. 15, pp. 2441-2448, 2005.
41. J. P. Holman, "*Heat transfer*", 9<sup>th</sup> ed., McGraw-Hill series, Boston, U.S.A, pp. 133-135, 2004.
42. J. Y. W. Seto, "The electrical properties of polycrystalline silicon films", *Journal of Applied Physics*, vol. 48, no. 12, pp. 5247-5254, 1975.
43. A. A. Voevodin, M. S. Donley and J. S. Zabinski, "Pulsed laser deposition of diamond-like carbon wear protective coatings", *Surface and Coatings Technology*, vol. 92, pp. 42-49, 1997.
44. J. Schwan, S. Ulrich, E. Ehrhardt, S. R. P. Silva, J. Robertson, R. Samlenski, and R. Brenn, "Tetrahedral amorphous carbon films prepared by magnetron sputtering and dc ion plating", *Journal of Applied Physics*, vol. 79, no. 3, pp. 416-422, 1996.
45. A. C. Ferrari, B. Kleinsorge, N. A. Morrison, A. Hart, V. Stolojan and J. Robertson, "Stress reduction and bond stability during thermal annealing of tetrahedral amorphous carbon", *Journal of Applied Physics*, vol. 85, no. 10, pp. 7191-7197, 1999.
46. M. Inoue, K. Hashizume and H. Tsuchikawa, "The properties of aluminium thin films sputter deposited at elevated temperatures", *Journal of Vacuum Science and Technology*, vol. 6, pp. 1636-1639, 1988.
47. D. S. Gardner and P. A. Flinn, "Mechanical stress as a function of temperature in aluminum films", *IEEE Transactions on Electron Devices*, vol. 35, no. 12, pp. 2160-2169, 1988.
48. G. H. Tang, Y. H. Zhang and D. R. Emerson, "Lattice Boltzmann models for non-equilibrium gas flows", *Physical Review E* 77, pp. 046701(1-6), 2008.
49. A. J. Chapman, "*Heat transfer*", 4<sup>th</sup> ed., Macmillan publishing company, Newyork, U.S.A, pp. 210-219, 1984.



50. S. A. Jacobson and W. C. Reynolds, "Active control of streamwise vortices and streaks in boundary layers", *Journal of Fluid Mechanics*, vol. 360, pp. 179-211, 1998.
51. T. Segawa, Y. Kawaguchi, Y. Kikushima and H. Yoshida, "Active control of streak structures in wall turbulence using an actuator array producing inclined wavy disturbances", *Journal of Turbulence*, vol. 3, pp. 1-14, 2002.
52. J. R. Frutos, D. Vernier, F. Bastien, M. D. Labachellerie and Y. Bailly, "An electrostatically actuated valve for turbulent boundary layer control", *Sensors 2005, IEEE*, pp. 82-88, 2005.
53. M. McCarthy, N. Tiliakos, V. Modi and L. G. Frechette, "Thermal buckling of eccentric microfabricated nickel beams as temperature regulated nonlinear actuators for flow control", *Sensors and Actuators A: Physical*, vol. 134, no. 1, pp.37- 46, 2007.
54. T. Seki, M. Sakata, T. Nakajima and M. Matsumoto, "Thermal buckling actuators for microrelays", *IEEE International Conference on Solid-State Sensors and Actuators*, no. 0-7803-3829-4, pp. 1153-1156, 1997.
55. T. Lisec, S. Hoerschelmann, H. J. Ouenzer, B. Wagner and W. Benecke, "Thermally driven microvalve with buckling behaviour for pneumatic applications", *IEEE Proceedings, Workshop on MEMS*, no. 0-7803-1833-1, pp. 13-17, 1994.
56. A. Cao, J. B. Kim, T. Tsao and L. Lin, "A bidirectional electrothermal electromagnetic actuator", *17<sup>th</sup> IEEE Conference on MEMS*, pp. 450-453, 2004.
57. M. Chiao and L. Lin, "Self-buckling of micromachined beams under resistive heating", *Journal of Microelectromechanical Systems*, vol. 9, no. 1, pp. 146-151, 2000.
58. L. Lin and S. H. Line, "Vertically driven microactuators by electrothermal buckling effects", *Sensors and Actuators A*, vol. 71, pp. 35-39, 1998.
59. P. T. Boyer, E. Scheid, G. Faugere and B. Rousset, "Residual stress in silicon films deposited by LPCVD from disilane", *Thin Solid Films*, vol. 310, pp. 234-237, 1997.
60. T. A. Friedman, J. P. Sullivan, J. A. Knapp, D. R. Tallant, D. M. Follstaedt, D. L. Medlin, and P. B. Mirkarimi, "Thick stress-free amorphous-tetrahedral carbon films with hardness near that of diamond", *Applied Physics Letters*, vol. 71, no. 26, pp. 3820-3822, 1997.
61. R. T. Howe and R. S. Muller, "Stress in polycrystalline and amorphous silicon thin films", *Journal of Applied Physics*, vol. 54, no. 8, pp.4674-4675, 1983.

62. X. L. Peng and T. W. Clyne, "Mechanical stability of DLC films on metallic substrates: Part I - Film structure and residual stress levels", *Thin Solid Films*, vol. 312, no. 1-2, pp. 207-218, 1998.
63. C. T. Kuo, C. R. Lin and H. W. Lien, "Origin of residual stresses in CVD diamond films", *Thin Solid Films*, vol. 290-291, pp. 254-259, 1996.
64. S. P. Murarka and T. F. Retajczyk Jr., "Effect of phosphorous doping on stress in silicon and polycrystalline silicon", *Journal of Applied Physics*, vol. 54, no. 4, pp. 2069-2072, 1983.
65. Y. Q. Fu, J. K. Luo, A. J. Flewitt, S. E. Ong, S Zhang and WI Milne, "Laser micromachining of sputtered DLC films", *Applied Surface Sciences*, vol. 252, pp. 4914-4918, 2006.
66. N. G. Shang, C. S. Lee, Z. D. Lin, I. Bello and S. T. Lee, "Intrinsic stress evolution in diamond films prepared in a CH<sub>4</sub>-H<sub>2</sub>-NH<sub>3</sub> hot filament chemical vapour deposition system", *Diamond and Related Materials*, vol. 9, pp. 1388-1392, 2000.
67. H. Yamada, O. Tsuji and P. Wood, "Stress reduction for hard amorphous hydrogenated carbon thin films deposited by the self-bias method", *Thin Solid Films*, vol. 270, pp. 220-225, 1995.
68. S. G. Wang, Q. Zhang, S. F. Yoon, J. Ahn, Q. Wang, D. J. Yang, Q. Zhou, and N. L. Yue, "Optical properties of nano-crystalline diamond films deposited by MPECVD", *Optical materials*, vol. 24, pp. 509-514, 2003.
69. H. Windischmann, G. F. Epps, Y. Cong and R. W. Collins, "Intrinsic stress in diamond films prepared by microwave plasma CVD", *Journal of Applied Physics*, vol. 69, no. 4, pp. 2231-2237, 1991.
70. J. Robertson, "Diamond-like carbon", *International Union of Pure and Applied Chemistry*, vol. 66, pp.1789-1796, 1994.
71. J. Robertson, "Improving the properties of diamond-like carbon", *Diamond and Related Materials*, vol. 12, pp. 79-84, 2003.
72. A. C. Ferrari, S. E. Rodil, J. Robertson and W. I. Milne, "Is stress necessary to stabilise sp<sup>3</sup> bonding in diamond-like carbon?" *Diamond and Related Materials*, vol. 11, no. 3-6, pp. 994-999, 2002.
73. T. A. Friedman and J. P. Sullivan, "Method of forming a stress relieved amorphous tetrahedrally-coordinated carbon films", *United States Patent*, No. Patent no. 6103305, 2000.
74. R. Maeda, J. J. Tsaur, S. H. Lee and M. Ichiki, "Piezoelectric microactuator devices", *Journal of Electroceramics*, vol. 12, no. 1-2, pp. 89 - 100, 2004.

75. J. Friend, A. Umeshima, T. Ishii, K. Nakamura and S. Ueha, "A piezoelectric linear actuator formed from a multitude of bimorphs", *Sensors and Actuators A*, vol. 109, pp. 242-251, 2004.
76. P. J. Rayner, S. A. Wilson, R. W. Whatmore and M. Cain, "An automated performance testing system for piezoelectric micromotors", *The IET Seminar on MEMS Sensors & Actuators, London*, pp. 233-236, 2006.
77. S. Priya, H. Kim, S. Ural and K. Uchino, "High power universal piezoelectric transformer", *IEEE Transactions on Ultrasonics, Ferroelectrics and Frequency Control*, vol. 53, no. 4, pp.361-367, 2006.
78. X. Yang, Z. Zhou, H. Cho and X. Luo, "Study on PZT actuated diaphragm pump for air supply for micro fuel cells", *Sensors and Actuators A*, vol. 1301-131, pp. 531-536, 2006.
79. D. C Roberts, H. Li, L. Steyn, O. Yaglioglu, S. M. Spearing, M. A. Schmidt, and N. W. Hagood, "A Piezoelectric microvalve for compact high-frequency, high-differential pressure hydraulic micropumping system", *Journal of Microelectromechanical Systems*, vol. 12, no. 1, pp. 81-92, 2003.
80. S. R. Platt, S. Farritor and H. Haider, "On low frequency electric power generation with PZT ceramics", *IEEE / ASME Transactions of Mechatronics*, vol. 10, No. 2, pp. 240-252, 2005.
81. H. Jaffe and D. A. Berlincourt, "Piezoelectric transducer materials", *Proceedings of the IEEE*, vol. 53, no. 10, pp.1362-1386, 1965.
82. R. F. S. Hearmon, "The elastic constants of piezoelectric crystals", *British Journal of Applied Physics*, vol. 3, no. 4, pp. 120-124, 1952.
83. J. G. Gualtieri, J. A. Kosinski and A. Ballato, "Piezoelectric materials for acoustic wave applications", *IEEE Transactions on Ultrasonics, Ferroelectrics and Frequency control*, vol. 41, no. 1, pp. 53-59, 1994.
84. D. L. DeVoe and A. P. Pisano, "Modelling and optimal design of piezoelectric cantilever microactuators", *Journal of Microelectromechanical Systems*, vol. 6, no. 3, pp.266-270, 1997.
85. Q. M. Wang and L. E. Cross, "Performance analysis of piezoelectric cantilever bending actuators", *Ferroelectrics*, vol. 215, pp. 187-213, 1998.
86. Q. M. Wang, X. H. Du, B. Xu and L. E. Cross, "Electromechanical coupling and output efficiency of piezoelectric bending actuators", *IEEE Transactions on Ultrasonics, Ferroelectrics and Frequency Control*, vol. 46, no. 3, pp. 638-646, 1999.
87. Y. Jeon, R. Sood, L. Steyn and S. G. Kim, "Energy harvesting MEMS devices based on  $d_{33}$  mode piezoelectric  $\text{Pb}(\text{Zr}, \text{Ti})\text{O}_3$  thin film cantilever",

- CIRP Seminar on Micro and Nano Technology, Copenhagen, Denmark, 2003.*
88. R. Waser, "Nanoelectronics and Information Technology", 2<sup>nd</sup> ed., Wiley-VCH, pp. 61-78, 2005.
  89. V. M. Fridkin and S. Ducharme, "General features of the intrinsic ferroelectric coercive field", *Physics of Solid State*, vol. 43, no. 7, pp.1320-1324, 2001.
  90. I. I. D. Kim, Y. Avrahami and H. L. Tuller, "Study of orientation effect on nanoscale polarization in BaTiO<sub>3</sub> thin films using piezo-response force microscopy", *Applied Physics Letters*, vol. 86, pp. 192907(1-3), 2005.
  91. H. B. Sharma and A. Mansingh, "Sol-gel processed barium titanate ceramics and thin films", *Journal of Materials Science*, vol. 33, no. 17, pp. 4455-4459, 1998
  92. M. Sayer, "Piezoelectric thin film devices", *Proceedings of the IEEE Ultrasonics Symposium*, pp. 595-603, 1991.
  93. S. K. Pandey, A. R. James, C. Prakash, T. C. Goel and K. Zimik, "Electrical properties of PZT thin films grown by sol-gel and PLD using a seed layer", *Materials Science and Engineering B*, vol. 112, pp. 96-100, 2004.
  94. N. A. Pertsev, J. R. Contreras, V. G. Kukhar, B. Hermanns, H. Kohlstedt and R. Waser, "Coercive field of ultrathin Pb(Zr<sub>0.52</sub>Ti<sub>0.48</sub>)O<sub>3</sub> epitaxial films", *Applied Physics Letters*, vol. 83, no. 16, pp. 3356-3358, 2003.
  95. C. Ayela, L. Nicu, C. Soyer, E. Cattan and C. Bergaud, "Determination of the d<sub>31</sub> piezoelectric coefficient of PbZr<sub>x</sub>Ti<sub>1-x</sub>O<sub>3</sub> thin films using multilayer buckled membranes", *Journal of Applied Physics*, vol. 100, pp. 054908(1-9), 2006.
  96. A. W. Warner, M. Onone and G. A. Coquin, "Determination of elastic and piezoelectric constants for crystals in class (3m)", *The Journal of the Acoustical Society of America*, vol. 42, no. 6, pp. 1223-1231, 1967.
  97. S. Kim, V. Gopalan and A. Gruverman, "Coercive fields in ferroelectrics: A case study in lithium niobate and lithium tantalate", *Applied Physics Letters*, vol. 80, no. 15, pp. 2740-2742, 2002.
  98. C. S. Brown, R. C. Kell, R. Taylor and L. S. Thomas, "Piezoelectric materials, A review of progress", *IRE Transactions on Component Parts*, vol. 9, no. 4, pp. 193-211, 1962.
  99. H. Wang, Q. M. Zhang, L. E. Cross and A. O. Sykes, "Piezoelectric, dielectric and elastic properties of poly (vinylidene fluoride/trifluoroethylene)", *Journal of Applied Physics*, vol. 74, no. 5, pp. 3394-3398, 1993.

100. K. Tanaka, R. Kubo, K. Ohwada, A. Umeda, K. Ueda and T. Usuda, "Measurement of piezoelectric constant of ZnO film on Si microstructure", *Japanese Journal of Applied Physics*, vol. 34, pp. 5230-5232, 1995.
101. I. L. Guy, S. Muensit and E. M. Goldys, "Extensional piezoelectric coefficients of gallium nitride and aluminum nitride", *Applied Physics Letters*, vol. 75, no. 26, pp. 4133-4135, 1999.
102. P. E. J Sebastain, "Monitoring of refractory wall recession using high temperature impact-echo instrumentation", *U.S Department of Energy, contract DE\_FG36-02GO12051, UDR-TR-2004-00018 report*, 2004.
103. J. E. A. Southin, S. A. Wilson, D. Schmitt and R. W. Whatmore, " $e_{31,f}$  determination for PZT films using conventional ' $d_{33}$ ' meter", *Journal of Physics D: Applied Physics*, vol. 34, pp. 1456-1460, 2001.
104. R. Bechmann, "Elastic and piezoelectric constants of alpha-quartz", *Physical Review*, vol. 110, no. 5, pp.1060-1061, 1958.
105. A. O. dos Santos, W. H. yaegashi, R. Marcon, B. B. Li, R. V. Gelamo, L. P. Cardoso, J. M. Sasaki, M. A. R Miranda, and F. E. A. Mello, "Rochelle salt piezoelectric coefficients obtained by x-ray multiple diffraction", *Journal of Physics: Condensed Matter*, vol. 13, pp. 10497-10505, 2001.
106. R. Zhang, B. Jiang and W. Cao, "Elastic, piezoelectric and dielectric properties of multi domain  $0.67\text{Pb}(\text{Mg}_{1/3}\text{Nb}_{2/3})\text{O}_3 - 0.33\text{PbTiO}_3$  single crystals", *Journal of Applied Physics*, vol. 90, no. 7, pp.3471-3475, 2001.
107. H. Maiwa and N. Ichinose, "Electrical and electromechanical properties of  $\text{Pb}(\text{Mg}_{1/3}\text{Nb}_{2/3})\text{O}_3$  (50%) –  $\text{PbTiO}_3$  (50%) thin films prepared by chemical solution deposition", *Japanese Journal of Applied Physics*, vol. 42, no. 2A, pp. 850-854, 2006.
108. R. Zhang, B. Jiang, W. Jiang and W. Cao, "Complete set of properties of  $0.92\text{Pb}(\text{Zn}_{1/3}\text{Nb}_{2/3})\text{O}_3-0.08\text{PbTiO}_3$  single crystal with engineered domains", *Materials Letters*, vol. 57, pp. 1305-1308, 2003.
109. M. Sitti, D. Campolo, J. Yan and R. S. Fearing, "Development of PZT and PZN-PT based unimorph actuators for micromechanical flapping mechanisms", *Proceedings of the 2001 IEEE Intl. conference on Robotics and Automation, Seol, Korea*, pp. 3839-3846, 2001.
110. J. Yin and W. Cao, "Effective macroscopic symmetries and materials properties of multidomain  $0.955\text{Pb}(\text{Zn}_{1/3}\text{Nb}_{2/3})\text{O}_3-0.045\text{PbTiO}_3$  single crystals", *Journal of Applied Physics*, vol. 92, no. 1, pp. 444 - 448, 2002.
111. S. Zhang, L. Lebrun, S. Rhee, C. A. Randall and T. R. Shrout, "Dielectric and Piezoelectric properties as a function of temperature for  $\text{Pb}(\text{Yb}_{1/2}\text{Nb}_{1/2})\text{O}_3-$

- PbTiO<sub>3</sub> single crystals", *Proceedings of the Thirteenth IEEE International symposium on Applications of Ferroelectrics*, pp. 455-458, 2002.
112. S. J. Zhang, S. Rhee, C. A. Randall and T. R. Shrout, "Dielectric and piezoelectric properties of high curie temperature single crystals in the Pb(Yb<sub>1/2</sub>Nb<sub>1/2</sub>)O<sub>3</sub> – PbTiO<sub>3</sub> solid solution series", *Japanese Journal of Applied Physics*, vol. 41, no. 2A, pp. 722-726, 2002.
  113. Q. F. Zhou, Q. Q. Zhang and S. T. McKinstry, "Structure and piezoelectric properties of sol-gel-derived (001)-oriented Pb[Yb<sub>1/2</sub>Nb<sub>1/2</sub>]O<sub>3</sub>-PbTiO<sub>3</sub> thin films", *Journal of Applied Physics*, vol. 94, no. 5, pp. 3397-3402, 2003.
  114. D. Cebon and M. F. Ashby, "Materials selection for precision instruments", *Measurement Science and Technology*, Vol. 5, pp.296-306, 1994.
  115. A. D. Nashif, D. I. G. Jones and J. P. Henderson, "*Vibration damping*", John Wiley and Sons, New York, USA, 1985.
  116. J. D. Irwin and R. M. Nelms, "*Basic engineering circuit analysis*", 8<sup>th</sup> ed., John Wiley and Sons Inc., USA, pp. 173-175, 2005.
  117. E. T. Carlen and C. H. Mastrangelo, "Electrothermally actuated paraffin microactuators", *Journal of Microelectromechanical Systems*, vol. 11, no. 3, pp. 165-174, 2002.
  118. A. Mullen, "Temperature variation of the piezoelectric constant of quartz", *Journal of Applied Physics*, vol. 40, no. 4, pp. 1693-1696, 1969.
  119. S. Noge and T. Uno, "Measurement of piezoelectric and elastic stiffness constants of β phase quartz at high temperature region", *IEEE Ultrasonics Symposium*, pp. 585-597, 1998.
  120. J. Valasek, "Piezoelectric and allied phenomena in Rochelle salt", *Physical Reviews*, vol. 17, No. 4, pp. 475-481, 1921.
  121. W. G. Cady, "The longitudinal piezoelectric effect in Rochelle salt crystals", *Proceedings of the Physical Society*, vol. 49, pp. 646-653, 1937.
  122. M. Iwata and Y. Ishibashi, "Theory of morphotropic phase boundary in solid solution systems of perovskite-type oxide ferroelectrics: Engineered domain configuration", *Japanese Journal of Applied Physics*, vol. 39, pp. 5156-5163, 2000.
  123. H. Sehr, A. G. R. Evans, A. Brunnschweiler, G. J. Ensell and T. E. G. Niblock, "Fabrication and test of thermal vertical bimorph actuators for movement in wafer plane", *Journal of Micromechanics and Microengineering*, vol. 11, pp. 306-310, 2001.

124. P. Krulevitch, A. P. Lee, P. B. Ramsey, J. C. Trevino, J. Hamilton and M. A. Northrup, "Thin film shape memory alloy microactuators", *Journal of Microelectromechanical Systems*, vol. 5, no. 4, pp. 270-282, 1996.
125. H. Takao, M. Ishida and K. Sawada, "A pneumatically actuated full in-channel microvalve with MOSFET-like function in fluid channel networks", *Journal of Microelectromechanical Systems*, vol. 11, no. 5, pp.421-426, 2002.
126. H. Takao, K. Miyamura, H. Ebi, M. Ashiki, K. Sawada and M. Ishida, "A thermo-pneumatic microvalve with PDMS diaphragm for integrated blood examination system on silicon", *The 12th International Conference on Solid State Sensors, Actuators and Microsystems, Boston, U.S.A.*, pp. 139-142, 2003.
127. W. K. Schomburg, R. Ahrens, W. Bacher, S. Engermann, P. Krehl and Martin J., "Long-term performance analysis of thermo-pneumatic micropump actuators", *International Conference on Solid State Sensors and Actuators, Chicago, U.S.A.*, pp. 365-368, 1997.
128. R. H. Liu, J. Yang, R. Lenigk, J. Bonanno and P. Grodzinski, "Self-contained fully integrated bio-chip for sample preparation, polymerase chain reaction amplification and DNA microarray detection", *Analytical Chemistry*, vol. 76, pp. 1824-1831, 2004.
129. B. Zalba, J. M. Martin, L. F. Cabeza and H. Mehling, "Review on thermal energy storage with phase change: materials, heat transfer analysis and applications", *Applied Thermal Engineering*, vol. 23, pp. 251-283, 2003.
130. Y. C. Chen and et al., "Ultra-thin phase change bridge memory device using GeSb", *IEEE International Electron Devices Meeting, IEDM '06*, pp.1-4, 2006.
131. D. P. Colvin and Bryant Y. G., "Protective clothing containing encapsulated phase change materials", *ASME Heat Transfer Division Publication*, vol. 362, pp. 123-132, 1998.
132. P. L. Bergstrom, J. Ji, Y. Liu, M. Kaviani and K. D. Wise, "Thermally driven phase-change microactuation", *Journal of Microelectromechanical Systems*, vol. 4, no. 1, pp. 10-17, 1995.
133. S. A. Whalen, S. Y. Won, R. F. Richards, D. F. Bahr and C. D. Richards, "Characterization and modelling of a liquid-vapour phase change membrane actuator with an integrated SU-8 micro capillary wicking structure", *IEEE, The 13th International Conference on Solid State Sensors, Actuators and Microsystems*, pp. 342-347, 2005.
134. M. Kabei, M. Kosuda, H. Kagamibuchi, R. Tashiro, H. Mizuno, Y. Ueda, and K. Tsuchiya, "A thermal expansion type microactuator with paraffin as

- the expansive material (Basic performance of a prototype linear actuator)", *JSME International Journal, Series C*, vol. 40, no. 4, pp. 736-742, 1997.
135. K. Kong, J. Cha, D. Jeon and D. D. Cho, "A rotational type micro biopsy device for the capsule endoscope", *IEEE/RSJ, International Conference on Intelligent Robots and Systems*, pp. 1839-1843, 2005.
  136. V. C. Miles, "*Thermostatic Control: Principles and Practice*", Newnes, 1965.
  137. E. T. Carlen and C. H. Mastrangelo, "Surface micromachined paraffin-actuated microvalve", *Journal of Microelectromechanical Systems*, vol. 11, No. 3, pp. 408-420, 2002.
  138. P. Atkins and J. de Paula, "*Physical Chemistry*", 7 ed., Oxford university press, 2002.
  139. M. Sheplak and J. Dugundji, "Large deflections of clamped circular plates under initial tension and transitions to membrane behaviour", *Journal of Applied Mechanics*, vol. 65, pp. 107-115, 1998.
  140. Y. H. Su, K. S. Chen, D. C. Roberts and S. M. Spearing, "Large deflection analysis of a pre-stressed annular plate with a rigid boss under axi-symmetric loading", *Journal of Micromechanics and Microengineering*, vol. 11, pp. 645-653, 2001.
  141. Y. H. Su and S. M. Spearing, "Nonlinear buckling of microfabricated thin annular plates", *Thin Walled Structures*, vol. 42, pp.1543-1565, 2004.
  142. M. Elwenspoek, T. S. J. Lammerink, R. Miyake and J. H. J. Fluitman, "Towards integrated microliquid handling systems", *Journal of Micromechanics and Microengineering*, vol.4, pp. 227-245, 1994.
  143. S. Dutor and et al., "High pressure speed of sound and compressibilities in heavy normal hydrocarbons:  $nC_{23}H_{48}$  and  $nC_{24}H_{50}$ ", *Journal of Chemical Thermodynamics*, vol. 33, pp. 765-774, 2001.
  144. A. Wego, H. W. Glock, L. Pagel and S. Richter, "Investigations on thermo-pneumatic volume actuators based on PCB technology", *Sensors and Actuators A*, vol. 93, pp. 95-102, 2001.
  145. J. Kim, "Control of turbulent boundary layers", *Physics of Fluids*, Vol. 15, No. 5, pp.1903-1105, 2003.
  146. W. C. Crone, A. N. Yahya and J. H. Perepezko, "Bulk shape memory NiTi with refined grain size synthesized by mechanical alloying", *Materials Science Forum*, vol. 386-388, pp. 597-602, 2002.
  147. Q. Su, S. Z. Hua and M. Wuttig, "Martensitic transformation in  $Ni_{50}Ti_{50}$  films", *Journal of Alloys and Compounds*, vol. 211-212, pp. 460-463, 1994.



148. C. P. Frick, T. W. Lang, K. Spark and K. Gall, "Nanoindentation of NiTi shape memory alloys", *MRS Proceedings on Materials and Devices for Smart System II*, vol. 888, pp. 0888-V04-07 2006.
149. J. P. Bons, M. E. Franke, D. M. Borgeson, M. G. Daniel and W. D. Cowan, "Composite metal-polysilicon MEMS actuators for flow control", *41<sup>st</sup> AIAA Aerospace Sciences Meeting and Exhibit, Nevada, U.S.A.*, no. AIAA-2003-784, 2003.
150. S. S. Dearing, G. G. Arthur, J. Morrison and Z. Cui, "Electroactive polymers for flow control", *IET Seminar on MEMS Sensors and Actuators*, pp. 49-54, 2006.
151. H. Schlichting, "*Boundary-layer theory*", 7<sup>th</sup> ed., McGraw-Hill, 1979.
152. J. R. Roth and X. Dai, "Optimization of the aerodynamic plasma actuator as an electrohydrodynamic (EHD) electrical device", *44<sup>th</sup> AIAA Aerospace Sciences Meeting and Exhibit, Nevada, U.S.A.*, no. AIAA 2006-1203, pp. 1 - 28, 2006.
153. L. B. Freund and S. Suresh, "*Thin film materials - stress, defect formation and surface evolution*", Cambridge university press, 2003.
154. Y. C. Zhou, Z. Y. Yang and X. J. Zheng, "Residual stress in PZT thin films prepared by pulsed laser deposition", *Surface and Coatings Technology*, vol. 162, no. 2-3, pp. 202-211, 2003.
155. M. C. Shine and F. M. d'Heurle, "Activation energy for electromigration in aluminium films alloyed with copper", *IBM Journal of Research and Development*, vol. 15, no. 5, pp. 378-383, 1971.
156. J. R. Black, "Electromigration failure modes in aluminium metallization for semiconductor devices", *Proceedings of the IEEE*, vol. 5, no. 9, pp. 1587-1594, 1969.